THE INFLUENCE OF SYNOPTIC FEATURES ON PRECIPITATION IN THE ARCTIC - LESSONS LEARNED FROM CASE STUDIES AND CLIMATOLOGY

Autor:
Melanie Lauer

Berichterstatter:
Prof. Dr. Susanne Crewell
Prof. Dr. Nikki Vercauteren

Inaugural-Dissertation
zur Erlangung des Doktorgrades
der Mathematisch-Naturwissenschaftlichen Fakultät
der Universität zu Köln

Februar 2024

Declaration

Hiermit versichere ich an Eides statt, dass ich die vorliegende Dissertation selbstständig und ohne die Benutzung anderer als der angegebenen Hilfsmittel und Literatur angefertigt habe. Alle Stellen, die wörtlich oder sinngemäß aus veröffentlichten und nicht veröffentlichten Werken dem Wortlaut oder dem Sinn nach entnommen wurden, sind als solche kenntlich gemacht. Ich versichere an Eides statt, dass diese Dissertation noch keiner anderen Fakultät oder Universität zur Prüfung vorgelegen hat; dass sie - abgesehen von unten angegebenen Teilpublikationen und eingebundenen Artikeln und Manuskripten - noch nicht veröffentlicht worden ist sowie, dass ich eine Veröffentlichung der Dissertation vor Abschluss der Promotion nicht ohne Genehmigung des Promotionsausschusses vornehmen werde. Die Bestimmungen dieser Ordnung sind mir bekannt. Darüber hinaus erkläre ich hiermit, dass ich die Ordnung zur Sicherung guter wissenschaftlicher Praxis und zum Umgang mit wissenschaftlichem Fehlverhalten der Universität zu Köln gelesen und sie bei der Durchführung der Dissertation zugrundeliegenden Arbeiten und der schriftlich verfassten Dissertation beachtet habe und verpflichte mich hiermit, die dort genannten Vorgaben bei allen wissenschaftlichen Tätigkeiten zu beachten und umzusetzen. Ich versichere, dass die eingereichte elektronische Fassung der eingereichten Druckfassung vollständig entspricht.

Melanie Lauer

Köln, Februar 2024

TEILPUBLIKATIONEN

- Lauer, M., A. Rinke, I.V. Gorodetskaya, M. Sprenger, M. Mech, and S. Crewell (2023). "Influence of atmospheric rivers and associated weather systems on precipitation in the Arctic." In: *Atmospheric Chemistry and Physics, 3, 8705-8726. DOI: 10.5194/acp-23-8705-2023*

  Dieser Artikel wurde als Kapitel 3 in die Dissertation eingebunden. Alle Analysen wurden eigenständig durchgeführt und die Abbildungen von mir selbst erstellt. Das Konzept dieses Artikels wurde mit Hilfe von Susanne Crewell und Annette Rinke entwickelt. Irina Goroetskaya hat den Algorithmus für die Detektion von atmosphärischen Flüssen zur Verfügung gestellt. Michael Sprenger hat die detektierten Zyklonen und Fronten zur Verfügung gestellt. Die Eregbnisse wurden selbst analysiert und im Anschluss mit allen Koautoren diskutiert und bei Bedarf angepasst.

- Lauer, M., M. Mech, B. Guan (2023). "Global Atmospheric Rivers catalog for ERA5 reanalysis". In: *PANGEA. DOI: 10.1594/PANGAEA.957161*

  Dieser Datensatz enthält die detektierten atmosphärischen Flüsse basierend auf ERA5 Reanalysedaten. Der Algorithmus zur Detektion wurde von Bin Guan zur Verfügung gestellt. Die dafür notwendigen Daten wurden selbstständig prozessiert und der Detektionsalgorithmus selbstständig angewendet. Mario Mech stand für technische Fragen zur Verfügung.

- Kirbus, B., S. Tiedeck, A. Camplani, J. Chylik, S. Crewell, S. Dahlke, K. Ebell, I. Gorodetskaya, H. Griesche, D. Handorf, I. Höschel, M. Lauer, R. Neggers, J. Rückert, M. D. Shupe, G. Spreen, A. Walbröl, M. Wendisch, and A. Rinke (2023). "Surface impacts and associated mechanisms of a moisture intrusion into the Arctic observed in mid-April 2020 during MOSAiC." In: *Frontiers in Earth Science, 11:1147848. DOI: 10.3389/feart.2023.1147848*

  Die Idee zu diesem Artikel entstand im Cross-Cutting-Activity Projekts 4 im Rahmen des *Transregional Collaborative Research Centre 172: Arctic Amplification: Climate Relevant Atmospheric and Surface Processes and Feedback Mechanisms (AC)*^{3}. Abbildung 8 wurde in Kapitel 2 eingebunden. Die Abbildung wurde selbst erstellt und analysiert.

Abstract

During the last decades, the Arctic has warmed faster than the rest of the globe. This phenomenon is known as Arctic amplification (AA). Many processes contribute to changes in the Arctic, including the increased poleward moisture transport. The poleward moisture transport increases the cloud cover and water vapor content in the Arctic which amplifies the near-surface warming and sea ice melting. In addition, the increased water vapor transport influences the precipitation in the Arctic. Precipitation is a key climate variable and plays a crucial role in the Arctic climate system. It can affect the atmosphere due to thermodynamic processes and surface characteristics such as the surface mass balance, surface energy budget, surface albedo, and also the formation of sea ice. As a warmer atmosphere has a higher moisture capacity, it is expected that Arctic precipitation will increase in the future. Further, a phase transition from snow to rain will lead to a rain-dominated Arctic which could accelerate the sea ice melting and consequently near-surface warming (the so-called ice-albedo feedback).

In this thesis, the goal is to investigate the influence of poleward moisture transport related to atmospheric rivers (ARs), cyclones, and fronts on precipitation in the Arctic. For the analyses, the ERA5 global reanalysis data with its high spatial and temporal resolution is used. The ERA5 data is initially evaluated by comparing it with ground-based and spaceborne remote-sensing measurements for two AR events. For the first AR event, the vertical profile of radar reflectivities and hydrometeors are compared, while for the second AR event, the focus was on the surface snowfall rate. Generally, ERA5 reanalyses represent the vertical structure of the precipitation systems very well. There are also deviations, especially over complex terrain, and in representing small-scale features. Nevertheless, ERA5 represents larger precipitation features and AR positioning that are related to synoptic features in a satisfying way.

Within the framework of this thesis, a new methodology has been established to distinguish between AR-, cyclone-, and front-related precipitation. This method takes into account whether these synoptic features are co-located or separated (not co-located) from each other. First, the method is applied for two distinct periods from two airborne campaigns: ACLOUD (Arctic Cloud Observations Using airborne measurements during polar day; May/June 2017) and AFLUX (Aircraft campaign Arctic Boundary Layer Fluxes; March/April 2019). The contribution of ARs, cyclones, and fronts to precipitation differs between the periods. During the early summer campaign, the precipitation is mainly associated with AR- (40%) and front-related (55%) components, especially when they are co-located. The early spring campaign shows another pattern. During this campaign, the precipitation was mainly concentrated in the cyclone-related components (62%), especially when they were not co-located. The difference in contribution during the early summer and early spring campaigns was later confirmed in the climatological analyses.

Throughout the ERA5 period (1979 – 2021), the precipitation is not evenly distributed over the Arctic. 45% of the total precipitation is concentrated over the Arctic North Atlantic sector and the Kara and Barents Seas. The remaining precipitation (55%) is more evenly distributed over the other regions. The analyses showed also spatio-temporal variations in the total accumulated precipitation. During summer, the precipitation is evenly distributed over the entire Arctic and has its maximum

in August. In the other seasons, the Arctic North Atlantic and the Kara and Barents Seas are most affected by precipitation. Further, there are differences in the type and form of precipitation. Considering the type of precipitation, 86% is classified as large-scale precipitation, and only 14% is convective precipitation. 70% of the precipitation is in the form of snow, while 30% is in the form of rain. Generally, snowfall is the dominant type of precipitation from October to May, and rainfall in July and August. Further, rainfall is located mostly over the Arctic North Atlantic.

Slightly more than half of the total precipitation (56%) is attributable to ARs, cyclones, and fronts. The precipitation is mainly associated with cyclones (30%). Only 13% of the total precipitation is associated with ARs and 19% with fronts. The sum of these values exceeds the 56% mentioned, as part of the precipitation occurs when the synoptic features are co-located. The AR-, cyclone- and front-related precipitation shows also spatio-temporal differences as well as differences between rain and snow. Throughout the year, cyclones contribute similary to the total precipitation, while ARs and fronts become more effective in summer. During winter, the cyclone-related precipitation is mainly concentrated over the Arctic North Atlantic and the Kara and Barents Seas. In summer, the AR-, cyclone-, and front-related precipitation is more evenly distributed with a higher contribution over the Barents, Kara, and Laptev Seas. Generally, cyclones and fronts contribute more to precipitation than ARs. This correlates with the frequency of their occurrence. Cyclones occur three times and fronts two times more often than ARs, and they also cover a greater area. Nevertheless, AR-related precipitation is more intense compared to cyclone- and front-related precipitation.

It is worth noting that 44% of the precipitation cannot be assigned to any of the synoptic features. This amount is classified as residual. The residual is higher for snowfall (50%) than for rainfall (24%) and has its maximum in winter over the Arctic North Atlantic. Further analyses reveal that the residual over the Arctic North Atlantic can mainly be attributed to marine cold air outbreaks (CAOs). Considering CAOs, the occurrence of the residual would decrease from 15% to 5% over this region. The residual over the other regions is less affected by CAOs. Applying a threshold of 0.1 mm hr^{-1} has shown that these regions are mainly affected by light precipitation rates which are not associated with synoptic features. Especially over the Arctic Ocean, up to 50% of the total precipitation has precipitation rates lower than 0.1 mm hr^{-1}. This highlights the importance of light precipitation, especially with regard to snowfall. Applying a threshold would not only decrease the residual, but it would also increase the contribution rates of synoptic features, especially ARs, to the total precipitation in the Arctic.

Trend analyses show a significant increase in convective and large-scale rainfall over the Arctic North Atlantic and the Kara and Barents Seas. The positive trend over the Arctic North Atlantic is mainly related to ARs and fronts, while the positive trend over the Kara and Barents Seas is mainly related to cyclones and CAOs. There are also differences between convective and large-scale precipitation. A significant increase in convective precipitation over the Kara and Barents Seas is evident which could be associated with sea ice retreat leading to local evaporation. For the large-scale precipitation, the significance is less pronounced because of compensating trends, i.e., a negative trend in snowfall and a positive trend in rainfall. This highlights a phase change from snow to rain in these regions and no increase in total precipitation.

Zusammenfassung

In den letzten Jahrzehnten hat sich die Arktis schneller erwärmt als der Rest der Welt. Dieses Phänomen wird als arktische Amplifikation (Arctic amplification, AA) bezeichnet. Zu den Veränderungen in der Arktis tragen mehrere Prozesse bei, darunter ein verstärkter polwärts gerichteter Feuchtetransport. Dieser verstärkt die Wolkendecke und den Wasserdampfgehalt in der Arktis, was die oberflächennahe Erwärmung und das Abschmelzen des Meereises verstärkt. Darüber hinaus beeinflusst der verstärkte Wasserdampftransport den Niederschlag in der Arktis. Niederschlag ist eine wichtige Klimavariable und spielt eine entscheidende Rolle im arktischen Klimasystem. Er kann durch thermodynamische Prozesse die Atmosphäre und Oberflächeneigenschaften wie die Massenbilanz der Oberfläche, den Energiehaushalt der Oberfläche, die Oberflächenalbedo und die Bildung von Meereis beeinflussen. Da eine wärmere Atmosphäre mehr Feuchtigkeit aufnehmen kann, ist zu erwarten, dass der Niederschlag in der Arktis zukünftig zunehmen wird. Außerdem wird ein Phasenübergang von Schnee zu Regen zu einer von Regen dominierten Arktis führen, was das Abschmelzen des Meereises und damit die oberflächennahe Erwärmung beschleunigen könnte (so genannte Eis-Albedo-Rückkopplung).

In der vorliegenden Arbeit soll der Einfluss des polwärts gerichteten Feuchtigkeitstransports im Zusammenhang mit atmosphärischen Flüssen (atmospheric rivers, ARs), Zyklonen und Fronten auf den Niederschlag in der Arktis untersucht werden. Für die Analysen werden ERA5-Reanalysedaten verwendet, die eine hohe räumliche und zeitliche Auflösung bieten. Die ERA5-Daten werden zunächst durch einen Vergleich mit bodengestützten und Fernerkundungs-Messungdaten zu zwei ARs bewertet. Für das erste AR-Ereignis wird das vertikale Profil der Radarreflexion und der Hydrometoren verglichen, während bei einem zweiten AR-Ereignis der Schwerpunkt auf der Oberflächenschneefallrate gelegt wird. Grundsätzlich bilden die ERA5-Reanalysen die vertikale Struktur der Niederschlagssysteme sehr gut ab. Insbesondere über komplexem Gelände und bei der Darstellung kleinräumiger Merkmale treten jedoch Abweichungen gegenüber den tatsächlichen Gegebenheiten auf. Dennoch stellt ERA5 größere Niederschlagsmerkmale, die mit synoptischen Merkmalen verbunden sind, zufriedenstellend dar.

Im Rahmen dieser Arbeit wird eine neue Methode enwtickelt, um zwischen AR-, zyklonen - und frontenbedingtem Niederschlag zu unterscheiden. Bei dieser Methode wird berücksichtigt, ob diese synoptischen Merkmale zusammen oder getrennt voneinander auftreten. Zunächst wird die Methode für zwei unterschiedliche Zeiträume aus zwei Flugzeugkampagnen angewandt: ACLOUD (Arctic Cloud Observations Using airborne measurements during polar day; Mai/Juni 2017) und AFLUX (Aircraft campaign Arctic Boundary Layer Fluxes; März/April 2019). Der Beitrag von ARs, Zyklonen und Fronten zum Niederschlag ist in den beiden untersuchten Zeiträumen unterschiedlich. Während der Frühsommerkampagne war der Niederschlag hauptsächlich mit AR-(40%) und frontbezogenen (55%) Komponenten verbunden, insbesondere wenn diese zusammen auftreten. Die Kampagne im Frühjahr zeigte ein anderes Muster. Während dieser Kampagne zeigte sich der Niederschlag hauptsächlich im Zusammenhang mit Zyklonen (62%) – vor allem,

wenn diese einzeln auftraten. Der unterschiedliche Beitrag der synoptischen Merkmale zum Niederschlag in den beiden Kampagnen wurde später durch die klimatologischen Analysen bestätigt.

Während des gesamten ERA5-Zeitraums (1979 - 2021) ist der Niederschlag nicht gleichmäßig über die Arktis verteilt. 45% des Gesamtniederschlags konzentrieren sich auf den arktischen Nordatlantik sowie die Kara- und Barentssee. Die Analysen zeigten auch räumliche und zeitliche Schwankungen des akkumulierten Niederschlags. Im Sommer ist der Niederschlag gleichmäßig über die gesamte Arktis verteilt und hat sein Maximum im August. In anderen Jahreszeiten sind der arktische Nordatlantik sowie die Kara- und Barentssee am stärksten von Niederschlag betroffen. Darüber hinaus treten Unterschiede in der Art und Form des Niederschlags zutage. Bei 86% des Niederschlags handelt es sich um großräumigen Niederschlag und nur 14% sind konvektiver Niederschlag. 70% des Niederschlags fallen in Form von Schnee, während Regen 30% des Niederschlags ausmacht. Bei der vorherrschenden Niederschlagsart handelt es sich von Oktober bis Mai um Schnee; im Juli und August hingegen um Regen. Die Untersuchung zeigt weiter, dass die Niederschläge hauptsächlich über dem arktischen Nordatlantik fallen.

Etwas mehr als die Hälfte des Gesamtniederschlags (56%) ist auf ARs, Zyklonen und Fronten zurückzuführen. Dabei ist der Niederschlag hauptsächlich mit Zyklonen verbunden (30%). Nur 13% des Gesamtniederschlags werden mit ARs und 19% mit Fronten in Verbindung gebracht. Die Summe dieser prozentualen Werte übersteigt den zuvor genannten Anteil von 56% am Gesamtniederschlag, da Niederschlag, der mit mehreren gleichzeitig auftretenden synoptischen Merkmalen zusammenhängt, in der Einzelauswertung bei jedem dieser Merkmale – mithin doppelt – erfasst wird. Im Hinblick auf den Niederschlag im Zusammenhang mit ARs, Zyklonen und Fronten treten ebenfalls raum-zeitliche Unterschiede sowie Unterschiede zwischen Regen und Schnee auf. Zyklonen tragen das ganze Jahr über in ähnlicher Weise zum Gesamtniederschlag bei, während der Einfluss von ARs und Fronten im Sommer zunimmt. Im Winter konzentrieren sich die zyklonenbedingten Niederschläge hauptsächlich auf den arktischen Nordatlantik sowie die Kara- und Barentssee. Im Sommer sind die AR-, zyklonen - und frontenbedingten Niederschläge zwar insgesamt gleichmäßiger verteilt; ein Schwerpunkt liegt gleichwohl über der Barents-, Kara- und Laptewsee. Grundsätzlich tragen Zyklonen und Fronten mehr zum Niederschlag bei als ARs. Dies korreliert mit der Häufigkeit ihres Auftretens. Zyklonen treten dreimal und Fronten zweimal häufiger auf als ARs; darüber hinaus bedecken sie ein größeres Gebiet als ARs. Gleichwohl sind AR-bedingte Niederschläge im Vergleich zu zyklonen - und frontenbedingten Niederschlägen intensiver.

Es ist weiter erwähnenswert, dass 44% der Niederschläge keinem der synoptischen Merkmale zugeordnet werden können. Dieser Niederschlag wird als Residuum eingestuft. Das Residuum ist bei Schneefall (50%) höher als bei Regen (24%) und hat sein Maximum im Winter über dem arktischen Nordatlantik. Weitere Analysen haben gezeigt, dass das Residuum über dem arktischen Nordatlantik auf marine Kaltluftausbrüche (cold air outbreaks, CAOs) zurückgeführt werden kann. Unter Berücksichtigung der CAOs würde das Residuum über dieser Region von 15% auf 5% sinken. Das Residuum über anderen arktischen Regionen wird durch CAOs weniger beeinflusst. Die Festsetzung eines Schwellenwerts für den Niederschlag von 0.1 mm hr^{-1} hat gezeigt, dass diese Regionen hauptsächlich von leichten Niederschlagsmengen betroffen sind, die nicht mit synoptischen Merkmalen verbunden

sind. Insbesondere über dem Arktischen Ozean stehen bis zu 50% des Gesamtniederschlags mit Niederschlagsmengen von weniger als 0.1 mm hr^{-1} in Verbindung. Dies unterstreicht die Bedeutung der leichten Niederschläge, insbesondere im Hinblick auf Schneefall. Die Anwendung des Schwellenwerts verringert nicht nur den Anteil des Residuums , sondern auch den prozentualen Anteil des Beitrags, den die synoptischen Merkmale , insbesondere ARs, zum Gesamtniederschlag in der Arktis leisten.

Trendanalysen zeigen eine signifikante Zunahme des konvektiven und großräumigen Regens über dem arktischen Nordatlantik und der Kara- und Barentssee. Der positive Trend über dem arktischen Nordatlantik hängt im Wesentlichen mit ARs und Fronten zusammen, während der positive Trend über der Kara- und Barentssee hauptsächlich mit Zyklonen und CAOs in Verbindung steht. Es treten ferner Unterschiede zwischen konvektivem und großräumigem Niederschlag auf. Auf der Grundlage der ERA5-Daten ist eine signifikante Zunahme des konvektiven Niederschlags über der Kara- und Barentssee erkennbar. Dies könnte mit einem Rückgang des Meereises zusammenhängen, der lokale Verdunstung begünstigt. Bei großräumigen Niederschlägen ist die Signifikanz weniger ausgeprägt, da zum einen ein negativer Trend beim Schneefall, zum anderen ein positiver Trend beim Regen zu verzeichnen ist. Dies deutet auf einen Phasenwechsel von Schnee zu Regen in diesen Regionen hin und nicht auf eine Zunahme des Gesamtniederschlags.

Contents

Chapter 1

Introduction

The Arctic cryosphere is an integral part of the Earth's climate system. In recent decades, the Arctic has changed significantly due to climate change (Cohen et al., 2014; Turner and Marshall, 2011; Yang and Kane, 2021; Wendisch et al., 2023). The higher temperatures in the Arctic have caused the retreat of glaciers, the thawing of permafrost as well as a decline in sea ice extent and thickness (Overland et al., 2019). The rapid loss of sea ice is one of the most important reasons for the recent Arctic warming. These changes in the Arctic have consequences for the Arctic itself and the mid-latitudes (Turner and Marshall, 2011).

In general, the warming amplifies the hydrological cycle and increases the precipitation in the Arctic (Bintanja, 2018; Box et al., 2019; Bintanja et al., 2020). According to the Clausius-Clapeyron relation, an increase in temperature enhances the atmospheric water vapor which is one of the most effective greenhouse gases by roughly 7% per degree warming (Bintanja and Selten, 2014). There are two main moisture sources for enhanced water vapor in the Arctic. These are the locally enhanced evaporation due to the missing insulation effect of sea ice (Bintanja and Selten, 2014) and the poleward moisture transport from lower latitudes (Zhang et al., 2013). The increased moisture content in the atmosphere contributes to cloud formation in the Arctic and could affect near-surface Arctic warming in two different ways. First, water vapor and clouds increase the downward longwave radiation to the surface, which amplifies the near-surface warming and sea-ice decline (Sejas et al., 2014; Naakka et al., 2019). Second, it enhances the precipitation in the Arctic (Bintanja and Selten, 2014; Bintanja, 2018).

Precipitation is a critical component in the Arctic climate system. It plays an essential role in the Arctic hydrological cycle and has a direct impact on the Arctic ocean and land freshwater budget (Vihma et al., 2016). It influences atmospheric thermodynamics due to phase changes (Bintanja, 2018) and surface characteristics like snow depth, mass balance, and surface albedo (Naakka et al., 2019; Vihma et al., 2016). In the Arctic, snow is the predominant type of precipitation and contributes significantly to the mass balance of the Greenland ice sheet, the ice caps, and the glaciers. Further, it influences sea ice growth and decay through different mechanisms (Leppäranta, 1993; Cheng et al., 2008). In contrast, rain on sea ice decreases the albedo and is related to sea ice melting (Gimeno-Sotelo et al., 2019). However, it also provides a source for superimposed ice formation which temporally favoring the thickness of the Arctic sea ice (Vihma et al., 2016; Gimeno-Sotelo et al., 2019).

Climate models project a strong increase in Arctic precipitation (Bintanja and Andry, 2017; McCrystall et al., 2021; Bintanja et al., 2020). Bintanja et al., 2020 argued that the precipitation in the Arctic increases by 4.2% per degree warming. An

increase in precipitation could affect the Greenland and Antarctic ice sheet, weaken the thermohaline circulation, and intensify the ice- and snow-albedo feedback which modulates the growth and melt of sea ice throughout the year. In the future, rain will be the dominant type of precipitation (Bintanja, 2018). In a warmer climate, there will be a phase transition from snow to rain. The largest changes will be in spring and autumn. Therefore, the snow-rain transition will be earlier in spring and the rain-snow transition will be later in autumn (Vihma et al., 2016). This local warming does explain 70% of the increase in rainfall (Bintanja et al., 2020). The other 30% is due to the higher moisture capacity of the warmer atmosphere (Bintanja et al., 2020). The phase change from snow to rain could have significant consequences on sea ice and Arctic warming.

Further, Bintanja et al., 2020 suggest that the increase in precipitation is mainly related to an increase in poleward moisture transport. The role of poleward moisture on precipitation for the past climate in the Arctic has not yet been investigated. As the poleward moisture transport is often associated with extratropical cyclones and atmospheric rivers (ARs) (Sorteberg and Walsh, 2008; Woods et al., 2013; Woods and Caballero, 2016; Rinke et al., 2017), the overarching goal of this thesis is to gain a better understanding of the extent to which these synoptic features contribute to precipitation in the Arctic.

1.1 Arctic Amplification

As early as the 19th century, the Swedish scientist Svante Arrhenius predicted that changes in carbon dioxide (CO_2) concentrations would lead to changes in the Earth's near-surface temperature. These changes in surface temperature would be particularly pronounced in the polar regions (Arrhenius, 1896). This has been particularly evident in recent decades. Over the last four decades, the increase in near-surface air temperature in the Arctic has been almost four times higher than that of the global average (Rantanen et al., 2022) (Fig. 1.1). This phenomenon is known as Arctic amplification (AA) (Serreze and Barry, 2011). The AA is more pronounced in autumn and winter and over the Arctic Ocean than in spring and summer and over land (Serreze and Barry, 2011; Cohen et al., 2014). The lower warming occurs in summer because most of the absorbed solar energy is used for melting processes (Turner and Marshall, 2011). The additional heat absorbed by the ocean is released back into the atmosphere in autumn and early winter, contributing to the warming in these seasons (Jeffries et al., 2013).

In the 2004 Arctic Climate Impact Assessment (ACIA) report (Berner et al., 2005), they highlight some possible causes for the faster warming in the Arctic than in the lower latitudes:

- The melting of snow- and ice-covered surfaces exposes darker surfaces. These snow- and ice-free surfaces absorb much of the solar radiation, leading to the warming that drives further melting.
- In the Arctic, much of the radiation absorbed by greenhouse gases contributes directly to atmospheric warming, while at lower latitudes, some of the energy is used for evaporation.

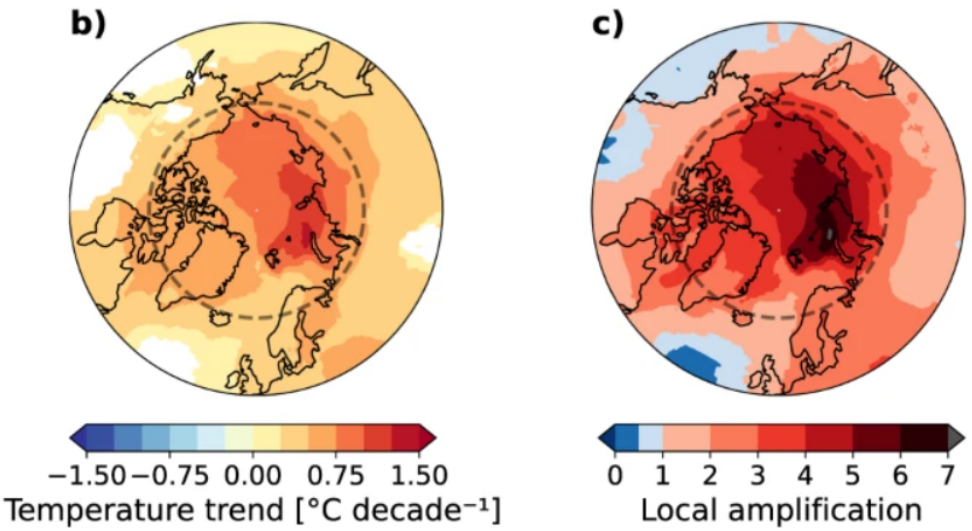

FIGURE 1.1: Regional map highlighting warming in the Arctic. Left: Annual mean temperature trends for 1979-2021; right: Local amplification ratio calculated for the period 1979-2021. Source Rantanen et al., 2022.

- The atmosphere in the polar regions is thinner than in the rest of the world. It therefore heats up more quickly.
- The heat exchange between the ocean and the atmosphere increases as the ice cover decreases. As a result, the ocean releases more heat energy into the atmosphere during the winter months.
- Changes in the atmospheric and oceanic circulation could increase the warming in the Arctic.

Several factors contribute to Arctic winter warming. These include feedback mechanisms such as the lapse-rate and snow- and ice-albedo feedback, the poleward heat and moisture transport and the associated increasing downward longwave radiation caused by clouds and water vapor, the poleward heat and moisture transport, and reduced summer sea ice (Kim and Kim, 2017; Serreze and Barry, 2011; Bintanja and Van Der Linden, 2013; Cohen et al., 2014; Pithan and Mauritsen, 2014; Sejas et al., 2014).

The poleward moisture transport increases the water vapor concentration and cloud cover. The greenhouse effect of water vapor and clouds increases the downward longwave radiation leading to higher near-surface air temperatures (Jeffries et al., 2013). The increase in the near-surface air temperature slows the growth and thickness of sea ice in winter. As a result, the thinner sea ice in spring is more susceptible to melting (Cohen et al., 2014). This melting creates open, dark ocean surfaces that absorb incoming radiation and consequently enhance the sea ice melt in summer (Jeffries et al., 2013; Cohen et al., 2014). In addition, meltwater ponds and soot deposition could cause further melting of sea ice and snow (Jeffries et al., 2013). Due to the lack of insulation from sea ice, the Arctic Ocean absorbs more solar radiation in summer (Kim et al., 2016). The warmer ocean in turn limits the formation of sea ice in the following autumn and winter. In autumn, the ocean is warmer than the atmosphere, so the heat absorbed in summer is released to the atmosphere via radiative

and turbulent fluxes, warming the lower Arctic troposphere (Francis and Hunter, 2007; Serreze and Barry, 2011; Graversen et al., 2008). Thus, the rapid warming and sea-ice loss have had significant local impacts, particularly in late summer and early autumn (Cohen et al., 2014). These described processes highlight the importance of poleward heat and moisture transport, in particular the effect on sea ice.

However, not only the sea ice but also the snow cover in spring and summer has decreased (Cohen et al., 2014). Melting snow and ice exposes darker ocean and land surfaces, reducing the surface albedo. These ice- and snow-free surfaces absorb the incoming solar radiation and warm the oceanic mixed layer and land surface. Thus, the combination of sea ice loss and snow cover retreat in spring and summer amplifies Arctic warming (Cohen et al., 2014).

1.2 Arctic precipitation

Water is a fundamental component of the Earth. While the oceans contain 97% of the world's water, the rest is stored in lakes, rivers, ground reservoirs, ice caps, and snow. The atmosphere, in particular, holds only 0.001% of all water (Chahine, 1992), whereby only 1.5% of the atmospheric moisture is concentrated in the Arctic (Vihma et al., 2016). This highlights the dry conditions in the Arctic. Globally, the water is exchanged between the ocean, the atmosphere, and the biosphere due to evaporation and precipitation. Arctic precipitation plays a vital role in the water and energy cycles that sustain the ecosystem of the Arctic (Yang and Kane, 2021). Precipitation influences atmospheric thermodynamics due to phase changes (Bintanja, 2018) and surface characteristics like snow cover and depth, mass balance, and albedo (Vihma et al., 2016; Naakka et al., 2019). Over the Arctic Ocean, precipitation has an impact on the Arctic freshwater budget, ocean circulation, surface energy budget, and the sea ice cover (Serreze and Hurst, 2000).

In general, snow increases the albedo over land and sea ice. As snow is a thermal isolator, it separates the underlying surface from the atmosphere above. Depending on the season, snow over sea ice has a positive and negative effect. In winter, the snow cover over sea ice enhances the thermal insulation. Consequently, the snow cover over sea ice reduces the sea ice growth (Gimeno-Sotelo et al., 2019). However, snow on sea ice can also enhance the sea ice growth via snow-to-ice transformation. Here, sea water floods into the snow layer and refreeze to slush (Vihma et al., 2016). In summer and spring, snow increases the surface albedo. The higher surface albedo prevents the sea ice from melting (Gimeno-Sotelo et al., 2019). Over land, snow also has a thermal insulation effect for permafrost. Thus, snow is responsible for both the persistence and decay of permafrost (Yang and Kane, 2021). In contrast, rain on sea ice reduces the surface albedo. The lower albedo contributes to sea ice melting (Gimeno-Sotelo et al., 2019). However, rain also provides a source for superimposed ice formation, which temporally favors the Arctic sea ice thickness (Vihma et al., 2016; Gimeno-Sotelo et al., 2019). Further, rain melts the terrestrial snow cover (Vihma et al., 2016).

Due to the different effects of snow and rain on the surface characteristics, a future phase change from snow to rain would affect the sea ice albedo and the surface

mass balance (Vihma et al., 2016). Climate models simulate a later autumn freeze-up leading to less snow that remains on sea ice in spring and summer (Vihma et al., 2016). Thus, a decrease in summer snowfall and an increase in rain will significantly contribute to the Arctic sea ice decline (Vihma et al., 2016). As mentioned above, a decrease in snow on sea ice decreases the albedo. The lower albedo causes the melting of sea ice and the forming of melt ponds on sea ice, further lowering the albedo (Vihma et al., 2016).

Light rain and snowfall that is not measurable is called trace precipitation. Trace precipitation mainly occurs in regions with extremely low temperatures, and is very common in the Arctic (Yang and Kane, 2021). Since the total precipitation amount in the Arctic is very small, the sum of all trace amounts makes up a significant proportion of the total Arctic precipitation (Yang and Kane, 2021). Thus, trace precipitation increases the amount of total precipitation by 20% (Yang and Kane, 2021). In terms of total wet days in summer and winter, 51% and 69% of the total wet days, respectively, have precipitation rates below 1 mm (Yang and Kane, 2021). This highlights how important it is to improve the measurements for light precipitation rates.

Due to the cold conditions in the Arctic, snow is the dominant type of precipitation. For a warmer climate, climate models simulate a phase transition from snow to rain. Consequently, there will be a rain-dominated Arctic in the future (Bintanja, 2018; McCrystall et al., 2021). Precipitation derived from reanalysis data, however, does not increase with time as expected (Boisvert et al., 2018; Barrett et al., 2020). However, a decrease in snowfall is found (Boisvert et al., 2018) which is compensated by an increase in rainfall amount and frequency. This phase transition from snow to rain can be related to a warming Arctic climate and is especially pronounced over the North Atlantic which is the region most affected by cyclones (Boisvert et al., 2018).

1.2.1 Challenges in precipitation measurements

Precipitation is one of the most critical variables for the Arctic terrestrial hydrology but is also one of the most challenging variables to measure due to various reasons: the cold snow-dominated environment, the sparsely distributed in-situ observations, low precipitation amounts, the scarcity of long-term records, the heterogeneity of the landscape, and the difficulties in remote sensing over sea ice (Serreze and Hurst, 2000; Yang et al., 2005; Boisvert et al., 2018).

The main challenge concerns sparse and accurate in-situ observations. The sparse in-situ observations are a problem, particularly over the Arctic Ocean (Vihma et al., 2016). Figure 1.2 shows the uneven and sparsely distributed precipitation measuring stations in the Arctic. Since 1990, there has been a substantial decrease in the number of precipitation stations in the Arctic (Yang and Kane, 2021). North of 65°N, there are only 38 radiosonde stations over land that measure the vertical profiles of air (Vihma et al., 2016; Nygård et al., 2014). Consequently, representative measurements due to the northern regions' sparse observation systems are impossible (Walsh, 2022).

Solid precipitation which is the dominant type of precipitation in the Arctic, is difficult to measure accurately - especially windy conditions that favour the undercatchment of blowing or drifting snow (Vihma et al., 2016; Walsh, 2022; Yang and

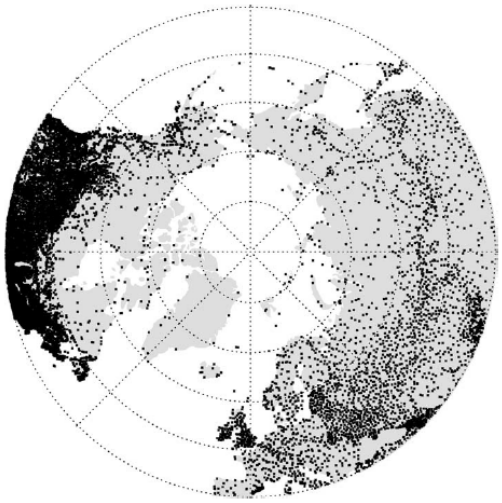

FIGURE 1.2: Distribution of precipitation measuring stations north of 40° N with at least ten years of records for the period 1960–89. Source: Serreze and Barry, 2014.

Kane, 2021). Therefore, measurements have to be bias-corrected. Thus, during the last decades, bias corrections have been developed (Vihma et al., 2016). The bias correction factor depends on the choice of the correction method (Fuchs et al., 2001). It is largest for solid precipitation and ranges up to 300% (Fuchs et al., 2001). Another problem with measuring Arctic precipitation is that the instruments can be affected by ice if they are unheated or unventilated (Vihma et al., 2016).

Over the Arctic Ocean, the snowfall is measured by the Russian North Pole (NP) drifting stations since 1930. They provide measurements of the amount, occurrence, and phase of precipitation as well as the snow cover. As for ground-based measurements over land, they undercatch the snowfall due to the harsh and windy conditions in the Arctic. There are also uncertainties due to evaporation from gauges, condensation on the inside of gauges, neglect of trace precipitation, and false precipitation due to blowing snow (Barrett et al., 2020). Despite these uncertainties, they are the best data source over the Arctic Ocean.

In addition to the sparse ground-based measurements, satellites can provide full aerial coverage – for land and ocean. Similar to ground-based measurements, satellite remote sensing measurements also contain significant uncertainties (Behrangi et al., 2012). This is particularly true in high latitudes, as satellites do not continuously cover the whole Arctic (Vihma et al., 2016; Behrangi et al., 2012). For example, the polar-orbiting satellite CloudSat does not reach further than 82° of the respective hemisphere. Furthermore, the temporal sampling of repeated ground tracks every 16 days is too coarse to analyse short-lived precipitation events.

Additionally, satellites have problems distinguishing the signal originating from the snow/ice-covered Earth's surface and the atmosphere (Vihma et al., 2016). This reduces the accuracy of satellite remote-sensing observations on cloud water and ice contents. As satellites do not measure the precipitation directly, they use retrieval products to measure precipitation which also include errors (Serreze et al., 2005).

On board of satellites, four major types of sensors make precipitation estimation possible. These are infrared (IR) and microwave (MW) imagers, sounders, and radars. IR imagers have problem with precipitation on fine spatiotemporal scales and for warm rain events (Behrangi et al., 2009; Yang and Kane, 2021). Compared to IR, MW imagers are more closely related to precipitation (Yang and Kane, 2021). The advantage of MW imagers is that they operate during the night, and thus during polar night in the Arctic, and they can penetrate clouds. Therefore, they are able to detect hydrometeors throughout the atmosphere. MW imagers are sensitive to liquid water (at low frequencies) and ice particles (at high frequencies) (Wilheit, 1986; Yang and Kane, 2021). However, MW imagers also have limitations: MW sensors are not sensitive enough to light rain and snowfall, they lack knowledge of the surface emissivity over snow and frozen ground, and they have problems distinguishing light rain from clouds (Ferraro et al., 2013; Berg et al., 2006; Lebsock and L'Ecuyer, 2011).

Further, there are difficulties with MW-based retrievals of precipitation at high latitudes due to the poor knowledge of the microphysics of precipitation and, thus, of the precipitation phase (Petty, 1997; Liu, 2008; Yang and Kane, 2021). Compared to IR and MW imagers, radars typically provide the most direct and fine-scale observations of precipitation (Yang and Kane, 2021). However, they are not sensitive enough to retrieve light rain and snow (Yang and Kane, 2021).

1.2.2 Uncertainties in reanalysis data

The sparse ground-based observations and the lack of continuous satellite observations make it difficult to analyse the poleward moisture transport and its influence on precipitation. Reanalyses are therefore an important tool for analysing climate in data-poor regions such as the Arctic. Reanalysis data assimilate information from various sources, e.g. surface stations, radiosondes, satellites, buoys, ships, and aircraft. The estimation of precipitation over the Arctic Ocean depends on the quality of the input precipitation fields (Barrett et al., 2020).

The uncertainties in measuring snowfall also affect the precipitation products from reanalyses. In the last decade, several studies compared reanalysis-derived precipitation with observations from the Russian NP drifting stations (Serreze et al., 2005; Boisvert et al., 2018; Boisvert et al., 2021; Barrett et al., 2020). Serreze et al., 2005 found that reanalyses (e.g. ERA-40) performed better than satellite-retrieved precipitation from the Global Climatology Project (GPCP) compared to NP stations. In 2011, Cullather and Bosilovich, 2011 compared MERRA reanalyses precipitation with NP stations and found that MERRA overestimates the precipitation by 11%. Further, MERRA estimates for 56% of the observations precipitation, while NP stations reported no precipitation.

In recent years, precipitation from different reanalysis products has been compared. Boisvert et al., 2018 focused on the period from 2000-2016. Generally, the interannual variability is similar among all reanalyses, through there are deviations in magnitude, frequency, and phase of precipitation. In another study, Boisvert et al., 2021 focused on wintertime precipitation over the North Atlantic from 2000-2019, including ERA5 reanalysis data. Here, they found that large differences in the magnitude occur especially in areas with higher precipitation rates. They conclude that

observations and reanalyses agree in regions with lower precipitation rates and not in areas with higher rates. A similar pattern has been found for mid-latitudes and tropics for which most reanalyses underestimate the magnitude of heavy precipitation events (Boisvert et al., 2021).

Barrett et al., 2020 extend the period from 1979 to 2019 and also include ERA5. Similar to Boisvert et al., 2018, the time series of annual precipitation over the central Arctic Ocean correlates between all reanalyses and they capture the spatial and seasonal pattern of Arctic precipitation. However, they differ strongly concerning the amount of precipitation. Comparing different reanalyses, MERRA2 and CSFR are wetter, while MERRA is drier. In general, ERA5 is similar to ERA-Interim and JRA55, however it overestimates the precipitation compared to NP stations.

In general, reanalyses have difficulties in producing accurate precipitation in the Arctic. The discrepancies in the magnitude, frequency, and phase of precipitation over the Arctic Ocean are related to the difficulty and complexity of modeling precipitation processes in the atmosphere. This includes the representation of cloud microphysical properties and boundary layer processes at higher latitudes, large-scale atmospheric circulations, and limited reliable observations (Boisvert et al., 2018). Especially, the cloud microphysical scheme that produces modeled precipitation varies between each reanalysis (Boisvert et al., 2018).

The difficulty of accurately determining precipitation also influences modeling of sea ice. For instance, if too much or too little snowfall or rainfall is estimated, this affects the depth of the snowpack, the albedo, and insulating properties which have an influence on the snowpack and underlying sea ice throughout the year. The amount of snow on top of the Arctic sea ice is an important factor in the growth and decay of Arctic sea ice (Boisvert et al., 2018). Despite these deviations, Barrett et al., 2020 argue to use ERA5 as a basis scheme to obtain snow over sea ice to enable improved retrievals of sea ice thickness from satellite data. Further, Lavers et al., 2022 evaluated ERA5 precipitation against observations and recommended to use ERA5 for extratropical regions.

1.3 Poleward moisture transport and associated weather systems

In the Arctic, two main moisture sources could affect the water vapor content and therefore the precipitation in the Arctic (Fig. 1.3). These are the enhanced local evaporation due to the missing insulation of sea ice and the poleward moisture transport from lower latitudes (Bintanja and Selten, 2014).

The poleward moisture transport results from the global radiative imbalance between the tropics and poles. Throughout the year, the Arctic surface reaches less solar energy due to the high albedo and the Earth's geometry. This poleward moisture transport from lower to higher latitudes increases the local moisture content in the Arctic. As water vapor is one of the most important greenhouse gases, poleward moisture transport is a crucial process that affects the surface and mid-tropospheric Arctic warming (Graversen et al., 2008; Vihma et al., 2016; Nash et al., 2018). The increased water vapor content and cloud cover enhance the downward longwave

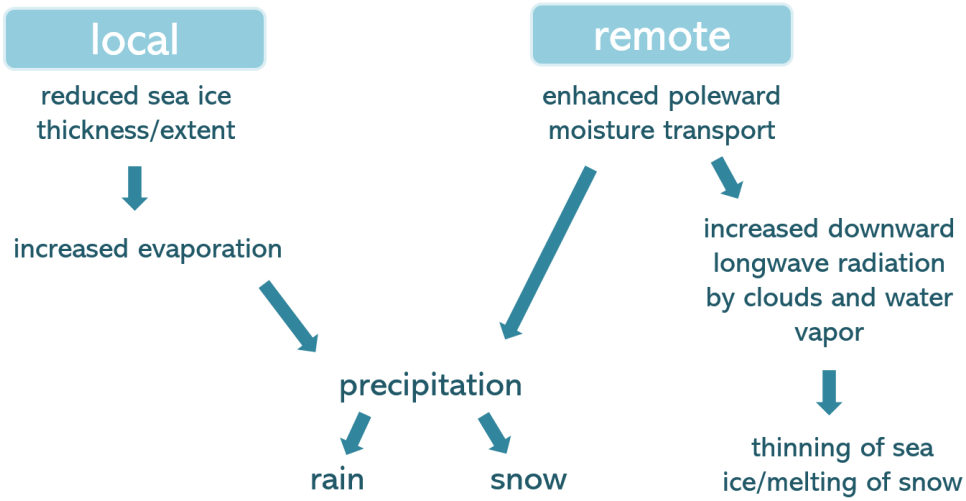

FIGURE 1.3: Schematic of moisture sources for Arctic precipitation.

radiation and warm the Arctic surface (Curry et al., 1996; Francis and Hunter, 2007). Gong et al., 2017 found that the downward longwave radiation associated with the poleward moisture flux is responsible for the majority of the winter warming trend north of 70°N. The surface warming has consequences for the sea ice extent (Vázquez et al., 2018). The poleward moisture transport is related to sea ice decline (Gimeno-Sotelo et al., 2018). Further, the additional moisture has consequences for precipitation (Vihma et al., 2016). Changes in Arctic precipitation can modify the snowfall onto the nearby continents and ice sheets (Liu and Barnes, 2015). The effects of Arctic precipitation on the surface depend strongly on the type of precipitation and the season (Gimeno-Sotelo et al., 2018; Vihma et al., 2016). Generally, rainfall is associated with sea ice melting. Snowfall has different effects: Snowfall on sea ice enhances the thermal insulation which reduces the growth of sea ice in cold seasons (Leppäranta, 1993). In the warm season, it increases the albedo and prevents sea ice from melting (Cheng et al., 2008).

Previous studies identified major pathways for the meridional and latent energy transport into the Arctic. These are the North Atlantic and the North Pacific. The moisture transport from the North Atlantic affects the Baffin Bay and Labrador Sea east of Greenland and the Fram Strait, the Norwegian, Barents, and Kara Seas west of Greenland. In summer, continental areas over North America and Siberia become important moisture sources (Naakka et al., 2019).

Gimeno et al., 2019 confirm that the poleward moisture transport is related to specific Arctic modes. These are the Arctic Dipole (AD), the Arctic Oscillation (AO), and the North Atlantic Oscillation (NAO). In the case of AD, the high pressure over the Arctic regions of North America and the low pressure over Eurasia favors the moisture transport from the Pacific into the Arctic. During the positive AO lower air pressure over the Arctic is paired with higher pressure over the North Pacific and North Atlantic. This shifts the jet stream further north and consequently associated storms. During the positive NAO, there is a strong pressure gradient between the Icelandic low and the Azores high which leads to a northeast shift of the Atlantic storm track. This situation is more intense if the positive NAO is coupled with the

Ural Anticyclone blocking which often occurs in winter (Luo et al., 2016). Further blocking events that lead to increased poleward moisture transport are the Beaufort Sea High in summer (You et al., 2022) and the Greenland blocking in summer and winter (Barrett et al., 2020). In general, these blocking patterns result from a disrupted polar vortex (Fig.1.4). In a warmer climate, it is expected that these blocking events will increase which would favor a stronger poleward moisture transport.

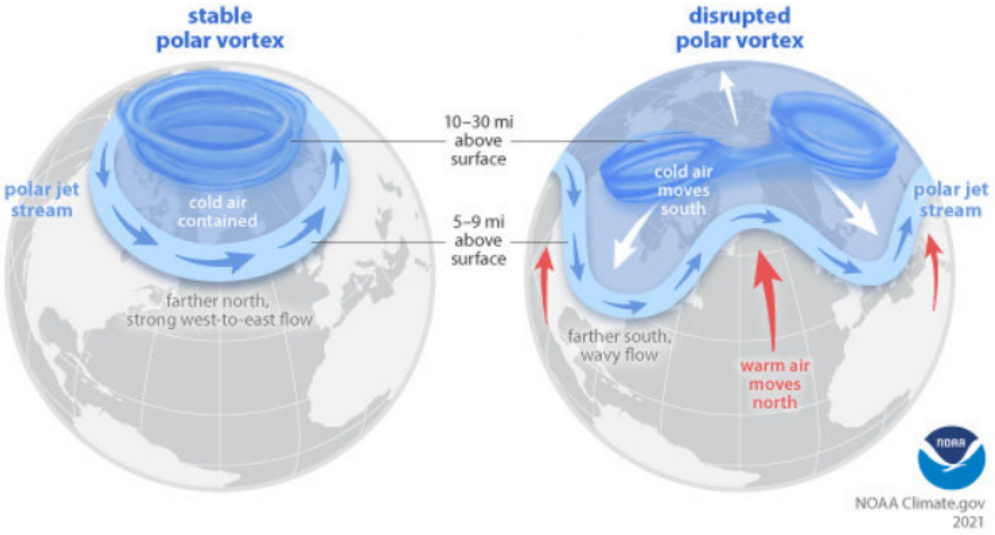

FIGURE 1.4: Schematic of the Arctic polar vortex when it is stable (left) and weaken (right). Source NOAA, 2024.

The poleward moisture transport is directly related to the cyclones (Crawford and Serreze, 2017; Fearon et al., 2021). Therefore, the interannual variability of moisture transport toward the Arctic is primarily accomplished by the variability of cyclone activity over Greenland and the Eastern Siberian Sea (Sorteberg and Walsh, 2008; Rinke et al., 2017). Extreme transport events are closely related to Rossby wave breaking (Liu and Barnes, 2015). These events are so-called *moisture intrusions* (Woods et al., 2013) and are often known as atmospheric rivers (Hegyi and Taylor, 2018; Komatsu et al., 2018; Vázquez et al., 2018).

1.3.1 Atmospheric fronts

Atmospheric fronts are fundamental components to describe the weather. The concept of atmospheric fronts dates back to the Norwegian meteorologist Wilhelm Bjerknes (Bjerknes, 1919). An atmospheric front is a boundary between air masses of different temperatures or densities (Bjerknes, 1919; Niebler et al., 2022). Generally, they are associated with changes in temperature, wind, humidity, and pressure (Simmonds et al., 2012; Schemm et al., 2015). They are frequently associated with extratropical cyclones (Simmonds et al., 2012) and play a significant role in the formation of extreme precipitation (Catto et al., 2012; Catto and Pfahl, 2013; Hénin et al., 2019).

Although fronts play an important role in the weather and climate, no universally accepted definition of fronts exists (Rüdisühli et al., 2020; Niebler et al., 2022). Consequently, detecting fronts often relies on different approaches, as described by

Schemm et al., 2018 and Thomas and Schultz, 2019.

In the past, fronts were described manually over a specific location (Rüdisühli et al., 2020). Therefore, understanding frontal systems' behavior from a climatological perspective is still missing (Simmonds et al., 2012). During the last years, different methods have been developed to automatically detect fronts based on reanalysis data (Schemm et al., 2015). Schemm et al., 2015 describe two common methods to detect fronts automatically. These methods rely on detecting strong gradients in either humidity and temperature fields or wind fields.

The first method is a thermal approach. It is based on a framework established by Hewson, 1998 and introduced by Renard and Clarke, 1965. This approach was applied in previous studies (Kašpar, 2003; Jenkner et al., 2010; Berry et al., 2011). It explores the structure of the so-called 'thermal front parameter' (TFP). This parameter describes the position of the fronts and can be derived from thermodynamic variables such as the equivalent potential temperature or the wet bulb temperature. In contrast to dry fields, these moist variables have a stronger and sharper gradient and deliver a more precise location (Jenkner et al., 2010). Further, the equivalent potential temperature acts as a good airmass tracer, especially over land and close to orography, and allows a realistic description of the air mass properties (Kašpar, 2003). In addition, it is a useful variable to detect large-scale mobile fronts (Schemm et al., 2018). The thermal approach can identify warm and cold fronts in baroclinic cases (Schemm et al., 2015).

The second method is based on the temporal changes in the 10m wind field. It was introduced by Simmonds et al., 2012, who studied fronts for the southern hemisphere. The method is particularly suited for strongly elongated meridionally oriented moving fronts but has limited ability to identify zonally oriented warm fronts (Schemm et al., 2015).

Previous studies (Serreze et al., 2001; Berry et al., 2011; Schemm et al., 2015) examined the global climatology of atmospheric fronts based on the thermal approach. In 2001, Serreze et al., 2001 applied the NCEP/NCAR reanalysis from 1979-1998 and studied the seasonal frontal activity in the northern hemisphere. They highlight the high maximum in frontal activity over Eurasia in summer, which was already identified in Dzerdeevski (1945) (from 1937-1939) and Reed and Kunkel, 1960 (1952-1956) (Serreze et al., 2001). This high-latitude frontal feature is known as the Arctic frontal zone. Dzerdeevski (1945) considered the Arctic frontal zone as a summer feature resulting from differential heating between the snow-free land and the cold Arctic Ocean. Further, it is associated with orography (Serreze et al., 2001). Serreze et al., 2001 also found higher frontal activity over Alaska but to a lesser extent. This Alaskan feature occurs throughout the year, with its maximum in summer. In winter, they are more common over the North Atlantic and North Pacific, with a maximum over the North Atlantic and at the east coast of Greenland. They called this 'Greenland wintertime Arctic frontal.' The frontal activity decreases in spring over the North Atlantic and the North Pacific and in autumn over Eurasia.

1.3.2 Extratropical cyclones

The poleward moisture transport is also related to extratropical cyclones (Sorteberg and Walsh, 2008). They are low-pressure systems associated with cold, warm, and occluded surface fronts.

Two conceptual models describe the development of extratropical cyclones. These are the Norwegian model (Henry, 1922) and the Shapiro-Keyser model (Shapiro and Keyser, 1990). In both models, the cyclone develops along the polar front due to the temperature gradient between the polar regions and the lower latitudes. A disturbance then develops at the polar front. In the eastern part of this disturbance, warm air moves northwards. Meanwhile, in the western part, cold air moves south. Subsequently, a frontal system consisting of a warm and a cold front develops, with a warm sector located in between. Due to the Coriolis force, the warm air at the warm front moves over the cold air, and the cold air at the cold front slides under the warm air. These vertical movements lead to the formation of clouds and precipitation. The result is a sharp drop in pressure at the center.

In the Norwegian model, the cold front begins to catch up with the warm front, causing the warm sector to shrink. The stage when the cold front catches up with the warm front is called occlusion. The cyclone reaches its peak intensity at this point. This occlusion marks the new polar front, where a new cyclone begins to form (Henry, 1922). In contrast to the Norwegian model, in the Shapiro-Keyser model the cold front does not catch up with the warm front. Therefore, no occlusion develops. Instead, the 'T-bone' structure is formed where the cold front is perpendicular to the warm front. During this process, the warm front curves around the cyclone's center. This phase, known as seclusion, isolates the warm air in the cyclone's center from the surrounding colder air (Shapiro and Keyser, 1990).

Based on the conveyor belt model (Carlson, 1980), three air currents are characteristic of a low-pressure system. These are the 'warm conveyor belt', the 'dry air intrusion' (or dry conveyor belt), and the 'cold conveyor belt'. For this thesis, the warm conveyor belt is of importance. The warm conveyor belt is located ahead of the cold front. It has a poleward direction and ascends the warm and moist air of the warm sector above the warm front. During this ascend, stratiform clouds and precipitation are formed. Therefore, the warm conveyor belt is accompanied by heavy precipitation.

1.3.2.1 Influence in the Arctic

Extratropical cyclones are responsible for 74% of the annual poleward moisture transport (Fearon et al., 2021). After reaching the polar regions, extratropical cyclones modulate the Arctic weather (Rinke et al., 2017), affect the sea ice cover (Graham et al., 2019b), and impact the surface energy balance (Boisvert et al., 2016). In winter, they could affect the sea ice decline in two ways. First, they increase the water vapor content in the atmosphere and enlarge the cloud cover (Schreiber and Serreze, 2020). The enhanced water vapor and cloud cover increase the downward longwave radiation towards the surface and lead to surface warming and sea ice melting (Graham et al., 2019). Graham et al. (2017) have shown that intense cyclones can cause large anomalous warming over the Arctic Ocean in winter. These intense cyclones lead to

temperatures around 0 °C, when normally -30 °C is expected. Second, extratropical cyclones cause snowfall on sea ice. The snowfall isolates the sea ice from the cold atmosphere which suppresses the ice growth during the winter season (Graham et al., 2019b). In contrast, Schreiber and Serreze, 2020 found that winter cyclones support sea ice growth. Further, they found that cyclones in summer seem to reduce the melting as they cause cooler conditions and reduce the incoming shortwave radiation (Schreiber and Serreze, 2020).

Strong winds often associated with cyclones break the sea ice into smaller fragments which then are more vulnerable to melt. Further, the cyclone could push the sea ice further north which exposes greater open ocean surfaces that are relevant for the interaction between the atmosphere and ocean. Thus, cyclones alter the sea ice thermodynamically and dynamically (e.g. through wave action and ice drift) (Francis et al., 2020). This plays an important role in winter, when cyclones are thought to be the primary transporter of heat and moisture into the polar regions (Francis et al., 2020).

1.3.2.2 Occurrence and trends of extratropical cyclones

During the last decades, several cyclone identification and tracking algorithms have been used to analyse cyclones in the Arctic (Sorteberg and Walsh, 2008). Although there are regional differences among the different reanalyses, there is an agreement on the large-scale distribution of cyclones. The cyclone activity is most pronounced in the Atlantic sector (Greenland and Norwegian Seas), the Barents and Kara Seas, the East Siberian, and the Chukchi Sea. For all seasons, the number of cyclones traveling onto the Arctic is approximately the same. The average residence time of cyclones in the Arctic is on average 2.6 days, while cyclones coming from the Pacific Ocean stay 20% longer in the Arctic than cyclones entering from the Atlantic.

Overall, the most intense Arctic cyclones are observed in the Atlantic sector over the Greenland and Norwegian Seas and Baffin Bay in winter. This is the season where the changes in the Arctic are the largest (Rinke et al., 2017). On average, cyclones in these regions are 20% more intense when they cross 70°N compared to the East Siberian and Chukchi Seas (Sorteberg and Walsh, 2008).

In summer, cyclone activity is higher over the central Arctic Ocean and land (Zahn et al., 2018). There is a peak in the cyclone frequency close to the North Pole which is described as cyclone convergence from many regions over the central Arctic (Zahn et al., 2018). During this time of the year, the cyclones are less intense but live longer than during winter (Zhang et al., 2004). From July-September the cyclone activity is about 50% higher than in February-April. However, the annual course of deep cyclones is the opposite, they are more than 3 times more frequent in winter than in summer (Zahn et al., 2018). Therefore, the intense cyclones are more frequent in winter, the number of weak cyclones peaks in summer (Chang et al., 2012; Vavrus, 2013).

Rinke et al., 2017 found that 20-40 extreme cyclone events (also called 'weather bombs' (Rinke et al., 2017) occur in the Arctic North Atlantic per winter season. Based on 6 hourly station data from Ny-Ålesund in Svalbard, the occurrence increased by 6 events per decade over 1979-2015. This trend is mostly pronounced

in November and December (3-4 events more per decade) and is consistent with winter warming. This indicates, that the meridional heat and moisture transport associated with cyclones is responsible for a rising in temperature (Rinke et al., 2017). Zahn et al., 2018 confirm this significant increase over the northern part of the North Atlantic around Spitsbergen in winter. This positive trend stretches also from the North Pole into the Beaufort Sea toward northern Canada, northern Laptev, and the Eastern Siberian Seas. From December to January, there is a negative trend over the Barents and Kara Seas (Rinke et al., 2017; Zahn et al., 2018).

In summer, the pattern is opposite: Thus in the Barents Sea region where the largest decline is found in winter, cyclone frequency increases in summer, and the increase in cyclone frequency between the North Pole and the Beaufort Sea in winter turns into a strong decline in summer (Zahn et al., 2018).

1.3.3 Atmospheric Rivers

Atmospheric Rivers (ARs) – also known as ‚rivers in the sky' – are one of the key mechanisms of the global moisture transport. They are long (> 2000km length) and narrow (300-500 km width) corridors in the lower troposphere that transport anomalous amounts of moisture meridionally from lower to higher latitudes. Newell et al., 1992 first introduced the term 'tropospheric rivers'. In 1994, Zhu and Newell, 1999 changed it to atmospheric rivers. Over the past few decades, a wide range of alternative terms have been used for this meteorological phenomenon, including moist conveyor belts (Bao et al., 2006) and tropical moisture exports (TMEs) (Knippertz and Wernli, 2010). In 2018, the American Meteorological Society published a precise definition of ARs in the Glossary of Meteorology:

"A long narrow and transient corridor of strong horizontal water vapour transport that is typically associated with a low-level jet stream ahead of the cold front of an extratropical cyclone. The water vapor in atmospheric rivers is supplied by tropical and/or extratropical moisture sources. Atmospheric rivers frequently lead to heavy precipitation where they are forced upwards – for example, by mountains or by ascent in the warm conveyor belt. Horizontal water vapor transport in the mid-latitudes occurs primarily in atmospheric rivers and is focused in the lower troposphere. Atmospheric rivers are the largest 'rivers' of fresh water on Earth, transporting on average more than double the flow of the Amazon River."

Thus, ARs are often accompanied by extratropical cyclones (Zhu and Newell, 1998). They are filaments of large amounts of water vapor (between 1 to 2.5 km altitude), which are fuelled by the transport from (sub-) tropical to higher latitudes and/or the moisture convergence along the pre-cold frontal low-level jet of extratropical cyclones, which is identified in the warm sector of the extratropical cyclone (Fig. 1.5) (Ralph et al., 2004). Thus, the moisture in an AR has two origins (Bao et al., 2006): the local moisture convergence along the cold front of the extratropical cyclone and the poleward transport of tropical moisture.

Newell et al., 1992 found that 4 to 5 ARs occur at the same time in each hemisphere. They are responsible for more than 90% of the poleward moisture transport while covering only 10% of the Earth's circumference at midlatitudes (35 °N) (Zhu and Newell, 1998). They mostly affect the coasts of North America, South America, Europe, Russia, China, New Zealand, and the Polar Regions (Guan and Waliser,

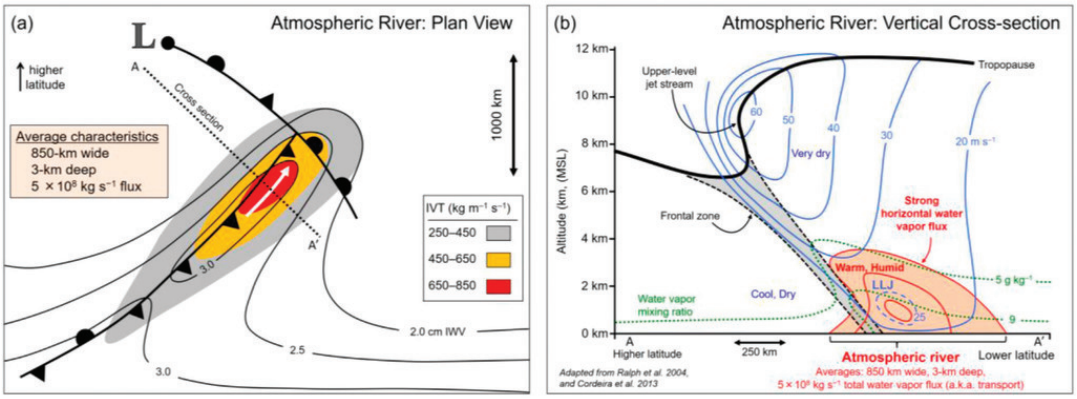

FIGURE 1.5: Schematic summary of the structure and strength of a typical AR. The magnitudes of variables represent an average mid-latitude atmospheric river (a) Plan view shows the position of the AR in relation to an extratropical cyclone with its cold (black triangles), warm (black semi-circles), and warm-occluded (black triangles and semi-circles). The AR core is located ahead of the cold front with the strongest moisture transport in the warm sector. (b) Vertical cross-section (A-A' in (a)) shows the location of the pre-cold frontal low-level jet which forms due to the temperature gradient between the cold air of the cold front and the warm sector of the extratropical cyclone. The red contour lines characterise the AR core, the green contour lines the water vapor mixing ratio, and the blue contour lines the wind speed. Source Ralph et al., 2004

2015a; Gimeno et al., 2016). When a vapor-rich AR reaches coastal and mountainous terrain, it is forced upwards. The orographic enhancement can produce extreme precipitation events and catastrophic flooding (Ralph et al., 2006; Dettinger et al., 2011; Lavers et al., 2013; Leung and Qian, 2009). Previous studies have shown that they contribute up to 30% of precipitation in California and European countries (Guan and Waliser, 2015a), 20% in Australia (Reid et al., 2022), and about 70% in New Zealand (Prince et al., 2021). In California, for example, they are a significant source of water resources and provide 25-50 % of California's water supply (Dettinger et al., 2011). Thus, ARs play a substantial role in the global hydrological cycle (Guan and Waliser, 2015a).

As ARs are responsible for the poleward moisture and heat transport, they affect the atmospheric water budget in higher latitudes. The extratropical atmospheric water budget for a region north of 60°N is shown in Fig. 1.6. It highlights that the change of water vapor in this region depends on the source of water vapor from surface evaporation (E), the loss of water vapor due to condensation and precipitation P, and their moisture input from latitudes south of 60°N (Δ IVT) (Nash et al., 2018).

Figure 1.6 shows the common pathways of ARs. These are the Atlantic and Pacific pathways. In 2018, Komatsu et al., 2018 identified ARs coming from Siberia in summer. In summer, the Siberian continent heats up. The warm air coming from Siberia glides up over the cold air dome above the sea ice and cools. Through condensation of water vapor, the air provides the upper troposphere with extra heat. This heating drives increased buoyancy and further strengthens the ascent and heating of the mid-troposphere. This form of ARs is known as Siberian Atmospheric Rivers (SAR). Vázquez et al., 2018 published a climatology of ARs over the Arctic

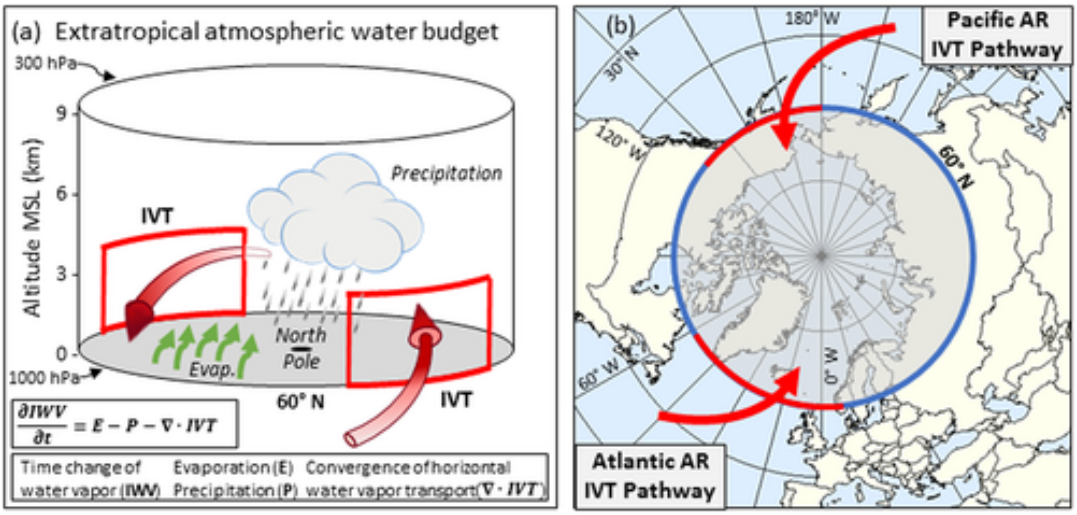

FIGURE 1.6: (a) Scheme of the atmospheric water budget for a region north of 60°N. The red arrows indicate the integrated water vapor transport (IVT), the green arrows the surface evaporation (E), and the clouds and rain indicate the water vapor loss due to condensation or precipitation (P). All these terms describe the change in water vapor storage. (b) Top-down view of IVT flux at 60°N. The red line indicates the common pathways of IVT fluxes and ARs. Source Nash et al., 2018

from 1997 to 2014 based on ERA-Interim reanalyses. They have shown that there are regional and seasonal differences. Over the Atlantic Ocean and Pacific Ocean, the ARs are more frequent during autumn and summer, respectively. Along the Atlantic pathway, the ARs are mainly located over the Norwegian Sea. Along the Pacific pathway, the ARs are mainly located in the Gulf of Alaska. Further, they have shown that the main moisture sources are the North Atlantic and North Pacific Oceans. These are the regions with a maximum AR frequency. During winter, the moisture source is the evaporation from oceans, while during summer the moisture has its origin in the continental areas (Vázquez et al., 2018). The evaporation from the surface of the North Atlantic and North Pacific Oceans accounts for much of the moisture in this poleward transport.

Extreme moisture transport events which are frequently associated with ARs occur during blocking events (Woods et al., 2013; Liu and Barnes, 2015; You et al., 2022). These blocking events divert the moisture flux northward into the Arctic. For example, Woods et al., 2013 examined the poleward moisture transport across 70°N during boreal winter and found that ARs account for 28% of the poleward moisture transport.

The large amounts of heat and moisture transported within an AR have significant consequences for the near-surface temperature, surface mass balance, and sea ice. Earlier studies that have focused on ARs in Antarctica found that ARs have both a positive and negative effect on the surface mass balance. Gorodetskaya et al., 2014 reported that ARs contribute to anomalous snowfall events in East Antarctica. In contrast, Wille et al., 2019 have shown that ARs increase the water vapor greenhouse effect. The increase in water vapor and the formation of clouds enhance the downward longwave radiation and warm the surface. Further, rainfall increases the surface melt and decreases the surface albedo. A recent study (Francis et al., 2020)

found that ARs cause sea ice melt, leading to open water and thin ice in the vicinity of thicker ice. This involves the formation of two large Wedell Polynya in 1973 and 2017.

In the Arctic, ARs have a great influence on the Greenland ice sheet and sea ice. ARs over Greenland lead to increased melting of the Greenland ice sheet due to enhanced longwave radiation and warm air advection (Neff et al., 2014; Neff, 2018; Mattingly et al., 2018; Mattingly et al., 2020). Box et al., 2023 analysed an AR event that reached the Greenland ice sheet in mid-August 2021. This AR event was of particular interest as it delivered rainfall on the Greenland ice sheet. However, the condensation or sensible heat flux from the warm air has contributed more to melting. Hegyi and Taylor, 2018 found that ARs were responsible for the low sea-ice volume between October 2016 and March 2017. The advected water vapor within the ARs increased the downward longwave radiation and induced sea ice melting in winter. The 2016/17 ice season had one of the lowest end-of-season Arctic sea ice extent and volume values ever recorded.

Changes in sea ice can be driven dynamically or thermodynamically. The dynamic changes are due to strong winds associated with ARs. This favors the sea ice to move. The thermodynamic changes are due to the enhanced downward longwave radiation, heat advection, or precipitation (Li et al., 2022). Zhang et al., 2023 have found that more frequent ARs (driven by thermodynamics) in early winter slow down sea ice formation over the Barents and Kara Seas and in the central Arctic. The increased downward longwave radiation and rainfall caused a stronger melting and slowed the seasonal recovery of sea ice. They found that ARs accounted for 34% of the sea ice cover decline in the Barents and Kara Seas. In addition to the downward longwave radiation and rainfall, snowfall associated with ARs can influence sea-ice growth due to the insulation effect at the sea-ice surface (Merkouriadi et al., 2017).

These studies provide the first evidence that ARs make an important contribution to Arctic warming. Therefore it is of interest to understand possible changes in the frequency and intensity of ARs and how they contribute to precipitation in the Arctic.

1.4 Thesis overview

As described in previous studies (Sorteberg and Walsh, 2008; Woods et al., 2013) and already mentioned in Section 1.3 the poleward moisture transport is mainly associated with extratropical cyclones and ARs. However, there is still a lack of knowledge of the extent to which they contribute to precipitation in the Arctic. In order to gain a better understanding therefore, the following questions are addressed in this thesis:

1. How do synoptic features contribute to precipitation in the Arctic?
2. To what extent do trace precipitation and marine cold air outbreaks affect the residual?
3. Are there trends in synoptic feature-related precipitation?

To answer these questions, the fifth generation of the European Centre for Medium-Range Weather Forecasts (ECMWF) global climate and weather reanalysis ERA5 (Hersbach et al., 2020b) is used. The high spatial and temporal resolution allows a detailed analysis of precipitation in the Arctic. ERA5 provides hourly data from different types and phases of precipitation. This allows to distinguish between convective and large-scale snowfall and rainfall.

Previous studies have compared ERA5 reanalysis data with other reanalysis data sets and observations and have found that ERA5 data is confident products for the Arctic region (Graham et al., 2019a; Barrett et al., 2020). Nevertheless, it is important to analyse the extent to which ERA5 can be trusted. For this purpose, the ERA5 reanalysis data is compared with space-borne and ground-based remote measurements for three AR events detected during two field campaigns (Chapter 2).

After this evaluation, a new method is introduced that was established to analyse the precipitation related to ARs, extratropical cyclones, and fronts. This method is based on the ERA5 reanalysis and different detection algorithms for ARs and extratropical cyclones. It is applied for two airborne campaigns that were carried out in 2017 and 2019 within the framework of the *Transregional Research Center 172 Arctic Amplification: Climate Relevant Atmospheric and Surface Processes and Feedback Mechanisms (AC)*[3] (Chapter 3).

This method is then applied to the ERA5 climatology. In this thesis, the investigated period ranges from 1979-2021. First, there will be an overview of the spatiotemporal variation of precipitation in the Arctic. This is the first study that also distinguishes between convective and large-scale precipitation. Subsequently, the spatiotemporal variations in the influence of ARs, cyclones, and fronts on precipitation are analysed (Chapter 4).

Precipitation that is not associated with ARs, cyclones, and fronts is classified as residual. The reasons for the residual should therefore be addressed. Here, the focus is on the so-called trace precipitation and marine cold air outbreaks (CAO) (Chapter 5).

Finally, Chapter 6 will provide first insights into the trends of synoptic feature-related precipitation during the last four decades.

The thesis will conclude with a summary and give recommendations for future research (Chapter 7).

Chapter 2

Evaluation of ERA5 reanalysis

The analyses in this thesis mainly rely on ERA5 reanalysis data. Therefore, this chapter compares ERA5 reanalysis and ground-based and remote-sensing observations for three AR events. In this way, confidence in using ERA5 should be gained, and possible limitations should be revealed. The first AR event occurred at the end of May 2017 during the Arctic Cloud Observations Using airborne measurements during polar Day (ACLOUD) (Wendisch et al., 2019) campaign, and the second and third ones in April 2020 during the Multidisciplinary drifting Observatory for the Study of Arctic Climate (MOSAiC) expedition (Shupe et al., 2022). Since each campaign had a specific measurement setup, this chapter is divided into two subchapters.

2.1 Part I: AR event during ACLOUD May/June 2018

The ACLOUD campaign, which was carried out as part of the $(AC)^3$ project, took place in May/June 2017 and was performed over the sea ice and the Arctic Ocean north-west of Svalbard and the Arctic Ocean (Ehrlich et al., 2019; Wendisch et al., 2019). The main focus of this campaign was to gain a better understanding of clouds in the Arctic. The meteorological conditions during the campaign are described in Knudsen et al. (2018). Of particular interest for this study are the intense intrusions of warm and humid air, which are categorized as ARs (Viceto et al., 2022; Lauer et al., 2023b). These AR events were mainly concentrated over the Kara, Barents, and Norwegian Seas. As the airborne measurements were limited to the area north-west of Svalbard, no airborne measurements exist to analyse one of these events. After thoroughly reviewing the existing datasets, the first AR event was selected to compare ERA5 data with observational data. This AR event was detected by the global detection algorithm (Guan et al., 2018) and from the polar-specific algorithm (Gorodetskaya et al., 2020) from 28 – 31 May 2017 (Viceto et al., 2022; Lauer et al., 2023b). It originated in Siberia and traveled along the Kara and Barents Seas towards Svalbard. The AR was detected at the research site Ny–Ålesund, Svalbard, 29 May 2017 from 9 to 23 UTC. The analyses, therefore, focus on 29 May.

Ground-based measurements from the Arctic Research Base AWIPEV at Ny-Ålesund and space-borne measurements from the polar orbiting satellite CloudSat are used to analyse this AR event. The ground-based measurements allow a temporal analysis of the AR event, while the space-borne measurements allow an analysis of a cross-section of the AR. Comparing these measurements with the ERA5 reanalysis, the classical observation-to-model and model-to-observation approaches are used (Lerber et al., 2022). For the observation-to-model approach, ERA5 variables are directly compared with observations. The comprehensive Passive and Active

Microwave TRAnsfer operator PAMTRA (Mech et al., 2020) is used in the model-to-observation approach. PAMTRA simulates passive and active observations in the microwave frequency region based on a given atmospheric state. The radar reflectivity factor Ze is derived from ERA5 output for this study.

This study provides an overview of the vertical structure of the hydrometeors within an AR and their spatial and temporal structure in order to analyse how well the hydrometeorological properties are represented in ERA5. The data and methods used for this purpose are presented in Sections 2.1.1 and 2.1.2. This involves ground-based measurements by cloud radar and microwave radiometer at Ny–Ålesund and by the Cloud Profiling Radar (CPR) on-board CloudSat together with corresponding ERA5 reanalysis data. Further, PAMTRA, which enables the model-to-observation approach, and the AR detection algorithms are introduced. Section 2.1.3 first puts the AR event into the long-term climatological perspective regarding precipitation. Subsequently, the AR cross-section derived from the CloudSat path and the temporal development of the AR after reaching Ny-Ålesund is analysed. The analyses include the vertical structure of the radar reflectivity, the hydrometeors, and ground-based analyses such as accumulated precipitation. These findings are compared with ERA5 reanalyses. The study concludes with a summary.

2.1.1 Data

2.1.1.1 ERA5 reanalysis

Throughout the entire thesis, the fifth generation of the European Centre for Medium-Range Weather Forecasts (ECMWF) global climate and weather reanalysis ERA5 (Hersbach et al., 2020b) is used. A large number of atmospheric, land, and oceanic climate variables are available from 1940 onwards. As satellite measurements, which are essential for the Arctic due to the scarcity of ground-based observations, have been included since 1979, the thesis uses data from 1979 onwards. The reanalysis is provided by the Copernicus Climate Change Service (C3S, 2024).

ERA5 reanalysis data have a temporal resolution of 1h and cover the Earth on a $\sim$31 km grid (0.25° x 0.25°). In the vertical, 137 model levels resolve the atmosphere from the surface up to 80 km. Further, the data are also available on 37 pressure levels from 1000 hPa to 1 hPa. In this part, both model and pressure levels are used. The higher vertical resolution of model levels is used for the comparison between observations and reanalysis, while the pressure levels are used for the detection of ARs. There are two reasons for this: First, the AR detection applied for previous reanalysis (Gimeno et al., 2015) also used pressure levels. Second, the high temporal and spatial resolution would require too much computing time. Table 2.1 provides an overview of the ERA5 variables and for which purpose they have been used. Total precipitation includes both large-scale and convective precipitation.

The ERA5 reanalysis data has been chosen for this study due to its high spatial and temporal resolution on a global scale. This is an advantage for the highly variable precipitation, one of the most important variables in this thesis. Previous studies have also shown that ERA5 provides high-quality reanalysis for the Arctic region (Mayer et al., 2019; Graham et al., 2019a). Further, a study focused on ARs in Antarctica (Gorodetskaya et al., 2020) has shown that ERA5 performs better than ERA-Interim reanalysis (Dee et al., 2011).

TABLE 2.1: Overview of ERA5 variables. The table contains the variable, the variable name, the level, and the purpose for which the variables were used.

Variable	Variable name	Level	Purpose
u10	10 m u-wind (zonal) component	Single	PAMTRA input
v10	10 m v-wind (meridional) component	Single	PAMTRA input
sp	Surface pressure Surface pressure	Single Single	PAMTRA input AR detection (Guan, Gorodetskaya)
tciw	Total column cloud ice water	Single	precipitation analyses
tclw	Total column cloud liquid water	Single	precipitation analyses
tcrw	Total column rain water	Single	precipitation analyses
tcsw	Total column snow water	Single	precipitation analyses
tcwv	Total column vertically-integrated water vapour	Single	precipitation analyses
tp	Total precipitation	Single	precipitation analyses
sf	Snowfall	Single	precipitation analyses
sicon	Sea ice are fraction	Single	PAMTRA input
z	Orography	Single	PAMTRA input
skt	Skin temperature	Single	PAMTRA input
lsm	Land-Sea mask Land-Sea mask	Single Single	PAMTRA input AR detection (Guan)
ciwc	Specfic cloud ice water content	Model	PAMTRA input
clwc	Specfic cloud liquid water content	Model	PAMTRA input
crwc	Specfic rain water content	Model	PAMTRA input
cswc	Specfic snow water content	Model	PAMTRA input
q	Specfic humidity	Model Pressure	PAMTRA input AR detection (Guan; Gorodetskaya)
t	Temperature	Model Pressure	PAMTRA input AR detection (Guan; Gorodetskaya)
U	U (zonal)-component of wind	Pressure	AR detection (Guan)
V	V (zonal)-component of wind	Pressure	AR detection (Guan)

2.1.1.2 Measurement site: Ny-Ålesund

This study uses ground-based measurements from the French-German Arctic Research Base AWIPEV. The Arctic Research Base is jointly operated by the Alfred Wegener Institute for Polar and Marine Research (AWI, Germany) and the Polar Institute Paule Emile Victor (IPEV, France). AWIPEV is located on the west coast of Svalbard, in the research station Ny-Ålesund (79°N, 11.9°E). Ny-Ålesund is located 13m above sea level along the coast of Kongsfjorden - a fjord on the west coast of Svalbard, surrounded by mountains reaching from 500-1000 m height and several glaciers. This characterizes the complex terrain around the research station.

At AWIPEV, various continuously running measurements of passive and active remote sensors provide information about the thermodynamic state, clouds, and precipitation. In the past, several studies used observations from this location to analyse the vertical structure of clouds (Nomokonova et al., 2019; Vassel et al., 2019; Gierens et al., 2020; Ebell et al., 2020). In this thesis, observations from the cloud radar JOYRAD-94 (Küchler et al., 2017) and the microwave radiometer HATPRO (Rose et al., 2005) are used. As part of the $(AC)^3$ project, the Jülich Observatory for Cloud Evolution (JOYCE) Radar-94 GHz (JOYRAD-94) has been deployed at AWIPEV from June 2016 to July 2017 and again from June 2019 onwards. JOYRAD-94 is a Frequency Modulated Continuous Wave (FMCW) radar manufactured by Radiometer Physics GmbH (RPG, Germany). It is a single-polarization, zenith-pointing W-band radar operating at 94 GHz in a vertical pointing mode. In addition to the active radiometric channel at 94 GHz, it has a passive radiometric channel at 89 GHz, which is sensitive to liquid water clouds. Technical features and details on data processing, in particular noise removal and Doppler aliasing correction, are described in detail by Küchler et al., 2017, In this thesis, the vertical profiles of radar reflectivity

(Ze), mean Doppler velocity (V_m), and Doppler spectral width from 150 m to 10 km above ground are used. The measurements have a temporal resolution of 2-3 s, and the vertical resolution ranges from 4 to 6.7 m (100-400 m: 4 m, 400-1200 m: 5.3 m, 1200-3000 m: 6.7 m). The minimum detection height is 100 m above the ground.

The Humidity and Temperature Profiler (HATPRO) is a microwave radiometer. In total, it has 14 channels that measure atmospheric brightness temperatures (TBs) at K-band (22.24-31.40 GHz) and V-band (51.25-58 GHz) frequencies with a temporal resolution of 1-2 s and an accuracy of 0.5 K. As the K-band channels are located at the water vapor absorption line (22 GHz), TBs measured at the K-band are used to retrieve the integrated water vapor (IWV), the liquid water path (LWP), and the humidity profile. The V-band channels are located along the oxygen absorption line (60 GHz). The TBs of these channels are used to retrieve the vertical temperature profile. A multivariate linear regression algorithm is routinely applied to the TB observations to derive LWP and IWV, temperature, and humidity profiles. Uncertainties for LWP are typically 20-25 g m^{-2} and for IWV smaller than 1 kg m^{-2}. HATPRO provides continuous measurements throughout the day, except during heavy precipitation. Nomokonova et al. (2019) give more details on the retrieval, technical aspects, and uncertainties.

2.1.1.3 Satellite remote-sensing

CloudSat is a polar-orbiting satellite launched in April 2006 as part of NASA's A-Train constellation of satellites (Stephens et al., 2002). CloudSat is in a sun-synchronous orbit with an inclination of 98.2°. The high inclination angle makes it possible to achieve almost global coverage, reaching 82.5° from north to south (Tanelli et al., 2008). CloudSat carries the Cloud Profiling Radar (CPR), a microwave radar operating at 94 GHz. CPR is the first satellite-based radar instrument that provides vertically resolved measurements sensitive enough to detect clouds, light precipitation, and falling snow in the Arctic (Stephens et al., 2008; Kulie and Bennartz, 2009). Therefore, CloudSat is an essential source of information for the characterization of snowfall in the Arctic (Edel et al., 2020). In addition to better interaction with hydrometeors, another advantage is that microwave frequencies are independent of sunlight. Cloudsat can, therefore be used during polar night and provides information throughout the year in the Arctic.

The CPR has a horizontal resolution of 1.7 km in the along-track direction and 1.4 km in the cross-track direction. Between the surface and 30 km altitude, the vertical resolution is 480 m. As the CloudSat products oversample the return power by a factor of 2 and the height of the CloudSat range bins are slightly variable over time, the data are mapped to a homogeneous grid. Thus, each vertical reflectivity profile consists of 125 bins each 240 m thick (Stephens et al., 2002; Tanelli et al., 2008). The minimum detectable reflectivity of CPR depends on several factors such as the cloud cover, the surface type, and atmospheric attenuation. Generally, the minimum detectable signal of the CPR is -30 dBZ. This low detection threshold allows observing light precipitation rates typical of the Arctic (Mitrescu et al., 2010). Regarding noise, the measurement uncertainties range from 3 dBZ for a reflectivity of - 30 dBZ to around 0.1 dBZ for reflectivities above - 10 dBZ (Wood and L'Ecuyer, 2018b). According to Stephens and Haynes, 2007 and Haynes et al., 2009, reflectivity values between -30 and -15 dBZ represent non-precipitating clouds, values between -15 and 0 dBZ typically characterise drizzle or light rain, and values greater than 0

dBZ indicate rain with increasing intensity. Unattenuated near-surface reflectivity values greater than 0 dBZ and -5 dBZ are almost certainly associated with surface rain or snow, respectively, of at least 0.03 mm hr^{-1}.

CloudsSat observations suffer from clutter contamination. The ground clutter prevents the detection of precipitation close to the surface. This is known as the so-called blind zone most pronounced below 1.2 km height (Maahn et al., 2014). In particular, observations over complex terrain such as mountains and fjords are affected (Kulie and Bennartz, 2009; Palerme et al., 2019).

The relevant CloudSat products used in this study are the 2B-GEOPROF (Marchand, 2018) and the 2C-SNOW-PROFILE (Wood and L'Ecuyer, 2018b) version R05. These products give information about the vertical distribution of the radar reflectivity and snowfall rate. In all products, the ground clutter effect is considered. The 2B-GEOPROF product contains the non-attenuated vertical radar reflectivity profile. The 2C-SNOW-PROFILE product provides information on the vertical distribution of snowfall rates and the associated uncertainties. The precipitation phase is first determined by ECMWF operational analyses based on the near-surface air temperature to determine the snowfall rate. The snowfall rate is estimated when the melted fraction of the assessed precipitation is below 10% (Woods and Caballero, 2016). Herein, the blind zone is defined as the two lowest bins over the open ocean and the four lowest bins over land and frozen surfaces, excluding sea ice. Therefore, the next highest bin at an altitude of 750 m (1250 m) over the ocean (land) is considered for snowfall retrieval (Wood and L'Ecuyer, 2018a).

The so-called blind zone can lead to a deviation from the true snowfall rate near the surface. For example, evaporation and microphysical processes below this height could lead to over- or underestimation of the near-surface snowfall rate. Using ground-based observations. Maahn et al. (2014) showed an underestimation of about ˜ 10% in the snowfall rate for Ny-Ålesund. Furthermore, there is an uncertainty in the retrieval that derives the snowfall rate from the measured radar reflectivity factor due to several assumptions, e.g., the type of ice particles considered (Kulie and Bennartz, 2009). Nevertheless, comparing the snowfall retrieval from the 2C-SNOW-PROFILE product with ground-based radar networks has shown that Cloudsat performs well for light precipitation, but tends to underestimate snowfall rates for moderate and heavy snowfall, e.g. Norin et al., 2015. Also, over the Arctic and Antarctica, the derived snowfall climatology has shown good agreement with observations from the ground (e.g. Souverijns et al., 2018).

2.1.2 Methodology

2.1.2.1 PAMTRA

To compare the ERA5 reanalysis with ground- and satellite-based remote sensing observations, the forward operator PAMTRA (Passive and Active TRAnfer; Mech et al., 2020) is used. This section provides a brief overview of PAMTRA; more detailed information can be found in Mech et al. (2020).

PAMTRA is a Fortran-Python model framework suitable for simulating passive and active observations in a plane-parallel, one-dimensional, and horizontally homogeneous atmosphere for the microwave frequency range. It allows the transformation of the atmospheric state into synthetic observations. In order to be able to apply the model, input parameters such as the boundary conditions (surface/space), atmospheric state, and hydrometeor settings are needed.

For the atmospheric state, the vertical temperature, pressure, and humidity profile from the ERA5 reanalysis is used as input to PAMRTRA. The gaseous absorption coefficient of oxygen, water vapor, and nitrogen are calculated as described in Mech et al. (2020). For the hydrometeors, PAMTRA needs information about the microphysical (particle size distribution, mass-size relation, velocity-size relation) and scattering properties (Lorenz-Mie, Reyleigh-Gans). The microphysical properties are described according to the microphysical scheme of the ECMWF Integrated Forecasting System (IFS). The scattering properties depend on different types of hydrometeors. ERA5 provides the four hydrometeor species cloud water, cloud ice, rain, and snow. As the cloud water and rain particles are assumed to be spherical, the Lorenz-Mie theory is used. In contrast, cloud ice and snow have a more complex structure and are assumed to be non-spherical. For non-spherical particles, the self-similar Rayleigh-Gans approximation (Hogan and Westbrook, 2014) is used as the spherical approximation would not provide realistic scattering characteristics at 94 GHz.

Once all the necessary input information is compiled, the simulations provide brightness temperatures for the passive part and the full radar Doppler spectrum and its moments (such as radar reflectivity, mean Doppler velocity, skewness) for the active part (Mech et al., 2020). In this study, the radar reflectivity at 94 GHz is forward simulated to compare the ERA5 reanalysis with the ground-based radar (JOYRAD-94) and satellite (CloudSat, CPR) observations.

2.1.2.2 Detection of Atmospheric Rivers

AR detection algorithms have been developed for specific regions (west coast of the US, Great Britain, Antarctica) (Shields et al., 2022). However, there is a lack of detection algorithms adapted to ARs in the Arctic. At the current time, two detection algorithms for the Arctic exist. These are the global detection algorithm introduced by Guan and Waliser (2015b) - refined by Guan et al. (2018) - and the detection algorithm developed by Gorodetskaya et al. (2014) and Gorodetskaya et al. (2020) for a specific application for the cold and dry troposphere of Antarctica and adapted for AR identification in the Arctic (Viceto et al., 2022). As neither detection algorithm has yet been applied to the ERA5 reanalysis, this was done as part of this work.

Guan's AR algorithm

The first version of the global AR detection algorithm is described in detail in Guan and Waliser, 2015a. Generally, this algorithm is based on the integrated water vapor transport IVT. The IVT is determined by the zonal (x) and meridional (y) components of the IVT:

$$IVT_x = -\frac{1}{g}\int_{p_1}^{p_2} qu\, dp \tag{2.1}$$

$$IVT_y = -\frac{1}{g}\int_{p_1}^{p_2} qv\,dp \tag{2.2}$$

$$IVT = \sqrt{IVT_x^2 + IVT_y^2} \tag{2.3}$$

with the zonal (u) and meridional (v) wind, the specific humidity (q) profiles from p1 (1000 hPa or nearest surface level) to p2 (300 hPa), the gravitational acceleration g (= 9.81 m s^{-2}), and the pressure p.

For the identification of an AR, different requirements have to be considered. These include the intensity, direction, and geometry of IVT. For the IVT intensity, a combination of a specific percentile and a fixed lower limit is used. In their first version, Guan and Waliser, 2015a determined the monthly-based 85^{th} percentile of IVT for each grid cell from 1997-2014. The percentile for each month is calculated by using the concerned month and the two months before and after the corresponding month (e.g., for March: January to May). For each grid cell, the IVT must exceed the 85^{th} percentile of IVT and the lower limit of 100 kg m^{-1} s^{-2}. In their second version (Guan et al., 2018), they set the lower limit to 50 kg m^{-1} s^{-2} in the polar regions due to their lower moisture capacity. If this requirement is fulfilled, the IVT direction and geometry are analysed. For the IVT direction, the IVT direction at individual grid cells has to be coherent, and the direction of the object-mean IVT must be within 45° of the AR shape orientation, with a significant poleward component. For the IVT geometry, the considered object has to be larger than 2000 km, and the length-to-width ratio should be higher than two.

If the IVT intensity criterium is fulfilled but not the geometrical (e.g., too short or too wide) and directional criteria, the object is not considered as an AR. In this case, the requirements in terms of percentile are modified in the second version (Guan et al., 2018) following the concept by Wick et al. (2013). The object is rejected if the IVT exceeds the 85^{th} percentile but does not fulfill the geometrical or directional criteria. Then, the process is repeated for higher IVT thresholds. The 87.5^{th} percentile is to be considered in the following. If the IVT intensity requirement is fulfilled, however, the geometrical and directional criteria are still not met, the process is repeated for the 90^{th}, 92.5^{th}, and 95^{th} percentile. In case the intensity requirement is not met at the 95^{th} percentile no AR is identified.

In the framework of this thesis, the second version (Guan et al., 2018) is applied to ERA5 reanalysis at hourly resolution. Compared to other reanalyses (ERA-Interim, MERRA2, NCAR-NCEP) for which an AR catalog already existed, the application to the ERA5 reanalysis was pursued to allow a better spatial and temporal resolution of ARs. This is particularly beneficial for precipitation, which is highly variable in both time and space.

All relevant variables, i.e. the zonal and meridional components of the IVT (IVT_x and IVT_y), as well as the IVT percentiles (85^{th} – 95^{th}, in 2.5 steps) for each grid cell from 1979-2020 for the whole globe have to be calculated. This calculation required considerable computing time due to the high temporal and spatial resolution of ERA5. Due to the large amount of data, the data processing was carried out on the high-performance computer Mistral (since September 2022: Levante) from

the German Climate Computing Centre (Deutsches Klimarechenzentrum, DKRZ) in Hamburg. In the following, the individual steps for data processing are described:

- Remapping required variables from the reduced Gaussian grid (N320) to a regular latitude-longitude grid with an ERA5 resolution of 0.25° (using the Climate Data Operators *cdo*). The required variables are the specific humidity, the zonal and meridional wind, the geopotential, the land-sea-mask, and the surface pressure.
- Calculating the zonal, meridional, and total components of IVT (as in Equations 2.1-2.3).
- Dividing the whole globe into 1296 boxes (latitude: 36 x 5° boxes, longitude: 36 x 10° boxes).
- Calculating the 85^{th} – 95^{th} percentiles for each month and grid cell in the individual boxes. The relevant months are selected by using cdo. The percentile is calculated with the $numpy.percentile()$ function in Python.
- Assembling the individual boxes in one output file.
- Applying the second version of Guan's algorithm to the calculated variables (IVTx, IVTy, land-sea-mask, 85^{th}-95^{th} percentile of IVT). The hourly detected ARs for the entire globe on a 0.25° grid and the ERA5 period from 1979-2021 are available on PANGEA (Lauer et al., 2023a).

Gorodetskaya's AR algorithm

The detection algorithm of Gorodetskaya et al., 2014; Gorodetskaya et al., 2020 was developed for the cold and dry conditions of Antarctica. It takes into account the reduced saturation capacity of the polar atmosphere compared to lower latitudes. The detection of ARs is based on the integrated water vapor (IWV). It considers a combination of a saturated IWV (IWV_{sat}) related threshold and geometric constraints. In this study, only the so-called potential ARs are used as the geometric part was not finished at the time of the work.

The threshold is based on the zonal mean and maximum values of (IWV_{sat} and on an AR coefficient (AR_{coef} = 0.2) that determines the relative strength of an AR, which is explained in detail in Gorodetskaya et al. (2014). For the AR algorithm, the IWV and IWV_s are computed from 1000 hPa (or nearest surface level, p_1) to 300 hPa (p_2):

$$IWV = -\frac{1}{g}\int_{p_1}^{p_2} q\, dp \tag{2.4}$$

$$IWV_s = -\frac{1}{g}\int_{p_1}^{p_2} q_s(T)\, dp \tag{2.5}$$

where g is the gravitational acceleration, p is the pressure, T is the air temperature, and q_s is the saturated specific humidity. As in Gorodetskaya et al., 2020, the variable q_s is calculated from the saturated vapor pressure e_s following Bolton (1980). Here, the saturation vapor pressure over water is used as the water vapor can be saturated in equilibrium with liquid or ice for T < 0°C:

$$e_s = 6.112 * exp(\frac{17.67 * T}{243.5 + T}) \tag{2.6}$$

$$q_s = \epsilon * \frac{e_{sat}}{p - e_{sat}} \tag{2.7}$$

where ϵ (=0.622) is the ratio between the specific gas constant for dry air R_d (287 J kg^{-1}) and the specific gas constant for water vapor R_v (461 J kg^{-1}).

The threshold is then calculated:

$$IWV \geq IWV_{s,mean} + AR_{coef} \cdot (IWV_{s,max} - IWV_{s,mean}) \tag{2.8}$$

where $IWV_{s,mean}$ is the zonal mean IWV_s along each latitude, and $IWV_{s,max}$ is the maximum values of IWV_s along the same latitude. If IWV is equal to or higher than this threshold: the advected moisture within the object exceeds the mean IWV_s along the same latitude. Consequently, the object can be classified as a potential AR.

Viceto et al., 2022 applied this algorithm for the Arctic for three case studies. For the Arctic, ARs are classified as an AR if the object reaches and crosses 70°N, and the IWV has to be continuous above the threshold for at least 2000km within a maximum width of 40° longitude. The axis of an AR is defined as the maximum values of IWV at each latitude. Within the framework of this thesis, the potential ARs are calculated for the ERA5 period (1979-2021).

2.1.3 Results

This study focuses on an AR event that occurred at the end of May during the ACLOUD campaign. Figure 2.1 shows the daily precipitation rate averaged for 28 – 31 May 2017, for which the AR was detected by Guan's AR algorithm based on ERA5 reanalysis. The AR starts to precipitate when it moves from Siberia over the sea ice of the Kara Sea towards Ny-Ålesund. In this area, the daily average precipitation rates reach between 10 and 15 mm day^{-1}. The highest precipitation rates (up to 25 mm day^{-1}) are concentrated on the east coast of the northern part of Novaya Zemlya. Here, the mountainous terrain with up to 800 m height favors orographic precipitation. After passing Novaya Zemlya, the AR moves along the Barents Sea to Svalbard, where the daily average precipitation rates drop to 3-5 mm day^{-1}. Setting the same period in a climatological perspective, the precipitation rates are about 10 and 22 mm day^{-1} higher over the Kara Sea and on the east coast of Novaya Zemlya, respectively. Although the precipitation rates decrease over the Barents Sea, they are still up to 5 mm day^{-1} higher compared to the climatology. The comparison of the daily averaged precipitation for this AR with the climatology highlights the importance of ARs in terms of precipitation (Fig. 2.1).

The comparison between ground-based and space-borne observations for the AR event at the end of May during the ACLOUD campaign focuses on 29 May 2017. On this day, the AR was first detected by Guan's algorithm at 9 UTC in Ny-Ålesund. Shortly before the AR reached Ny-Ålesund, it was captured by CloudSat (8:30-8:40 UTC) east of Svalbard. Figure 2.2 illustrates the AR shape approaching Ny-Ålesund and the CloudSat overpass. As the AR is captured by CloudSat before it reaches Ny-Ålesund, first the cross-section of AR (space-borne measurements), then the temporal development of the AR (ground-based measurements) are analysed.

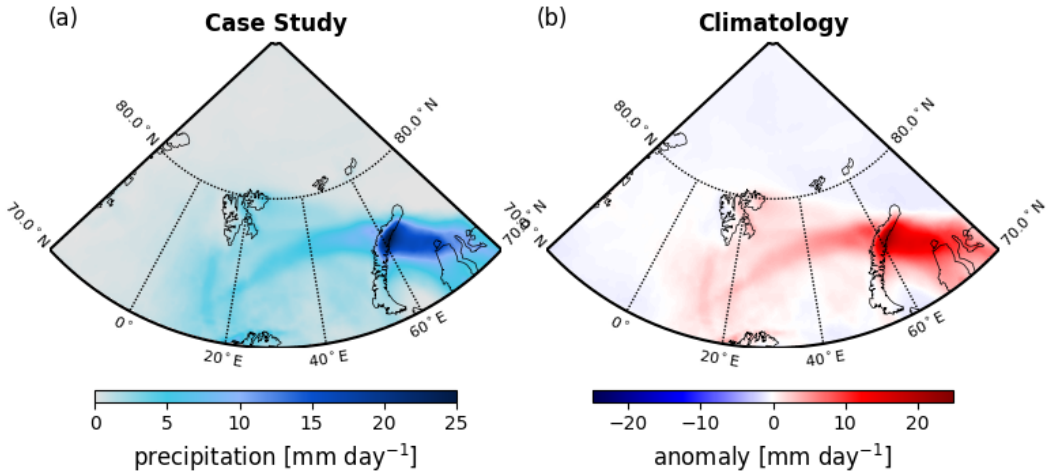

FIGURE 2.1: Daily precipitation averaged for 28 – 31 May 2017 (left) and deviation from climatology (right).

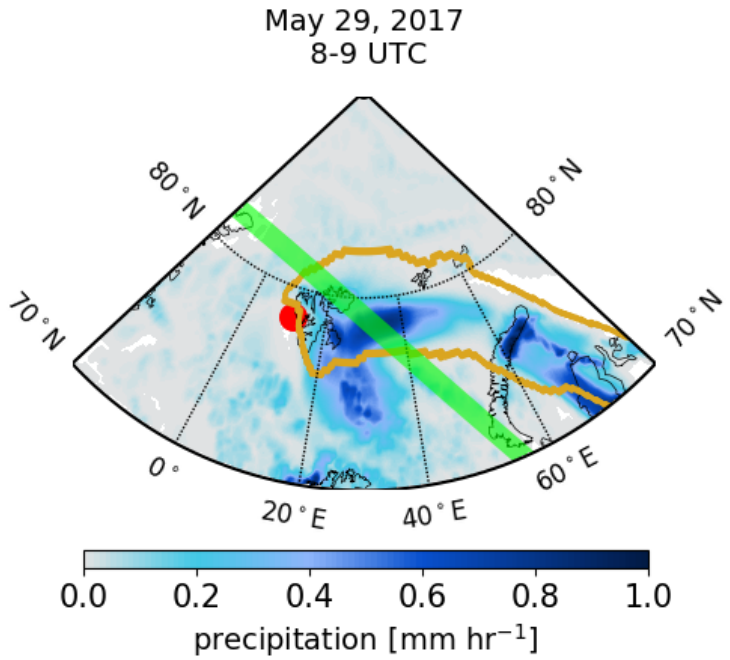

FIGURE 2.2: Hourly precipitation on 29 May 2017 between 8 and 9 UTC. AR contour (orange), CloudSat track (green) and location of Ny-Ålesund (red) are shown.

2.1.3.1 Comparison between CloudSat and ERA5

CloudSat encountered the AR on 29 May at 8:34 UTC for about two minutes east of Svalbard. The radar reflectivity from the 2B-GEOPROF product (CloudSat) ranges from -20 dBz up to 15 dBZ within the vertical AR cross-section (Fig. 2.3 top). The highest radar reflectivity values are concentrated at the southern edge of the AR and extend from about 4 km altitude down to the layer that is affected by the ground clutter effect. In the lowest 2 km, there is a sharp decrease in the radar reflectivity between the precipitation core within the AR and the northeast coast of Svalbard (at 8:36 UTC). The latter can be attributed to the ground clutter effect, which extends up to an altitude of 1.5 km. The increase in near-surface radar reflectivity in front of the northeast coast of Svalbard points at orographic ascend favoring precipitation formation. North of Svalbard, there is no radar reflectivity in the lower layers.

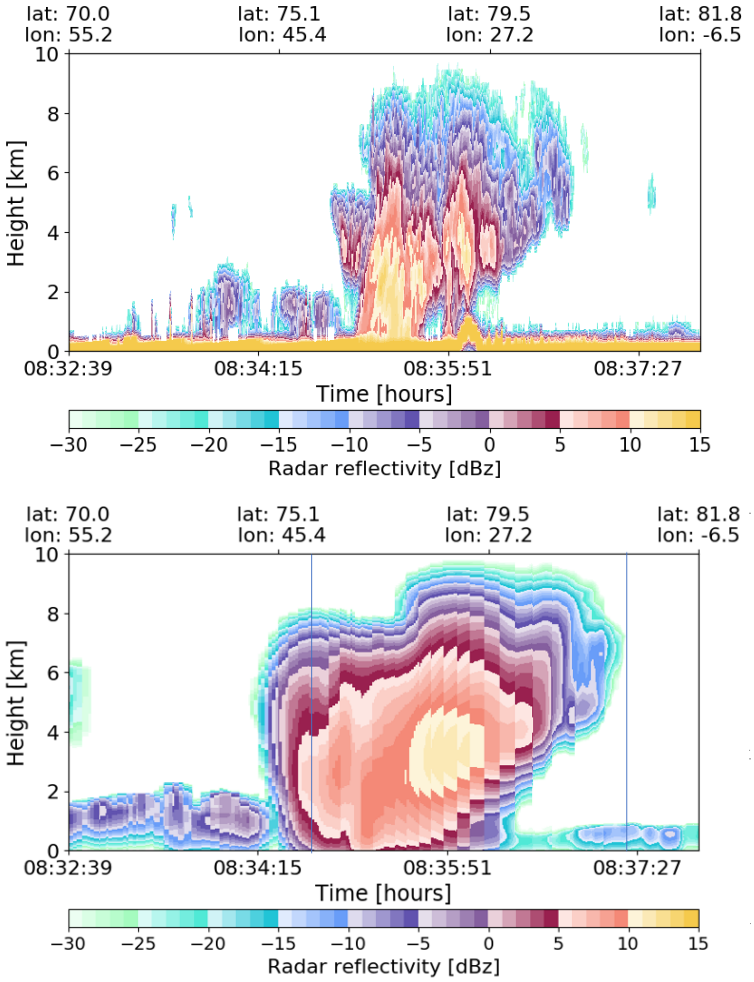

FIGURE 2.3: Vertical cross-section of the radar reflectivity [dBZ] for the CloudSat overpass (see Fig. 2.3) on 29 May from 8:30-8:38 UTC. Top: CloudSat; bottom: forward simulated radar reflectivity based on ERA5 reanalysis for the nearest CloudSat grid cell. Vertical lines indicate the location of AR as given by the AR detection algorithm.

The comparison of the radar reflectivity derived from the 2B-GEOPROF product with the radar reflectivity simulated by PAMTRA for ERA5 is performed for the nearest grid point to the CloudSat path (Fig. 2.3 bottom). The coarser resolution

of ERA5 is clearly evident in the vertical profiles, showing jumps in radar reflectivity when the track passes from one into another grid cell. Generally, the shape of the CloudSat and forward-simulated ERA5 profiles is quite similar: a major precipitating system with radar reflectivities higher than 0 dBZ and reaching up to 10 km height is visible within the AR shape. Also, the magnitude of the radar reflectivities is comparable. Looking at the average vertical profile of hydrometeors along the CloudSat path (Fig. 2.4) the vertical profile of hydrometeors corresponds very well with the vertical profile of the CloudSat radar reflectivities. Both CloudSat and ERA show the highest reflectivities with more than 0 dBZ at 3km height. The decrease towards the surface and towards the troposphere is slightly stronger for CloudSat. Especially in the center of the ERA5 hydrometeors are mainly composed of high-reaching ice and snow, and no liquid rain is evident (Fig. 2.5).

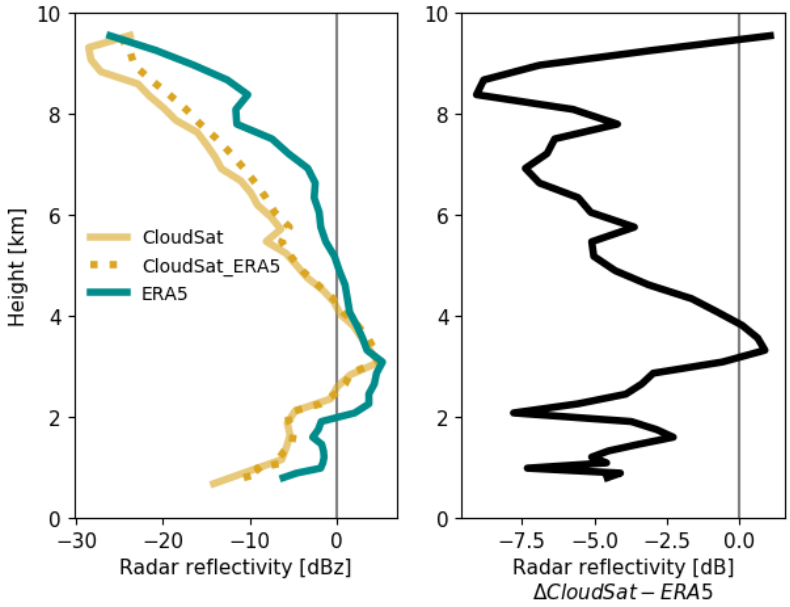

FIGURE 2.4: Vertical profile of mean radar reflectivity averaged from 8:30-8:38 UTC for CloudSat (solid yellow), CloudSat interpolated on ERA5 height (dashed yellow), and ERA5 reanalysis (solid cyan).

However, there are minor deviations compared to CloudSat. First, the coarser resolution of ERA5 leads to a slightly broader precipitation system. Secondly, ERA5 slightly underestimates the radar reflectivity (2-3 dB), especially in the precipitation core of the AR, which could be due to errors in the assumptions on ice particle habit. Similarly, the difference in radar reflectivities in the upper troposphere (Fig. 2.4) could be due to problems in the ice microphysics of ERA5's underlying model. Further differences occur for low clouds below 2 km south of Svalbard (Fig. 2.3) at the beginning of the overpass from 8:32 to 8:34 in the south. During this time, the radar reflectivities are less than 0 dBZ, which usually characterizes drizzle or light precipitation (Stephens and Haynes, 2007; Haynes et al., 2009). The ground clutter effect of CPR makes it difficult to interpret this result. However, small signals can also be recognized here. The model-to-observation approach allows the identification of the different contributions to radar reflectivity (Fig. 2.5). Clearly the reflectivities in ERA5 are caused by continuous clouds composed of liquid water. However, CloudSat shows isolated reflectivities indicative of more convective clouds. This illustrates

the difficulties of ERA5's ca. 30km resolution for which grid-scale clouds appear.

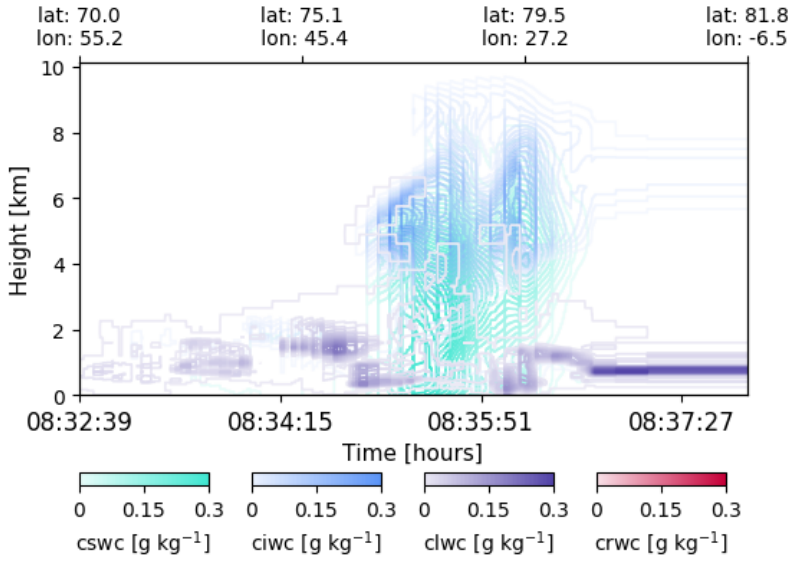

FIGURE 2.5: Vertical profiles of different hydrometer species for the ERA5 grid cells nearest to the CloudSat overpass on 29 May 2017.

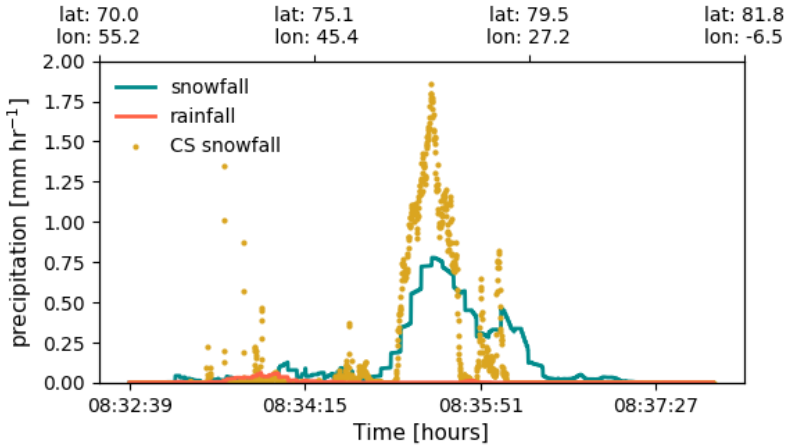

FIGURE 2.6: Time series of snowfall along the CloudSat path on 29 May 2017 for CloudSat (yellow dots), and ERA5 (cyan).

To shed more light on this AR case, in the following, the CloudSat snowfall rate is compared with the ERA5 precipitation (Fig. 2.6). It becomes obvious that snowfall rates up to 2 mm hr^{-1} are concentrated within the AR shape (Fig. 2.3). The higher snowfall rates are mainly concentrated between 1.5 and 4 km altitude. In the beginning of the overpass, especially light snowfall rates below 0.2 mm hr^{-1} are detected. The location of the light snowfall rates is consistent with the low cloud water and the reflectivity of less than 0 dBz (Fig. 2.3). Thus ERA5 shows a low precipitation amount of less than 0.1 mm hr^{-1} (Fig. 2.6). The precipitation rates strongly increase within the AR while CloudSat has more isolated events indicative of convective precipitation. In the near-surface bin of the 2C-SNOW-PROFILE, the snowfall rate ranges from 0.4 to 1.8 mm hr^{-1}. Although, the time for which the

maximum snowfall rate is detected is the same for CloudSat and ERA5, the ERA5-related snowfall does not exceed 0.8 mm hr^{-1}. Nevertheless, both CloudSat and ERA5 reveal two precipitation maxima along CloudSat's path. ERA5 has lower and wider maxima, illustrating the effect of its coarser resolution smoothing localized (convective) features resolved by CloudSat.

2.1.3.2 Comparison between JOYRAD-94 and ERA5

The AR event hit Ny-Ålesund on 29 May 2017 at 9 UTC (Fig. 2.2). The warm and moist air concentrated within the AR was also recorded by HATPRO. During this day, the temperature increases from 266 up to 272 K and IWV from 4 to 12 kg/m2 (Fig. 2.7). The arrival of the AR around 9 UTC corresponds to the strongest rise in IVW. This is even more pronounced in the independent HATPRO measurements confirming the quality of the ERA5 AR detection. However, none of the precipitation sensors at AWIPEV (Pluviometer, Parsival) detected precipitation during this day. Therefore, the temporal development of the radar reflectivity for JOYRAD-94 and ERA5 is examined (Fig. 2.8).

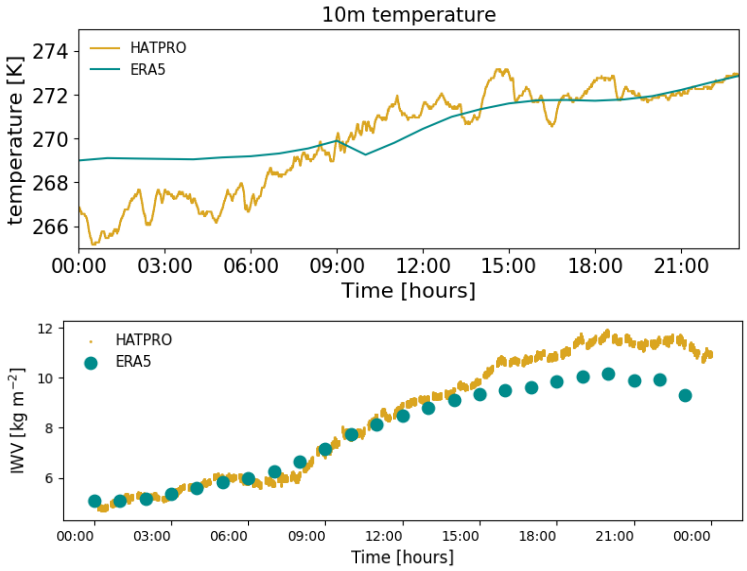

FIGURE 2.7: Time series of the near-surface temperature and IWV for HATPRO (yellow) and ERA5 (cyan).

The radar reflectivities in Ny-Ålesund start to increase after the AR has arrived. Especially between 2 and 4 km altitude the radar reflectivities reach up to 10 dBZ. The high values maintain until around 20 UTC. In particular, the time window from 16 to 20 UTC is of interest when the AR core passed AWIPEV. At 16 UTC, the higher radar reflectivities reach from the surface up to 6 km altitude. Then, from 16 to 20 UTC, they are again mainly located between 4 and 6 km altitude.

Comparing the radar reflectivity factor of JOYRAD with the forward simulated radar reflectivity for ERA5, the general structure of the vertical distribution appears comparable (Fig. 2.8). However, similar to the CloudSat comparison, ERA5 shows much broader and smoother structures due to its coarser resolution. However, there are also deviations. Especially in the beginning, when the AR arrived (9-12 UTC), radar reflectivities below 0 dBZ are simulated from the surface up to 8 km height

while only an ice anvil is visible from the ground. Further, PAMTRA simulates higher radar reflectivities, especially in the lowest 2 km from 12 to 21 UTC. Though the radar reflectivities are of the same magnitude with up to 10 dBZ in the mid-troposphere, JOYRAD does not show any reflectivities reaching all the way down to the surface. Around 18 UTC, radar reflectivities up to 10 dBZ are measured. This is also the time window for which ERA5 simulates precipitation at the surface. However, the maximum does not exceed 0.2 mm hr^{-1} (Fig. 2.9). Thus, both ERA5 and the measurements show a strong reduction of hydrometeors towards the surface, possibly due to sublimation. It is likely that due to the strong blocking of Svalbard's mountain range, snowfall is concentrated on the eastern side of the archipelago and AWIPEV is affected by lee effects. Both HATPRO and ERA5 show low LWP values (<50g m^{-2}) indicative of thin supercooled clouds (Fig. 2.9). While no surface precipitation is measured at Ny-Ålesund (not shown) ERA5 shows light snowfall rates as subzero temperatures prevail throughout the day (Fig. 2.7).

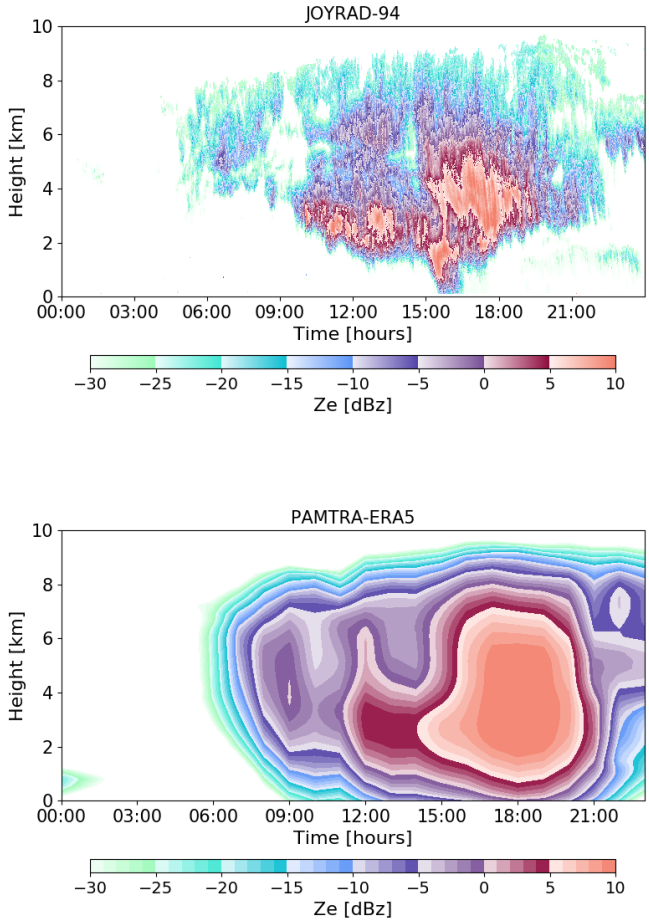

FIGURE 2.8: Time series of the radar reflectivity factor [dBZ] derived from JOYRAD94 at Ny-Alesund (red dot in Fig. 2.3 and for ERA5 (forward simulated).

Generally, the forward simulated radar reflectivities based on the ERA5 data are well represented. Local details which appear strongest in the high-temporal resolution column observations at Ny-Ålesund and also in CloudSat with its roughly 2

km resolution can naturally not be captured by ERA5 with its about 30 km resolution. Further, one has to note that the measurements at Ny-Ålesund are influenced by complex terrain and sub-grid processes can further lead to deviations between ERA5 and the measurements.

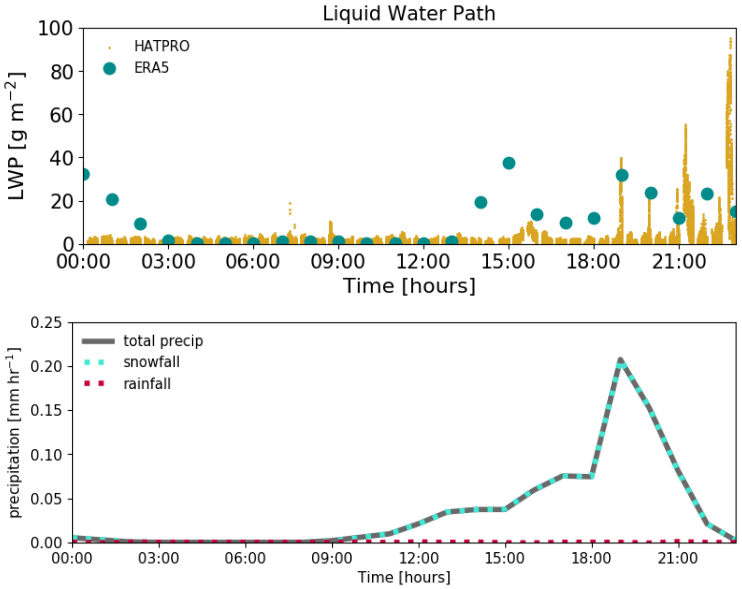

FIGURE 2.9: Time series of the LWP [g m^{-2}] derived from HATPRO (yellow) at Ny-Ålesund (red dot in Fig. 2.3 and for ERA5 (forward simulated) (cyan) and (top) and the precipitation for ERA5 on 29 May 2017.

2.2 Part II: AR events during MOSAiC mid-April 2020

This thesis also contributed to the Cross-Cutting Activity 4 (CCA4: Air mass transport and transformation) of (AC)^3, which analyses the transformation of air masses with emphasis on anomalous moisture transport and its effect on surface properties such as surface energy budget and precipitation. Kirbus et al., 2023 summarized initial results of CCA4 for two AR events that occurred within a very short time during the MOSAiC expedition in mid-April 2020. A major focus was to investigate the influence of ARs on surface snowfall based on ERA5 reanalyses and ground-based and space-borne observations. These analyses were carried out as part of this thesis and are presented in this section.

The largest Arctic expedition, MOSAiC, took place from September 2019 to September 2020. The aim of this expedition was to collect data from the ocean, ice, and atmosphere to gain a better understanding of changes in the Arctic and their global impact. In mid-April, the research vessel Polarstern was affected by two AR events (detected by Guan et al. (2018); based on ERA5). The first AR event originated in Siberia. The positive pattern of the North Atlantic Oscillation pattern pushed this AR towards the high Arctic. The second AR event originated over the Atlantic. A Scandinavian blocking pattern favored the transport of AR-related warm and moist air across the Fram Strait into the Arctic (Kirbus et al., 2023).

During MOSAiC, the snowfall rates were measured by two ground-based instruments: the Ka-Band Zenith Radar (KAZR) and the weighing bucket precipitation gauge Pluvio (Matrosov et al., 2022). The KAZR is a zenith-pointing radar that operates at 35GHz. The KAZR was designed for cloud observations and is used for snowfall measurements (Matrosov et al., 2022). The snowfall rate S has been retrieved using the Z-S relation: $Z = 63\,S^{-2}$. The snowfall rates have a temporal resolution of 30 s and are available at 0.17 and 0.23 km above the surface layer. The data are available from the ARM user facility archive (http://dx.doi.org/10.5439/1498936). Pluvio is a weighing bucket precipitation gauge. To reduce the influence of blowing snow, Pluvio was sheltered by a double windshield. The estimated precipitation rates from Pluvio are available at 1-min resolution. The Pluvio data are online available from the ARM user facility archive (http://dx.doi.org/10.5439/1338194).

In addition to the ground-based measurements, the surface snowfall rate is available from the Snow retrieval Algorithm fOr gpM-Cross Track (SLALOM-CT) (Sanò et al., 2022). This machine learning-based algorithm exploits Advanced Technology Microwave Sounder observations (ATMS). The high-frequency channels of ATMS are sensitive to falling snow and have been trained using concurrent CloudSat measurements. This study uses the ATMS observations from the near-polar orbiting satellites Suomi National Polar-orbiting Partnership (SNPP) and NOAA-20. The snowfall rates from these observations are compared with the ERA5 reanalysis. For ERA5 and SLALOM-CT, the nearest grid cell or the nearest pixel to the RV Polarstern will be used.

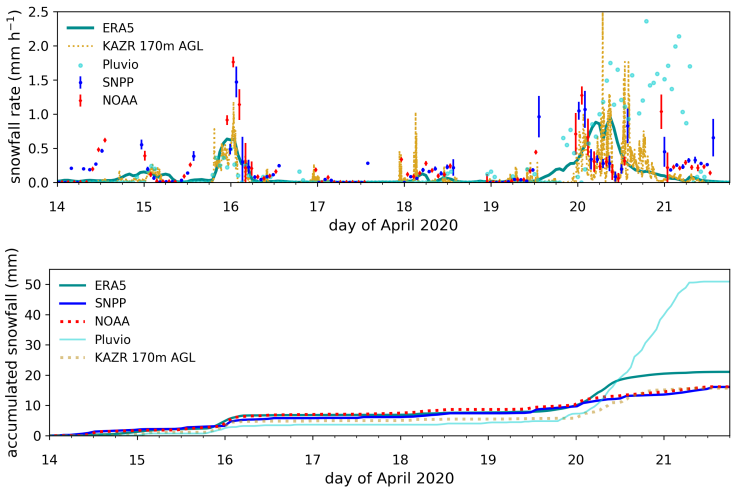

FIGURE 2.10: Time series of surface snowfall rate (SSR) at the research vessel Polarstern from 14 April, 0 UTC until 21 April, 23 UTC for the ground-based measurements KAZR at 170 m above ground (yellow dots) and Pluvio (turquoise dots), the satellite ATMS measurements (SNPP: blue dots; NOAA: red dots) with standard deviations on a 3x3 pixel window, and for ERA5 (cyan solid line) as published in (Kirbus et al., 2023)

.

In the time series of the surface snowfall rate at the RV Polarstern, the two periods in which the ARs occurred at the MOSAiC site can be identified. Both AR events brought a considerable amount of snowfall into the high Arctic. During the first period (15-16 April), snowfall rates up to 2 mm hr^{-1} are observed. During the second

period (19-21 April), the snowfall rates increased up to 2.5 mm hr^{-1}.

Comparing the snowfall rates from the different measurement platforms and ERA5 reanalysis, it becomes obvious that snowfall has strong variability and is difficult to measure/model (Fig. 2.10). For the first AR event, the ERA5 snowfall rate and ground-based measured (KAZR, Pluvio) snowfall agree relatively well. However, the snowfall rate measured by satellites is about a factor of two higher. For the second AR event, the temporal evolution of the ERA5 snowfall rate is similar to the ground-based measurements. However, ERA5 tends to underestimate the snowfall slightly and provides a much smoother distribution. The satellite product both over- and underestimates the snowfall rate by a factor of two. This discrepancy can arise from the difficulty of retrieving precipitation from passive measurements over sea ice. Also, it could partly be due to the fact that the precipitation rates in the area around RV Polarstern are spatially very different, resulting in different precipitation values for the nearest satellite pixels (Kirbus et al., 2023). Higher snowfall rates compared to the ground-based measurements could be the consequence of the nearest grid box, including precipitation rates that are not measured from the ground-based measurements. Further, ERA5 tends to underestimate the snowfall slightly compared to ground-based measurements. For the reanalyses, the precipitation is accumulated over the whole grid box. Therefore, strong events limited to a specific area cannot be represented.

2.3 Conclusions

In this section, the ERA5 reanalyses data were evaluated with various ground-based and space-borne observations based on two case studies. None of these observations were assimilated into ERA5 and are, therefore, completely independent. In the first case study, the focus was mainly on the vertical profile of radar reflectivities and the distribution of hydrometeors. For the second study, surface snowfall rates are analysed.

Generally, ERA5 reanalysis data agrees well with the observational data with respect to the general structure of the precipitation systems. However, there are also deviations, especially over complex terrain. Although ERA5 is the global reanalysis with a higher spatial and temporal resolution than other reanalyses, it is still too coarse to represent small-scale features, as shown for the time series for snowfall rates. In particular, strong precipitation events could be underestimated by ERA5 reanalysis as large-scale precipitation is spread over the respective grid box. Cloud radar measurements from the ground and space indicated that smaller convective clouds (and precipitation), for example, evident in cold air outbreaks, might be missed by ERA5. Nevertheless, ERA5 successfully represents AR timing and larger precipitation features related to AR shapes and is therefore used in the following studies. on.

Chapter 3

Influence of Atmospheric Rivers and associated weather systems on precipitation in the Arctic

In this study, the influence of ARs, cyclones, and fronts on precipitation in the Arctic is analysed for two airborne campaigns. Based on these case studies a new methodology is established that allows to distinguish the precipitation related to ARs, cyclones, and fronts. The study was published in the journal *Atmospheric Chemistry and Physics* (Lauer et al., 2023b) .

3.1 Abstract

In this study, we analyse the contribution of Atmospheric Rivers (ARs), cyclones, and fronts to the total precipitation in the Arctic. We focus on two distinct periods of different weather conditions from two airborne campaigns: ACLOUD (May/June 2017) and AFLUX (March/April 2019). Both campaigns covered the northern North Atlantic sector, the area in the Arctic that is affected by the highest precipitation rates. Using ERA5 reanalysis, we identify pronounced regional anomalies with enhanced precipitation rates compared to the climatology during ACLOUD due to these weather systems, whereas during AFLUX enhanced precipitation rates occur over most of the area.

We have established a new methodology, that allows us to analyse the contribution of ARs, cyclones, and fronts to precipitation rates based on ERA5 reanalysis and different detection algorithms. Here, we distinguish whether these systems occur co-located or separately. The contributions differ between the two periods. During ACLOUD (early summer), the precipitation rates are mainly associated with AR- (40%) and front-related (55%) components, especially if they are connected, while cyclone-related components (22%) play a minor role. However, during AFLUX (early spring) the precipitation is mainly associated with cyclone-related components (62%). For both campaign periods, snow is the dominant form of precipitation, and the small rain occurrence is almost all associated with ARs. About one-third of the precipitation can not be attributed to one of the weather systems, the so-called residual. While the residual can be found more frequently as convective than as large-scale precipitation, the rare occasion of convective precipitation (roughly 20%) can not completely explain the residual. The fraction of precipitation classified as residual is reduced significantly when a precipitation threshold is applied that is often used to eliminate "artificial" precipitation. However, a threshold of 0.1 mm h^{-1} reduces the total accumulated precipitation by a factor of two (ACLOUD) and three

(AFLUX) especially affecting light precipitation over the Arctic Ocean. We also show the dependence of the results on the choice of the detection algorithm serving as a first estimate of the uncertainty.

In the future, we aim to apply the methodology to the full ERA5 record to investigate whether the differences found between the campaign periods are typical for the different seasons in which they were performed and whether any trends in precipitation associated with these weather systems can be identified.

3.2 Introduction

During the last four decades, the increase in the Arctic mean near-surface air temperature is nearly a factor of four higher than that of the global mean (Rantanen et al., 2022). This phenomenon is known as Arctic Amplification (Serreze and Barry, 2011; Wendisch et al., 2017). Evidence that the Arctic is warming includes the melting of sea ice, the retreat of glaciers, and the thawing of permafrost (Overland et al., 2019). The Arctic warming is forced by many processes and feedback mechanisms such as the lapse rate and snow- and ice-albedo feedback, the increasing downward longwave radiation caused by clouds and water vapour, the reduction of sea ice in summer, and the poleward heat and moisture transport (Serreze and Barry, 2011; Bintanja and Van Der Linden, 2013; Pithan and Mauritsen, 2014; Sejas et al., 2014). However, the knowledge of the involved processes and the relative importance of the feedback mechanisms is still limited.

In general, Arctic warming affects the hydrological cycle and leads to an increase in the precipitation in the Arctic (Bintanja, 2018; Boisvert and Stroeve, 2015; Vihma et al., 2016; McCrystall et al., 2021). This results in an increased total amount of water vapor (Rinke et al., 2019), related to increased moisture holding capacity by warmer air (Bintanja, 2018), enhanced local evaporation due to the reduced sea ice cover (Bintanja and Selten, 2014), and increased poleward moisture transport from lower latitudes (Zhang et al., 2013; Gimeno et al., 2015; Bintanja et al., 2020).

Although precipitation plays a key role in the Arctic climate system, an accurate Arctic-wide observational assessment of rain and especially snowfall is still a challenge nowadays (Von Lerber et al., 2022) which particularly holds for the identification of trends (McCrystall et al., 2021). The consequence of the warming in the Arctic is not only an increase in precipitation but also a phase change from snow to rain (Bintanja and Andry, 2017; Łupikasza and Cielecka-Nowak, 2020). Therefore, rain is expected to be the dominant type of precipitation in the Arctic (Bintanja and Andry, 2017). Consequently, an increase in rain on snow and ice surfaces leads to a lower albedo that forces the snow-albedo feedback and causes sea ice melting (Perovich et al., 2002).

Poleward moisture transport is often associated with Atmospheric Rivers (ARs). ARs are long (>2000 km in length) and narrow (<1000 km in width) bands of anomalous moisture amount and transport, which can rapidly transport moisture and heat from lower latitudes to the mid-latitudes and polar regions (Ralph et al., 2020). Although ARs only cover about 10% of the Earth's surface circumference at mid-latitudes, they are responsible for more than 90% of the poleward moisture transport in and across these latitudes (Guan and Waliser, 2015a). ARs play an important

role in many regions' hydroclimate (Lavers and Villarini, 2015; Waliser and Guan, 2017; Viale et al., 2018). In the Arctic, ARs can bring extreme warming events both via strong heat advection and increase longwave cloud forcing (Neff et al., 2014; Komatsu et al., 2018; Mattingly et al., 2018; Bresson et al., 2022), as well as strong precipitation, including both snowfall and rainfall (Mattingly et al., 2018; Viceto et al., 2022).

Formation and existence of the ARs have been related to extra-tropical cyclones (Ralph et al., 2020; Dacre et al., 2015), warm conveyor belts (WCBs) (Dacre et al., 2019), and tropical moisture exports (TMEs) (Bao et al., 2006; Hu and Dominguez, 2019). While ARs, WCBs, and TMEs are interrelated, they also have distinct features: ARs can exist without WCB or TME, but they can also co-exist with TME feeding an AR with moisture, while WCB being the moisture sink due to the isentropic ascent and precipitation formation (Ralph et al., 2018). ARs can also influence the formation of extra-tropical cyclones (Sodemann and Stohl, 2013; Zhang and Ralph, 2021; Eiras-Barca et al., 2018). Guo et al. (2020) and Zhang et al. (2019) also highlighted the strong association of AR events to extratropical cyclones pointing to specific features such as the importance of anticyclone and the role of pressure gradient in the AR strength. Mo (2022) reviewed the history of the evolution of the WCB and AR concepts and their relationship to the earlier developments of a "moisture tongue" theory.

The core of the water vapour transport is concentrated in the first 2-2.5 km above ground typically in the pre-cold-frontal part of the extra-tropical cyclone (Ralph et al., 2017). At the same time, precipitation formation is often triggered by uplift along fronts and by WCBs and thus can form above the AR core. Catto et al. (2015) investigated the relation between WCBs and frontal features with respect to extreme precipitation. They found that about 70% of WCBs are linked to cold fronts during winter, and about 50% of WCBs are associated with warm fronts in the northern hemisphere. However, their study excluded the high Arctic (> 80° N), while in our study the focus is on the Arctic, and the association of precipitation to ARs, cyclones, and fronts.

The purpose of our study is to determine the origin of Arctic precipitation on the synoptic scale. For this purpose, we aim to identify which precipitation is mainly associated with ARs and compare its association with cyclones and frontal zones.

We exemplary focus on two periods coinciding with airborne campaigns recently performed in the northern North Atlantic sector of the Arctic. This region encompasses the Atlantic pathway which is prone to the strongest moisture intrusions (Nash et al., 2018). The campaigns were performed at and around Svalbard within the framework of the Collaborative Research Center TR172 "Arctic Amplification: Climate Relevant Atmospheric Surface Processes, and Feedback Mechanisms $(AC)^3$" (Wendisch et al., 2017). While the ACLOUD (Arctic Cloud Observations Using airborne measurements during polar Day) campaign (Wendisch et al., 2019) took place in early summer (May/June) in 2017, the AFLUX (Aircraft campaign Arctic Boundary Layer Fluxes) campaign (Mech et al., 2022) was performed in early spring (March/April) in 2019. For both campaigns, we investigate the occurring ARs in depth and develop a methodology to detect individual contributions to precipitation which can be applied to the long-term reanalysis data set in the future to investigate long-term changes in synoptical precipitation characteristics, and thus the role of air

mass transport into the Arctic.

The main objective of this study is to quantify the relative contribution of ARs, cyclones, and frontal systems to precipitation in the Arctic. For this purpose, we use ERA5 data (Hersbach et al., 2020b) and develop a new method to separate the precipitation within the AR shape from the precipitation related to cyclones and fronts (Sec. 3.3). After a comparison of the specific campaign conditions to the long-term climatology (Sec. 3.4.1), we quantify the precipitation associated with each of these systems and its variability for both periods (Sec. 3.4.2 - 3.4.4). Furthermore, we evaluate the precipitation types and phase partitioning of precipitation (Sec. 3.4.5) and assess the impact of different detection algorithms for ARs and cyclones (Sec. 3.4.6). The study concludes with a discussion and outlook to future work (Sec. 3.5).

3.3 Data and Methods

We chose two time periods with frequent AR occurrences that were encountered during the two campaigns performed at different seasons, i.e. 28 May - 11 June 2017 (ACLOUD, 14 days) and 18 March - 6 April 2019 (AFLUX, 19 days). Both campaigns took place around Svalbard within the Atlantic moisture pathway and stormtrack including major AR corridor (Nash et al., 2018) which is also associated with some of the highest precipitation rates of the Arctic (McCrystall et al., 2021). However, as earlier studies pointed to the importance of the Siberian origins of ARs (Komatsu et al., 2018; Viceto et al., 2022), we select the area 70°N to 90°N and 50°W to 80°E for our study (Fig. 3.1). For the detection and analysis of ARs and the associated weather systems, we use reanalysis data and apply different algorithms which are described in the following sections. Their performance is illustrated in a case study on 20 March 2019 at 00UTC, where moist air from the south was steered northward over the North Atlantic driven by a cyclone located in Eastern Greenland (Fig. 3.1).

3.3.1 Reanalysis Data

All analyses in this study are based on the global reanalyses dataset ERA5 (Hersbach et al., 2020b) from the European Centre of Medium Weather Forecast (ECMWF). The data for this reanalysis is available from 1979 to the present. They have a temporal resolution of 1 hour and a spatial resolution of 0.25° x 0.25° corresponding to ∼31 km. Specific humidity from 1000 (or the nearest surface level) to 300 hPa is used to calculate the integrated water vapor (IWV), and together with horizontal wind components the integrated water vapor transport (IVT). Precipitation type (rain/snow) is provided as well as total, convective, and large-scale precipitation. ERA5 gives surface precipitation as total accumulated precipitation in mm over the last hour for each grid point. For better comparability also with other studies, this is converted to mm per day [mm day^{-1}] (for ACLOUD 14 days, for AFLUX 19 days) for most of the analysis. Because the area of an ERA5 grid cell decreases towards the North Pole, we take this effect into account when precipitation over larger areas is considered. Therefore, if noted otherwise, the area-wide precipitation averages are computed as an area-weighted average.

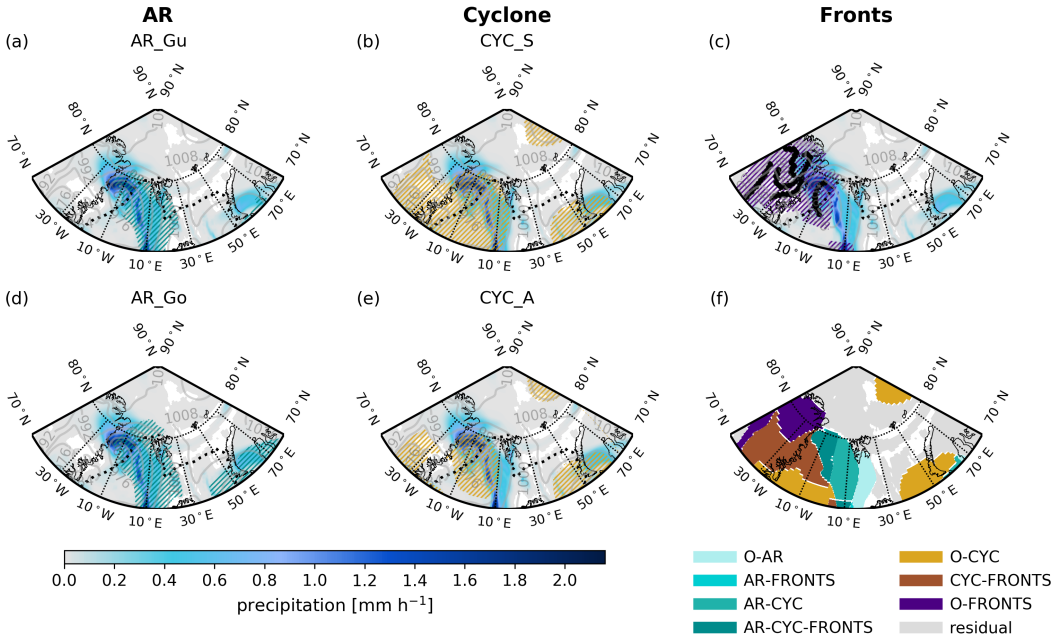

FIGURE 3.1: Precipitation rate in mm h^{-1} on 20 March 2019 at 00UTC from ERA5 over our study area. The detected areas of ARs (cyclones) are hashed in blue (yellow). AR detection by Guan et al. (2018) (a, AR_Gu) and Gorodetskaya et al. (2014) and Gorodetskaya et al. (2020) (d, AR_Go), and cyclone detection from Sprenger et al. (2017) (b, CYC_S) and Akperov et al. (2007) (e, CYC_A). The black bold lines represent the detected fronts and the purple hashed areas represent the area of these fronts (c). The dotted black line indicates the sea ice edge based on 15% sea ice concentration, and the sea level pressure (hPa) is shown in grey isolines in (a) - (e). Classification (f) according to the GuS (AR_Gu and CYC_S) standard configuration.

3.3.2 Methods: Detection of atmospheric rivers and associated weather systems

For the detection of ARs, cyclones, and fronts (Sec. 3.3.2.1 - 3.3.2.3) we use existing detection algorithms. As ARs are dynamically linked to extratropical cyclones and fronts, we make a final classification in which we define co-located and separately occurring components (Sec. 4.2.1.1).

3.3.2.1 Detection of Atmospheric Rivers

During the last years, different AR algorithms were developed (Shields et al., 2022). In this study, we apply the global AR detection algorithm originally introduced by Guan and Waliser (2015a) in its second version (Guan et al., 2018) (AR_Gu in the following) for our standard setting as it is a frequently used algorithm for worldwide application. Furthermore, we test the sensitivity of the results using the AR algorithm developed by Gorodetskaya et al. (2014) and Gorodetskaya et al. (2020) (AR_Go in the following) for a specific application for the cold and dry troposphere of Antarctica and adapted for AR identification in the Arctic (Viceto et al., 2022).

The AR_Gu detection algorithm considers a combination of intensity thresholds of IVT and geometry. The zonal (x) and meridional (y) components of the IVT are calculated by using the zonal (u) and meridional (v) wind, the specific humidity (q) profiles (from p_1 (1000 hPa, or the nearest surface level) to 300 hPa), the gravitational acceleration g and the pressure p:

$$IVT_x = -\frac{1}{g}\int_{p_1}^{p_2} u \cdot q \cdot dp \tag{3.1}$$

and

$$IVT_y = -\frac{1}{g}\int_{p_1}^{p_2} v \cdot q \cdot dp. \tag{3.2}$$

For the IVT threshold, a combination of a specific percentile and a fixed lower limit is used. In the first version of their algorithm, Guan and Waliser, 2015a first calculate the monthly-based 85th percentile of IVT for each grid cell from 1997-2014. The IVT must exceed this percentile and the lower limit of 100 kg m^{-1} s^{-1}. However, due to the lower moisture capacity of the polar regions, the lower limit in these regions is set to $>$ 50 kg m^{-1} s^{-1} in their second version (Guan et al., 2018). These lower IVT threshold criteria make the AR_Gu algorithm too permissive in the polar regions compared to the polar-specific algorithms (Shields et al., 2022). Further requirements to detect the object as an AR are the IVT direction and geometry. The IVT direction has to be within 45° of the detected AR axis, the length has to be larger than 2000 km, and the length-to-width ratio should be higher than two.

In case an object exceeds the IVT percentile threshold but does not fulfill geometrical (e.g. too wide, or too short) or directional criteria, AR_Gu includes a modification of this part of the algorithm in their second version (Guan et al., 2018). This modification is similar to the concept by Wick et al., 2013. A more stringent criterium is applied if the geometrical criteria reject the detected object as an AR that has been detected via the 85th percentile. First, the 87.5th percentile threshold is used to identify the possible AR grid cells. In case the geometrical criteria are still not met, the process is repeated for the 90th, 92.5th, and 95th percentile.

Because we want to perform our analysis with 1 h resolution we could not make use of any existing AR catalogue. Therefore, we applied the AR_Gu algorithm to ERA5 reanalysis. To do so we calculated all relevant variables, i.e., the zonal and meridional components of the IVT (IVT_x and IVT_y), as well as the IVT percentiles for each grid cell from 1979 - 2020. Subsequently, we apply the algorithm to these variables and we can detect ARs for the entire ERA5 period. Figure 3.1 (left) illustrates the shape of an AR event detected during AFLUX on 20 March 2019 00UTC together with the surface precipitation field from ERA5.

In order to investigate the sensitivity of our results to the AR detection technique, we perform the same analyses using the AR_Go detection algorithm. This algorithm considers a combination of threshold applied to IWV and geometry constraints. The threshold is calculated by comparing the IWV to the difference between the zonal mean and maximum values of the saturated IWV (IWV_{sat}) thus taking into account the lower saturation capacity of the polar troposphere with an AR coefficient (AR_{coef} = 0.2) determining the relative strength of an AR (Gorodetskaya et al., 2014; Gorodetskaya et al., 2020). For the AR analysis, we first calculated IWV and IWV_{sat} between pressure levels from 1000 (or nearest surface level) (p_1) to 300 hPa (p_2):

$$IWV = -\frac{1}{g}\int_{p_1}^{p_2} q \cdot dp \tag{3.3}$$

and

$$IWV_{sat} = -\frac{1}{g}\int_{p_1}^{p_2} q_{sat} \cdot dp \tag{3.4}$$

where q_{sat} is the saturation mixing ratio calculated using air temperature at each vertical level.

AR_Go determined an object as a potential AR when IWV is equal to or higher than this threshold:

$$IWV \geq IWV_{sat,mean} + AR_{coef} \cdot (IWV_{sat,max} - IWV_{sat,mean}) \tag{3.5}$$

where $IWV_{sat,mean}$ is the zonal mean IWV_{sat} along each latitude, and $IWV_{sat,max}$ is the maximum value of IWV_{sat} along the same latitude. Further, the object has to reach and cross 70° N and the IWV is continuous at all latitudes for at least 200 km within a maximum width of 40° longitude (Viceto et al., 2022).

3.3.2.2 Detection of Cyclones

The cyclones used in this study are derived from two different detection algorithms which apply the sea level pressure (SLP)-based method. The detection algorithm from Wernli and Schwierz (2006) and refined by Sprenger et al. (2017) (CYC_S in the following) is used in our standard configuration, while the algorithm from Akperov et al. (2015) (CYC_A in the following) is used for sensitivity testing.

For the detection of cyclones in CYC_S, a local SLP minimum is determined. If the SLP minimum is smaller than the value of the eight surrounded grid points, the grid point with the SLP minimum is considered a cyclone center. For every local SLP minimum, the outermost closed SLP contour is determined. For this purpose, the algorithm searches for every local SLP minimum enclosing contours with a pressure interval of 0.5 hPa. Further, they applied an elevation filter of 1500 m. The detected

cyclones are available on a 0.5° grid, and we interpolated them to the 0.25° ERA5 grid.

CYC_A is based on Bardin and Polonsky (2005) and Akperov et al. (2007) with some modifications for the Arctic. As CYC_S, the algorithm is based on SLP and identifies the cyclone center by the minimum in SLP. To detect the outermost closed isobar they used a pressure interval of 0.1 hPa. If the pressure no longer increases, the points are defined as the outermost closed isobar. For the Arctic, the following conditions are applied: All cyclones with a size less than 200 km or a depth less than 2 hPa have been excluded. In addition, cyclones that appear or pass over regions with surface elevations higher than 1000 m are also excluded (Akperov et al., 2018).

3.3.2.3 Detection of frontal systems

The identification of fronts is based on previous studies by Jenkner et al. (2010) and Schemm et al. (2015), who mainly focused on mid-latitudes but developed a worldwide dataset. For the detection of fronts the horizontal gradient of the equivalent potential temperature ($\nabla\theta_e$) at 700 hPa is determined and a threshold of 4 K 100 km^{-1} is applied. It needs to be noted that the threshold is arbitrary and that Rüdisühli et al. (2020) considered different thresholds to account for the strong seasonal cycle of humidity. Thus a test on the sensitivity is provided below. Though a classification into warm or cold front is also provided, we do not use this information due to the frequent occurrence of occluded fronts in the Arctic.

Once the frontal line is defined the question remains which area around the frontal line should be considered to be associated with frontal precipitation. The ascent along the surface front typically covers more than 100 km and depends strongly on the airmass. Thus, we test various distances using residual precipitation, i.e. precipitation that is not attributed to ARs, cyclones, or fronts, as a measure of the impact. Here the reasoning is that a too-short distance would provide a large residual. Accordingly, we test areas between 139 and 250 km in all directions to the front. Figure 3.2 illustrates how the residual precipitation declines if larger frontal areas are considered. Figure 3.2 illustrates how the residual precipitation declines if the frontal area, defined by the distance from the frontal zone, is reduced. Extending the distance from its shortest (139 km) to its largest (250 km) value, a drop in the residual of 8% for ACLOUD, and by 5% for AFLUX can be seen. This is basically independent of the precipitation threshold and the potential temperature gradient. Based on these results, we decided on a mean distance of about 200 km.

The residual is also used to study the dependence on $\nabla\theta_e$, where we test 4, 5 and 6 K 100 km^{-1}. Figure 3.2 illustrates that the residual varies less for this gradient than for the frontal distance. Therefore we stay with the original value of 4 K 100 km^{-1}.

3.3.2.4 Final Classification

For each ERA5 time step the techniques to detect ARs (Sec. 3.3.2.1), cyclones (Sec. 3.3.2.2), and frontal areas (Sec. 3.3.2.3) are applied to assign the appropriate system to each grid cell. Figure 3.1 shows exemplarily the results of the different detection schemes for 20 March 2019 at 00UTC. An AR produces precipitation along the

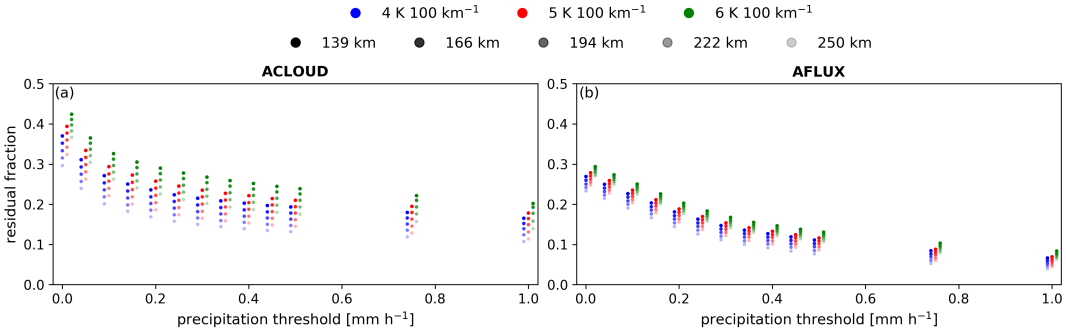

FIGURE 3.2: Fraction of residual precipitation for ACLOUD (a) and AFLUX (b) for different thresholds of precipitation [mm h^{-1}] related to the gradient of the equivalent potential temperature (blue: 4 K 100 km^{-1}, red: 5 K 100 km^{-1}, green: 6 K 100 km^{-1}), and the distance (139, 166, 194, 222 and 250 km) from the detected front line (distance increases from dark to light shaded dots). In the calculation of the residual the standard configuration, GuS (AR_Gu and CYC_S) was used.

Atlantic pathway and is detected by both AR algorithms with some differences in the position such as a slightly more northern extent produced by AR_Go than in AR_Gu (Fig. 3.1a,d). The AR is steered by an intense cyclone in the west which covers a larger region in CYC_S than in CYC_A (Fig. 3.1b,d). Connected to that are frontal regions over northeast Greenland (Fig. 3.1c).

We classify each grid cell using our standard configuration AR_Gu and CYC_S (GuS in the following). From Fig. 3.1, it becomes obvious that certain grid cells can be assigned not only to one but to multiple weather systems. Only in the region 15 - 25° E south of Svalbard, the AR is solely responsible (O-AR) for precipitation while in the western part, it is connected with a cyclone (AR-CYC), frontal areas (AR-FRONTS), and all systems together (AR-CYC-FRONTS). Considering all weather systems, we can identify in total seven different components which further include only cyclones (O-CYC), cyclones co-located with fronts (CYC-FRONTS), and only fronts (O-FRONTS).

Due to the fact that ARs, cyclones, and fronts are dynamic features associated with strong winds, precipitation may fall outside the identified shapes. Furthermore, we can see that the shapes of the detected weather systems can differ among the algorithms (Fig. 3.1). Precipitation outside of the area of the detected weather systems is classified as residual. The residual depends on the precipitation threshold: A drastic decrease of the residual with increasing precipitation threshold can be noted (Fig. 3.2). Because atmospheric models are known to produce very light precipitation, often thresholds of up to 0.1 mm h^{-1} are considered (Boisvert et al., 2018; Yang and Kane, 2021). The fact that the residual is roughly reduced by 30% during ACLOUD, and 16% during AFLUX by applying a threshold of 0.1 mm h^{-1}, highlights the importance of light precipitation for the Arctic. Therefore, we decided not to apply a threshold for our analyses. However, we discuss in Sec. 3.4.4 the sensitivity of the results by applying different precipitation thresholds.

3.4 Results

The influence of different weather systems (ARs, cyclones, and fronts) on the precipitation in the Arctic is analysed in this section for the early summer (ACLOUD) and early spring (AFLUX) campaigns. First (Sec. 3.4.1), we investigate how precipitation during both campaigns relates to long-term climatology. Second, we investigate the contribution of ARs, cyclones, and fronts to the total precipitation. For this purpose, we analyse their spatiotemporal evolution and the contribution of these weather systems (Sec. 3.4.2). Furthermore, we address the role of precipitation intensity (Sec. 3.4.3), the sensitivity of threshold (Sec. 3.4.4), the issue of precipitation phase (Sec. 3.4.5), and assess the impact of the choice of detection algorithms (Sec. 3.4.6).

3.4.1 Precipitation during the campaigns compared to climatology

How intense was the precipitation during the campaigns compared to the climatological perspective? To answer this question, we calculate the daily precipitation rate averaged over the two campaign periods (Fig. 3.3) as well as for the climatology (1979 - 2021) over the respective period. The climatology for both periods shows a strong north-south gradient with the lowest values in the central Arctic (and also Greenland) (not shown). Low precipitation values in the central Arctic (north of 80° N) are in agreement with (McCrystall et al., 2021) who find between 0.2 and 0.8 mm day^{-1} for the annual average based on ERA5.

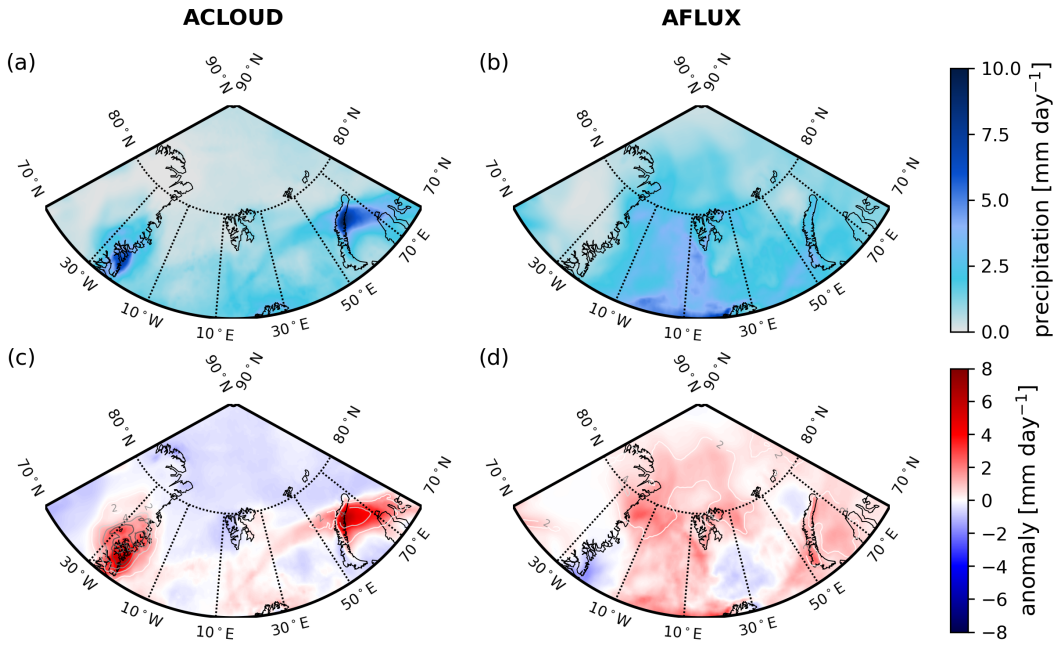

FIGURE 3.3: Daily precipitation rate [mm day^{-1}] averaged for ACLOUD (left) and AFLUX (right). For the campaign year ((a) and (b)), the anomaly with respect to the climatology period, and the deviation from the climatology as contour lines ((c) and (d)).

During ACLOUD (AFLUX), the amount of precipitation in the studied area is 12% (39%) higher compared to the climatological mean. For both campaigns, we can identify hot spots with enhanced precipitation likely originating from weather

systems. During ACLOUD, two clearly defined regions one on the east coast of Greenland and the other in the Kara Sea and the northern part of Novaya Zemlya show precipitation rates of more than 4 mm day^{-1}, which corresponds to anomalies of 8 mm day^{-1} (Greenland) and 5 mm day^{-1} (Kara Sea) with respect to the climatological value. The precipitation maximum over Novaya Zemlya is associated with an AR originating from Siberia, while maximum precipitation over eastern Greenland is associated with the Atlantic moisture pathways (Viceto et al., 2022). During AFLUX, the Atlantic corridor stands out with the highest values and a clear positive anomaly of precipitation in the Fram Strait. In contrast to ACLOUD, the enhanced precipitation rates are distributed over most of the area, also over the central Arctic (> 80° N) (Fig. 3.3d). The most enhanced precipitation compared to climatology (by a factor of three), however, is identified in northeast Greenland. The regionally distinct maxima in precipitation already indicate that transient synoptical features might determine the precipitation distribution on the time scale of weeks.

3.4.2 Contribution of ARs, cyclones, and fronts to the total precipitation

How much do ARs, cyclones, and fronts contribute to the precipitation during the two campaigns in the Arctic, especially to the hot spots shown in Fig.3.3? To answer this question, we use the methodology from Sec. (4.2.1.1) with the standard configuration GuS (AR_Gu and CYC_S) and analyse these contributions concerning their temporal variation (Fig. 3.4), spatial patterns (Fig. 3.11) and latitudinal dependency (Fig. 3.12).

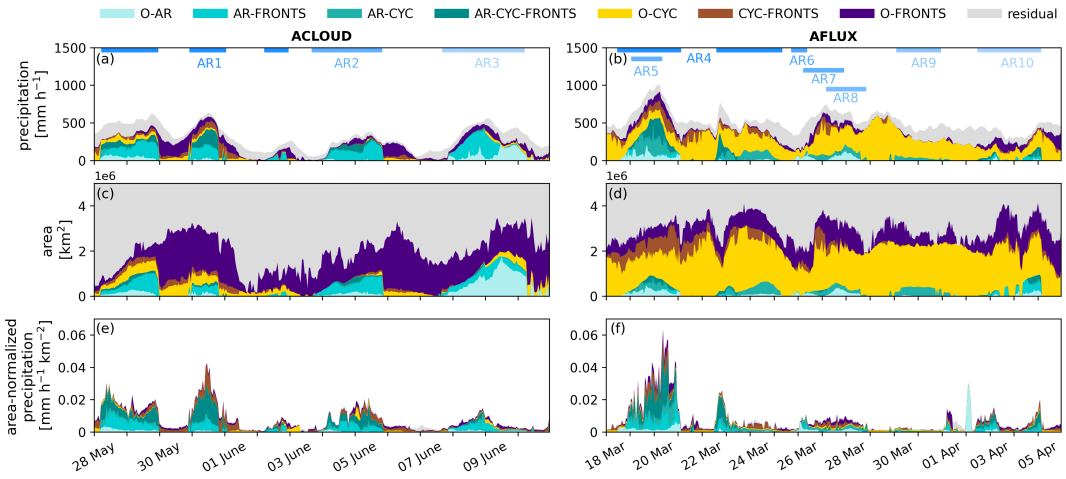

FIGURE 3.4: Time series of domain-accumulated hourly precipitation rate [mm h^{-1}] (a,b), the size of the area [km^2] (c,d), and the ratio between the precipitation rate and the area [mm h^{-1} km^{-2}] (e,f) for different weather systems for ACLOUD (left, 28 May - 11 June 2017) and AFLUX (right, 18 March - 6 April 2019). The colors represent the co-located and separated components.

During ACLOUD, the daily averaged precipitation rate accumulated over the whole study domain amounts to 7.6 x 10^3 mm day^{-1} (Table 3.1). Most of the precipitation was located between 70° and 80° N (Fig. 3.12). Considering the whole period, 40% (co-located: 31%, only: 9%) of the total precipitation can be explained by ARs, while only 22% (co-located: 14%, only: 8%) is related to cyclones. However,

with 55% (co-located: 40%, only: 15%) the majority of precipitation is associated with frontal signatures in both cases, i.e. when co-located with ARs and cyclones and also if regarded if occurring alone.

In total, we identify three ARs, two originated from Siberia (AR1 and AR2), and one from the Atlantic (AR3) (Table 3.2). Note, that AR_Gu does have a gap in the detection of AR1 and AR2 (Fig. 3.4, Tab. 3.2). During this detection gap of AR1 and AR2, the precipitation is then associated with fronts only. The temporal development of these ARs is visualized as movies in the supplement (see video supplement Lauer (2023a)). All of them reached at least 77° N (Table 3.2) and have been described in detail by Viceto et al., 2022. These ARs, especially in connection with other weather systems contributed to the enhanced precipitation rates over the Kara Sea and northern Novaya Zemlya (AR1) and at the east coast of Greenland (AR3), when they made landfall (Fig. 3.11). The slightly higher precipitation rates over the southern part of the Barents and Norwegian Seas are caused by AR2. AR1 and AR2 were mainly co-located with fronts and cyclones (AR-FRONTS, AR-CYC-FRONTS), whereas AR3 was co-located with fronts (AR-FRONTS) or occurred alone (O-AR). Thus, most precipitation is generated when ARs are collocated with cyclones and/or fronts (Table 3.1, Fig. 3.4).

TABLE 3.1: Daily averaged area-weighted precipitation rate over the study domain [mm day^{-1}] and total precipitation area (km^2) as average over the ACLOUD and AFLUX periods. The contribution of ARs, cyclones, fronts as well as of the residual (*res*) is given in percent for all classes involving the respective feature ("total" as *t*), for their co-location ("co-located" as $c-l$) and for their individual occurrence ("only" as *o*). Numbers are given for the different combinations of AR detection algorithms by Guan et al. (2018) (AR_Gu) and Gorodetskaya et al. (2014) and Gorodetskaya et al. (2020) (AR_Go), and the cyclone detection from Sprenger et al. (2017) (CYC_S) and Akperov et al. (2007) (CYC_A): GuS (AR_Gu & CYC_S), GuA (AR_Gu & CYC_A), GoS (AR_Gu & CYC_S), and GoA (AR_Go & CYC_A)

	ACLOUD				AFLUX			
daily precipitation (x10^3) [mm day^{-1}]	7.6				12.5			
	ARs t / c-l / o	cyclones t / c-l / o	fronts t / c-l / o	res	ARs t / c-l / o	cyclones t / c-l / o	fronts t / c-l / o	res
GuS	40 / 31 / 9	22 / 14 / 8	55 / 40 / 15	29	16 / 12 / 4	62 / 15 / 47	19 / 14 / 5	25
GuA	40 / 32 / 8	28 / 18 / 10	55 / 42 / 13	28	16 / 8 / 8	41 / 8 / 33	19 /12 / 7	38
GoS	19 / 16 / 3	22 / 14 / 8	55 / 27 / 28	35	40 / 32 / 8	62 / 33 / 29	19 /15 / 4	22
GoA	19 / 17 / 2	28 / 17 / 11	55 / 30 / 25	33	40 / 22 / 18	41 / 21 / 20	19 /13 / 6	30
area (x10^7) [km^2]	189				257			
	ARs t / c-l / o	cyclones t / c-l / o	fronts t / c-l / o	res	ARs t / c-l / o	cyclones t / c-l / o	fronts t / c-l / o	res
GuS	8 / 4 / 4	6 / 2 / 4	28 / 13 / 15	65	5 / 3 / 2	38 / 5 / 33	18 / 11 / 7	47
GuA	8 / 4 / 4	10 / 3 / 7	28 / 13 / 15	62	5 / 2 / 3	25 / 2 / 23	18 / 10 / 8	57
GoS	4 / 3 / 1	6 / 2 / 4	28 / 11 / 17	68	13 / 7 / 6	38 / 11 / 27	18 / 11 / 7	45
GoA	4 / 3 / 1	10 / 2 / 8	28 / 12 / 16	65	13 / 6 / 7	25 / 6 / 19	18 / 10 / 8	53

The picture changes strongly for AFLUX. During this period, the daily averaged precipitation rate of 12.5 x 10^3 mm day^{-1} accumulated over the study domain is more than 60 % higher than during ACLOUD. The main source of precipitation is

TABLE 3.2: Detected Atmospheric River (AR) events during the ACLOUD (May/June 2017) and AFLUX (March/April 2019) campaigns. For each event, the start, the end, the origin (region in which the AR was first detected), and the most northern grid point of the AR, and affected areas are specified.

# of AR	start (date / time [UTC])	end (date / time [UTC])	origin	furthest point (°N)	affected areas
AR1	28 May / 05 31 May / 00 02 June / 06	29 May / 23 31 May / 19 02 June / 21	Siberian	83.00	Kara Sea, Barents Sea Norwegian Sea Norwegian Sea
AR2	03 June / 18	05 June / 20	Siberian	77.00	Kara Sea, Barents Sea Norwegian Sea
AR3	07 June / 16	10 June / 06	Atlantic	85.25	Greenland, Norwegian Sea
AR4	18 March / 12 22 March / 15	21 March / 02 25 March / 08	Labrador Sea	86.75 77.75	Greenland, Norwegian Sea Barents Sea, Kara Sea
AR5	19 March / 01	20 March / 08	Europe	72.00	Kara Sea
AR6	25 March / 17	26 March / 09	Atlantic	77.00	Greenland, Norwegian Sea
AR7	26 March / 05	27 March / 22	Africa	77.75	Kara Sea
AR8	27 March / 04	28 March / 20	Labrador Sea	76.50	Greenland, Norwegian Sea Barents Sea
AR9	30 March / 02	31 March / 23	Siberia	84.75	Kara Sea
AR10	02 April / 15	05 April / 03	Greenland	81.50	Greenland, Norwegian Sea Barents Sea

also different compared to ACLOUD (with dominating fronts). For AFLUX precipitation is mainly associated with cyclones (62%; co-located: 15%, only: 47%), especially if they occur separately (O-CYC) whereas the contribution of fronts (19%; co-located: 14%, only: 5%) and ARs (16%; co-located: 12%, only: 4%) is comparably small (Fig. 3.4, Table 3.1, Fig. 3.12). Thus, although seven ARs were detected during AFLUX, their contribution to the total precipitation rate is a factor of 2.5 lower compared to ACLOUD (Table 3.1).

In contrast to ACLOUD, the ARs came mainly from the Atlantic or Labrador Sea (Table 3.2) and were first meridionally orientated with a subsequent zonal alignment over the studied area (see supplement Lauer (2023a)). Although the majority of the ARs (5 out of 7) reached 77° N or higher, their contribution did not exceed 16%. These ARs precipitated mostly out in the lower latitudes between 60° and 67° N (Fig. 3.12). At higher latitudes, the AR-related precipitation rates were mainly associated with AR4 that reached up to 87° N (Table 3.2). This AR4 was mainly associated with cyclones (AR-CYC) and contributed to the enhanced precipitation over the Norwegian Sea and Fram Strait (Fig. 3.3, Fig. 3.11).

In summary, we can highlight two differences between the campaign periods. First, the precipitation during ACLOUD was mainly associated with ARs and fronts, whereas during AFLUX, the precipitation was mainly concentrated within cyclones. Second, during ACLOUD, the systems were more effective when occurring in concert, i.e. the contribution of ARs and fronts is about three times higher if they occur together or with cyclones, compared to when occurring alone (Table 3.1). While this is also valid for ARs during AFLUX, it is not the case for cyclones whose contribution is highest when occurring alone.

3.4.3 Area and time-dependent precipitation intensity

The differences in the contribution of ARs, cyclones, and fronts betwee both campaign periods can be explained, among others, by the area of the individual systems. In percentage terms, ARs and fronts cover a greater area during ACLOUD than during AFLUX, while cyclones cover a smaller area during ACLOUD than during AFLUX. This applies to both co-located and separate components (Table 3.1). However, a larger area does not necessarily mean higher precipitation rates (Fig. 3.4, Table 3.1, Fig. 3.12). During ACLOUD, the area covered by fronts is a factor of 3.5 (co-located: 3.3, only: 3.8) higher than the area covered by ARs. However, the precipitation rate associated with fronts is only a factor of 1.4 (co-located: 1.3, only: 1.6) higher than that associated with ARs. The same behavior is also seen during AFLUX (Table 3.1). In general, higher precipitation rates related to ARs are concentrated within a smaller area - independent of whether co-located or separated. Therefore, the precipitation rate with respect to the area is dominated by ARs, especially in conjunction with fronts and cyclones, during both campaigns (Fig. 3.12). This is surprising for fronts (during ACLOUD) and cyclones (during AFLUX) which affect a greater area than ARs (co-located and separated). Consequently, we demonstrate that the front and cyclone-related precipitation rates, during ACLOUD and AFLUX, respectively, are not as intense as AR-related precipitation rates.

To further investigate precipitation intensity, we look at how the average precipitation is distributed over the different hourly precipitation rates. Note, that for these distributions we do not weigh precipitation rates by the area of the respective grid point (Fig. 3.5). By treating each ERA5 grid point equally more emphasis is put on the central Arctic. The snowfall which is the dominating precipitation type during both campaigns (see Sec. 3.4.5) can be classified as light (< 1 mm h^{-1}), moderate (1 – 2.5 mm h^{-1}) and heavy (> 2.5 mm h^{-1}) precipitation (DWD, 2023). The light precipitation rates are mainly associated with components that are not co-located (O-AR, O-FRONTS, O-CYC). In contrast, the occurrence of the highest precipitation rates in the Arctic is most likely when different weather systems occur in conjunction. This mainly concerns precipitation associated with ARs. Especially in connection with fronts (ACLOUD) and cyclones (AFLUX), we observe moderate precipitation (1 – 2.5 mm h^{-1}) amounts. More than 92% of the AR-related precipitation can be classified as moderate precipitation during ACLOUD and AFLUX. Only a small amount of light precipitation (< 6%) is related to AR-related components. The reason for the rare occurrence of light precipitation might be the strict AR detection focusing on the innermost AR area. Precipitation that is still connected to the AR but occurring outside the AR shape is likely lower than precipitation in the core area. This would be a similar effect as for fronts where a reduced frontal area leads to an increase in the residual (Fig. 3.2). As the detection of ARs depends on the moisture content, the moisture might be too low to be detected as an AR. For example, the gap in the detection of AR1 on 30 May during ACLOUD (Fig. 3.4) might hint at this phenomenon.

Comparing both campaigns, there are differences regarding AR-related precipitation intensity. During ACLOUD, AR events caused several maxima in precipitation rate while for AFLUX only AR4 brings significant precipitation into the studied domain (Fig. 3.4). AR4 was a meridionally orientated AR and reached up to 87° N. It crossed a strong temperature gradient when crossing the sea ice edge around 77° N. Thus, it experienced a strong drop in moisture saturation, which led to the release of precipitation. While other ARs during AFLUX were also meridionally orientated,

they did not reach that far north or touched the studied domain only marginally. Therefore, their contribution to the total precipitation in the studied region is comparable low. The higher precipitation amount during ACLOUD is mainly due to the higher number of ARs at higher latitudes – two of them (AR1 and AR2) were zonally orientated (see videos in the supplement (Lauer, 2023a)). Together, ACLOUD and AFLUX provide a variety of AR appearances to test our methodology, but long-term studies are needed to detect seasonal differences.

3.4.4 Residual Contribution and Threshold of Precipitation

During ACLOUD and AFLUX, 29 and 25%, respectively, of the precipitation cannot be associated with any of the weather systems (Tab. 3.1). Especially in the central Arctic (> 80° N), where the weather systems are quite rare or are difficult to detect, the residual explains up to 100% of the precipitation for individual grid cells (Fig. 3.11). However, the occurrence of the residual decreases with higher latitudes (Fig. 3.12). Fig. 3.5 shows that more than 95% (85%) of the residual precipitation has rates lower than 0.1 mm h^{-1} during ACLOUD (AFLUX).

Imura and Michibata (2022) have shown that dynamic models produce too light and too frequent precipitation, especially in the Arctic. Therefore, in several studies a precipitation threshold of 0.1 mm h^{-1} is used to suppress this 'artificial precipitation' (Boisvert et al., 2018). However, others argue that light precipitation rates, especially drizzle over the Arctic Ocean would be underestimated by using this threshold (Barrett et al., 2020). For our study, the introduction of such a threshold would not only affect the residual but also suppress the lower precipitation rates for other categories such as AR-FRONTS, O-CYC, CYC-FRONTS, and O-FRONTS during ACLOUD, as well as AR-CYC, CYC-FRONTS, and O-FRONTS during AFLUX. Especially during AFLUX, this light precipitation is important as can be seen in the case of cyclones. Here, cyclones have mostly precipitation rates below 0.1 mm h^{-1} but contribute most (47%) to the total precipitation (Fig. 3.5).

Section 3.3.2 has already shown the sensitivity of the residual to the introduction of a precipitation threshold. Figure 3.2 has shown that a threshold of 0.1 mm h^{-1} instead of 0 mm h^{-1} would roughly lead to a reduction of the residual fraction by one-third. But still, the question remains how the weather systems are affected by the threshold in particular for lightest precipitation. Figure 3.6 shows how drastically precipitation is reduced when the threshold is increased stepwise to 0.1 mm h^{-1}. Daily precipitation decreases from 7.6 x 10^3 to 3.9 x 10^3 mm day^{-1} during ACLOUD, and from 12.4 x 10^3 to 4.5 x 10^3 mm day^{-1} during AFLUX. Consequently, the precipitation rate decreases by 50% during ACLOUD and 64% during AFLUX. Furthermore, the contribution of AR-related components (ACLOUD: +21%; AFLUX: + 15%), cyclone-related components (ACLOUD: +5%; AFLUX: +12%), and front-related components (ACLOUD: +20%; AFLUX: +8%) increases, whereas the residual decreases (ACLOUD: - 19%; AFLUX: -14%). In summary, the contribution of ARs connected with fronts (ACLOUD) and cyclones (AFLUX) would become much more dominating if a threshold would be introduced.

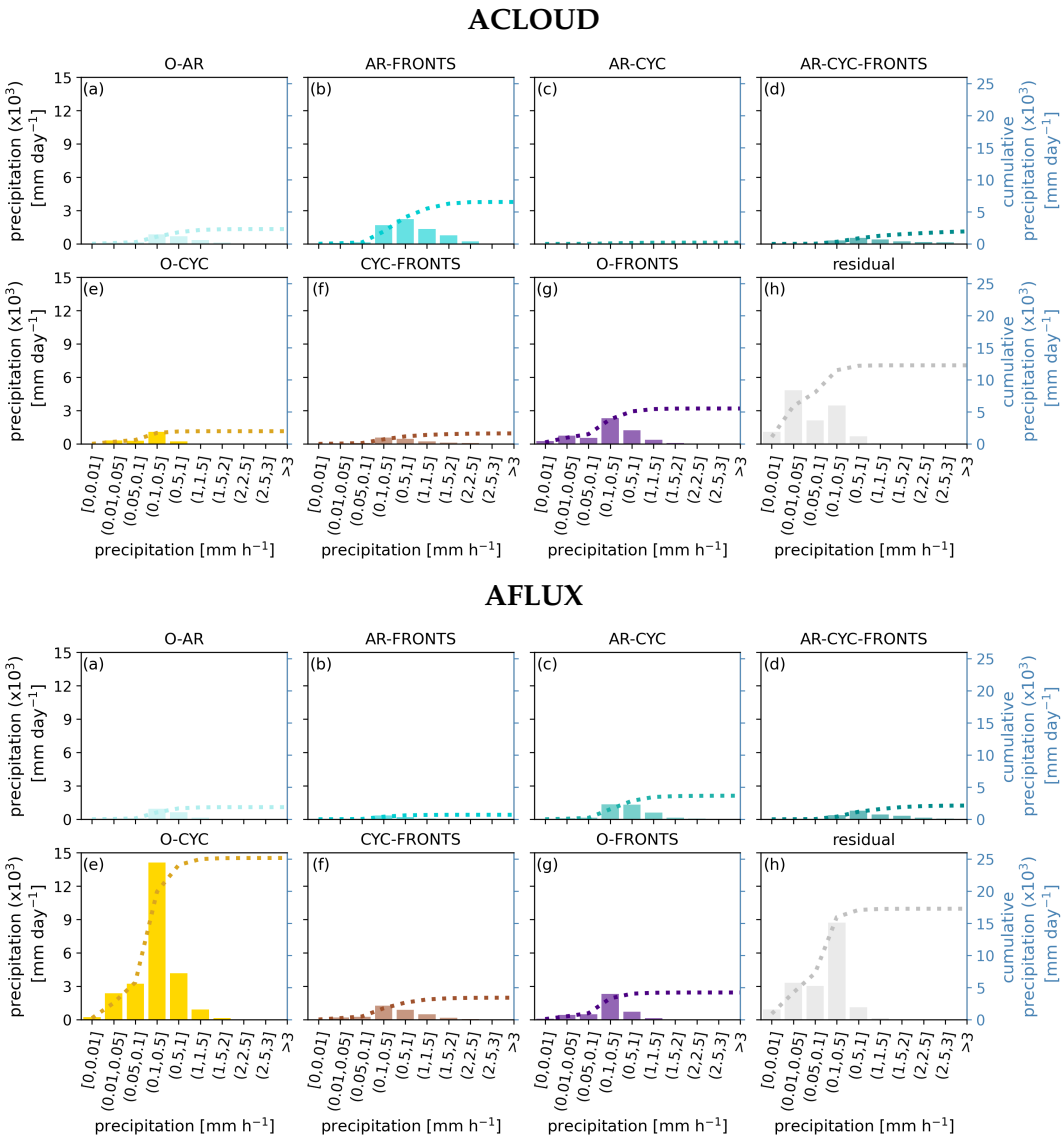

FIGURE 3.5: Contribution of different precipitation rates [mm h^{-1}] to the daily averaged precipitation [mm day^{-1}] for co-located and separated components (a-h) during ACLOUD (top) and AFLUX (bottom). The accumulated daily precipitation rate [mm day^{-1}] is shown by the dotted line and their value is given by the y-axis. Note, that each 0.25 x 0.25 grid cell is not area-weighted. Thus, the sum of the cumulative precipitation deviates from Table 3.1 which includes the area-weighted precipitation. The same analysis for area-weighted precipitation is shown in Fig. 3.13.

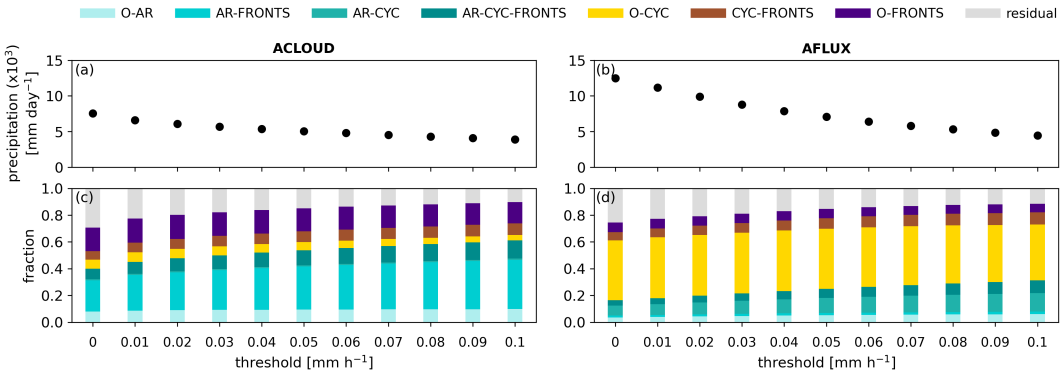

FIGURE 3.6: Daily averaged precipitation ((a) and (b)) and the fraction of ARs, cyclones, and fronts (co-located and separated) ((c) and (d)) for different precipitation thresholds [mm h^{-1}].

3.4.5 Type and form of precipitation

We now analyse the phase composition of total precipitation and its distribution for the different weather systems (Table 3.3). At the same time, we also investigate whether any differences with respect to convective and large-scale rain and snow exist. Snow is the dominant type of precipitation for both campaigns with 67% for ACLOUD and 90% for AFLUX which took place in March/April exhibiting colder temperatures than ACLOUD. Considering the snowfall rates of the different weather systems we again see the stronger effect of ARs for ACLOUD (co-located: 26%, only: 7%) compared to AFLUX (co-located: 11%, only: 3%) and the clear dominance of cyclones for AFLUX (co-located: 14%, only: 48%) compared to ACLOUD (co-located: 12%, only: 7%). Nevertheless, ARs are even more important for rain than for snowfall with even higher percentages, i.e. AR fraction amounts to 54% (co-located: 42%, only: 12%) for ACLOUD, and 42% (co-located: 29%, only 13%) for AFLUX. However, the result needs to be interpreted carefully as also the AR_Gu detection algorithm is too permissive in the polar regions which are more prone to snowfall. One indication of this hypothesis is the lower residual for rain (ACLOUD: 20%, AFLUX: 12%) than for snow (ACLOUD: 34%, AFLUX: 27%).

TABLE 3.3: Daily averaged, area accumulated total (tot), convective (con), and large-scale (l-s) rain and snowfall rate, as well as total precipitation (tot pres) expressed in 10^3 mm day^{-1} during ACLOUD and AFLUX. The contribution of ARs, cyclones, fronts as well as of the residual (*res*) is given in percent for all classes involving the respective feature ("total" as t), for their co-location ("co-located" as $c-l$) and for their individual occurrence ("only" as o).

	ACLOUD					AFLUX				
	total rate	ARs t / c-l / o	cyclones t / c-l / o	fronts t / c-l / o	res	total rate	ARs t / c-l / o	cyclones t / c-l / o	fronts t / c-l / o	res
con snow	0.6	9 / 4 / 5	17 / 4 / 13	17 / 10 / 7	66	2.2	4 / 3 / 1	62 / 3 / 59	6 / 5 / 1	34
l-s snow	4.5	37 / 29 / 8	20 / 13 / 7	57 / 40 / 17	29	9.0	16 / 12 / 4	62 / 17 / 45	21 / 15 / 6	25
tot snow	5.1	33 / 26 / 7	19 / 12 / 7	52 / 36 / 16	34	11.0	14 / 11 / 3	62 / 14 / 48	18 / 13 / 5	27
con rain	0.8	33 / 22 / 11	25 / 10 / 15	42 / 30 / 12	33	0.7	21 / 12 / 9	72 / 14 / 58	9 / 7 / 2	17
l-s rain	1.7	63 / 51 / 12	26 / 21 / 5	70 / 57 / 13	14	0.6	67 / 49 / 18	73 / 50 / 23	31 / 30 / 1	5
tot rain	2.5	54 / 42 / 12	26 / 18 / 8	61 / 49 / 12	20	1.3	42 / 29 / 13	72 / 30 / 42	20 / 19 / 1	12
tot precip	7.6	40 / 31 / 9	22 / 14 / 8	55 / 40 / 15	29	12.5	16 / 12 / 4	62 / 15 /47	19 / 14 / 5	25

Looking at the precipitation formation mechanism it becomes clear that large-scale precipitation prevails for both campaigns (Tab. 3.3) which is not surprising as the focus of this study is on dynamical weather systems. Furthermore, the campaign periods were selected for AR occurrence. For snowfall, the large-scale component dominates compared to the convective component, which contributes less than 3% and 25% for ACLOUD and AFLUX, respectively. The fraction of rain to the total precipitation is higher for ACLOUD (33%; convective: 10%, large-scale: 23%) than for AFLUX (10%; convective: 5%, large-scale: 5%). Regarding the contribution of ARs, cyclones, and fronts, we can see that ARs and fronts mainly contribute to the large-scale than to the convective rain and snow, whereas the contribution of cyclones to the convective and large-scale rain and snow is quite similar. The residual is higher for the convective than the large-scale component, which is reasonable as large-scale precipitation should be explained by synoptic features. Thus, large-scale residuals might be connected to problems in the detection algorithms or related to dynamical features producing precipitation by vertical displacement outside the object shape.

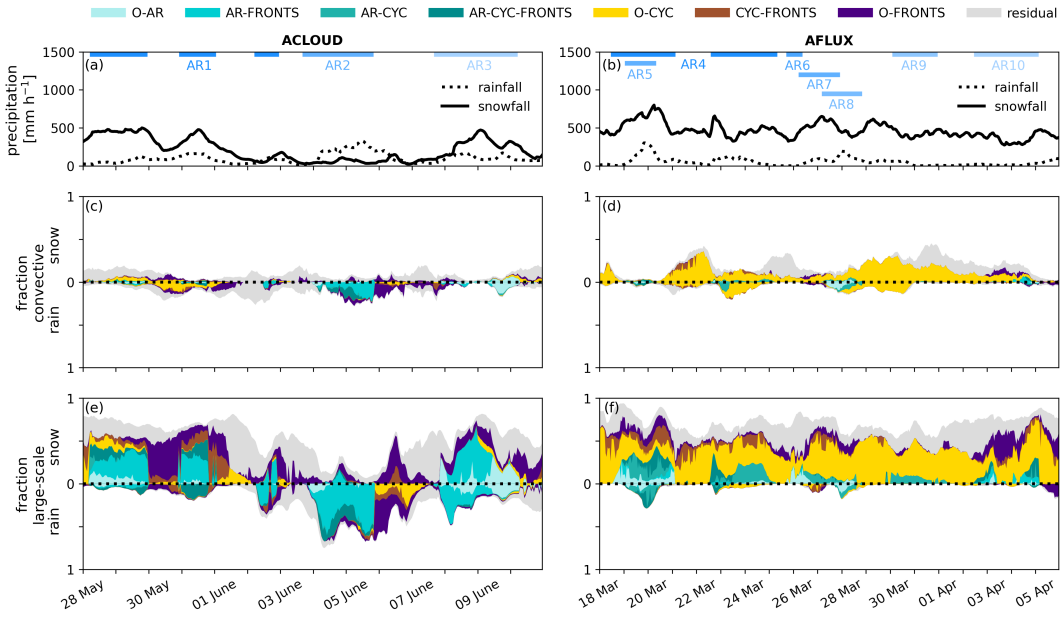

FIGURE 3.7: Time series of hourly rain (dotted) and snowfall (solid) [mm h^{-1}] ((a) and (b)) and the fraction of convective ((c) and (d)) and large-scale ((e) and (f)) rain and snow to the total precipitation for ACLOUD (left) and AFLUX (right) and for co-located and separated components (colors as in Fig. 3.1)

The temporal development (Fig. 3.7) shows that during ACLOUD a brief phase during 3-6 June occurs when rain becomes the dominant type of precipitation although snowfall is the dominant precipitation overall. In this period, the rainfall is mainly associated with AR2 with some convective contribution. As described in the previous section, this AR moved over the southern part of the Barents and Norwegian Seas. Thus, the rainfall was mainly concentrated in the lower latitudes (70 - 75° N) (Fig. 3.8). On 6 June, no AR was detected and the rainfall was more related to O-FRONTS and O-CYC. During this day, there was a slight increase in snowfall. In general, the major precipitation events during ACLOUD occur when ARs were connected with fronts (Fig. 3.7). In between the AR events occurrences, precipitation is low but prominently associated with residual snowfall, which might be due

to weak/fading synoptical systems not detected by the algorithms.

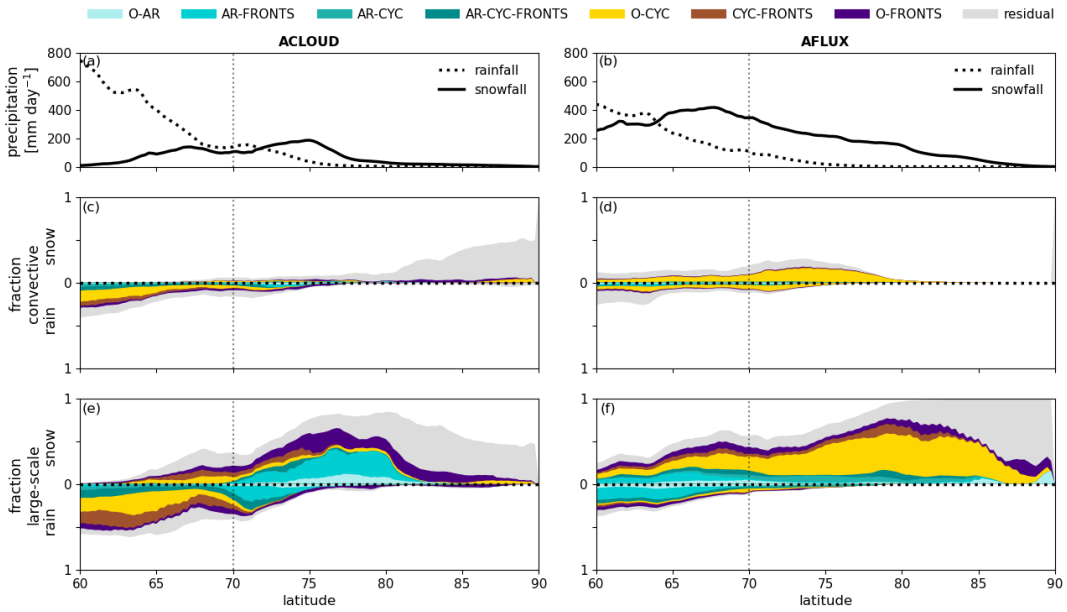

FIGURE 3.8: Latitudinal dependence (60 - 90° N) of daily averaged rain (dotted) and snowfall (solid) [mm day^{-1}] (a,b) for ACLOUD (left) and AFLUX (right). The fraction of convective (c,d) and large-scale (e,f) precipitation to the total precipitation is shown for co-located and separated components. The dashed vertical line at 70° N represents the minimum latitude that we use for all other analyses.

Throughout AFLUX, significant rainfall occurs mainly during the event of AR4 (Fig. 3.7). Also here, the rainfall is concentrated below 75° N (Fig. 3.8). Thus, for both campaigns, snow is the dominant type of precipitation north of 75° N (Fig. 3.8). The residual for the convective snow and rain as well as for the large-scale snowfall is about two times higher during ACLOUD than during AFLUX (Table 3.3, Fig. 3.7).

The differences in the latitudinal distribution of precipitation between the early spring AFLUX and early summer ACLOUD campaigns are shown in Fig. 3.8. While rain occurs up to 75°N for both periods, significant amounts of snow reach higher latitudes during AFLUX (up to 85° N) compared to ACLOUD (up to 78° N). For ACLOUD, ARs together with fronts bring snow into the Arctic up to 80° N while during AFLUX, cyclone-affected precipitation reaches up to the pole. The residual for the convective and large-scale snow is mainly found in the central Arctic, a region where weather systems occur rarely. During AFLUX 100 % of the precipitation above 80° N is large-scale with the residual getting more important close to the pole. For the warmer ACLOUD campaign already up to 50 % of the residuals close to the pole is convective. Nevertheless, the total precipitation amount is very low above 85° N and thus the question arises whether this is a real effect or due to model instabilities (see previous section).

3.4.6 Sensitivity of the results to the detection algorithms

All results discussed up to now have been achieved using the standard configuration with AR_Gu and CYC_S (GuS). But, how strongly do these results depend on the choice of algorithms? First, we investigate the difference between the two AR algorithms keeping CYC_S also in combination with AR_Go (GoS) (Fig. 3.9, top). During ACLOUD, we can see that the area which is affected by ARs is greater for AR_Gu than AR_Go (Tab. 3.1, Fig. 3.4 and 3.14). Therefore, much less precipitation is related to AR for GoS (19%; co-located: 16%; only: 3%) compared to GuS (40%; co-located: 31%; only: 9%). In Fig. 3.9, we can see that the precipitation which is related to AR-FRONTS for GuS is mainly attributed to fronts only (O-FRONTS) for GoS. This is possible because the threshold in AR_Go is based on the IWV, thus only on the moisture content that is reduced by precipitation. Since the AR is typically found in the pre-cold frontal zone, the precipitation associated with the AR is defined as frontal precipitation at the time when the AR is longer defined. Furthermore, precipitation only related to ARs (O-AR) in GuS is classified as residual by GoS, especially at the end of the campaign. However, while GuS led to a gap in the detection of AR1 on 30 May this is not the case for GoS which detects the AR continuously (Fig. 3.14). This implies that IVT decreases within the AR and therefore the criteria in GuS to detect the AR are not fulfilled anymore but the IWV criterium still holds. During AFLUX, we see the opposite behaviour. The precipitation related to ARs is lower for GuS than for GoS for all events during this campaign. Thus, GuS produces the strong precipitation contribution by cyclones discussed before, while for GoS precipitation is most frequently related to AR-CYC (Fig. 3.9). Thus, the contribution of the AR- and cyclone-related components differ among the algorithms. Consequently, for GoS the contribution of ARs is 24% (co-located: 20%, only: 4%) higher, whereas the contribution of O-CYC is 18% lower compared to GuS.

Regarding the latitudinal dependence (Fig. 3.10, top), we can see that the higher precipitation rates for GuS during ACLOUD, and GoS during AFLUX depend on the size of the area. Thus, during ACLOUD, the area of ARs detected by GuS is a factor of two higher than the area of ARs detected by GoS (Table 3.1). The largest deviation is between 70 and 75° N which are the latitudes with the greatest precipitation rates (see Fig. 3.8). In this area, the higher precipitation rates are associated with O-FRONTS or none of these systems (residual). During AFLUX, we can see the opposite effect. Applying the detection algorithm by GuS, ARs do not have a strong effect in higher latitudes (Fig. 3.9). In general, the greatest amount of precipitation during AFLUX is classified as light precipitation (Fig. 3.5). Therefore, we assume that the moisture content is too low and the threshold of AR_Gu cannot be exceeded in the higher latitudes (Fig. 3.10). Consequently, the precipitation in the higher latitudes is mainly associated with O-CYC. However, when we apply the detection algorithm GoS, we can see that O-CYC is replaced by AR-CYC. Thus, the total contribution of ARs would increase from 16 (GuS) to 40% (GoS).

Second, we compare the two cyclone detection algorithms keeping AR_Gu for the AR detection (Fig. 3.9, top) (Fig. 3.9 and 3.10, bottom). The difference between GuS and GuA in terms of precipitation rate is not as strong as for the choice of the AR algorithm except AR4 where GuS has the AR connected with a cyclone while GuA attributes the precipitation to AR only. The reason lies in the much larger area which cyclones occupy in GuS compared to GuA during AFLUX. Here we can see a strong difference between both campaigns. During ACLOUD, the area of cyclones north

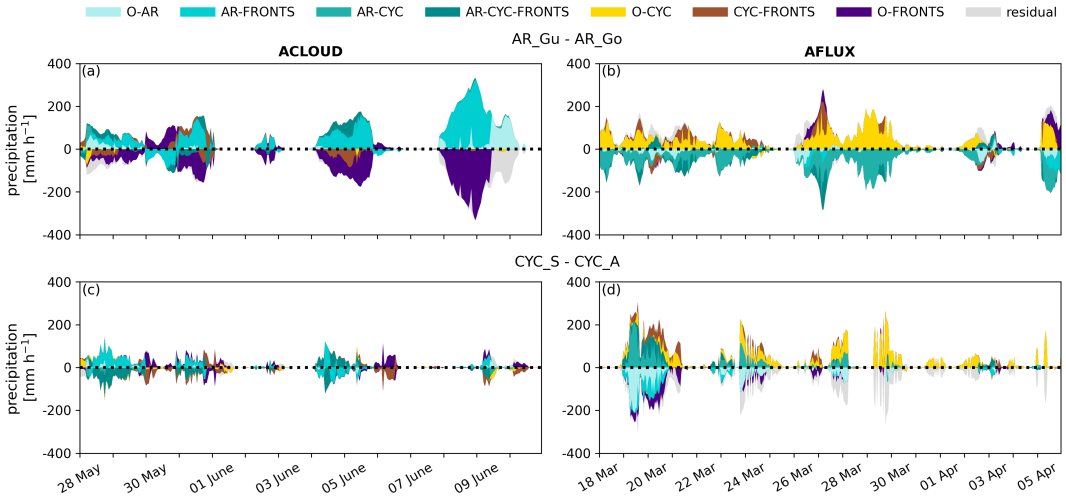

FIGURE 3.9: Time series for ACLOUD (left) and AFLUX (right) showing the difference of the contribution to precipitation by using different algorithms. Comparison of AR algorithms (GuS - GoS) ((a) and (b)), and comparison of cyclone algorithms (GuS - GuA) ((c) and (d)) for co-located and separated components (colors as in Fig. 3.1).

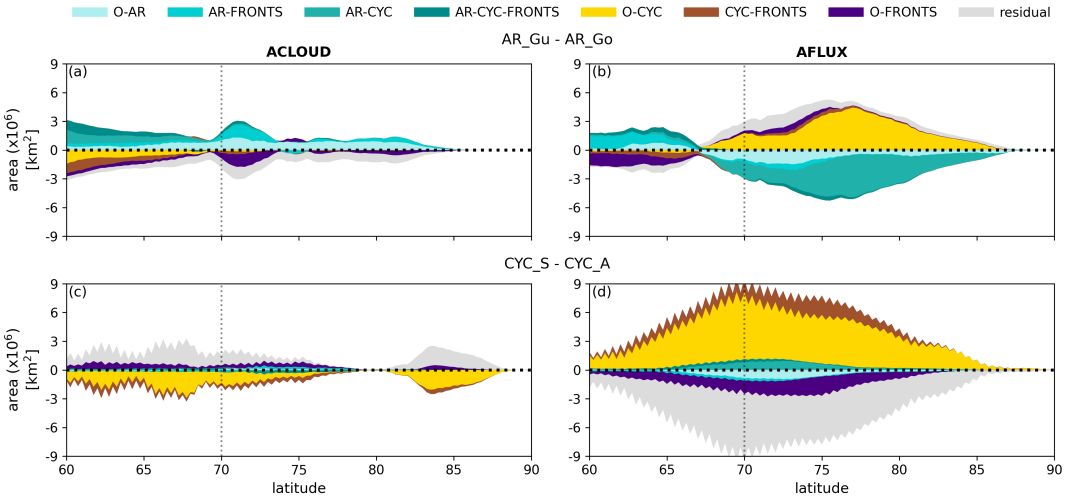

FIGURE 3.10: Latitudinal dependence for ACLOUD (left) and AFLUX (right) regarding the difference of the affected area by using different algorithms. Comparison of AR algorithms (GuS - GoS) ((a) and (b)), and comparison of cyclone algorithms (GuS - GuA) ((c) and (d)) for co-located and separated components (colors as in Fig. 3.1). The zigzag pattern in (c) and (d) is caused by the interpolation to the 0.25° ERA5 grid.

of 70° N detected by GuS is smaller compared to GuA whereas, during AFLUX, the area of cyclones is higher compared to GuA.

The area detected by the algorithm also influences the classification of the residual. This is best illustrated in the meridional distribution (Fig. 3.10). Up to 85° N a large part of the precipitation is assigned to be residual by GuA while it is contained in the cyclone category in GuS during AFLUX raising trust in the latter algorithm. However, we see the opposite albeit weaker behaviour during ACLOUD. Here, GuS produces some residual precipitation while this is assigned to cyclones in GuA.

The choice of the algorithm has a strong effect on the assignment of different categories of precipitation. Table 3.1 illustrates how the distribution of precipitation to the different categories changes in terms of daily precipitation rate and area when different combinations of algorithms are considered. For all combinations, the area residual is larger than the precipitation residual. For ACLOUD our standard configuration (GuS) produces the lowest precipitation residual (28%) and is among the lower ones in terms of precipitation area. For AFLUX, GoS features the lowest residual for both precipitation and area. For this campaign period, CYC_A produces a rather small cyclone area which especially in conjunction with AR_Gu (GuA) leads to a high residual of 38 % in precipitation rate and 57% in area. As already mentioned before, ACLOUD shows different behaviour. Here the residual precipitation area is especially high but does not vary too much between the different algorithms (62-68 %). This might indicate that weather systems are less important here and precipitation might also be produced locally as visible by the higher likelihood of convective precipitation for ACLOUD (Tab. 3.3).

3.5 Conclusions

We analysed the contribution of ARs, cyclones, and fronts to the total precipitation during two different periods, namely ACLOUD (early summer, May/June 2017) and AFLUX (early spring, March/April 2019). Both campaigns covered the northern North Atlantic sector which exhibits the highest precipitation rates in the Arctic. The two campaign periods differed from climatology in so far as localized hotspots of positive precipitation anomalies due to the weather systems and a drier central Arctic occurred for ACLOUD, while AFLUX showed enhanced precipitation over most of the area.

We have established a new methodology that allows us to analyse the contribution of ARs, cyclones, and fronts to Arctic precipitation. As these features can be connected, we have defined seven different components: O-AR, AR-CYC, AR-FRONTS, AR-CYC-FRONTS, O-CYC, CYC-FRONTS, and O-FRONTS. Further, the precipitation rate which is not associated with any of these systems (so-called residual) is also taken into account. In its standard configuration the AR detection algorithm by Guan et al. (2018) and the cyclone detection algorithm by Sprenger et al. (2017) is used. We tested the method over the two campaign periods in detail, having an application over the full ERA5 period in mind.

Although the campaign periods were chosen around the occurrence of ARs, we find that the precipitation related to ARs is not the main contributor to precipitation.

During ACLOUD, precipitation is mainly associated with front-related components (55%) followed by AR-related components (40%), while cyclone-related components (22%) play a minor role. During AFLUX, however, the precipitation is mainly associated with cyclone-related components (62%) and already 47 % of precipitation is only due to cyclones. AR and front-related components, 16%, and 19%, respectively play a minor role. While precipitation associated to cyclone related components is rather light during AFLUX, it shows a much higher daily averaged, area accumulated precipitation rate (12.5 x 10^3 mm day^{-1}) compared to ACLOUD (7.6 x 10^3 mm day^{-1}) due to their frequent occurrence. Snow is the dominant form of precipitation being nearly exclusive for the colder AFLUX period (90%) than for ACLOUD (68%). Because ARs contribute more to rain than snowfall during both campaigns, any changes in AR characteristics might be important for Arctic precipitation.

Several studies employ thresholds such as 0.1 mm h^{-1} (Boisvert et al., 2018) to eliminate "artificial" precipitation generated by numerical models. Here, we did not use any threshold. However, we performed a sensitivity study in which we tested different thresholds.
In accordance with Boisvert et al. (2018), we stress the importance of trace precipitation (precipitation < 0.1 mm h^{-1}) for the Arctic; the introduction of a 0.1 mm h^{-1} threshold drastically reduces the total accumulated precipitation by a factor of 2 (ACLOUD) and 3 (AFLUX). The higher the threshold the more light precipitation especially over the Arctic Ocean disappears. Thus, the contribution of ARs connected with fronts and cyclones increases (by a factor of two), whereas the residual decreases (by a factor of three) with higher thresholds, which might also hint at limits in the detection algorithms as they are often not adapted to the Arctic.

We investigated the impact of the AR detection algorithm by comparing the standard setting (AR_Gu) with the AR_Go algorithm by Gorodetskaya et al., 2014; Gorodetskaya et al., 2020. Comparing both algorithms, we can highlight two differences. First, AR_Gu uses IVT (humidity and wind), whereas AR_Go uses IWV and IWV_{sat} (humidity and temperature). Second, although both algorithms make use of a threshold, these thresholds differ conceptually. Due to the different concepts of the algorithms, we can see differences in the time period, the area, and the precipitation amount associated with ARs (Tab. 3.1, Figs. 3.4, 3.9, 3.10, and 3.14). During ACLOUD, the area, as well as the amount of AR-related precipitation, is a factor of two higher for AR_Gu compared to AR_Go (Tab. 3.1). Especially precipitation rates associated with ARs and fronts are affected (Figs. 3.9 and 3.10), e.g. for AR2, AR_Go detects a more confined AR area, while AR_Gu broadened this AR area by the comma head of the cyclone and the frontal precipitation. For AFLUX, the opposite effect occurs. During this campaign period, the precipitation rate, as well as the area is more than a factor of two higher for AR_Go than AR_Gu. Here, especially precipitation rates associated with ARs and cyclones are affected (Figs. 3.9 and 3.10). Here, we assume that the moisture content is too low and the threshold of AR_Gu cannot be exceeded in the higher latitudes (Fig. 3.10), while AR_Go is specifically tailored to the relatively dry conditions of the high latitudes.

In summary, based on the limited campaign periods, we cannot conclude about the generality of the differences. Therefore, a long-term statistical analysis is needed.

Comparing the contribution of cyclones when using the algorithm CYC_A by Akperov et al. (2007), we can also see strong differences during the campaigns.

During ACLOUD, cyclones detected by CYC_A cover a greater area, which results in higher cyclone-associated precipitation compared to the standard configuration. The opposite effect occurs during AFLUX: Here precipitation within cyclones detected by the standard configuration is higher compared to CYC_A. These differences could be the consequence of different pressure intervals to detect the outermost closed isobar and elevation filters. Generally, the higher (coarser) pressure interval for CYC_S (0.5 hPa) could reduce the size of the cyclone, compared to CYC_A which uses a smaller pressure interval of 0.1 hPa. This explains, that CYC_A detects larger cyclones and cyclone-associated precipitation during ACLOUD. In addition, different elevation filters in CYC_S and CYC_A affect cyclone detection and related precipitation. These results highlight the importance of understanding the limitations of the underlying detection algorithms.

For the early spring period (AFLUX) we found much higher importance of cyclones for precipitation, while ARs dominate in the early summer period (ACLOUD). However, for drawing robust conclusions about these seasonal differences, a long-term assessment exploiting the full ERA5 record is planned in the future. Within this exercise, it might be possible to identify changes in precipitation (phase) associated with different weather systems supporting a better understanding of the role of air-mass transport in the Arctic.

3.6 Appendix

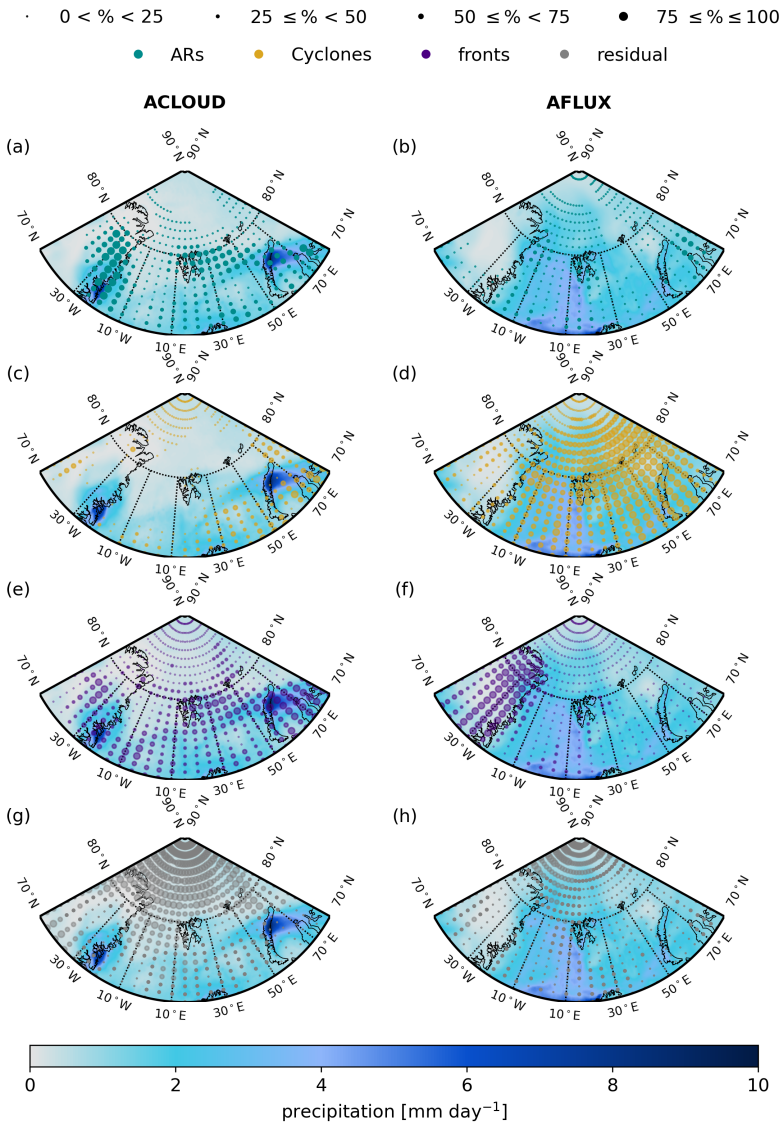

FIGURE 3.11: Daily averaged precipitation rate [mm day^{-1}] for ACLOUD (left) and AFLUX (right). The dots represent for each pixel the contribution of ARs (turquoise) ((a) and (b)), cyclones (yellow) ((c) and (d)), and fronts (purple) ((e) and (f)) to the total precipitation. The grey dots indicate the residual fraction ((g) and (h)) which is not classified either as ARs, cyclones, or fronts. The increasing magnitude of the contribution (0-25%, 25-50%, 50-75%, and 75-100%) is shown by the increasing size of the dots.

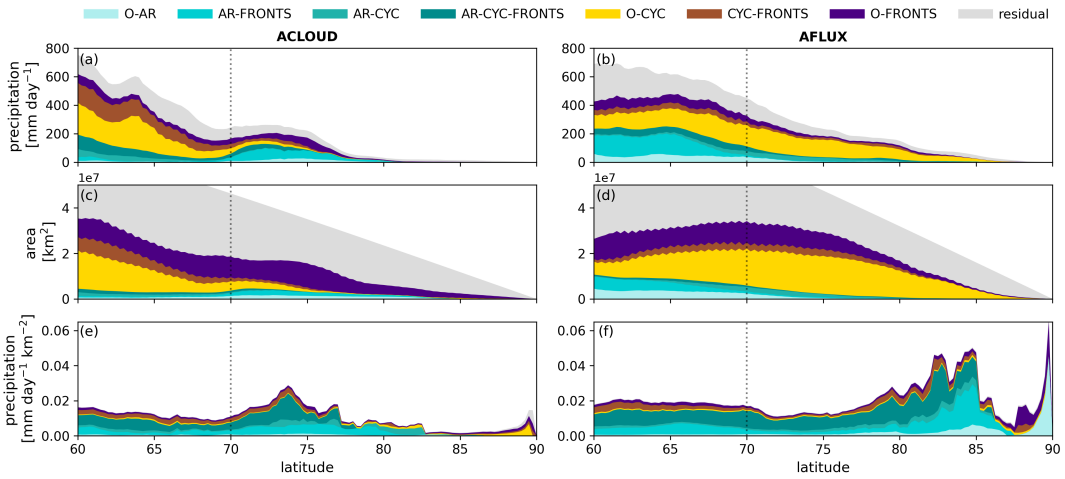

FIGURE 3.12: Latitudinal dependence (60 - 90° N) of daily averaged precipitation rate [mm day^{-1}] ((a) and (b)), the size of the area [km^2] ((c) and (d)), and the ratio between the precipitation rate and the area [mm day^{-1} km^{-2}] ((e) and (f)) for ACLOUD (left) and AFLUX (right) for the co-located and separated components (colors as in Fig. 3.1). The dashed vertical line at 70° N represents the minimum latitude that we use for the other analyses.

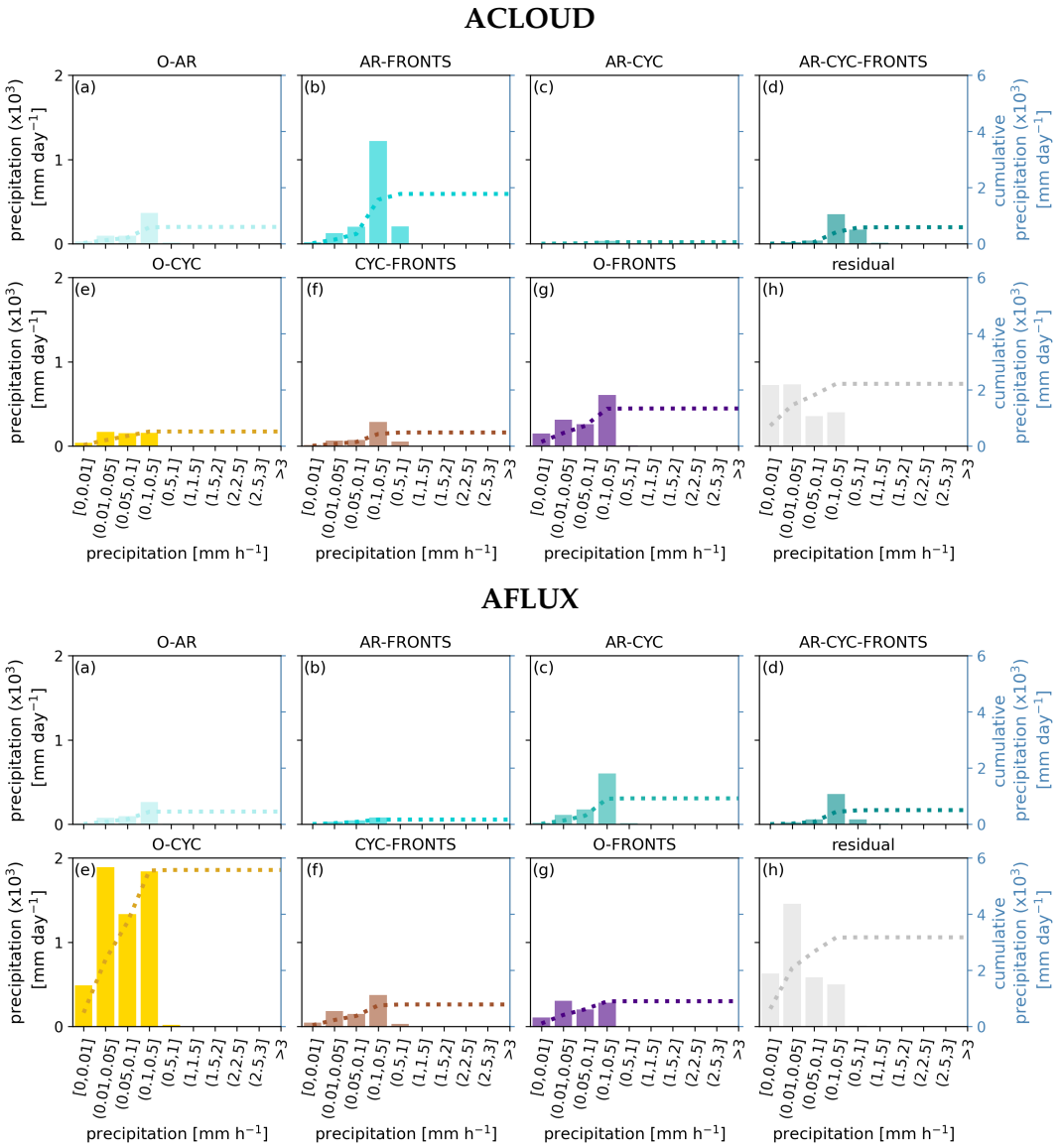

FIGURE 3.13: Contribution of different precipitation rates [mm h^{-1}] to the daily averaged precipitation [mm day^{-1}] for co-located and separated components (a-h) during ACLOUD (top) and AFLUX (bottom). The accumulated daily precipitation rate [mm day^{-1}] is shown by the dotted line and their value is given by the y-axis. Note, that each 0.25 x 0.25 grid cell is area-weighted.

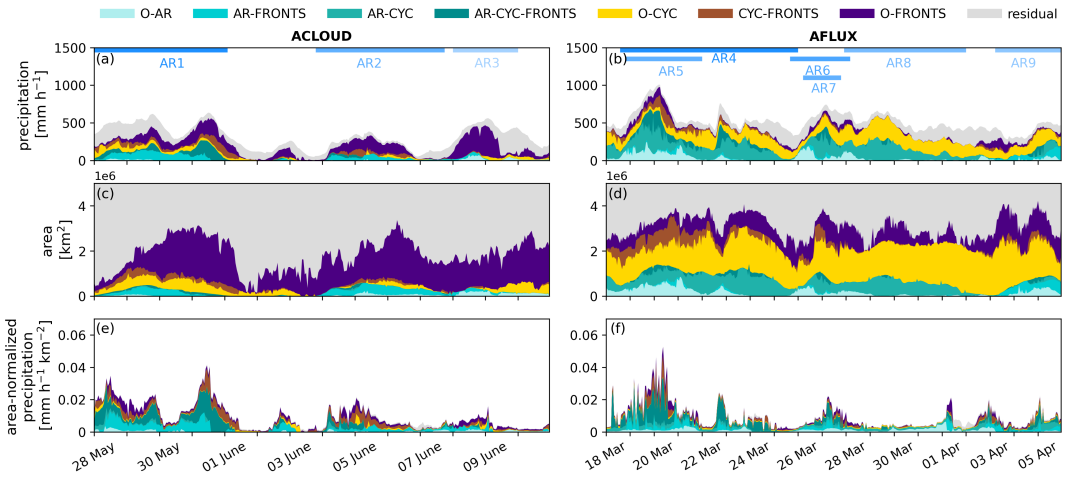

FIGURE 3.14: Time series of domain-accumulated hourly precipitation rate [mm h^{-1}] (a,b), the size of the area [km^2] (c,d), and the ratio between the precipitation rate and the area [mm h^{-1} km^{-2}] (e,f) for different weather systems for ACLOUD (left, 28 May - 11 June 2017) and AFLUX (right, 18 March - 6 April 2019) for GoS. The colors represent the co-located and separated components.

Code availability: The AR detection algorithms are provided by Bin Guan (see https://ucla.box.com/ARcatalog), and Irina Gorodetskaya (upon request).

Data availability: The reanalysis datasets used in this study were provided by ECMWF for ERA5 (https://doi.org/10.24381/cds.adbb2d47) and (https://doi.org/10.24381/cds.bd0915c6); (Hersbach et al., 2018; Hersbach et al., 2020a). The global Atmospheric Rivers catalog for ERA5 reanalysis is available on PANGEA (https://doi.org/10.1594/PANGAEA.957161).

Video supplement: The videos illustrate the temporal evolution of ARs during ACLOUD and AFLUX. The videos are available at the following links:
https://av.tib.eu/media/62348 (ACLOUD) and
https://av.tib.eu/media/62349 (AFLUX).

Author contribution: ML performed and interpreted most analysis and produced all figures. ML and SC conceptualized the paper with the help of AR. IG supported the AR analysis, including AR-related precipitation and physics, and developed the AR_Go algorithm codes. MS provided the cyclone and frontal classification expertise. All authors contributed to editing and revising the manuscript.

Competing Interests: The contact author has declared that neither they nor their co-authors have any competing interests.

Acknowledgements: We gratefully acknowledge the funding by the Deutsche Forschungsgemeinschaft (DFG, German Research Foundation) – Project 268020496 – TRR 172, within the Transregional Collaborative Research Center "ArctiC Amplification: Climate Relevant Atmospheric and SurfaCe Processes, and Feedback Mechanisms (AC)3". AR was partly supported by the European Union's Horizon 2020 research and innovation framework program under Grant agreement no. 101003590 (PolarRES). IG thanks the support by the strategic funding to CCIMAR (UIDB/04423/2020, UIDP/04423/2020) and FCT individual support 2021.03140.CEEDIND. We thank Mirseid Akperov for providing his cyclone classification with a 1-h resolution for the ACLOUD and AFLUX campaigns. This work used resources from the Deutsches Klimarechenzentrum (DKRZ) granted by its Scientific Steering Committee (WLA) under project ID bb1086. Further, we would like to thank Bin Guan for providing the second version of the AR detection algorithm, and Carolina Viceto for her help to apply the AR_Go algorithm in the Arctic. Finally, we thank the two reviewers for their constructive comments that helped to improve this paper.

Chapter 4

Influence of Atmospheric Rivers and associated weather systems on precipitation in the Arctic - A Climatological Perspective

This study addresses the climatology of Arctic precipitation and investigates the extent to which the precipitation is associated with ARs, cyclones, and fronts. For this purpose, ERA5 reanalysis data and the method (described in Chapter 3) that allows to distinguish precipitation associated with ARs from precipitation associated with cyclones and fronts are used. While Chapter 3 focused on the Arctic North Atlantic and the Kara and Barents Seas, the climatological study will cover the entire Arctic.

4.1 Introduction

The Arctic warms faster than the rest of the globe (Serreze and Barry, 2011; Wendisch et al., 2019). The warming in the Arctic affects the hydrological cycle, and therefore the precipitation in the Arctic (Vihma et al., 2016; Bintanja, 2018; Bintanja et al., 2020). Previous studies (Bintanja and Van Der Linden, 2013; Bintanja and Selten, 2014; McCrystall et al., 2021) have shown that climate models simulate an increase in precipitation. They particularly predicted the rain-dominated Arctic in the future (Bintanja and Andry, 2017). The increase in rain has two reasons: First the warmer atmosphere can hold more moisture (Clausius-Clapeyron relation) which could increase the amount of precipitation (Bintanja and Selten, 2014). Second, warmer temperatures favor the transition from snow to rain. Further, the models simulate a longer rain period. That means, the rain will start earlier and last longer in the year (Vihma et al., 2016; Bintanja et al., 2020). However, the changes in precipitation variability and the processes involved are unknown and require further research (Bintanja et al., 2020).

Although it is of particular interest to analyse the future change of precipitation in the Arctic, it is also important to analyse the past change of precipitation. While previous studies focus mainly on the total precipitation (Gimeno-Sotelo et al., 2018; Boisvert et al., 2021), in this study, the precipitation is divided into convective and large-scale total precipitation, snowfall, and rainfall. Further, the focus is on different synoptic features such as ARs, cyclones, and fronts and how they affected the precipitation in the Arctic during the last four decades.

Although observational data are available for the Arctic, they are not sufficient for the climatological analysis. First, the ground-based observations are not well distributed over the Arctic (Vihma et al., 2016). Second, satellites can cover the Arctic Ocean and reach further north, however, they also contain significant uncertainties in retrieving precipitation from the measured electromagnetic signal (Behrangi et al., 2012), further they do not cover a specific area for the whole day (Behrangi et al., 2012; Vihma et al., 2016). As ARs-, cyclones-, and fronts are dynamical systems, it is possible that the satellites miss these synoptic features. Third, high-quality measurements such as those by CloudSat (launched in 2006) are too short. The ERA5 reanalysis data has a high spatial ($\sim$ 30 km) and temporal (hourly) resolution and has shown a better performance compared to other reanalysis (Graham et al., 2019a; Barrett et al., 2020). The long-term data set allows climatological analyses for the last four decades which is advantageous when investigating whether any relative changes have occurred with respect to Arctic warming. Therefore, the results in this study are based on the ERA5 reanalysis data. Since the type of precipitation can affect surface characteristics such as mass balance and albedo as well as the formation of sea ice, the ability of ERA5 to distinguish between convective and large-scale precipitation, snow, and rain is also a key reason for using the ERA5 reanalysis data.

In Chapter 3, the temporal differences in the contribution of ARs, cyclones, and fronts become apparent for the first time. During the ACLOUD campaign, which took place in May/June 2017, ARs and fronts contributed more to the precipitation than cyclones. Cyclones contributed more to precipitation in March/April 2019 during the AFLUX campaign. Thus, a main objective of this study is to investigate whether there are seasonal differences in the distribution of precipitation and the precipitation associated with ARs, cyclones, and fronts.

As shown in previous studies, Arctic warming and wettening is not uniform over the entire Arctic (Serreze and Barry, 2011; Cohen et al., 2014; Gimeno-Sotelo et al., 2018). Therefore, the climatological study will cover the entire Arctic region. This will provide a better understanding of seasonal and regional differences in precipitation and the influence of different synoptic features on precipitation in the Arctic. In order to achieve a better understanding, the monthly precipitation distributions are analysed first. Based on an analysis of previous studies, this also appears to be the first study to differentiate between forms and types of precipitation.

4.2 Data and Methods

4.2.1 ERA5 reanalysis data

For the climatological analyses, the ERA5 reanalysis data from the ECMWF (Hersbach et al., 2020b) is used (described in Sec. 2). The investigated period ranges from 1979 to 2021. The available ERA5 period from 1950 to 1978 is not used as it does not contain satellite observations. Satellite observations are important for the Arctic due to the scarcity of ground-based measurements. The ERA5 reanalyses data have a temporal resolution of one hour and a spatial resolution of 0.25° x 0.25° ($\sim$ 31km). Of especially interest are the precipitation-related variables such as the convective, large-scale, and total precipitation and snowfall. The rainfall is calculated by subtracting snowfall from the total precipitation. The data are retrieved from the German Climate Computing Center in Hamburg.

4.2.1.1 Classification of AR-, cyclone, and front-related components

To analyse the influence of ARs, cyclones, and fronts on precipitation in the Arctic, the methodology described in Chapter 3 is applied for the respective period and the entire Arctic north of 70° N. Thus, it is possible to analyse, for which grid cells, the systems are co-located or not co-located (separated) from each other. Grid cells with precipitation not assigned to any of the synoptic features are classified as *residual*.

For the climatological analysis, only one detection algorithm for ARs and cyclones, respectively, is used. Gorodetskaya's algorithm was not yet available for the entire ERA5 period. Consequently, the detection algorithm by Guan (Guan and Waliser, 2015a; Guan et al., 2018) introduced in Chapter 2 is used for the climatological analyses. Regarding the cyclones, the algorithm by Akperov et al., 2007 was only available with a six-hourly resolution for the entire ERA5 period. Therefore, cyclones retrieved from the detection algorithm (Sprenger et al., 2017) are used. The uncertainty between the different algorithms was quantified in Chapter 3.

4.2.1.2 The whole Arctic divided into 8 subregions

Previous studies have shown that there are regional differences in AA (Serreze and Barry, 2011; Cohen et al., 2014), the poleward moisture transport (Nash et al., 2018; Komatsu et al., 2018; Gimeno et al., 2019), and precipitation (Gimeno-Sotelo et al., 2018). Therefore, the Arctic is divided into 8 sub-regions: Arctic Ocean Pacific, Arctic Ocean Atlantic, Arctic North Atlantic, Kara and Barents Seas, Laptev Sea, Chukchi and Beaufort Seas, Canadian Archipelago, and Greenland. The regions are shown in Figure 4.1 and the associated coordinates are listed in Table 4.1. In this study, the focus is on the entire Arctic northerly than 70°N.

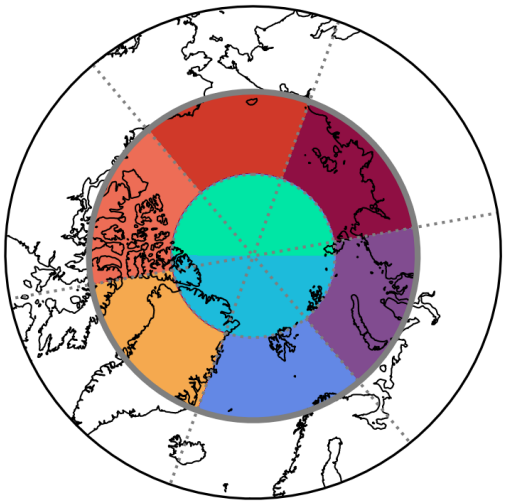

FIGURE 4.1: Entire Arctic divided into 8 equally sized subregions: Arctic Ocean Pacific (green), Arctic Ocean Atlantic (cyan), Arctic North Atlantic (blue), Kara and Barents Seas (purple), Laptev Sea (dark red), Chuckchi and Beaufort Seas (bright red), Canadian Archipelago (orange), and Greenland (yellow).

TABLE 4.1: The coordinates of the defined subregions in Sec. 4.2.1.2

Region	Latitude	Longitude
Arctic Ocean Pacific	80° - 90°N	90°E - 90°W
Arctic Ocean Atlantic	80° - 90°N	90°W - 90°E
Arctic North Atlantic	70° - 80°N	20°W - 40°E
Kara and Barents Seas	70° - 80°N	40°E - 100°E
Laptev Sea	70° - 80°N	100°E - 160°E
Chukchi and Beaufort Seas	70° - 80°N	160°E - 140°W
Canadian Archipelago	70° - 80°N	80°W - 140°W
Greenland	70° - 80°N	20°W - 80°W

4.3 Results

In this part, the precipitation over the entire Arctic is analysed for the ERA5 period from 1979 to 2021. It will be distinguished between convective, large-scale, and total precipitation as well as between snow and rain. Subsequently, the influence of ARs, cyclones, and fronts is investigated, and possible reasons for the residual are discussed.

4.3.1 Regional patterns of annual precipitation

The daily averaged precipitation for the investigated ERA5 period (1979 – 2021) is shown in Figure 4.2. There are regional differences, as well as differences among the type and form of precipitation. Regarding the total precipitation (Fig. 4.2a), the precipitation rates are not evenly distributed across the Arctic. The highest precipitation rates in the lower latitudes are concentrated over the North Atlantic and on the south coast of Greenland (< 70°N) (Fig. 4.2a). Over the North Atlantic, the precipitation consists mainly of rain, while in the area around the south east coast of Greenland, both snow and rain occur. At the south east coast of Greenland, there is a steep gradient in daily averaged precipitation rates from the ocean (> 3.5 mm day^{-1}) towards land (< 1.5 mm day^{-1}) (Fig. 4.2a). Here, the mountainous terrain prevents moisture from being transported inland by the formation of orographic precipitation. Consequently, the daily averaged precipitation rates over land decrease towards the north. Over Greenland, snow is the dominant type of precipitation (Figs. 4.2b and 4.2c). However, the southwest coast of Greenland can also experience temperatures above the freezing point, which can lead to rainfall (Fig. 4.2c). Apart from the North Atlantic, northern Europe, western Siberia, the Chukchi Sea, and Alaska are also affected by higher total precipitation rates (up to 2.5 mm day^{-1}). Depending on the season, precipitation in these regions consists of rain and snow with the rain being more pronounced (Fig. 4.2b,c).

The high precipitation amount over the North Atlantic and Northern Europe extends up to 75°N (Fig. 4.2a). The daily averaged precipitation rates range from 2 mm day^{-1} over the open ocean of the Norwegian, Laptev, and Barents Seas to 1 mm day^{-1} over sea ice and the open ocean of the Kara Sea (Fig. 4.2a). In Fig. 4.2a, the precipitation gradient from open ocean to sea ice clearly reveals the sea ice edge.

Almost 44% of the total precipitation is concentrated over the Arctic North Atlantic (27%) and the Kara and Barents Seas (17%) (Fig. 4.3a). The remaining precipitation (56%) is evenly distributed over the other subregions (Fig 4.2a, 4.3a). In

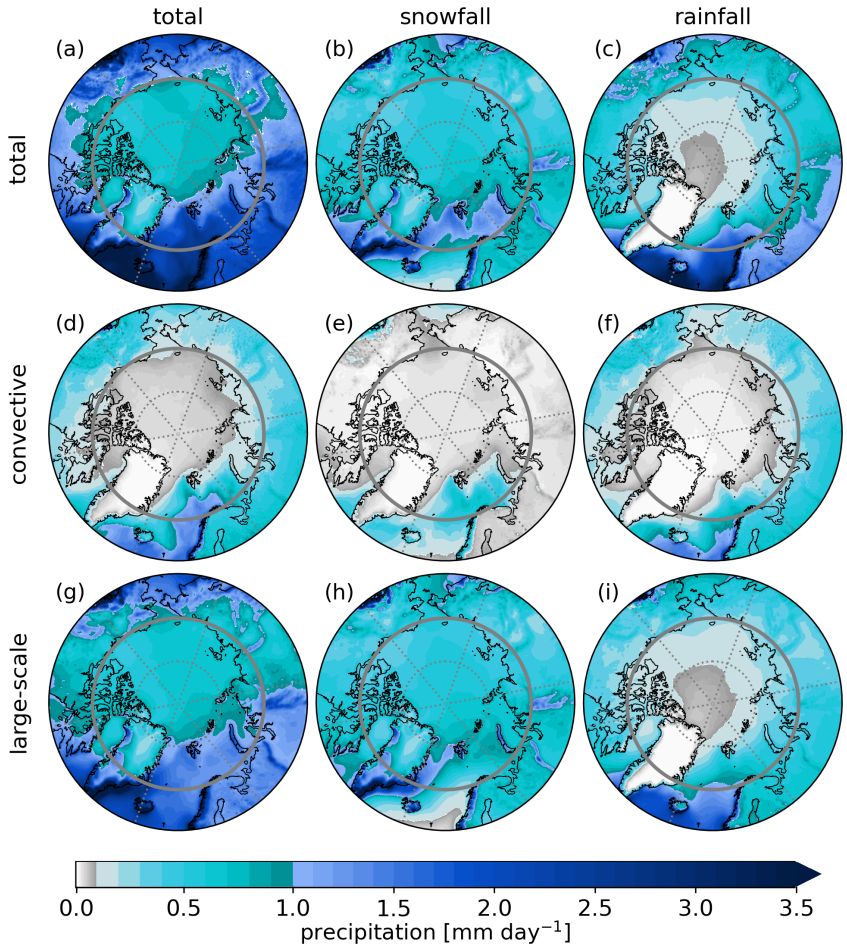

FIGURE 4.2: Daily averaged precipitation [mm day^{-1}] for the entire ERA5 period (1979-2021). For the total precipitation (a), snowfall (b), and rainfall (c), as well as for convective (d-f), and large-scale (g-i) total precipitation, snowfall, and rainfall. The grey shades represent daily averaged precipitation between 0 and 0.1 mm day^{-1}, the turquoise shades between 0.1 and 1 mm day^{-1}, and the blue shades higher than 1 mm day^{-1}.

these subregions, the daily averaged precipitation rates do not exceed 1 mm day^{-1}. In particular, the precipitation rates over the northern part of Greenland (< 0.1 mm day^{-1}) are comparable low. This is because Greenland's cold and dry conditions do not favour high precipitation (Fig. 4.2a).

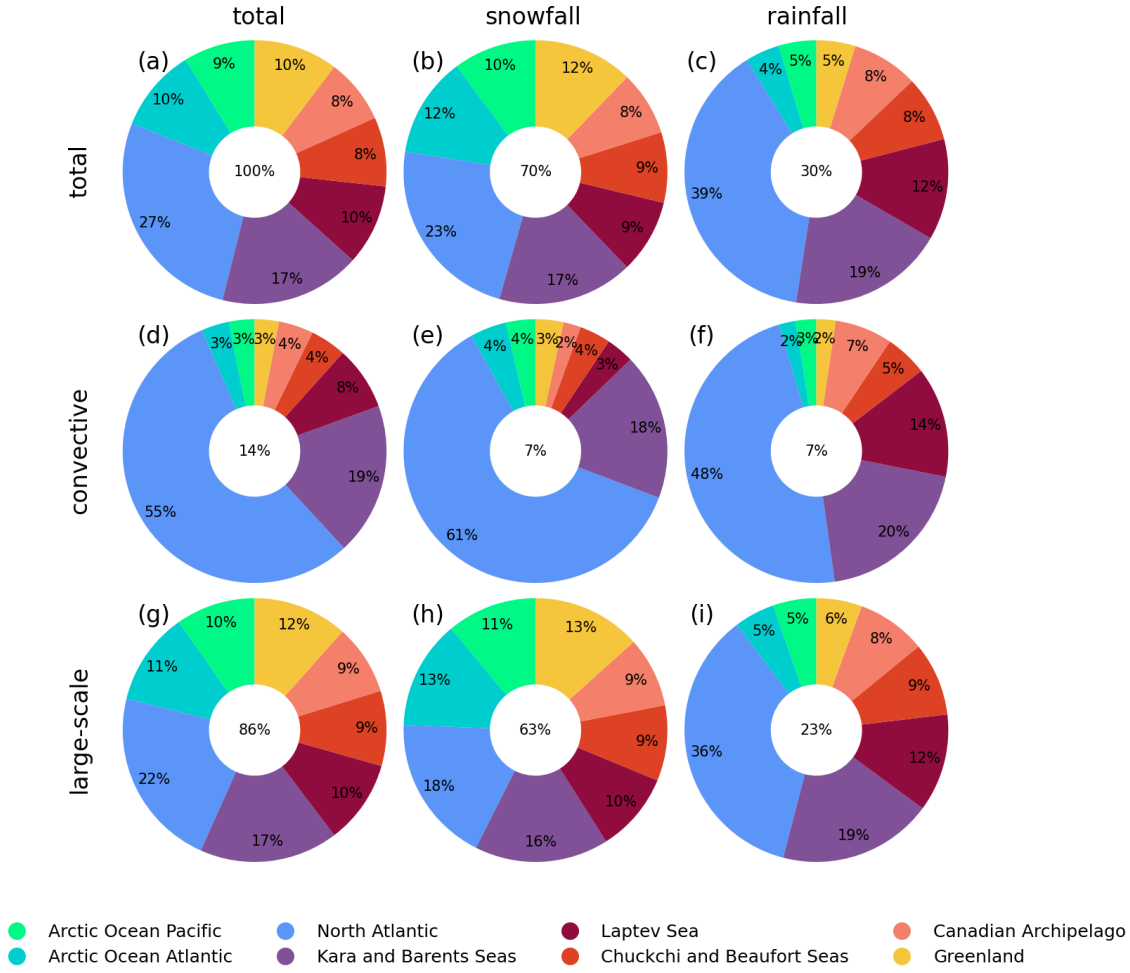

FIGURE 4.3: The percentage amount of the subregions of total precipitation, snowfall, and rainfall (a-c), as well as for the convective (d – f), and large-scale (g – i) total precipitation, snowfall, and rainfall for the entire ERA5 period from 1979-2021. The colors indicate the 8 subregions defined in Fig. 4.1.

The total precipitation can be divided into convective and large-scale snow- and rainfall (Fig. 4.2d-i). In general, the amount of large-scale precipitation (86%) is around six times higher compared to the convective precipitation (14%) (Figs. 4.3d and g), which highlights the importance of synoptic features. The distribution of the large-scale precipitation is similar to the total precipitation. Around 40% of the large-scale precipitation is concentrated over the Arctic North Atlantic (22%) and the Kara and Barents Seas (17%). This corresponds to 19% and 15% of the total precipitation, over the respective region. While convective precipitation in these two regions accounts for only 11% of the total precipitation, 74% of the convective precipitation is concentrated here (Arctic North Atlantic: 55%, Kara and Barents Seas: 19%). The

convective precipitation is most pronounced over the Norwegian Sea south of Svalbard. This convective precipitation could be attributed to marine cold air outbreaks that favour convective precipitation (Mateling et al., 2023). The proportion of convective rain- (70%) and snowfall (80%) is similar in this area (Fig. 4.2e and f). In the other sub-regions, the daily averaged convective rain- and snowfall rates do not exceed 0.1 mm day^{-1} (Fig. 4.2d).//

In contrast to convective rain- and snowfall, there are differences between large-scale rain- and snowfall (Fig. 4.2h and i), and consequently between total rain- and snowfall (Fig. 4.2b and c). The large-scale and total rainfall rates are highest between 60° and 70°N (especially over the North Atlantic and the southeast coast of Greenland) (Fig. 4.2i). Northerly than 70°N, the rainfall rates strongly decrease towards the Arctic Ocean which is consistent with the temperature decrease towards higher latitudes. The large-scale snowfall has its maximum over the Fram Strait (up to 1.5 mm day−1). Comparing the total snow and rainfall over the Arctic North Atlantic and Kara and Barents Seas, the transition zone from rain to snow at around 75°N is recognizable (Fig. 4.2b and c).

4.3.2 Spatiotemporal variation in total precipitation and its phases (snow and rain)

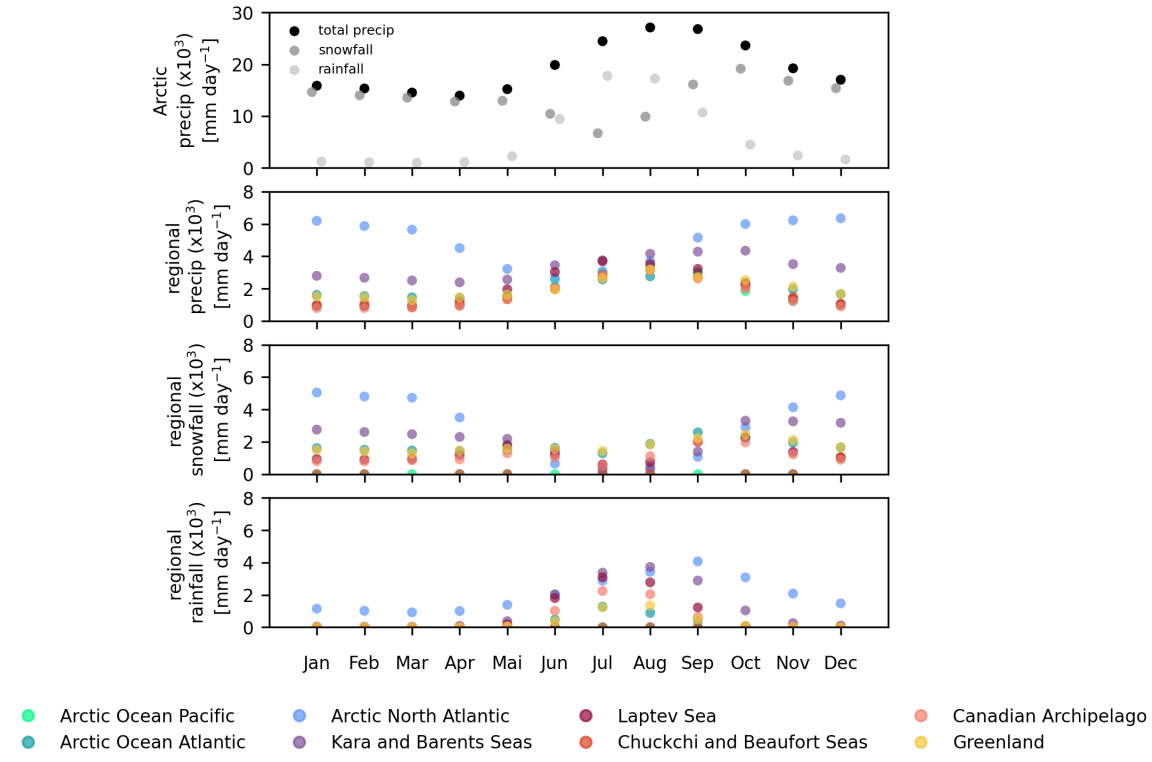

FIGURE 4.4: Daily averaged precipitation (black dots), snowfall (dark grey dots), and rainfall (light grey dots) [mm day^{-1}] for the entire Arctic (north of 70° N) as well as for each subregion based on ERA5 (1979-2021) for January to December. The colors indicate the subregions as defined in Fig. 4.1

Across the Arctic, there are not only regional differences (Section 4.3.1). There are also temporal differences in the amount and type of precipitation (Figs. 4.4 and

4.5).

For the whole Arctic, the precipitation rates are similar from January to May (Fig. 4.4a). During this time more than 50% of the total accumulated precipitation is concentrated over the Arctic North Atlantic and the Kara and Barents Seas (Fig. 4.4b). The remaining precipitation is distributed among the other regions. Although snow is the dominant type of precipitation during this season, part of the precipitation over the Arctic North Atlantic (between 70 and 75°N – south of Svalbard) consists of rain (Fig. 4.4c and Fig. 4.4d).

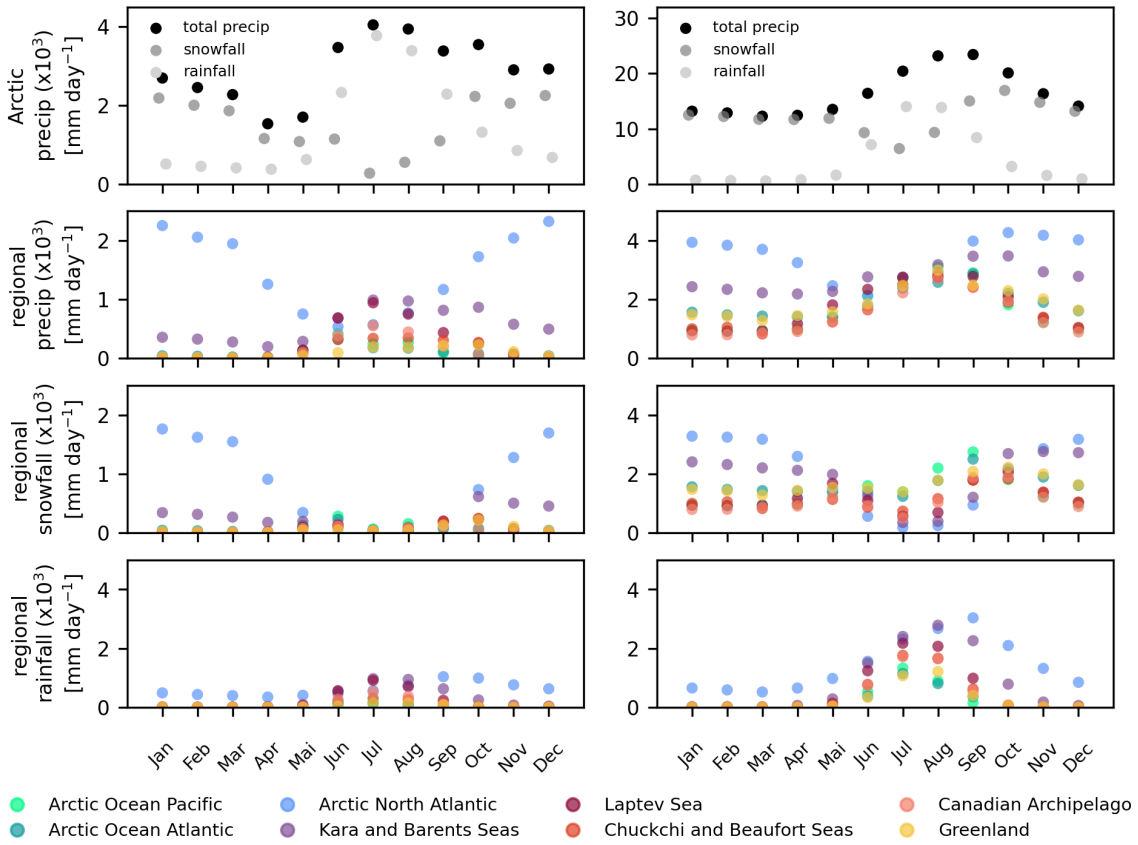

FIGURE 4.5: Daily averaged convective (left) and large-scale (right) precipitation (black dots), snowfall (dark grey dots), and rainfall (light grey dots) [mm day^{-1}] for the entire Arctic (north of 70° N) as well as for each subregion based on ERA5 (1979-2021) for January to December. The colors indicate the subregions as defined in Fig. 4.1

During the summer months (June, July, August), the amount of precipitation increases to an overall maximum in August (Fig. 4.4a). While in June the amount of rain and snow is similar, rain dominates in July and August. Compared to the previous months, no specific region with enhanced precipitation rates can be identified (Fig. 4.4b). Although precipitation is fairly evenly distributed in all regions during this period, there are differences between rain and snow (Figs. 4.4c and d). While accumulated snowfall is higher over the central Arctic Ocean and Greenland (Fig. 4.4c), rain is the dominant type over the Arctic North Atlantic, the Kara, Barents, and Laptev Seas (Fig. 4.4d).

Later in the year, from September to December, precipitation - especially rain - begins to decrease (Fig. 4.4a). However, the amount of precipitation is higher than at the beginning of the year. In September, snowfall is slightly higher than rainfall. From October to May, snow remains the dominant form of precipitation (Fig. 4.4a). During this time of the year, the precipitation is mainly concentrated over the Arctic North Atlantic and the Kara and Barents Seas.

In summary, the high precipitation rates over the Arctic North Atlantic and Kara and Barents Seas occur from September to April. Of particular interest is the rainfall over these regions in September and October which could influence the fraction and refreeze of sea ice.

Since precipitation consists mainly of large-scale precipitation, it is not surprising that the annual cycle of large-scale precipitation is the same as that of total precipitation (Figs. 4.4a and 4.5b). The annual cycle of the convective precipitation is slightly different than that for large-scale and total precipitation. The convective precipitation decreases from January to April when it reaches its minimum. Although the convective amount starts to increase in May, it is only slightly higher than in April. In July, the convective amount reaches its maximum and then declines again slightly until the end of the year. As for the large-scale and total precipitation, convective snow is the dominant type of convective precipitation from October to May, rain in July and August, and in June and September, snow is higher than rain, however, the amount of rain is not negligible. This annual cycle is visible in all regions, except the Arctic North Atlantic. However, there are differences between convective snow and rain. The convective snowfall has its minimum in summer, and its maximum in winter, while the convective rainfall has its maximum in September. This could be the consequence of the local evaporation due to the missing insulation effect of sea ice. To shed light on the large-scale phenomena, the next section will investigate the influence of ARs, cyclones, and fronts on Arctic precipitation.

4.3.3 Precipitation related to ARs, cyclones, and fronts

The subject of this section is to investigate the influence of ARs, cyclones, and fronts on Arctic precipitation by using the method described in Chapter 3.

After a general overview that covers the contribution of ARs, cyclones, and fronts to precipitation in the entire Arctic and for the ERA5 period from 1979-2021 (Section 4.3.3.1), the regional and temporal differences are analysed (Section 4.3.3.2)

4.3.3.1 Annual contributions and differences for precipitation forms and types

The precipitation over the entire Arctic can be assigned with ARs, cyclones, and fronts (Fig. 4.6). In summary, 56% of the total, convective and large-scale precipitation is associated with at least one of these components (Figs. 4.6a, d, g). Considering the total precipitation across the Arctic, it is largely - to nearly 40% - associated with cyclones (Fig. 4.6). This corresponds to 70% of the component-related total precipitation. More than half of the cyclone-related precipitation (58%) is concentrated in the area where cyclones are separated from ARs and fronts.

AR-related precipitation accounts for the smallest proportion of total precipitation (19%), while fronts contribute 25% to the total precipitation. In contrast to cyclones, the AR- and front-related precipitation is higher when they are associated with other components. Only about a third of the AR- (26%) and front- (32%) related precipitation is separated from the other components (Fig. 4.6).

The general pattern is similar for convective and large-scale precipitation, but there are differences between convective and large-scale precipitation. In percentage terms, ARs and fronts contribute slightly more to large-scale (ARs: 19%; fronts: 27%) than to convective (ARs: 15%; fronts: 20%) precipitation, while the contribution of cyclones is slightly higher for convective (42%) than large-scale precipitation (39%) (Fig. 4.6).

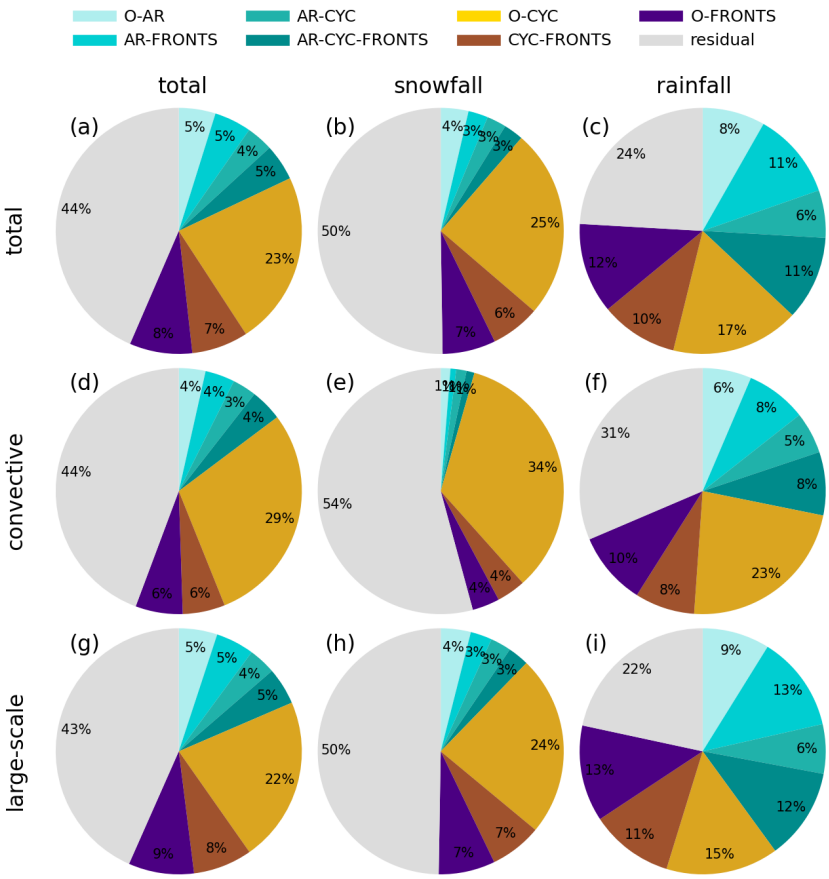

FIGURE 4.6: Fraction of the synoptic features on total precipitation, snowfall, and rainfall (a-c), as well as for the convective (d-f) and large-scale (g-i) precipitation, snowfall, and rainfall. The colors indicate the different synoptic features (co-located or separated) and the residual (grey) as described in Fig. 3.1.

However, there are also regional differences as shown in Fig. 4.7. In this figure, the black diamonds represent for each subregion the fraction of the synoptic features to the total Arctic precipitation (Fig. 4.7 top). Together with the residual, this gives the total precipitation percentage for the entire Arctic. For each region, more than 50% of the precipitation is associated with at least one of the synoptic features. The highest precipitation fractions are concentrated within ARs, cyclones, and fronts over the Arctic North Atlantic and the Kara and Barents Seas. Around 70% of the

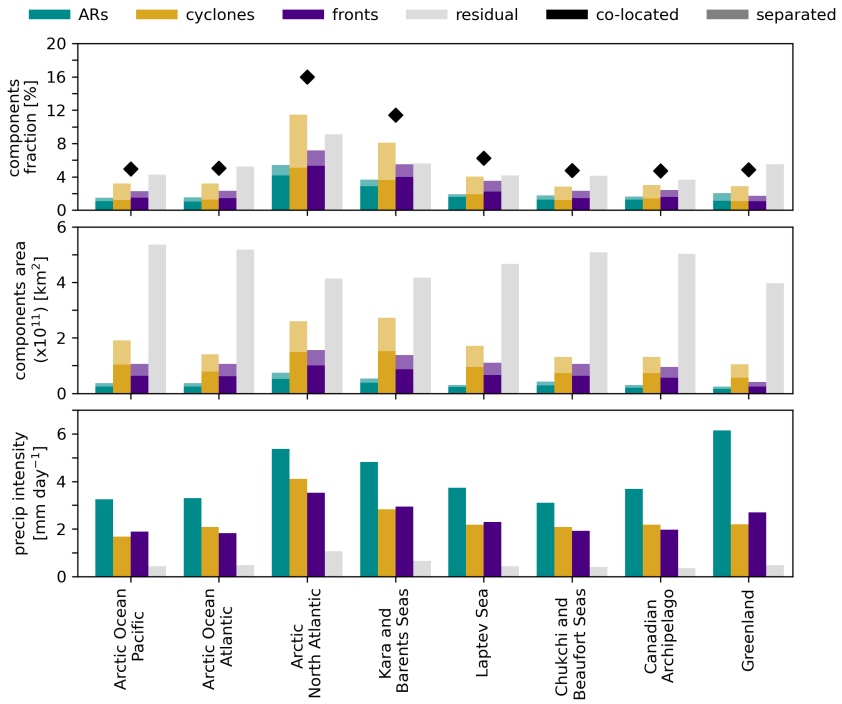

FIGURE 4.7: Top: Regional fraction [%] of ARs (turquoise), cyclones (yellow), fronts (indigo), and residual (grey) on total Arctic precipitation. Darker colors indicate precipitation which is related to co-located synoptic features, while brighter colors indicate precipitation for the individual occurrence. The black diamond represents the regional fraction of the synoptic features on the total Arctic precipitation. Note that the total amount of synoptic feature-related precipitation is lower than the sum of the three colored bars because precipitation associated with multiple synoptic features is represented in each of the respective colored bars. Middle: Area of ARs, cyclones, fronts, and residuals covered with precipitation. Bottom: Precipitation intensity within ARs, cyclones, fronts, and residuals for each subregion.

synoptic feature-related precipitation is confined to these two areas. The other 30% are evenly distributed over the other subregions. Before analysing the contribution of ARs, cyclones, and fronts in detail, it needs to be clarified that Fig. 4.7 illustrates the total fraction of ARs, cyclones, and fronts. The co-located precipitation fractions are highlighted in darker colors, and the non-co-located precipitation fractions are highlighted in brighter colors. Consequently, the sum of all three synoptic features exceeds the fraction of the synoptic features (black diamond). The contribution of the individual components is shown in Fig. A.1.

Depending on the region, 60-70% of the synoptic feature-related precipitation is concentrated within cyclones, 40-60% within fronts, and 30-40% within ARs (Fig. A.1, Table 4.2). In general, the fronts-related precipitation is higher than the AR-related precipitation. Precipitation over Greenland is an exception. In this region, 40% of the synoptic-feature-related precipitation is concentrated within ARs. About half of this is concentrated within O-AR.

In each region, the contributions for non-co-located precipitation are higher for cyclones (O-CYC) and the co-located precipitation is higher for ARs and fronts.

TABLE 4.2: Regional fraction of all synoptic features (Fraction), of ARs, cyclones, fronts, and the residual is given in percent for all classes involving the respective feature ("total" as *t*), for their co-location ("co-located" as $c - l$) and for their individual occurrence ("only" as *o*) to the total precipitation.

Region	Fraction	ARs t / c-l / o	Cyclones t / c-l / o	Fronts t / c-l / o	residual
AO Pacific	5	30/21/9	65/25/40	47/30/17	4
AO Atlantic	5	31/20/11	63/25/38	46/28/18	5
North Atlantic	16	34/26/8	72/32/40	45/33/12	9
Kara-Barents Seas	11	32/25/7	71/31/40	48/35/13	6
Laptev Sea	6	30/25/5	65/31/34	56/36/20	4
Chukchi-Beaufort Seas	5	37/26/11	60/25/34	49/30/19	4
Canadian Arch.	5	34/26/8	64/29/35	51/33/18	5
Greenland	5	42/23/19	60/22/38	36/22/14	5

Therefore, the AR- and front-related precipitation is mainly confined to areas for which the synoptic features occur at the same point in time and space. For AR-related precipitation, the precipitation fraction is higher when they are co-located with fronts (AR-FRONTS, AR-CYC-FRONTS). In the case of the fronts, this applies more to the components that are connected to the cyclones (CYC-FRONTS) (Fig. A.1). The higher precipitation fraction concentrated within cyclones and fronts is because they occur more frequently and cover a larger area than ARs (Figs. A.1 and 4.8). In general, cyclones and fronts are 2 to 4 times and 2 to 3 times larger than ARs, respectively; and they occur 2-3 times more often than ARs.

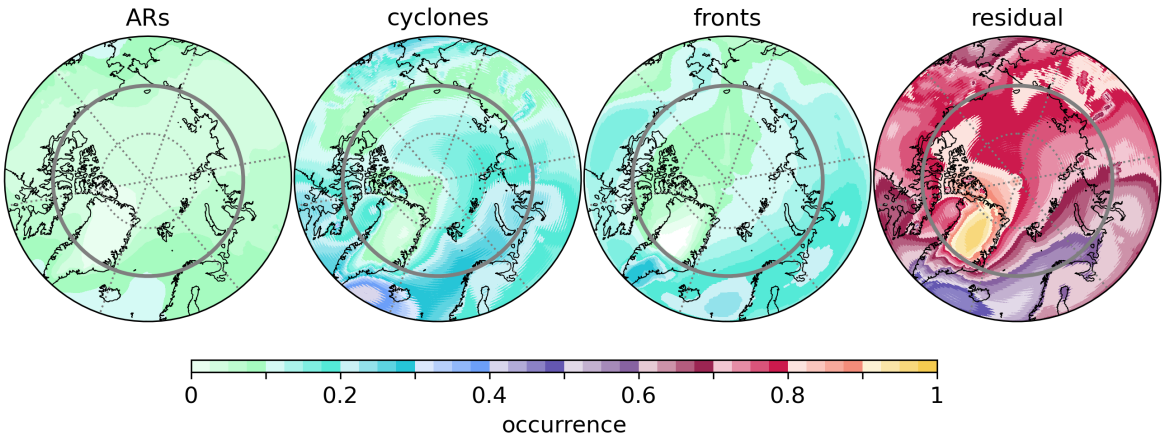

FIGURE 4.8: Occurrence of ARs, cyclones, fronts, and residual based on ERA5 period from 1979-2021.

Although the AR-related precipitation rates are lower compared to cyclones and fronts, they are more intense. ARs are most intense over the Arctic North Atlantic (5.5 mm day^{-1}), the Kara and Barents Sea (4.8 mm day^{-1}), and Greenland (6 mm day^{-1}). Compared to cyclones and fronts, ARs are 2-3 times more intense. Regarding the individual components, it becomes obvious that ARs, cyclones, and fronts are most intense when they are co-located (Fig. A.1). The AR-related components are most intense for AR-CYC and AR-CYC-FRONTS. Therefore, it is expected that ARs are most intense along the low-level jet. Here, the temperature gradient between the warm AR and the cold front could force the AR to precipitate out. Over

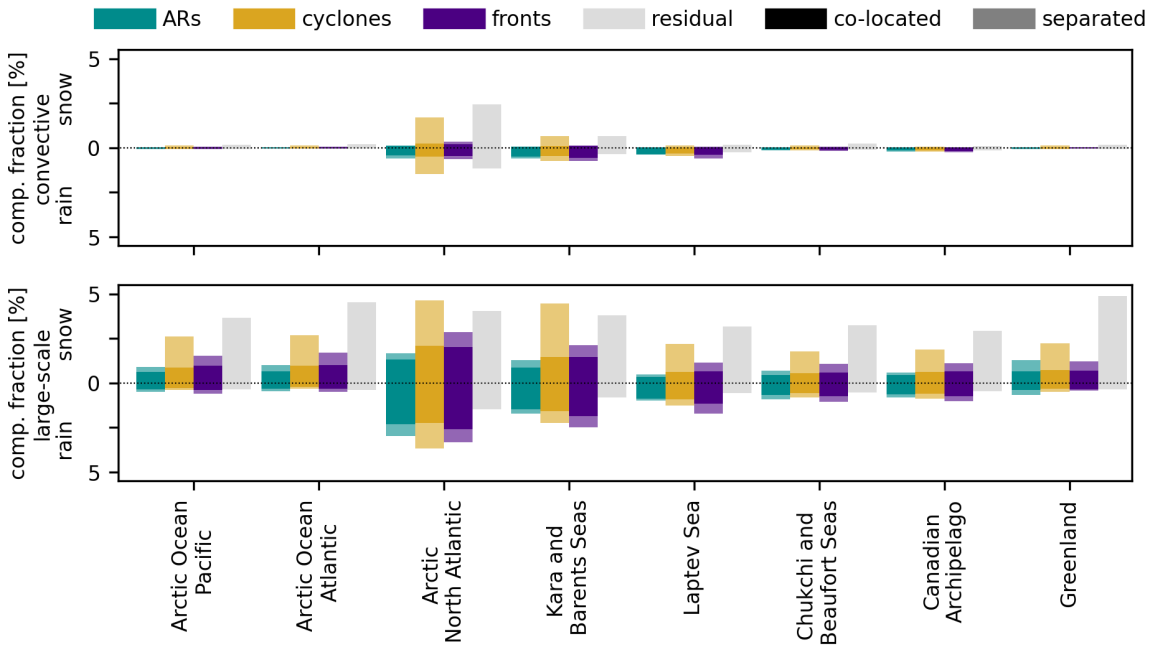

FIGURE 4.9: Regional fraction [%] of ARs- (turquoise), cyclones- (yellow), fronts- (indigo), and residual- (grey) related convective and large-scale rainfall and snowfall on total Arctic precipitation. Darker colors indicate precipitation which is related to co-located synoptic features, while brighter colors indicate precipitation for the individual occurrence. Note that the total amount of synoptic feature-related precipitation is lower than the sum of all three colored bars.

the Arctic North Atlantic, Kara and Barents Seas, and Greenland the AR-related intensity reaches 10-12 mm day^{-1}. In addition to the AR-related intensity, the intensity related to CYC-FRONTS should be emphasized. The higher intensities in this area could be connected to the WCB related to the cyclone when the warm moist air ascends above the warm front.

In addition, there are differences between rain and snow. For the entire Arctic, only half of the snowfall (total: 50%, convective: 54%, large-scale: 50%) can be assigned to one of the synoptic features (Fig. 4.6). As snow is the dominant type of precipitation, it is no surprise that the contribution of the synoptic features to snowfall is similar to their contribution to the total precipitation (cyclones: 37%, ARs: 13%, fronts: 19%). The largest deviation concerns the AR-related convective snowfall for which only 4% of the convective snowfall is concentrated within ARs. However, the patterns change in terms of rainfall. Up to 78% (total: 76%, convective: 69%, large-scale: 78%) of rainfall is concentrated within the synoptic features (Fig. 4.6). In contrast to snowfall, rainfall is more influenced by AR and front-related components (cyclones: 44%, ARs: 36%, fronts: 44%). In percentage terms, they contribute 2-3 times more to rainfall than to snowfall. Therefore, the precipitation is concentrated differently in the synoptic features. This concerns both the non-co-located and co-located synoptic features. The higher rainfall fraction associated with ARs could be the consequence as ARs transport warm and moist air. The warmer temperatures could lead to a phase change from snow to rain.

Figure 4.9 highlights once again the dominance of large-scale precipitation over the entire Arctic. The distribution of the large-scale snowfall is similar to the total precipitation. For each region, the large-scale snowfall is mainly concentrated within O-CYC and is most pronounced over the Arctic North Atlantic and the Kara and Barents Seas. Although the fraction of convective snowfall is comparable low it is mainly concentrated over the Arctic North Atlantic and the Kara and Barents Seas.

Regarding the large-scale rainfall, the differences among the synoptic features are minor compared to large-scale snowfall. While for large-scale snowfall, cyclones play a dominant role, ARs and fronts become more effective for large-scale rainfall. Consequently, the large-scale rainfall is mostly concentrated within fronts over all regions, except over the Arctic North Atlantic and Greenland. Over the Arctic North Atlantic and Greenland, cyclones and ARs, respectively, become more apparent.

Based on these results it can be concluded that the synoptic features are mainly concentrated over the Arctic North Atlantic and the Kara and Barents Seas. Although the Pacific Ocean is also a common pathway for ARs and cyclones, they are less effective in this region. It is expected that ARs over the Arctic North Atlantic can reach the Arctic more effectively than ARs coming from the Pacific. Over the Pacific side, the transition from the Bering Strait to the Chukchi Sea is a narrow band of open ocean. Therefore, the synoptic features already precipitate when reaching the land of Russia and Alaska.

However, 44% of the total precipitation (convective: 44%, large-scale: 43%) cannot be attributed to any of the synoptic components (Fig. 4.6). This amount of precipitation is classified as residual. As with the synoptic features, there are regional differences as well as differences between convective and large-scale snowfall and precipitation. For almost all subregions except the Arctic North Atlantic and the Kara and Barents Seas, the fraction of the residual is similar to the component-related precipitation fraction (black diamond). In these two subregions, the residual is only half as large as the component-related precipitation (Fig. A.1). In these subregions, the synoptic features are more common than in the other subregions (Fig. 4.8). Nevertheless, in absolute terms, the residual is higher and also more intense over the Arctic North Atlantic and the Kara and Barents Sea than in the other subregions (Fig. A.1). In contrast to the synoptic features, the residual is much less intense. Except over the Arctic North Atlantic, the intensity does not reach 1 mm day^{-1} (Fig. A.1).

Comparing the residual for the convective and large-scale snowfall and rainfall, it is - in percentage terms - higher for convective snowfall and rainfall than for large-scale snowfall and rainfall, respectively (Fig. 4.6). Half of the snowfall (total: 50%, convective: 54%, large-scale: 50%) and only one-fourth of the rainfall (total: 24%, convective: 31%, large-scale: 22%) is classified as residual. Generally, the convective rainfall- and snowfall-related residual is most pronounced over the Arctic North Atlantic (Fig. 4.9). For the large-scale components, the large-scale snowfall residual ranges between 3 and 5% over all regions, with its maximum in Greenland, while the large-scale rainfall has its maximum over the Arctic North Atlantic.

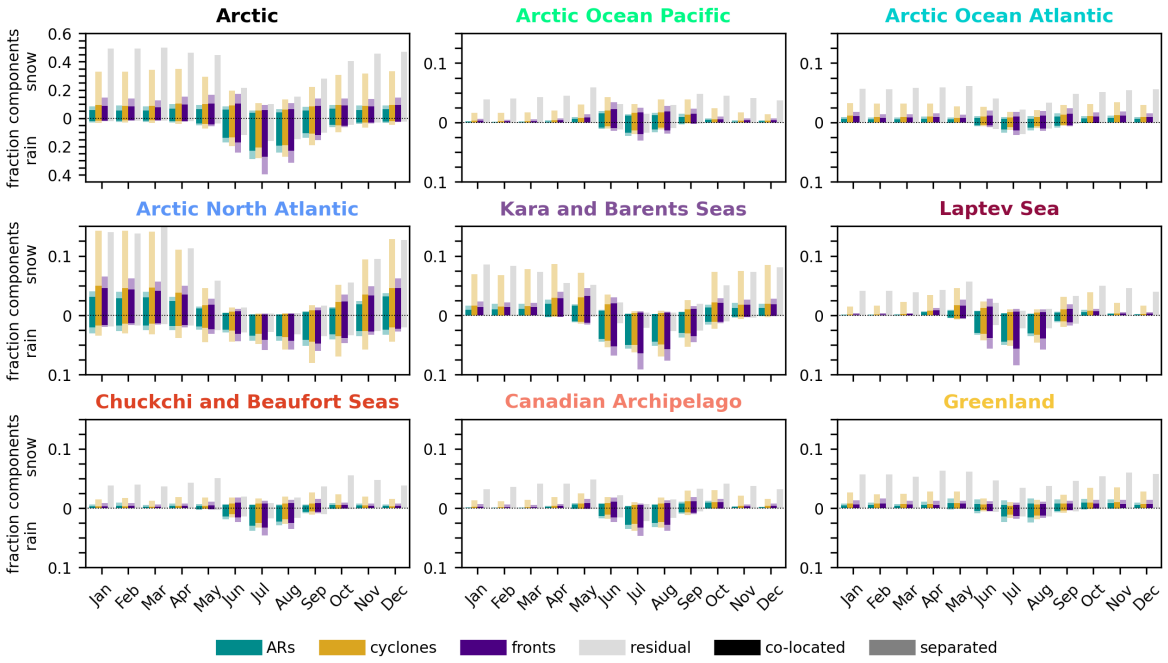

FIGURE 4.10: Monthly co-located (dark) and non-co-located (light) snow and rain fractions of ARs (turquoise), cyclones (yellow), fronts (indigo), and residual (grey) to the total monthly Arctic precipitation. Note that the y-axis is different for the whole Arctic than for the subregions (see Fig. 4.1).

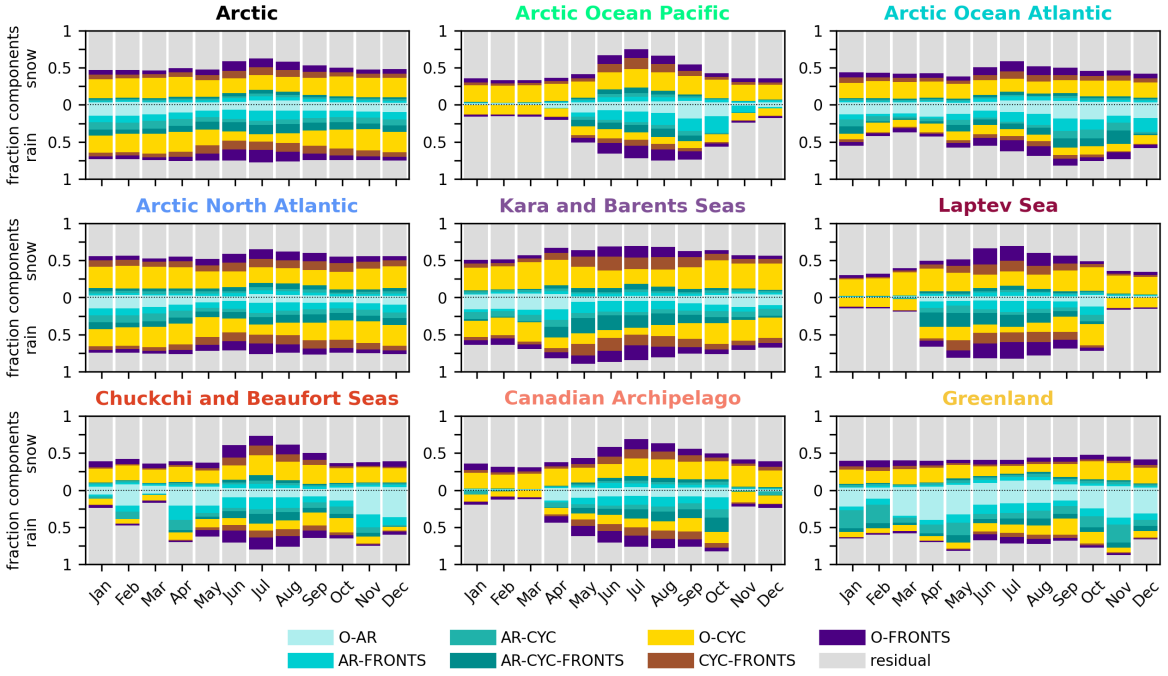

FIGURE 4.11: Contribution of individual components (co-located) to the total snowfall and rainfall for the entire Arctic as well as the individual subregions (see Fig. 4.1).

4.3.3.2 Seasonal cycle and related regional differences

Snowfall and rainfall related to ARs, cyclones, and fronts and classified as residual are temporal and regional different (Fig. 4.10). For a better overview, the focus is on four different periods: October to May (snow dominant), June (transition from snow to rain), July to August (rain dominant), and September (transition from rain to snow).

During October to May, more than half of the synoptic features-related precipitation (ARs: 55 – 80%; cyclones: 50 – 70%; fronts: 60 – 65%) is concentrated over the Arctic North Atlantic and the Kara and Barents Seas (Fig 4.10). However, they are most pronounced over the Arctic North Atlantic. Over the Arctic North Atlantic, the AR- and front-related precipitation is 3 – 4 times, and the cyclone-related precipitation is 2 times higher than over the Kara and Barents Seas (Fig 4.10).

In general, the precipitation over the Arctic North Atlantic and the Kara and Barents Seas is mainly associated with cyclone-related components (Fig. 4.10). In percentage terms, cyclones contribute similarly to snowfall and rainfall (Fig. 4.11). However, there are differences between the cyclone-related components. The cyclone-related snowfall is mainly concentrated in areas for which cyclones are not co-located with ARs and fronts. Over the Arctic North Atlantic and the Kara and Barents Seas, O-CYC accounts for 65% and 75% of cyclone-related snowfall, respectively. For rainfall, however, the contribution of cyclones over the Arctic North Atlantic is quite similar, whether co-located or not.

For ARs and fronts, it is different: In percentage terms, they contribute more to rainfall (ARs: 30-40%; fronts: 16-31%) than snowfall (ARs: 9-13%; fronts: 13-28%). In general, ARs and fronts contribute more to precipitation if they are co-located with at least one other synoptic features.

Further, there are differences between convective and large-scale snowfall and rainfall (Figs. A.2, A.4). In general, the large-scale precipitation is around a factor of two higher compared to the convective precipitation. The large-scale precipitation is distributed over both regions, while the convective precipitation is mainly concentrated over the Arctic North Atlantic and to a certain extent over the Barents Sea (Figs. A.2, A.4). This convective precipitation (snow and rain) is either associated with O-CYC (30-40%) or classified as residual (40-50%) (Fig. A.5). In contrast, the AR- and front-related convective snowfall and rainfall are comparably low (< 25%) (Fig. A.4).

For large-scale snowfall and rainfall, however, the contributions are different. In percentage terms, cyclones contribute similarly to convective and large-scale precipitation. While for convective precipitation, cyclones are more effective if they are not co-located with one of the other synoptic features (for both snowfall and rainfall), for large-scale precipitation (especially for rainfall), cyclones are more effective if they are co-located. In contrast to convective precipitation, ARs and fronts contribute more to large-scale precipitation. In percentage terms, the ARs and fronts contribute up to 3 times more to large-scale rainfall than convective rainfall. For snowfall, the contribution of ARs and fronts is 5 to 7 and 3 to 4 times higher for large-scale snowfall, respectively. Generally, ARs and fronts are more effective when they are co-located - whether convective or large-scale snowfall and rainfall.

The residual is up to a factor of two higher over the Arctic North Atlantic than over the Kara and Barents Seas. In percentage terms, the residual is higher for snowfall than for rainfall (for both regions) as well as the residual for convective precipitation is higher than for large-scale precipitation.

In **June**, the total amount of precipitation starts to increase. This primarily affects the ARs-, fronts-, and cyclone-related rainfall over the Kara, Barents, and Laptev Seas (Fig. 9e, f) and is, to a lesser extent, also the case over the Chukchi and Beaufort Seas and the Canadian Archipelago (Fig. 4.10).

Generally, the synoptic features are more effective in the regions mostly affected by rainfall. Consequently, 87% of the total rainfall over the Kara and Barents Seas, 82% of the total rainfall over the Laptev Sea 82% can be assigned to ARs (Kara and Barents Seas: 44%, Laptev Sea: 36%), cyclones (Kara and Barents Seas: 43%, Laptev Sea: 46%), and fronts (Kara and Barents Seas: 66%, Laptev Sea: 62%). Although over both regions, the rainfall is mainly associated with fronts, 67%, and 77% of the front-related rainfall over the Laptev Sea and the Kara and Barents Seas, respectively, is mainly concentrated in areas for which fronts are co-located with ARs, cyclones, or both ARs and cyclones (Fig. 4.11). The increased rainfall over the Kara, Barents, and Laptev Sea related to ARs is due to the fact, that during this time of the year, ARs come from Siberia.

In the summer months **July** and **August**, the amount of precipitation reaches its maximum and it is more evenly distributed over the entire Arctic. During this time, rain is the dominant type of precipitation (Jul: 73%; Aug: 64%). As already seen for June, the ARs and fronts become more effective. Compared to the previously studied period (Oct-May), the fronts (Jul: 49%; Aug: 42%) and ARs (Jul: 34%, Aug: 30%) are 3 times more effective. As the contribution of cyclones is quite similar for each month, the increased contribution of ARs and fronts results in a decrease of the residual from 50% (Oct-May) to 30% (Jul-Aug).

In **September**, the phase transition from rain to snow occurs. That means snowfall starts to increase and rainfall starts to decrease. The rainfall in September is mainly concentrated over the Kara and Barents Seas and over the Arctic North Atlantic. Over the Arctic North Atlantic and the Kara and Barents Seas, 77% and 76% of the rainfall, respectively, are associated with ARs, cyclones, and fronts. In contrast to the summer months, the rainfall is mainly associated with cyclones. In percentage terms, almost half of the precipitation over the Arctic North Atlantic (53%) and the Kara and Barents Seas (49%) is associated with cyclones. For both regions, 43% of the cyclone-related rainfall is concentrated in the regions for which the cyclones are not co-located with ARs and fronts. Over both regions, 35% of the rainfall is associated with ARs and 40% with fronts. Also here, they are more effective if they are co-located with at least one of the other synoptic features.

In summary, there are temporal and regional differences. In autumn, winter, and early spring, the precipitation is mainly associated with cyclones, whereas in summer the precipitation is mainly associated with fronts. ARs seem to play a minor role compared to cyclones and fronts. The next step is to examine why cyclones and fronts contribute more to precipitation than ARs. For this purpose, the occurrence of ARs, cyclones, and fronts, as well as the residual for the entire year and each month

is shown (Figs. 4.8, A.6, and A.7). Regarding the whole year (Fig. 4.8), differences in the occurrence of ARs, cyclones and fronts are visible. While ARs only occur up to 10% of the total time, fronts contribute up to 20%, and cyclones up to 30%. In the area with the greatest precipitation rates, cyclones occurred by a factor of 2-3 more often than ARs, and a factor of 2 more than fronts. Therefore, it is no surprise that cyclones contribute more to rainfall than ARs and fronts. As seen in Figure 4.8, the residual is highest over Greenland and the central Arctic – the regions also identified with the lowest accumulated amount of precipitation and in percentage terms the highest residual in precipitation.

Also on the occurrence of the synoptic features, there are temporal differences. The occurrence of ARs increases from January to July and decreases until December. From January to May, the highest occurrence of ARs is over the Arctic North Atlantic and Norwegian Sea, in June is nearly evenly distributed over the entire Arctic, except over Greenland. In July, the AR occurrence reached its maximum with around 12%. During this month, the Arctic Ocean is also affected by ARs. In August, however, the occurrence of ARs starts to decrease. However, in August and September, the occurrence of ARs over the Arctic North Atlantic and over the Kara and Barents Seas is still up to 12%. Later in the year, most of the ARs did not reach higher than 70°N. Therefore, they precipitate out outside of the investigated area. Compared to ARs, cyclones occurred more often. Throughout the year, cyclones occurred over the most parts of the Arctic and reached up values up to 60%. Compared to ARs, cyclones can also reach up to 90°N. Throughout the year, cyclones occurred especially over the Arctic North Atlantic, over the Kara and Barents Seas, as well as over the Laptev Sea.

Compared to ARs and cyclones, fronts have a strong seasonal cycle. From January to April, they are mainly located in the Arctic North Atlantic as well as over the Kara and Barents Seas. In the summer months (June – August) they cover the entire Arctic. Here, especially the Laptev Sea is affected. From October to December, the fronts are again more located over the Arctic North Atlantic and the Kara and Barents Seas.

The seasonal fraction of ARs, cyclones, and fronts can be explained by the occurrence of these systems (Figs. A.6, A.7). Generally, cyclones occur more often than ARs and fronts from October to May.

Despite the fact, that cyclones and fronts occur more often, the AR-related components are much more intense than the cyclone- and front-related components (Fig. 4.12). The ARs are more intense in the colder months than in summer. Therefore, the temperature gradient in winter favors the AR to precipitate out on its way towards the Arctic.

4.3.4 Latitudinal dependence

As shown there are spatiotemporal variations in the contribution of ARs, cyclones, and fronts on precipitation in the Arctic. In autumn, winter, and spring, the synoptic feature-related precipitation is mainly concentrated over the Arctic North Atlantic and the Kara and Barents Seas between 70° and 80° N, while in summer they also reach the central Arctic (>80° N). Figure 4.13 shows the latitudinal change of the

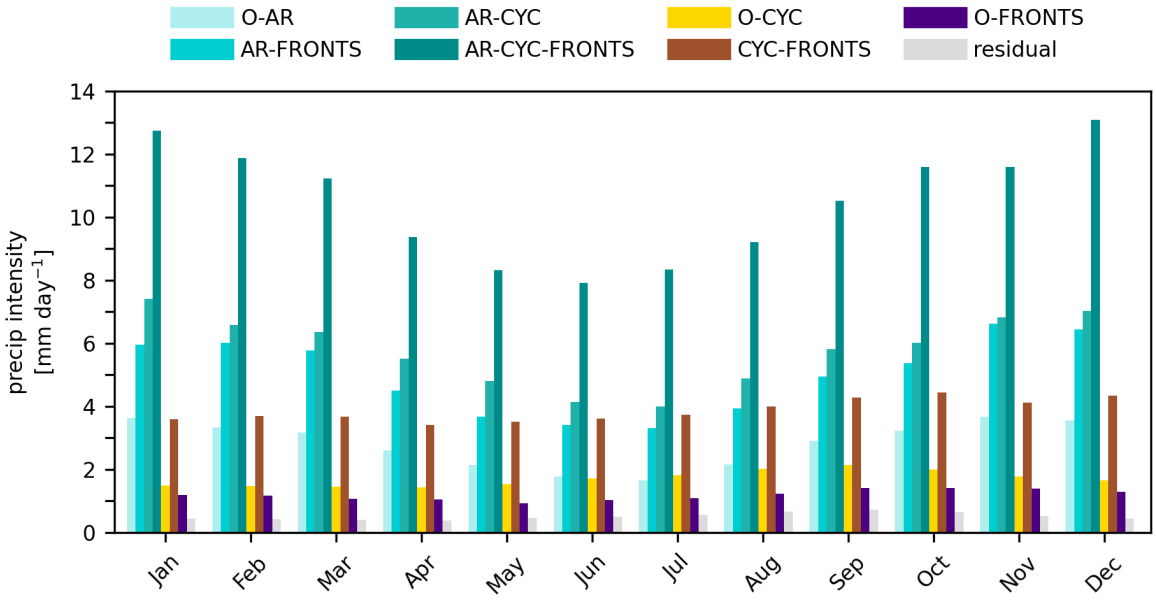

FIGURE 4.12: Monthly precipitation intensity for co-located and non-co-located synoptic features.

synoptic feature-related precipitation for each component from 60° - 90°N for January and July. Here, only these two months are depicted as they show the strong difference between winter and summer. The entire year is shown in Fig. A.8.

For both months, it becomes obvious that the daily averaged zonal precipitation decreases along higher latitudes. In January, the precipitation over the Arctic is mainly in the form of snow and in July, rain is the dominant type of precipitation. Comparing the latitudinal dependence, it becomes obvious that the contribution of ARs, cyclones, and fronts decreases towards higher latitudes. In January, snow and rainfall are mainly concentrated within O-CYC. Although below 70°N, ARs contribute nearly 10% to the total snowfall, their infleunce in higher latitudes is comparable low. Higher than 60°N, the snowfall is mainly concentrated in O-CYC. In general, the contribution of the synoptic features in the higher latitudes does not reach 50%. That means that more than half of the precipitation in the central Arctic is not affected by ARs, cyclones, and fronts. This effect is mainly seen over latitudes higher than 75°N. Along these latitudes, more than 80% of the time none of the synoptic features is detected.

In summer, it is different. Here the dominant type of precipitation is rainfall. Up to 75°N, rain is the dominant type of precipitation and is mainly concentrated within the synoptic features. In these latitudes, only 25% of the precipitation cannot be assigned with one of the synoptic features. At 75°N, snowfall starts to increase. Between 80 and 90°N, the precipitation is in the form of rain and snow, whereby the rainfall is mainly concentrated within AR-related components and snowfall with O-CYC. Compared to January, the synoptic features contribute more to precipitation in the higher latitudes.

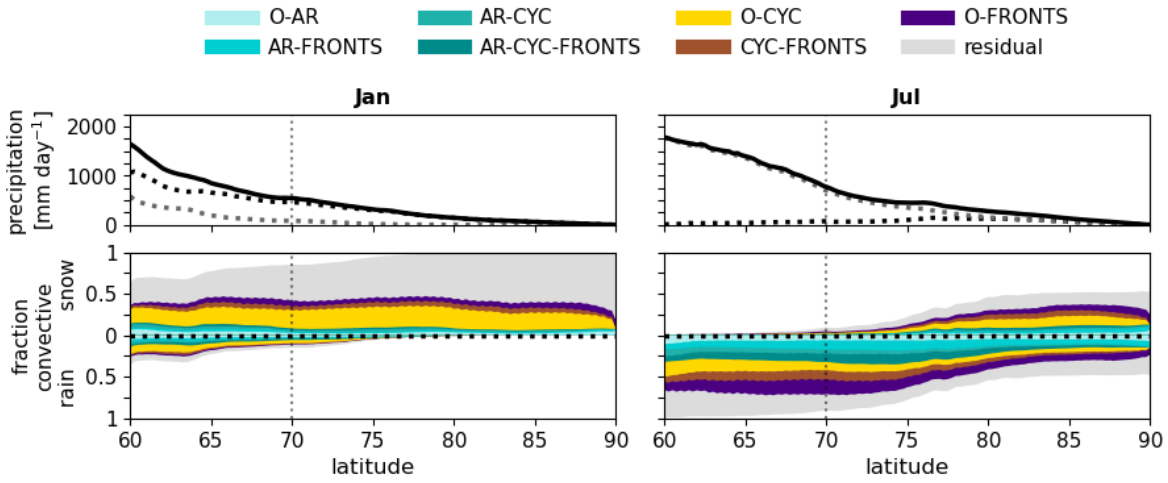

FIGURE 4.13: Latitudinal dependence (60 - 90° N) of daily averaged rain (dotted) and snowfall (solid) [mm day1] for the entire Arctic in January (left) and July (right). The fraction of total precipitation is shown for co-located and non co-located components. The dashed vertical line at 70° N represents the minimum latitude that is used for all other analyses.

4.3.5 Residual

In Section 4.3.3, it is shown that there are intra-annual and regional differences in the contribution of ARs, cyclones, and fronts on Arctic precipitation. Further, there is a significant amount of precipitation ($\sim$ 44%) that cannot be associated with one of these synoptic features. For the residual, there are differences between snow and rain. While 24% of the rainfall, 50% of snowfall is classified as residual. This results in higher residual rates for snow-dominated months (Jan - May, Sep-Dec). During these months, the residual amounts to 50%. Here, the question arises where the residual comes from. There are possible answers to this question:

1. In ERA5, each grid box contains the precipitation accumulated in each hour. The detected shapes of ARs, cyclones, and fronts, however, are instantaneous. This means, that the area covered by the ARs, cyclones, and fronts between two hours is not taken into account.

2. The synoptic features are not detected with the detection algorithm. In the second study (Section 3.4.2), there are some gaps in the detection of ARs. Further, there are differences in the detection algorithms. This shows, the sensitivity of the results by applying another detection algorithm.

3. Trace precipitation could affect the residual and also the fraction of ARs, cyclones, and fronts to total precipitation (see Section 3.4.4).

4. The precipitation can be assigned to another synoptic feature. As shown in Mateling et al., 2023, marine cold air outbreaks (CAOs) are common over the Arctic North Atlantic sector, the Barents Sea, and the Baffin Bay and mainly occur in autumn, winter, and spring. These are the seasons, for which the residual is higher over the Arctic North Atlantic and the Kara and Barents Seas.

Chapter 5

Importance of trace precipitation and cold air outbreaks

As already mentioned in Section 3.4.4, some studies did not include light precipitation rates (e.g. lower than 0.1 mm hr^{-1}) in their analyses to avoid trace precipitation. Trace precipitation could arise due to numerical instabilities within simulations. In the Arctic, however, where cold and dry conditions lead to a lower moisture capacity of the atmosphere, sensible precipitation rates below 0.1 mm hr^{-1} could occur and can be classified as drizzle (Boisvert et al., 2018). Barrett et al., 2020 have shown that 34-55% (different reanalysis products) of the total precipitation in the Arctic has precipitation rates below 0.1 mm hr^{-1}. One also has to note that ERA5 precipitation rates represent an average over a 30 km wide grid cell. Thus, locally occurring precipitation is averaged on a wider scale and the occurrence of higher precipitation rates is reduced compared to high-resolution reanalysis (Wahl et al., 2017). In Section 3.4.4, it was illustrated based on case studies that the consideration of a precipitation threshold decreases the total amount of precipitation by a factor of 2-3. However, applying a threshold would not only reduce the total amount of precipitation but also the residual fraction. Thus, it would increase the contribution of ARs, cyclones, and fronts to the total precipitation. This section quantitatively analyses the impact of a threshold on precipitation and the contribution of synoptic features on precipitation for the ERA5 climatology. For this purpose, a threshold of 0.1 mm hr^{-1} is applied for all forms and types of precipitation.

5.1 Impact on precipitation

Applying a threshold of 0.1 mm hr^{-1} for all forms and types of precipitation mainly concerns precipitation in the Arctic higher than 70°N (Fig. 5.1). However, this differs according to the form and type of precipitation. In percentage terms, the total and large-scale precipitation decreases by 50 to 60% over the Arctic Ocean, the Laptev, Chukchi, and Beaufort Seas, while the decrease over the Arctic North Atlantic and the Kara and Barents Sea is only 20-40%. In contrast, the decrease of convective precipitation reaches between 50 to 80% and strongly affects the central Arctic Ocean and Greenland (Fig. 5.1).

Comparing all types and forms of precipitation, there are differences between convective, large-scale, and total snowfall and rainfall. Generally, in percentage terms, the decrease in large-scale and total snowfall is comparable with the large-scale and total precipitation. For the convective component, this is different. Although the percentage decrease is similar over the central Arctic Ocean, there is a

stronger decrease in convective snowfall in the lower latitudes (70-80°N). The decrease in the convective precipitation and snowfall extends over the entire Arctic, with the lowest decrease over the Arctic North Atlantic. This shows that this is the region least affected by light precipitation. The decrease in rainfall is mainly concentrated over the central Arctic Ocean (70-80%) and Greenland (up to 100%).

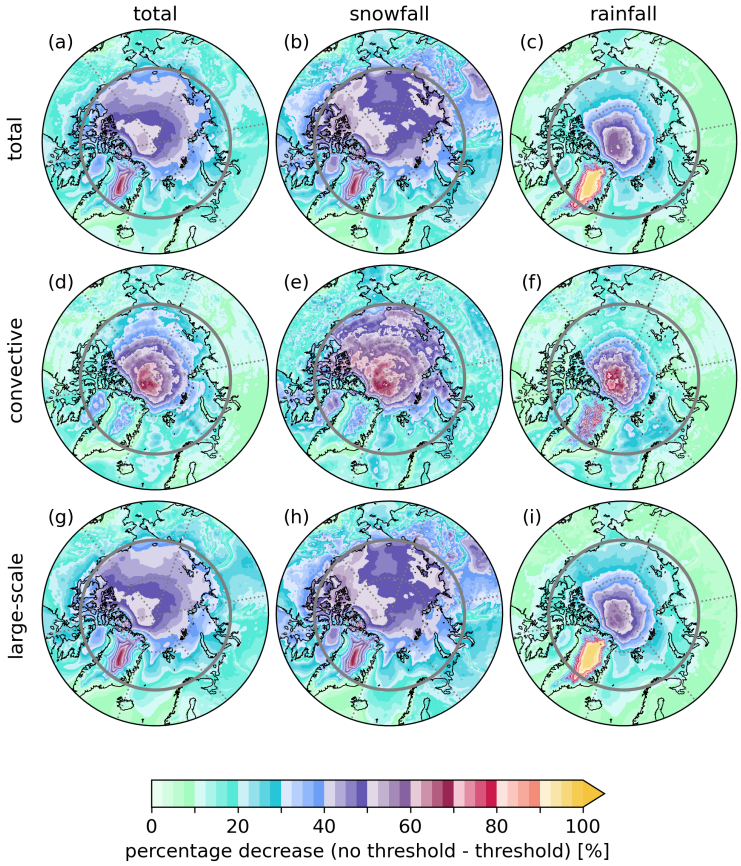

FIGURE 5.1: Percentage decrease of precipitation by applying a threshold of 0.1 mm hr^{-1} for all forms and types of precipitation: convective, large-scale, total precipitation, snowfall, and rainfall.

In general, the Arctic North Atlantic and the Kara and Barents Seas are the regions mostly affected by precipitation (Fig. 4.2). They are less affected by light precipitation rates. This shows that the precipitation in these regions is more intense. Further, in these regions, there are more ground-based observations that could improve the precipitation output for ERA5 reanalysis.

5.2 Seasonal and regional differences

The seasonal and regional differences are focused on the total precipitation. The total precipitation thresholds from 0.01 to 0.1 mm hr^{-1} (with 0.01 mm hr^{-1} steps) are analysed for the entire Arctic (north of 70°N) and each defined subregion (Fig. 4.1). For the entire Arctic, the amount of total precipitation is around 30% higher without applying a threshold of 0.1 mm hr^{-1}. The strongest decrease in precipitation for individual grids occurs over the central Arctic Ocean, the Laptev, Chukchi, and

Beaufort Seas, and over the Canadian Archipelago (Fig. 5.1). Over these regions, the total precipitation without a threshold is 35 - 50% higher than the total precipitation with a threshold of 0.1 mm hr^{-1}. Over Greenland, the Kara and Barents Seas, and over the Arctic North Atlantic, the difference is lower and reaches up to 25%. However, the lower decrease in Greenland only affects the coastal regions (see Fig. 5.1). Focusing on the range for different thresholds from 0.01 to 0.1 mm hr^{-1}, it becomes obvious that the greatest differences occur at low threshold levels. That means, that a great part of the light precipitation is in the range between 0.01 and 0.06 mm hr^{-1} (Fig. 5.2). For thresholds higher than 0.06 mm hr^{-1}, the ranges decrease and the precipitation rates are more equal.

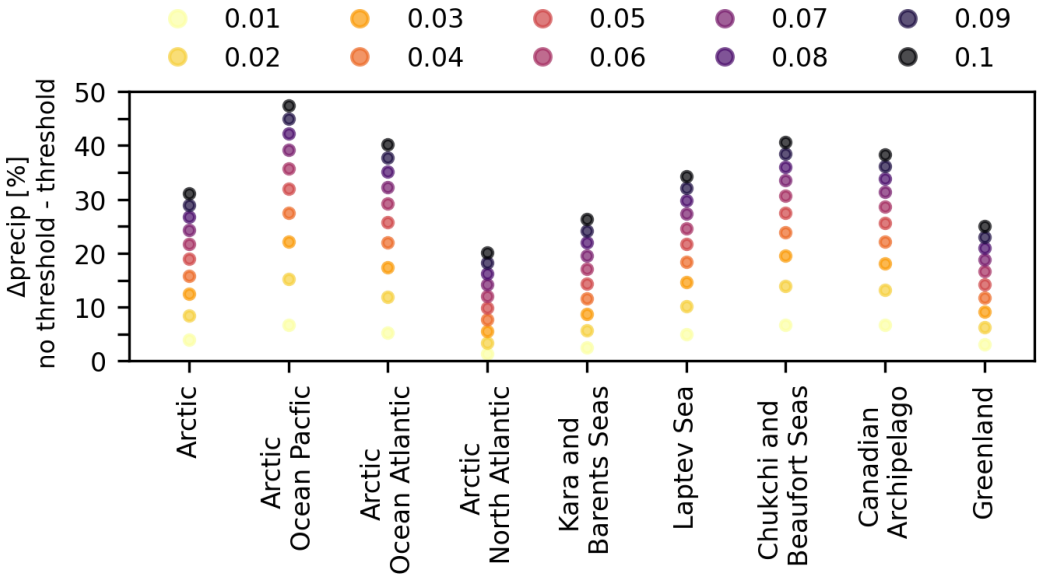

FIGURE 5.2: Relative difference (no threshold - threshold/no threshold) in precipitation between original precipitation amount and threshold applied precipitation for the ERA5 period (1979-2021). Here the threshold increases from 0.01 to 0.1 mm hr^{-1} (with 0.01 mm hr^{-1} steps). The relative difference is given for the entire Arctic (north of 70° N) and the defined subregions (see Fig. 4.1).

5.2.1 Spatiotemporal differences

There are also seasonal differences (Fig. 5.3). First, the focus is on the entire Arctic. For all months, a higher threshold decreases the amount of the total accumulated precipitation. The decrease is higher from October to May (37-45%) than in the summer months (July and August: $\sim$ 25%). Further, also the range between the different thresholds is lower in summer (5-25%) compared to the other seasons (5-45%). The lower decrease and range between individual thresholds in summer may be the consequence of the fact that a warmer atmosphere has a higher moisture capacity (Clausius-Clapeyron relation) and produces therefore higher precipitation rates. During the other seasons, cold and dry conditions dominate which reduces the moisture capacity of the atmosphere. From October to May, all regions are affected by precipitation rates lower than 0.1 mm hr^{-1}. In particular, the Arctic Ocean, the Laptev, Chukchi, and Beaufort Seas, and the Canadian Archipelago are affected. In these regions, there is a stronger decrease in total precipitation (50-70%) and a

higher range between 0.01 and 0.1 mm hr^{-1} (35-55%). Comparing all regions, the Arctic North Atlantic is less affected by a threshold. Generally, only 20-30% of the total precipitation over this region has precipitation rates below 0.1 mm hr^{-1}. Further, the range between 0.01 and 0.1 mm hr^{-1} is lower compared to the other regions. This shows that the higher daily averaged precipitation rates over the Arctic North Atlantic are the result of higher hourly precipitation rates. Over all the regions, the decrease from June to September is lower than the decrease from October to May. During this time of the year, rain is the dominant type of precipitation. From this, it can be concluded that snowfall is mostly affected by light precipitation rates.

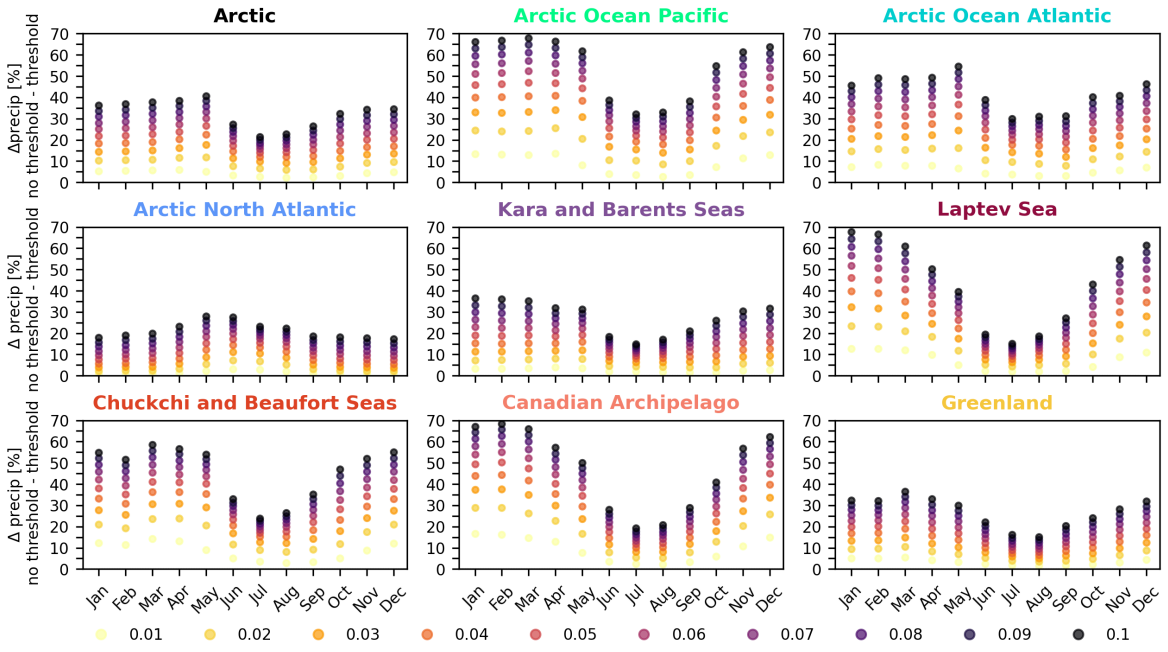

FIGURE 5.3: Relative difference (no threshold - threshold/no threshold) in precipitation between original precipitation amount and threshold applied precipitation for the ERA5 period (1979-2021). Here the threshold increases from 0.01 to 0.1 mm hr^{-1} (with 0.01 mm hr^{-1} steps). The relative difference is given for the entire Arctic (north of 70° N) and the defined subregions (see Fig. 4.1) for each month.

5.2.2 Impact on the contribution of the synoptic features to precipitation

Comparing the results for the overall threshold (0.1 mm hr^{-1}) with the contribution of ARs, cyclones, fronts, as well as the residual, it becomes obvious that light precipitation is mainly associated with cyclone-related components and with the residual (Fig. 5.4). This means that a huge amount of light precipitation cannot be assigned to one of the synoptic features. Thus, the light precipitation is either not inside the shape of the synoptic features, or it is locally produced or artificial precipitation. As seen, especially the snowfall over the Arctic Ocean, the Laptev, Chukchi, and Beaufort Seas, and the Canadian Archipelago are affected. These are regions for which fewer ground-based observations exist. Further, the complex terrain over Canada could be a problem for the model and lead to artificial precipitation.

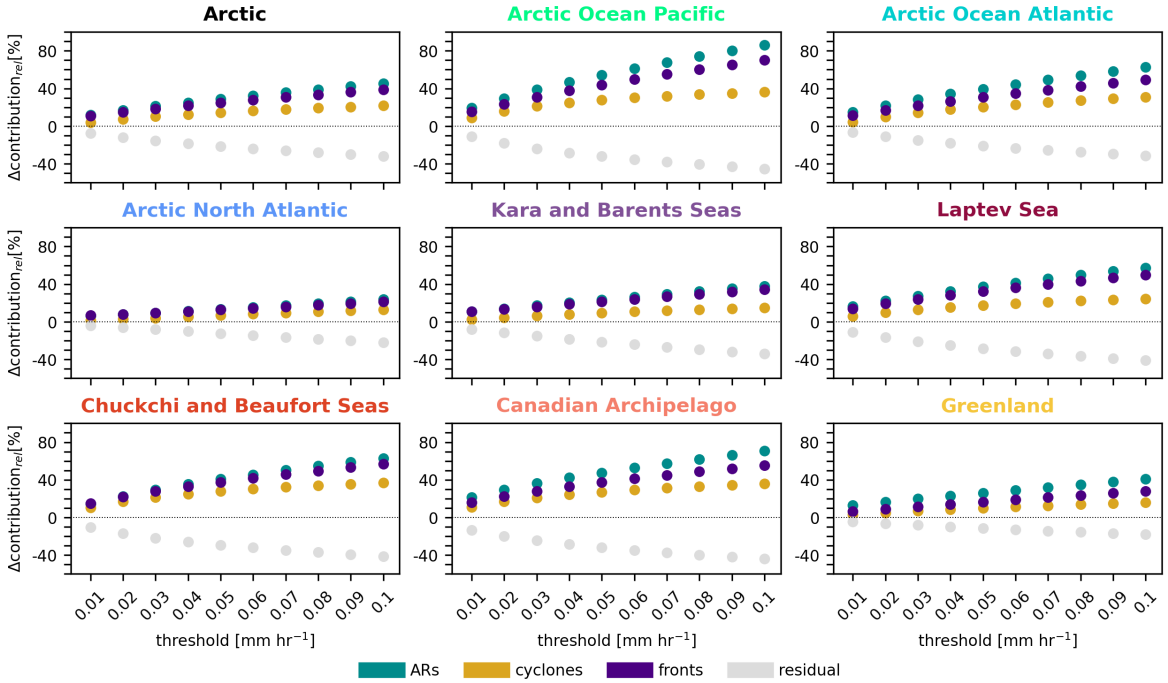

FIGURE 5.4: Relative change between the ARs,- cyclones-, and fronts-related precipitation with varying threshold up to 0.1 mm hr^{-1} and without a threshold.

In summary, applying a threshold has a great impact on the total precipitation. In particular, regions with lower daily averaged precipitation rates are mainly affected by precipitation rates below 0.1 mm hr^{-1}. Further, these are also the regions for which most of the precipitation is classified as residual. In Chapter 3, it is shown that applying a threshold would decrease the residual, and increase the contribution of ARs, cyclones, and fronts. This result is based on two case studies and a specific region. In the next section, the effect of a threshold is analysed for the entire Arctic and the whole ERA5 period.

5.2.3 Impact on the contributions of the synoptic features

Applying a threshold of 0.1 mm hr^{-1} would generally increase the contribution of ARs, cyclones, and fronts to precipitation, and consequently decrease the residual (Fig. 5.5). In general, the increase is higher for ARs and fronts than for cyclones. Here, the increase is shown for different thresholds from 0.01 up to 0.1 mm hr^{-1}. While for the lower thresholds, the changes for ARs, cyclones, and fronts are quite similar, the differences between the contribution of these components to precipitation increase with higher thresholds (Fig. 5.4). Whereby the contribution of ARs is most pronounced, followed by the contribution of fronts and cyclones. Further, the threshold mainly affects the co-located components (AR-CYC-FRONTS, AR-CYC, AR-FRONTS, and CYC-FRONTS) (Fig. A.9). The lowest increase is related to O-CYC. Regarding the entire Arctic, the contribution of ARs and fronts would increase by 45% and 39%, respectively, while the contribution of cyclones would increase by 22%. Considering the individual components, in particular, the components for which ARs are co-located with cyclones and fronts increase by up to 50% (Fig.

5.4). The increase of these components occurs throughout the year and is more pronounced from October to May (Fig. 5.5).

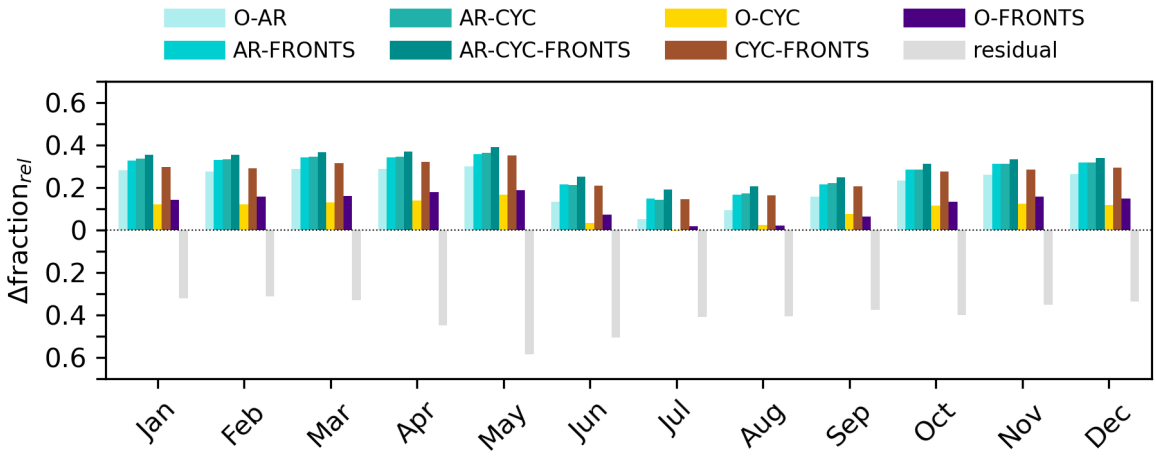

FIGURE 5.5: Relative change [%] between the ARs,- cyclones-, and fronts-related precipitation with threshold and without a threshold of 0.1 mm hr^{-1}.

There are also regional and temporal differences. Comparing the relative changes for the different regions, it becomes obvious that the contribution of ARs, cyclones, and fronts mainly increases in regions which are mainly affected by light precipitation rates (< 0.1 mm hr^{-1}). Therefore, the central Arctic Ocean, the Laptev, Chukchi, and Beaufort Seas, and the Canadian Archipelago are mostly affected (Fig. **??**)). In these regions, the increase in the contribution of cyclones to precipitation ranges from 24-36%, for fronts from 49-70%, and for from 57-86%. This results in a decrease of the residual by 40%. However, not only the regions with the highest amount of light precipitation but also the seasons, especially from October to May are affected (Fig. 5.5). Here, in particular over the Laptev Sea and the Canadian Archipelago, the AR-related components increase by 200%. This shows how much the light precipitation rates influence the contribution of the different synoptic features, especially the AR- and front-related components, to the total precipitation.

5.3 Cold air outbreaks

Another source of precipitation that could be included in residual precipitation are marine cold air outbreaks (CAOs) which are common over the Arctic North Atlantic, the Barents Sea, and the Baffin Bay. They mainly occur in autumn, winter, and spring (Mateling et al., 2023). In contrast to warm air intrusions, CAOs advect cold and dry air from cold land or sea ice over relatively warmer open water. The interaction between the warmer water and the colder air leads to convection, cloud formation, and consequently to precipitation (Mateling et al., 2023). For the detection of CAOs the so-called MCAO-index M has to be determined. For this index, the difference between the sea surface potential temperature Θ_{SST} at the potential temperature at 850 hPa Θ_{850} is calculated:

$$M = \Theta_{SST} - \Theta_{850} \tag{5.1}$$

$$\Theta = T(\frac{p_0}{p})^{\frac{R}{c_p}} \tag{5.2}$$

with p_0 = 1000 hPa and R/c_p = 0.286. To identify the grid cell as a marine cold air outbreak, further assumptions are necessary. First, M has to be higher than 0. Further, only grid cells with open water have to be taken into account (Mateling et al., 2023). In this study, open water is defined as grid cells in which the sea ice concentration is below 0.15%.

The focus of this section is to analyse how far CAOs contribute to the residual. For this purpose, the amounts of precipitation within the CAOs are set in relation to the residual precipitation. For this purpose, grid cells for which CAOs are co-located with the residual are considered. The relation between the CAO-related precipitation and the residual is shown in Fig. 5.6. CAOs contribute mainly to the residual over the Arctic North Atlantic and the Kara and Barents Seas. This especially affects the convective and large-scale snowfall.

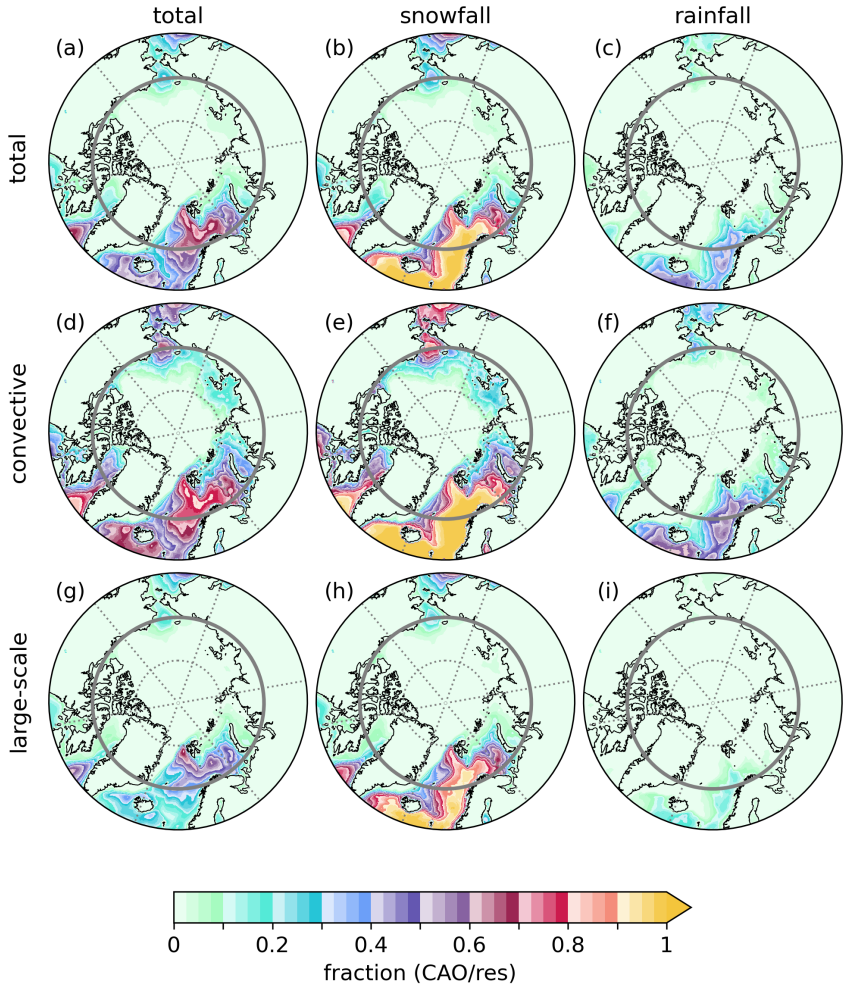

FIGURE 5.6: Fraction of CAO-related precipitation on residual of total precipitation, snowfall, and rainfall (a-c), as well as for the convective (d-f) and large-scale (g-i) precipitation, snowfall, and rainfall.

Figure 5.7 shows the seasonal cycle for the CAO-related precipitation and the

new residual. From October to March, the CAOs contribute up to 20% to the total precipitation in the Arctic. This reduces the residual from around 50% to around 38%. They mainly contribute to the precipitation over the Arctic North Atlantic and the Barents Sea (Kara Sea excluded (Fig. 5.6). This reduces the residual over the North Atlantic to less than 5%.

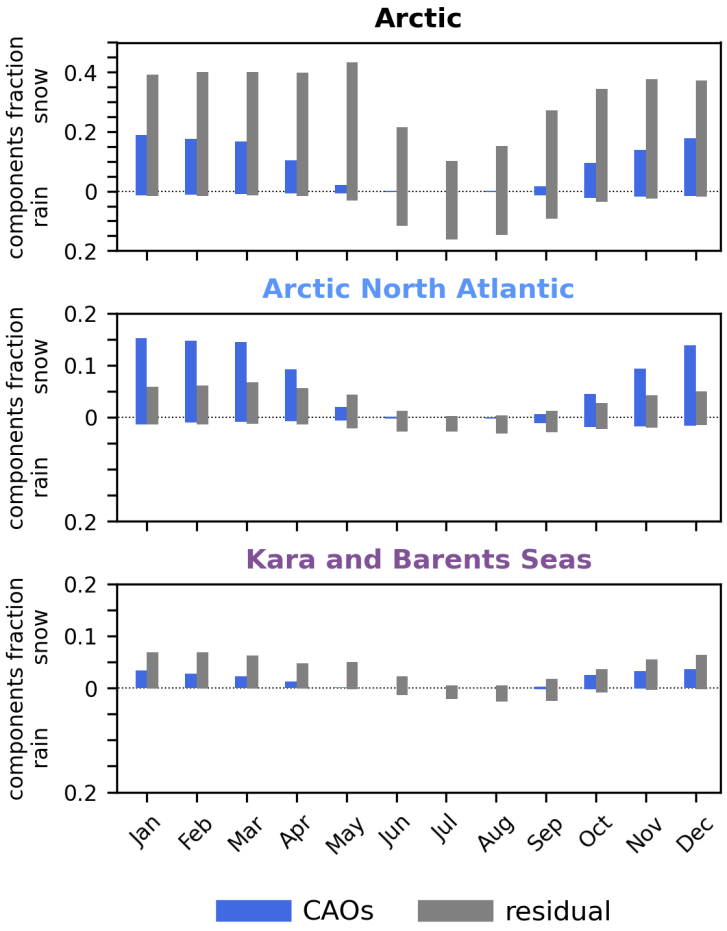

FIGURE 5.7: Fraction of CAO-related precipitation and the new residual over the entire Arctic, the Arctic North Atlantic, and the Kara and Barents Sea on the total Arctic precipitation.

Chapter 6

Trends in Arctic precipitation and the associated synoptic features

In a warmer climate, an increase in extratropical cyclones and AR is projected (Rinke et al., 2019; Zhang et al., 2023). This is largely driven by thermodynamic changes. According to the Clausius-Clapeyron relation, higher temperatures lead to an increase in the water vapor content of saturated air. In general, it is expected an increase in AR and cyclonic frequency and a poleward direction of ARs over the North Atlantic, and an equatorward shift of ARs due to wind changes over the North Pacific. How far this would affect the Arctic precipitation is analysed in this section.

For the climate trends, the Mann-Kendall test is used (Mann, 1945). The Mann-Kendall test is a non-parametric to analyse the significance of positive or negative trends. In this study, the annual trends in Arctic precipitation and the synoptic features-related precipitation is analysed. The trends are significant at a 0.05 significance level. For a better overview, only the significant trends are visualized. First, the focus is on in Arctic precipitation, then the trend of the synoptic features-related precipitation is analysed.

6.1 Trends in Arctic precipitation for the entire ERA5 period

The trend in Arctic precipitation for the total ERA5 period (1979 – 2021) differs among the type and form of precipitation (Fig. 6.1). For the entire ERA5 period, the total precipitation significantly increased over the Norwegian, Barents, and Kara Seas. The positive significant trend is most pronounced at 75°N along the sea ice edge and decreases towards the north. Thus, the positive trend in total precipitation is mainly concentrated in the region where the Arctic warming is most pronounced. It becomes obvious that the trend in total precipitation is a product of all types and forms of precipitation. That means, there are differences between convective and large-scale precipitation. Although the trend for large-scale precipitation is quite similar distributed as for the total precipitation, it is less pronounced. Compared to large-scale precipitation, convective precipitation increased significantly over the Arctic North Atlantic, the Barents, Kara, Laptev, and also over the Chukchi and Beaufort Seas. The strongest positive trend, however, is at the sea ice edge.

Further, there are differences between convective, large-scale, and total snow and rain. For snow, a dipole structure over the Arctic North Atlantic sector exists. Snow significantly decreased over the Norwegian Sea, and increased higher north over

some parts of sea ice. While the negative trend over the Norwegian Sea is also related to convective and large-scale snowfall, the positive trend is mainly related to convective snowfall. As for convective precipitation, the positive trend in convective snowfall is most pronounced at the sea ice edge. For rainfall, there is a positive significant trend over the Arctic North Atlantic, the Kara, Barents, and also over parts of the Laptev Seas. Thus, over the Arctic North Atlantic, there is a negative trend in snowfall and a positive trend in rainfall. The lack of a significant trend in total precipitation in this region is an indication of the phase change from snow to rain as a result of warmer temperatures.

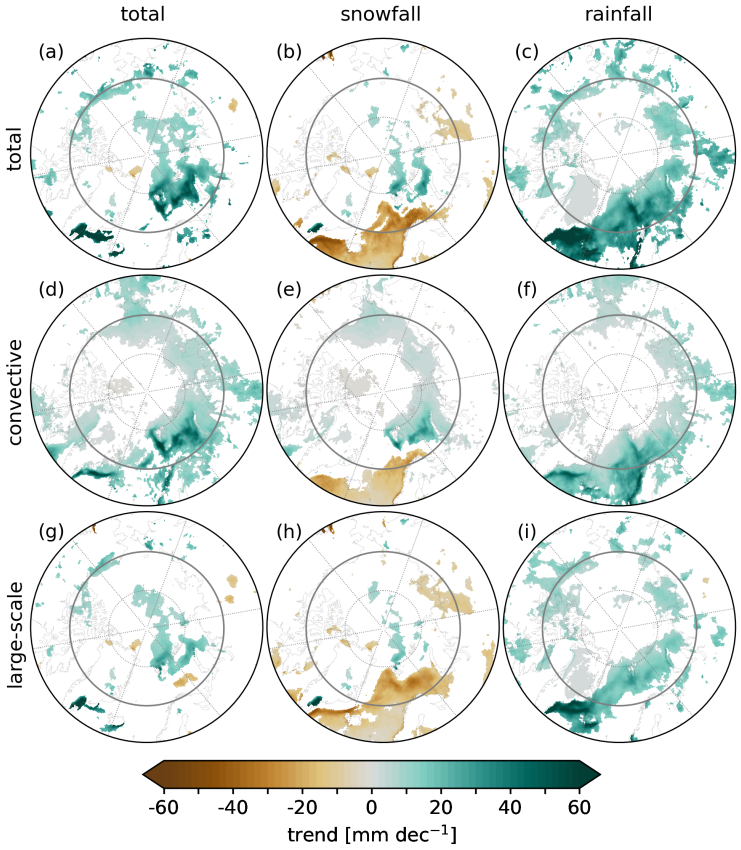

FIGURE 6.1: Significant trend of total precipitation, snowfall, and rainfall (a-c), as well as for the convective (d-f) and large-scale (g-i) precipitation, snowfall, and rainfall.

Comparing the trends for all types and forms of precipitation, it becomes clear that the negative trend for snow and the positive trend for rain offset each other. This mainly affects the trend in the total and large-scale precipitation. However, this is different for convective precipitation, snowfall, and rainfall. Here, especially the positive trend in convective snow and rain over the Barents, Kara, and Laptev Seas results in a positive significant trend in convective precipitation. These results have shown that the trend in precipitation depends strongly on the type and form of precipitation. Further, the total precipitation over the Arctic North Atlantic has not increased significantly. In the last few decades, there has been a phase change from snow to rain. Further, the trend is more pronounced for convective than large-scale precipitation. It becomes clear how important it is to distinguish between convective

and large-scale snow and rain.

6.1.1 Trends in AR-, cyclone-, front-related and residual precipitation

How far the AR-, cyclone-, and front-related precipitation has changed during the last four decades is analysed in this section. There are also differences between convective and large-scale precipitation as well as between snow and rain.

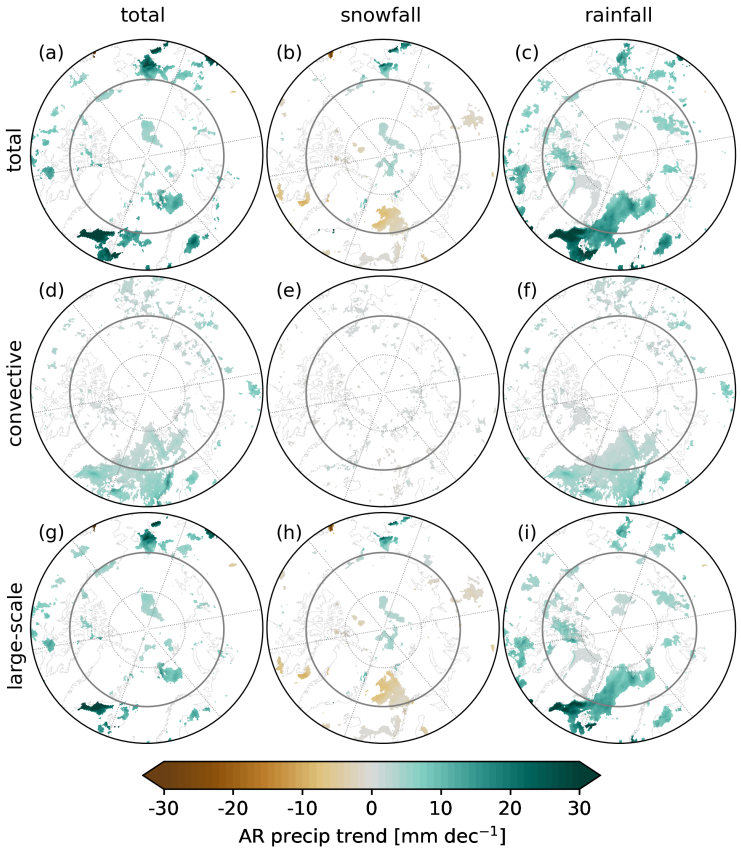

FIGURE 6.2: Significant trend of AR-related total precipitation, snowfall, and rainfall (a-c), as well as for the convective (d-f) and large-scale (g-i) precipitation, snowfall, and rainfall.

First, the focus is on AR-related precipitation (Fig. 6.2). There is a significant trend over the Arctic North Atlantic in convective total precipitation as well as for total, convective, and large-scale rainfall. This positive trend is confined in a narrow band that reaches from southeast Greenland to Svalbard. This shows that the AR-related precipitation is mainly concentrated along the east coast of Greenland and the sea ice edge. This increase in AR-related rainfall is associated with an increase in AR occurrence (Fig. 6.6). Regarding the occurrence trend, there is also a significant increase in ARs over the Pacific side and also over the Canadian Archipelago. In these regions, there are smaller significant patterns in AR-related precipitation compared to the ARs over the Arctic North Atlantic. The strongest increase over the Pacific Ocean is concentrated over the Bering Strait. Therefore, it is expected that the ARs precipitate out when they reach the narrow corridor between Eurasia and North America. Consequently, their influence on precipitation is weaker compared

to ARs coming from the Atlantic sector.

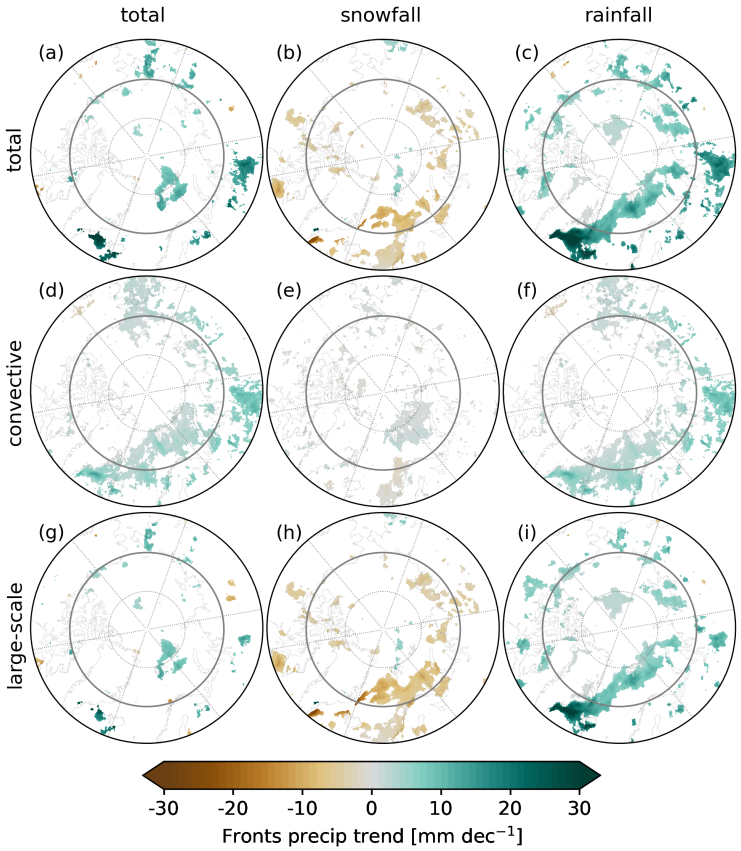

FIGURE 6.3: Significant trend of Fronts-related total precipitation, snowfall, and rainfall (a-c), as well as for the convective (d-f) and large-scale (g-i) precipitation, snowfall, and rainfall.

The front-related precipitation trends are similar to the AR trend. Thus, there is a significant trend in convective precipitation. In contrast to ARs, however, the positive significant trend in convective precipitation is not only concentrated over the Arctic North Atlantic, it is also concentrated over the Barents Sea. The positive trend in large-scale rainfall is similar to AR. Regarding the trend in frontal occurrence, there is no significant trend over the Arctic North Atlantic. As the front-related precipitation is mainly associated with ARs, it is expected that the positive trend in frontal-related precipitation is associated with the increase in ARs.

The cyclone-related precipitation trends (Fig. **??**) are similar to the trends in total precipitation (Fig. 6.1). In contrast to ARs, the positive trend in convective precipitation is more concentrated over the Kara, Barents, and Laptev Seas - in particular, along the sea ice edge. This increase in convective precipitation is associated with an increase in cyclone occurrence (Fig. 6.6). The significant trend in convective precipitation is related to convective snowfall and rainfall. In contrast to ARs, there is no significant trend of convective precipitation over the Arctic North Atlantic. The trends in convective snowfall and rainfall are opposite. While there is a significant decrease in convective snowfall, there is a positive trend in convective rainfall. This change from snowfall to rainfall could be the consequence of warming. Thus, in total, there is no trend in total convective precipitation, however, a phase change from

snow to rain. This is also the case for total and large-scale snowfall and rainfall.

In addition, there is a positive trend of CAO-related precipitation along the sea ice edge which is most pronounced at Baffin Bay, the east coast of Greenland, south of Svalbard, and the Barents Seas. This concerns the convective, large-scale, and total precipitation and snowfall. In contrast to the total precipitation, there is a negative trend in snowfall over the Norwegian Sea which is related to an increase in rainfall. Therefore, a phase transition from snow to rain due to higher temperatures is expected. In general, the increase in CAO precipitation is associated with an increase in CAO occurrence.

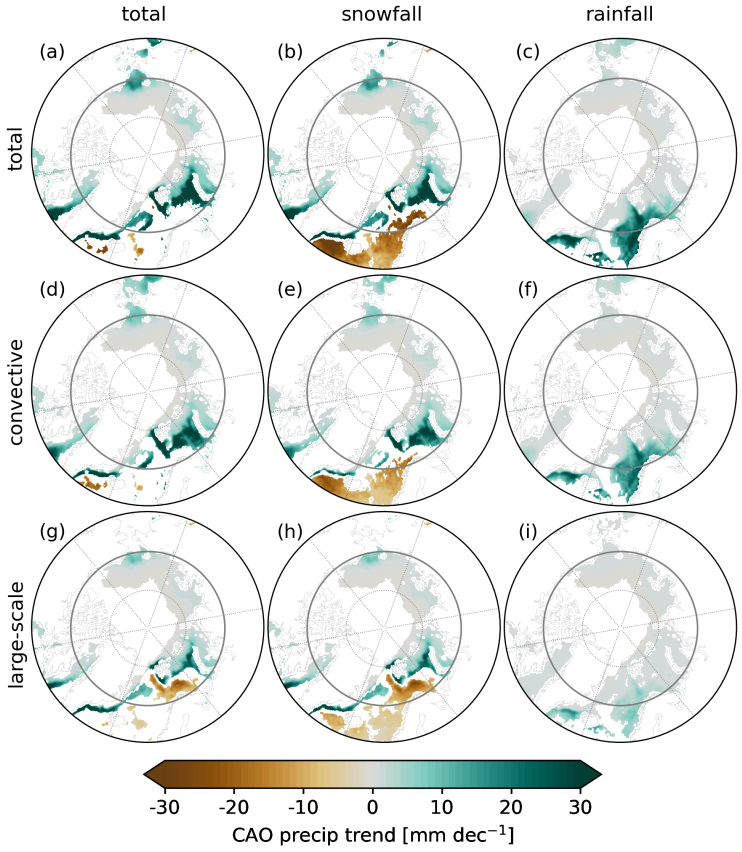

FIGURE 6.4: Significant trend of CAO-related total precipitation, snowfall, and rainfall (a-c), as well as for the convective (d-f) and large-scale (g-i) precipitation, snowfall, and rainfall.

Further, the trends of the residual precipitation are analysed. There is a significant trend of convective precipitation over the Kara, Barents, Laptev, Chukchi, and Beaufort Seas, especially related to rainfall. An increase is also seen in total rainfall over the Norwegian Sea which is mainly due to the transition from snow to rain. The positive significant trend in precipitation is mainly associated with a decrease in the residual occurrence. Therefore, a significant trend in the precipitation intensity related to the residual is expected.

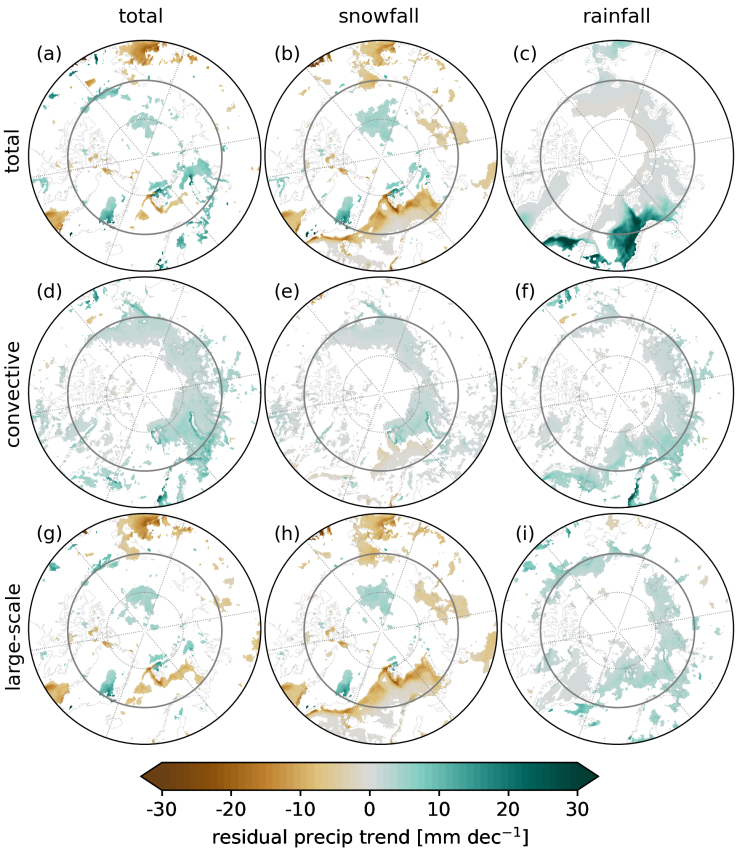

FIGURE 6.5: Significant trend of residual-related total precipitation, snowfall, and rainfall (a-c), as well as for the convective (d-f) and large-scale (g-i) precipitation, snowfall, and rainfall.

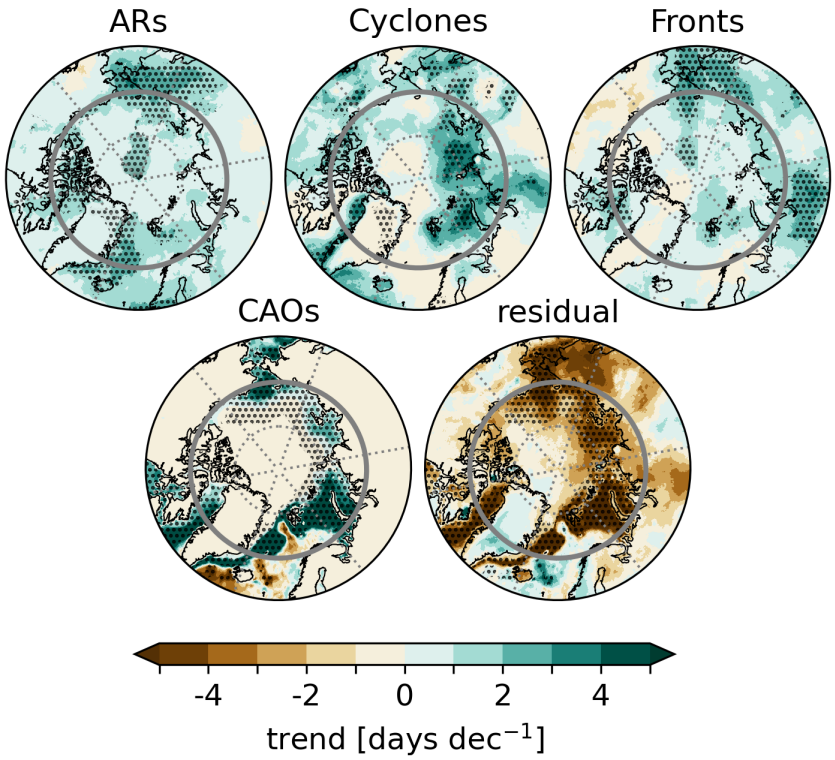

FIGURE 6.6: Significant occurrence trend of ARs, cyclones, fronts, CAOs, and residual.

6.2 Interpretation of the findings

Analysing the significant trends of precipitation has shown a positive significant trend in total precipitation over the Norwegian Sea south of Svalbard and over the Barents and Kara Seas. This is also the region mostly affected by Arctic warming. Further, the analyses have shown that it is important to distinguish between convective, large-scale, and total precipitation, snow, and rain. Although there is no significant trend in total precipitation, there is a negative trend in snowfall and a positive trend in rainfall. Both, the negative and positive trend offset each other. Thus, the warming in the Arctic favors the transition from snow to rain.

The increase in large-scale rainfall over the Arctic North Atlantic is mainly associated with ARs and fronts. The increase in AR-related rainfall is related to a significant increase in the AR occurrence. These positive trends could be related to blocking systems that favor the poleward shift of ARs into higher latitudes. Although the frontal occurrence also increases in this region, there is no significant trend in this context. The positive trend in large-scale rainfall over this region could have consequences for the Arctic sea ice and therefore, for the Arctic warming.

In contrast to ARs and fronts, the cyclone-related precipitation mainly increases over Kara and Laptev Seas. This is related to an increase in cyclone activity in these regions. The increase in cyclone-related precipitation in this region mainly affects the convective component. Therefore, it is expected that an increase in cyclone occurrence favors the convective precipitation over these regions. The increase in convective precipitation could be related to changes in sea ice. In contrast to ARs and

fronts, the large-scale increase is more shifted to the east and is concentrated over the Kara and Barents Seas.

The CAO-related precipitation will mainly increase along the sea ice edge. A possible reason for this increase could be that the temperature gradient increases due to an increase in the near-surface air temperature. This enhances the thermodynamical processes and therefore the convective precipitation.

Comparing all trends with each other, it becomes obvious that the large-scale rainfall trend over the Norwegian Sea is mainly associated with ARs and fronts, while over the Kara and Barents Seas, it is mainly associated with cyclones and fronts. There is also an increasing trend along the sea ice edge. Therefore, it is expected that when the synoptic features reach sea ice, they begin to precipitate out due to the lower moisture capacity of the atmosphere over the colder sea ice. Further, there is an increase in convective precipitation mainly related to cyclones and CAOs. The increase is due to an increase in the occurrence of these features. For both, cyclones and CAOs, the positive trends are mainly located in areas that are usually covered or surrounded by sea ice. It can therefore be assumed that the convective precipitation is also related to sea ice changes.

Chapter 7

Conclusion and outlook

This thesis's overarching goal was to understand how far different synoptic features contribute to precipitation in the Arctic. Therefore, the influence of ARs, cyclones, and fronts on Arctic precipitation was analysed for the entire ERA5 period from 1979-2021. Currently, ERA5 reanalysis provides the best spatial and temporal resolution information on a global scale for the last four decades. Specifically, it has been shown that ERA5 is a high-quality reanalysis for the Arctic region (Graham et al., 2019a), and it is recommended for precipitation analyses in the Arctic (Barrett et al., 2020). Within the framework of this thesis, ERA5 performance was further evaluated by comparing it with independent ground-based and spaceborne remote sensing observations for three different AR case studies. The comparison with different snowfall observations highlighted the difficulties in the accurate measurement of snowfall rates. In general, the observation-to-model and model-to-observation approaches showed a good agreement of ERA5 with observations in representing spatiotemporal structures of large-scale precipitation systems. However, problems in resolving small-scale features like convective clouds and local geographic effects were revealed. Further, it seems that ERA5 tends to overestimate/underestimate weaker/intense precipitation events due to its grid-scale smoothing. Although ERA5 reanalysis data has some uncertainties in representing local precipitation, it is the best dataset for analysing long-term changes in precipitation caused by synoptic systems over the Arctic.

After successfully evaluating the ERA5 reanalysis data, a new methodology was established to distinguish between AR-, cyclone-, and front-related precipitation. To apply this method, the synoptic features first had to be detected. Cyclones and fronts based on ERA5 reanalysis data were provided by Dr. Merseid Akperov (Russia) and Dr. Michael Sprenger (Switzerland). In contrast to cyclones and fronts, however, no established data base of AR shapes was available. For this purpose, two detection algorithms were implemented and applied. The first AR detection algorithm was provided by Bin Guan (USA) and the second by Irina Gorodetskaya and Carolina Viceto (Portugal). Within the framework of this thesis, a global AR detection catalog based on Guan's detection algorithm (Guan et al., 2018) was established for the ERA5 period from 1979-2021. The catalog is available online and can be accessed at PANGEA (Lauer, 2023b).

ARs, cyclones, and fronts are often connected and therefore cover the same areas. This had to be taken into account, as otherwise, the precipitation over a specific area would be counted for more than one system. Therefore, so-called co-located and non-co-located components were defined. In total, there were eight components classified: O-AR (only AR), AR-CYC (AR co-located with cyclones), AR-FRONTS (AR co-located with fronts), AR-CYC-FRONTS (AR co-located with cyclones and

fronts), CYC-FRONTS (cyclones co-located with fronts), O-CYC (only cyclones), O-FRONTS (only fronts), and residual (no synoptic feature). Subsequently, this method was applied to answer the research questions defined at the beginning (Chapter **??**) and addressed in the following.

How do synoptic features contribute to precipitation in the Arctic?

This method was first applied to two distinct periods during two airborne campaigns (ACLOUD: May/June 2017 and AFLUX: March/April 2019). Here, the focus was on the European Arctic and, therefore, on the poleward moisture transport from the North Atlantic and in summer from Siberia. The contribution of ARs, cyclones, and fronts differed between the two periods. During ACLOUD, the precipitation was mainly confined in areas for which ARs and fronts are co-located, while cyclone-related components play a minor role. However, during AFLUX, precipitation was mainly associated with cyclone-related components, especially with O-CYC. During both campaigns, snow was the dominant type of precipitation. However, during the ACLOUD campaign, AR-related rainfall was also detected. For both campaigns, about one-third of the precipitation could not be attributed to one of the synoptic features. In addition, it was found that the results are sensitive to the choice of the detection algorithm.

Applying the new methodology to the ERA5 climatology, it becomes obvious that there are spatiotemporal differences in the contribution of the synoptic features. From October to May, the precipitation is mainly concentrated over the Arctic North Atlantic and the Kara and Barents Seas, whereby the Arctic North Atlantic has higher precipitation values. During this time of the year, snowfall is the dominant type of precipitation and is mainly associated with cyclone-related components. For both regions, the non-co-located cyclone component O-CYC dominates. This affects the large-scale and convective snowfall. Additionally, the Arctic North Atlantic is also affected by rainfall. Although the rainfall, which is mainly associated with ARs and fronts, is comparably low, it could have consequences for the Arctic. The effect of rain on sea ice is not yet fully understood. However, it is expected that rain can lead to sea ice melting, which would enhance the ice-albedo feedback and, therefore, the Arctic warming.

In summer, the precipitation is more evenly distributed over the entire Arctic. From June to September, rain is the dominant type of precipitation. In contrast to autumn, winter, and spring, ARs and fronts become more effective, while the contribution of cyclones is quite similar. Although in summer the contribution of the synoptic features is quite similarly distributed, they are more pronounced over the Kara, Barents, and Laptev Seas. However, this is no surprise as these regions are also known as the 'Arctic frontal zone' (Serreze et al., 2001) due to the high occurrence of fronts during this time of the year. Further, it is expected that the AR-related rainfall is associated with the so-called 'Siberian Atmospheric Rivers' (described in Komatsu et al., 2018).

Although ARs, cyclones, and fronts contribute to precipitation in the Arctic, there is also a noteworthy amount of precipitation that was classified as residual. Generally, the residual is higher from October to May, mainly associated with snowfall.

The residual is mainly concentrated over the Arctic North Atlantic and the Barents Kara Seas. There are some hypotheses to explain the high occurrence of the residual. First, the synoptic feature-related precipitation is a product of the detected ARs, cyclones, and fronts. These detected shapes depend on the detection algorithm. Therefore, it could be possible that precipitation is not concentrated within the detected shape. Further, there may be gaps in the detection of the synoptic features, as seen for the AR event at the end of May 2017 during the ACLOUD campaign. Second, the precipitation in ERA5 is a product of accumulated precipitation over one hour. The shapes, however, are instantaneous. That means that precipitation rates accumulated between two hours are not counted as synoptic feature-related precipitation. Third, other features producing localized precipitation, such as marine cold air outbreaks, could play a role. Fourth, the residual frequently includes trace precipitation which is usually not related to synoptic features. It is not clear to which degree this very light precipitation is real or is caused by numerical effects in the underlying model of ERA5.

To what extent do trace precipitation and marine cold air outbreaks affect the residual?

Due to the cold and dry conditions, the Arctic is affected by light precipitation rates, also known as drizzle or trace precipitation. Based on ERA5 data, 30% of the Arctic precipitation has precipitation rates less than 0.1 mm hr^{-1}. Further, there are spatiotemporal differences. It mainly affects the Arctic Ocean, the Laptev, Chukchi, Beaufort Seas, and the Canadian Archipelago from October to May. In these regions, 50% - 70% of the total precipitation is lower than 0.1 mm hr^{-1}. This shows that snow is mainly affected by light precipitation. Applying a threshold also has consequences for the synoptic feature-related precipitation. Generally, the residual over the entire Arctic would decrease by 40%. Consequently, 27% of the Arctic precipitation would be classified as residual. Applying a threshold would not only decrease the residual, but it would also increase the fraction of the synoptic features on the total precipitation. This mainly concerns the AR-related components. However, the results have shown that the Arctic North Atlantic and the Kara and Barents Seas, which are most affected by the residual, are less affected by light precipitation rates.

Marine CAOs which are most common in the North Atlantic and the Kara and Barents Seas regions, and their contribution in total precipitation is analysed. The results showed that CAOs contribute between 10% and 20% to the total precipitation in the Arctic from October to March and are mainly concentrated over the Arctic North Atlantic. Considering CAOs, the residual for the entire Arctic would decrease from 50% to 40%. Over the Arctic North Atlantic, however, the effect is much stronger with a decrease from around 15% to 5%.

Are there trends in synoptic feature-related precipitation?

The trend analysis showed that it is important to distinguish between the form and type of precipitation. Generally, the significant increase in Arctic total precipitation was mainly concentrated over the Barents Sea. Distinguishing between convective and large-scale snowfall and rainfall, it becomes obvious that there is a significant

decrease in snowfall recently, which is related to a significant trend in rainfall over the Norwegian Sea. This indicates a phase change from snow to rain. The significant increase in rainfall extends over the Arctic North Atlantic and the Kara and Barents Seas. The increase in rainfall over the Arctic North Atlantic is mainly associated with ARs and fronts while over the Barents and Kara Seas, the increase in rainfall is mainly related to CAOs and cyclones. In general, the increase in synoptic feature-related precipitation is associated with a significant increase in occurrence rather than intensity.

The analyses in this thesis showed that the precipitation in the Arctic can be mainly attributed to ARs, cyclones, fronts, and marine CAOs. Thus, these features influence the surface characteristics not only through the downward longwave radiation but also through precipitation. Depending on the type and form of precipitation, this could have consequences for the sea ice, the ice-albedo feedback, and therefore the Arctic warming.

Future research

This study provides new findings in many respects and gives a detailed overview of the influence of ARs, cyclones, and fronts on precipitation in the Arctic. It is the first study that distinguishes between AR-, cyclone- and front-related precipitation. Based on the current knowledge, it is also the first study to investigate the influence of atmospheric fronts in the Arctic. However, a more detailed sensitivity study would be necessary to quantify the uncertainties due to the reanalysis data set and the detection algorithms for the synoptic features. Further research opportunities are given in the following.

1. Sensitivity studies with other detection algorithms or reanalyses
   The climatological analysis in this thesis is performed with ERA5 reanalysis and for one detection algorithm for each of the synoptic features only. As described in the beginning, there are still uncertainties in the definition of the synoptic features. Each detection algorithm applies different approaches. Based on case studies in Chapter 3, the sensitivity of the results by comparing different detection algorithms could be demonstrated. In the future, the analysis could at least be extended to the whole year to see if there are seasonal differences and to any new emerging algorithm.

2. Modification of the methodology
   A further possibility could be to modify the established methodology. In the current state, the method did not consider that the synoptic features cover a certain distance within an hour. Therefore, it could be possible that precipitation rates accumulated over one hour are not inside the detected shape. There are some possibilities: First, one could include a wind field that allows one to analyse the direction and velocity of the individual system. Second, it could be possible to include the detection of precipitation systems connected to AR shapes defined mainly by their water vapor content.

3. Extended analysis in trend
   In this study, the trends were shown for the entire ERA5 period. Preliminary seasonal analyses revealed seasonal differences. For example, the positive trend in large-scale rainfall over the Arctic is mainly related to ARs in

September. Thus, the ARs bring warm, moist air and rainfall into the Arctic, which could enhance the decrease in sea ice. Therefore, also compound events could be studied.

4. Influence of synoptic features on sea ice
   Trend analyses have shown that rainfall will increase in the future. Therefore, the question arises in how far this rainfall will affect the sea ice and, therefore, the Arctic warming.

Appendix A

Appendix

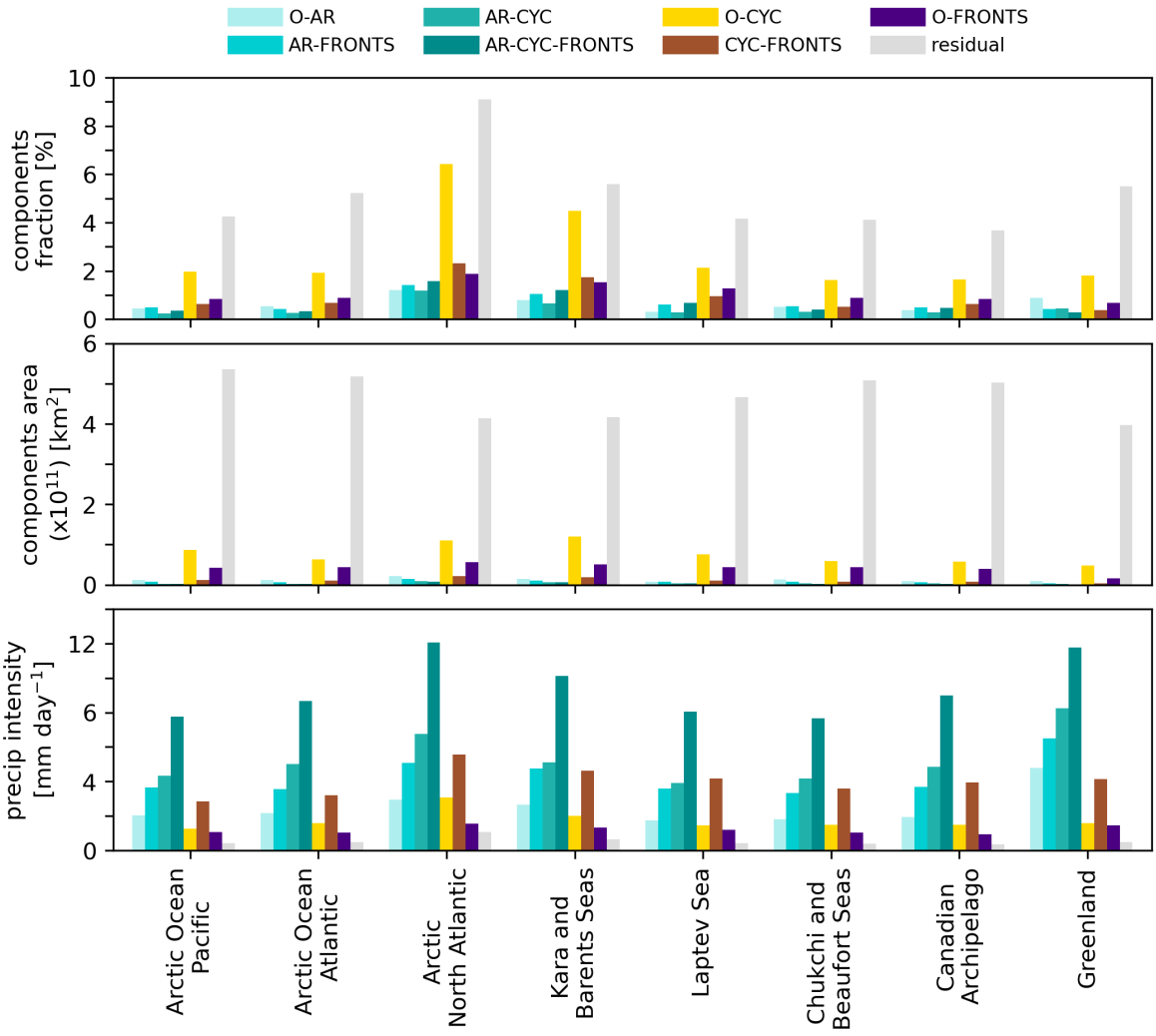

FIGURE A.1: Top: Regional fraction [%] of co-located and non-co-located ARs, cyclones, fronts, and residual on total Arctic precipitation. Middle: Area of co-located and non-co-located ARs, cyclones, fronts, and residuals covered with precipitation. Bottom: Precipitation intensity within co-located and non-co-located ARs, cyclones, fronts, and residuals for each subregion

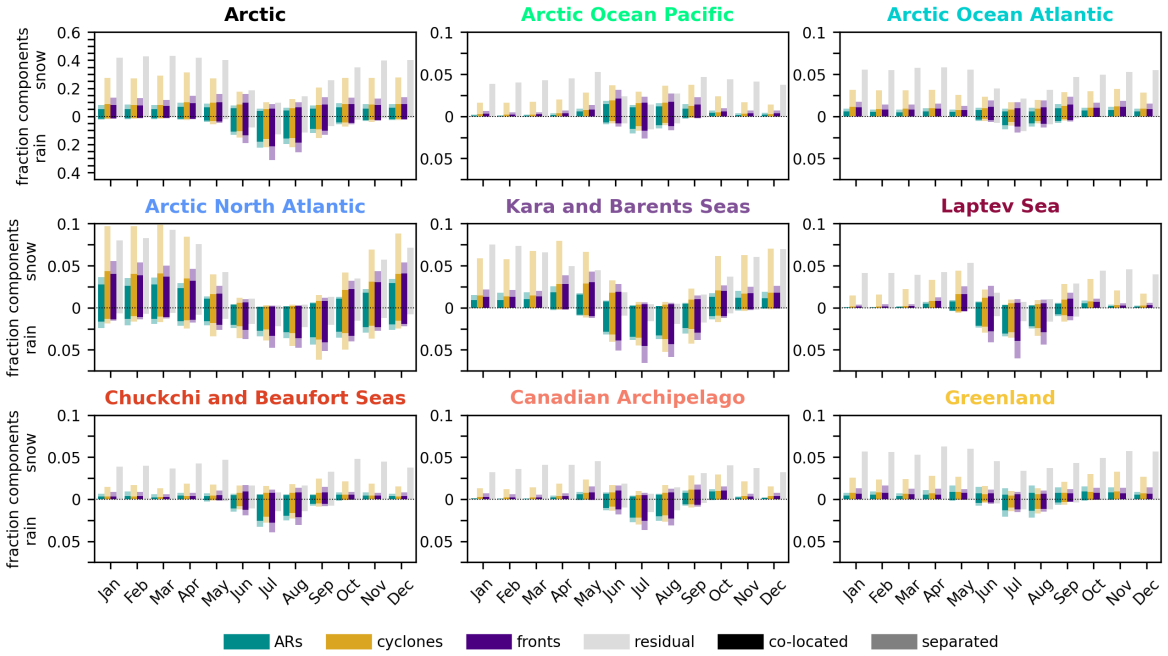

FIGURE A.2: Top: Monthly co-located (dark) and non-co-located (light) snow and rain fractions of ARs (turquoise), cyclones (yellow), fronts (indigo), and residual (grey) to the total monthly Arctic precipitation. Note that the y-axis is different for the whole Arctic than for the subregions (see Fig. 4.1).

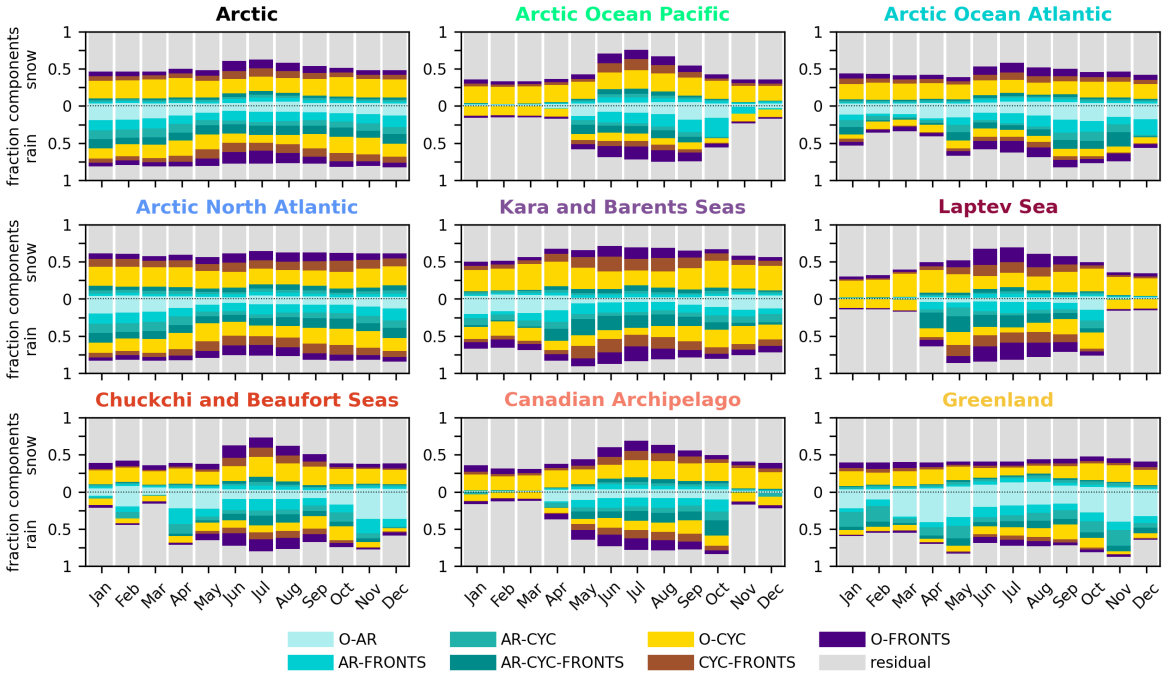

FIGURE A.3: Contribution of individual components (co-located) to the total snowfall and rainfall for the entire Arctic as well as the individual subregions (see Fig. 4.1).

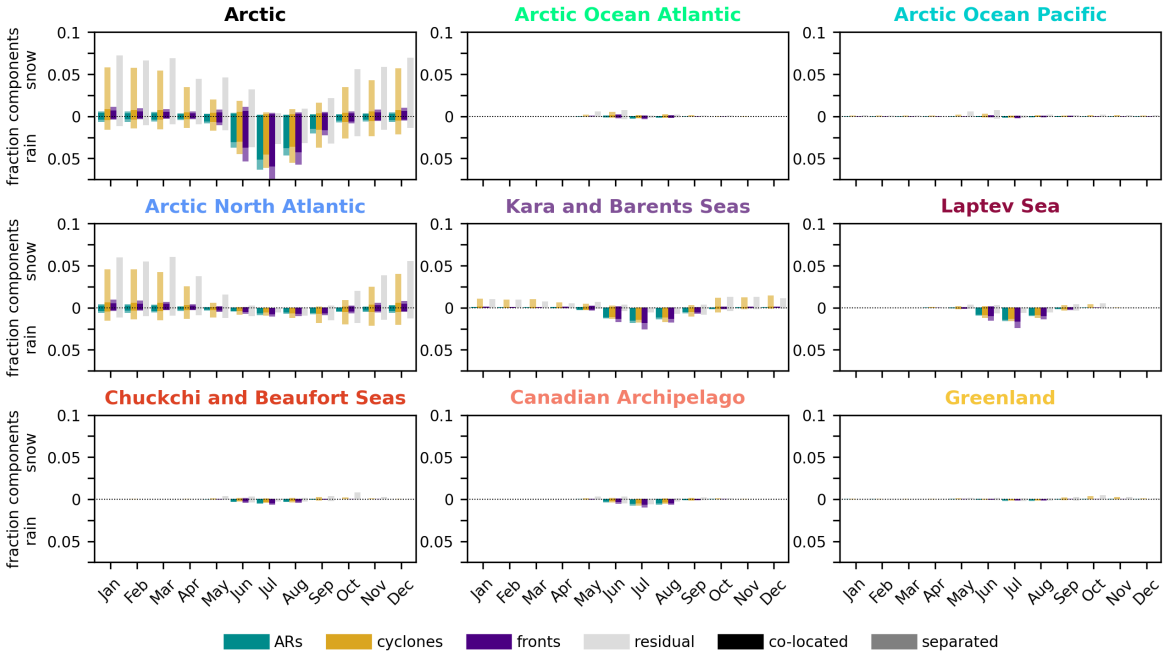

FIGURE A.4: Monthly co-located (dark) and non-co-located (light) convective snow and rain fractions of ARs (turquoise), cyclones (yellow), fronts (indigo), and residual (grey) to the total monthly Arctic precipitation. Note that the y-axis is different for the whole Arctic than for the subregions (see Fig. 4.1).

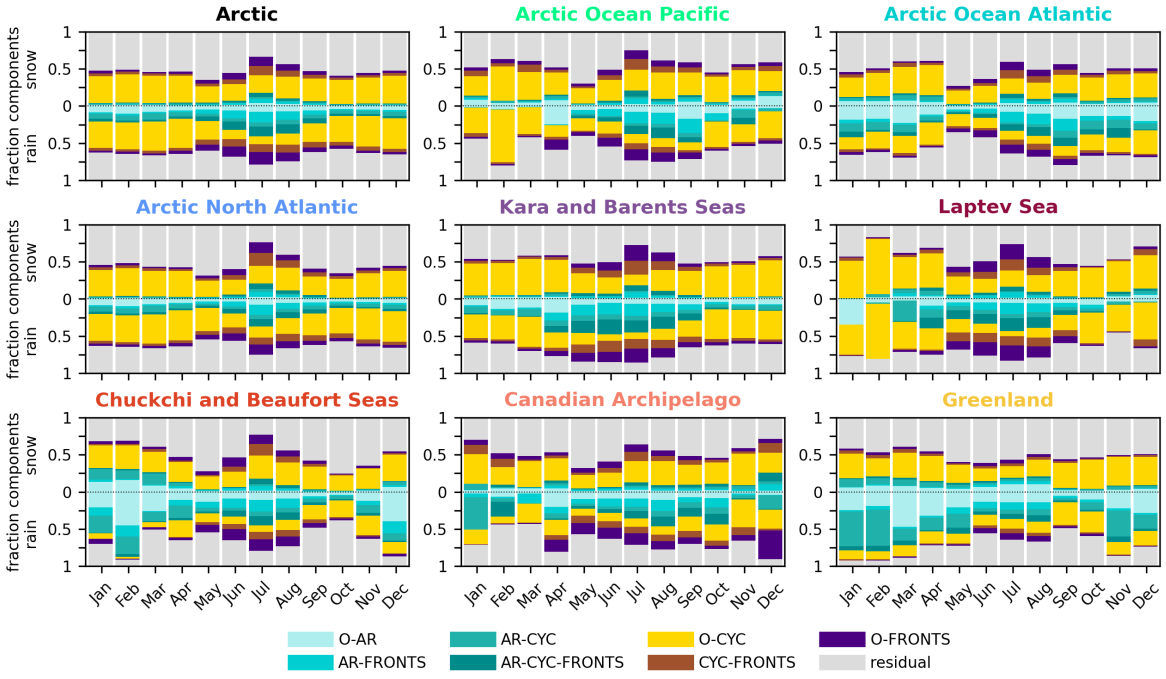

FIGURE A.5: Contribution of individual components (co-located) to the total snowfall and rainfall for the entire Arctic as well as the individual subregions(see Fig. 4.1).

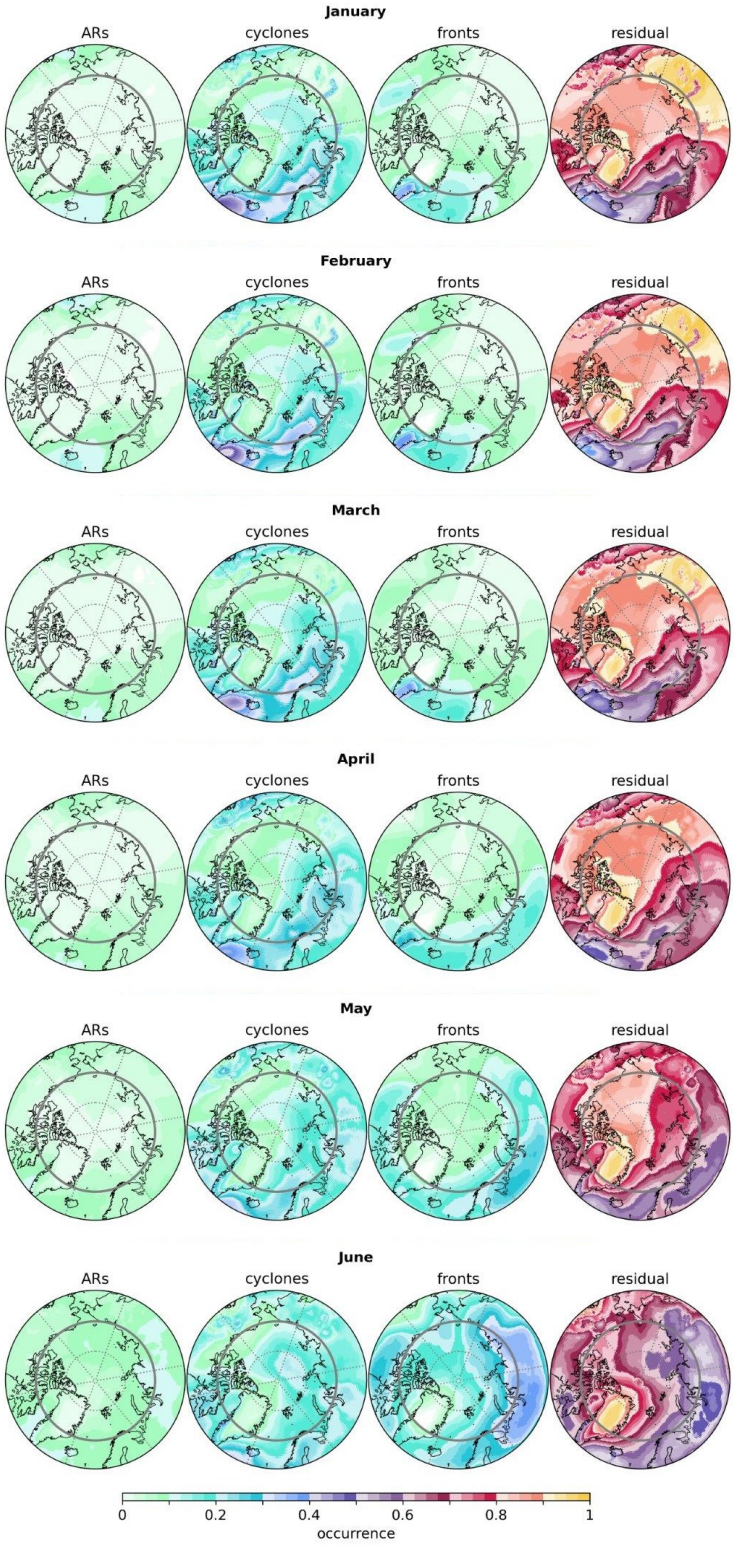

FIGURE A.6: Occurrence of ARs, cyclones, fronts, and residual from January to June.

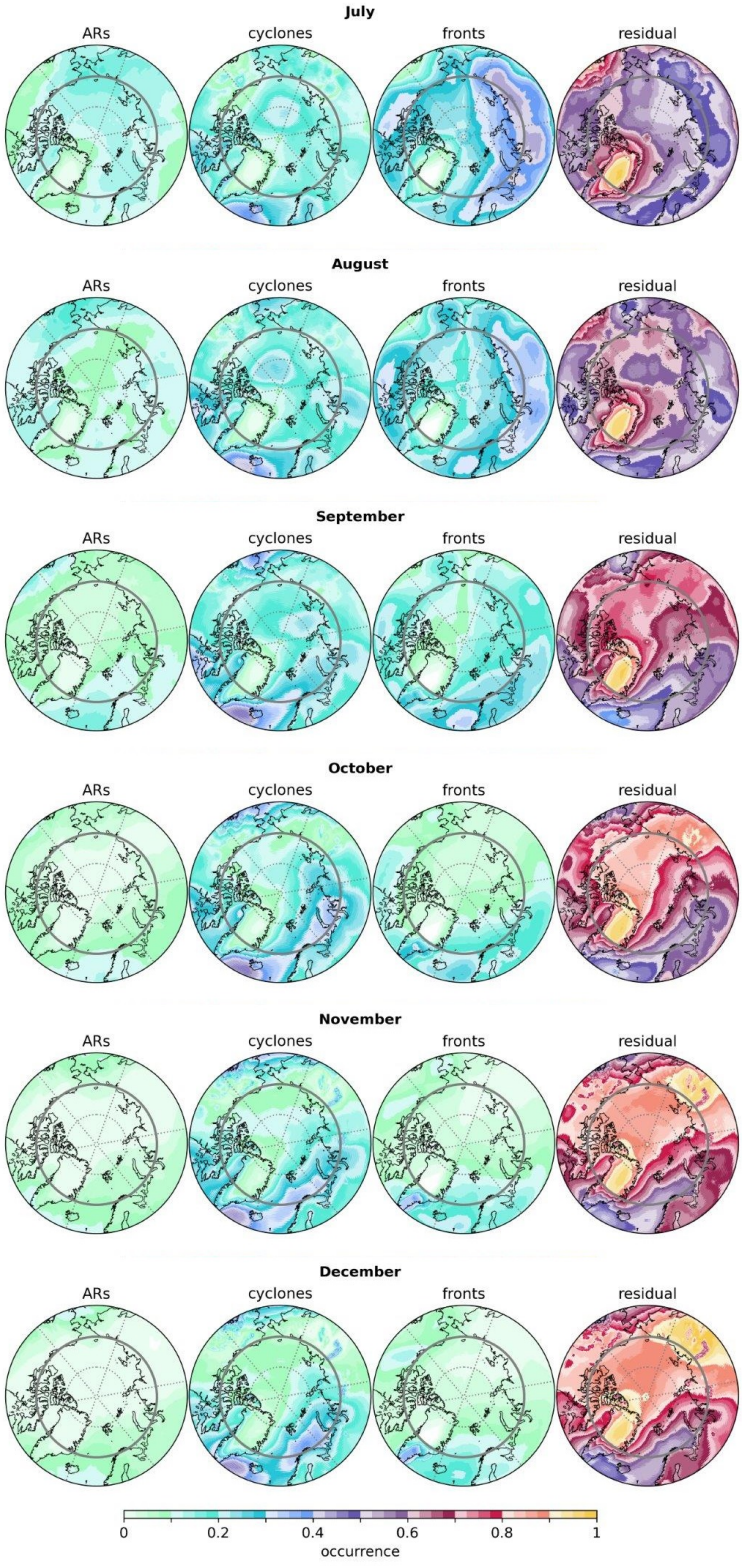

FIGURE A.7: Occurrence of ARs, cyclones, fronts, and residual from July to December.

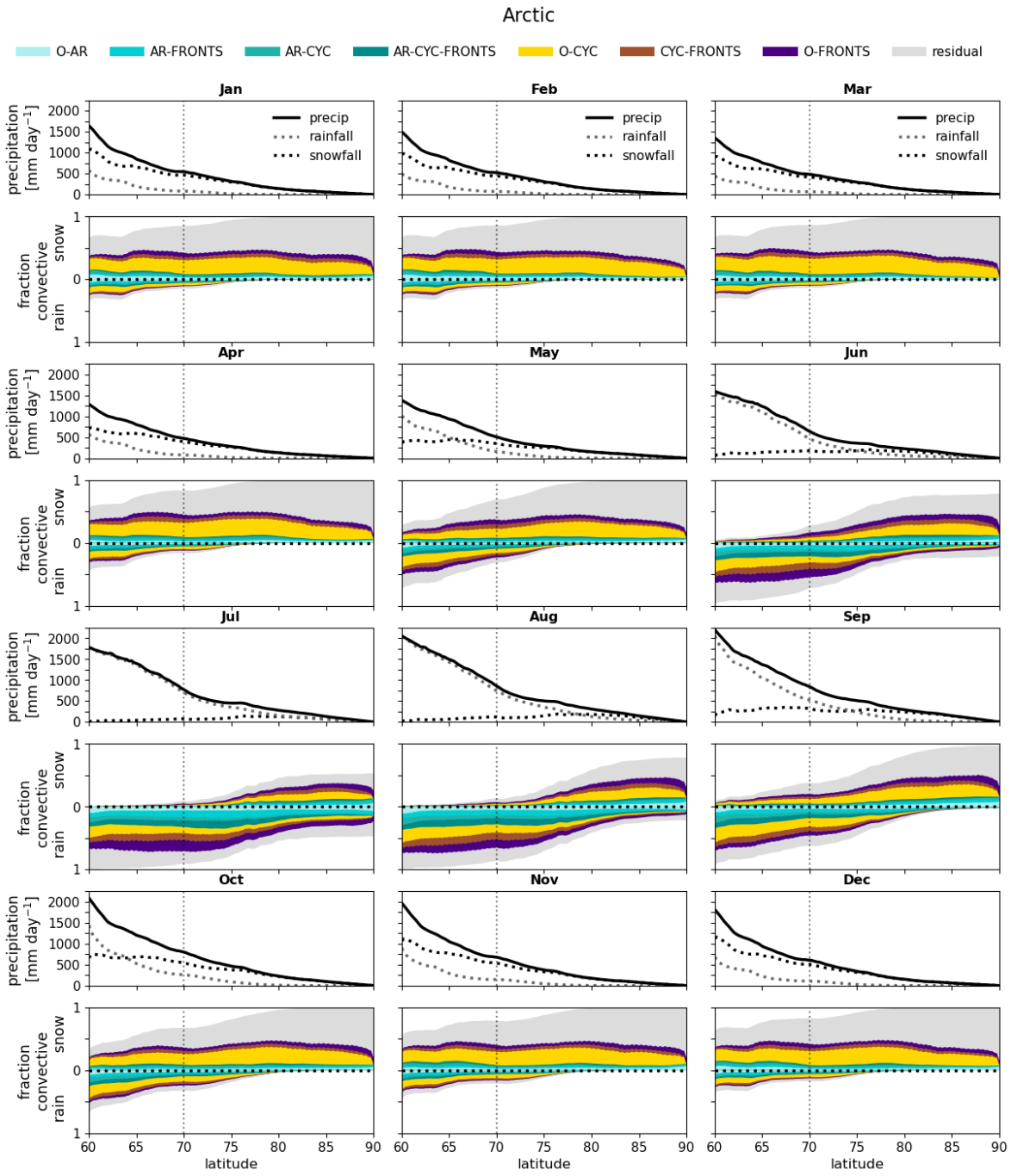

FIGURE A.8: Latitudinal dependence (60 - 90° N) of daily averaged rain (dotted) and snowfall (solid) [mm day1] for the entire Arctic from January to December. The fraction of total precipitation is shown for co-located and non-co-located components. The dashed vertical line at 70° N represents the minimum latitude that is used for all other analyses

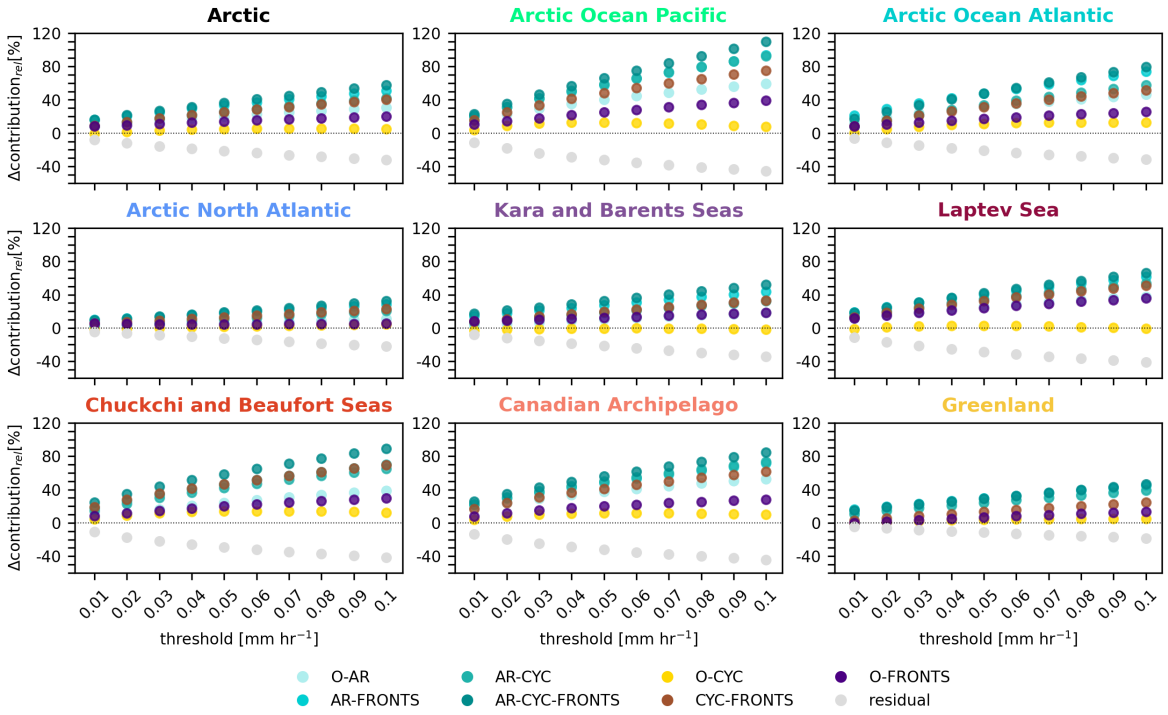

FIGURE A.9: Relative change [%] between the ARs,- cyclones-, and fronts-related precipitation with threshold and without a threshold of 0.1 mm hr^{-1}.

Bibliography

Akperov, M. G., M. Yu. Bardin, E. M. Volodin, G. S. Golitsyn, and I. I. Mokhov (2007). "Probability distributions for cyclones and anticyclones from the NCEP/NCAR reanalysis data and the INM RAS climate model". In: *Izvestiya, Atmospheric and Oceanic Physics* 43.6, pp. 705–712. ISSN: 0001-4338, 1555-628X. DOI: 10.1134/S0001433807060047. URL: http://link.springer.com/10.1134/S0001433807060047.

Akperov, Mirseid, Igor Mokhov, Annette Rinke, Klaus Dethloff, and Heidrun Matthes (2015). "Cyclones and their possible changes in the Arctic by the end of the twenty first century from regional climate model simulations". In: *Theoretical and Applied Climatology* 122.1, pp. 85–96. ISSN: 0177-798X, 1434-4483. DOI: 10.1007/s00704-014-1272-2. URL: http://link.springer.com/10.1007/s00704-014-1272-2.

Akperov, Mirseid, Annette Rinke, Igor I. Mokhov, Heidrun Matthes, Vladimir A. Semenov, Muralidhar Adakudlu, John Cassano, Jens H. Christensen, Mariya A. Dembitskaya, Klaus Dethloff, Xavier Fettweis, Justin Glisan, Oliver Gutjahr, Günther Heinemann, Torben Koenigk, Nikolay V. Koldunov, René Laprise, Ruth Mottram, Oumarou Nikiéma, John F. Scinocca, Dmitry Sein, Stefan Sobolowski, Katja Winger, and Wenxin Zhang (2018). "Cyclone Activity in the Arctic From an Ensemble of Regional Climate Models (Arctic CORDEX)". In: *Journal of Geophysical Research: Atmospheres* 123.5, pp. 2537–2554. ISSN: 2169-897X, 2169-8996. DOI: 10.1002/2017JD027703. URL: https://agupubs.onlinelibrary.wiley.com/doi/10.1002/2017JD027703.

Arrhenius, Svante (1896). "XXXI. *On the influence of carbonic acid in the air upon the temperature of the ground*". In: *The London, Edinburgh, and Dublin Philosophical Magazine and Journal of Science* 41.251, pp. 237–276. ISSN: 1941-5982, 1941-5990. DOI: 10.1080/14786449608620846. URL: https://www.tandfonline.com/doi/full/10.1080/14786449608620846.

Bao, J-W., S. A. Michelson, P. J. Neiman, F. M. Ralph, and J. M. Wilczak (2006). "Interpretation of Enhanced Integrated Water Vapor Bands Associated with Extratropical Cyclones: Their Formation and Connection to Tropical Moisture". In: *Monthly Weather Review* 134.4, pp. 1063–1080. ISSN: 1520-0493, 0027-0644. DOI: 10.1175/MWR3123.1. URL: http://journals.ametsoc.org/doi/10.1175/MWR3123.1.

Bardin, M Yu and AB Polonsky (2005). "North Atlantic oscillation and synoptic variability in the European-Atlantic region in winter". In: *Izvestiya atmospheric and oceanic physics* 41.2, pp. 127–136.

Barrett, Andrew P., Julienne C. Stroeve, and Mark C. Serreze (2020). "Arctic Ocean Precipitation From Atmospheric Reanalyses and Comparisons With North Pole Drifting Station Records". In: *Journal of Geophysical Research: Oceans* 125.1, e2019JC015415. ISSN: 2169-9275, 2169-9291. DOI: 10.1029/2019JC015415. URL: https://agupubs.onlinelibrary.wiley.com/doi/10.1029/2019JC015415.

Behrangi, Ali, Kuo-lin Hsu, Bisher Imam, Soroosh Sorooshian, George J. Huffman, and Robert J. Kuligowski (2009). "PERSIANN-MSA: A Precipitation Estimation

Method from Satellite-Based Multispectral Analysis". In: *Journal of Hydrometeorology* 10.6, pp. 1414–1429. ISSN: 1525-7541, 1525-755X. DOI: 10.1175/2009JHM1139.1. URL: http://journals.ametsoc.org/doi/10.1175/2009JHM1139.1.

Behrangi, Ali, Matthew Lebsock, Sun Wong, and Bjorn Lambrigtsen (2012). "On the quantification of oceanic rainfall using spaceborne sensors". In: *Journal of Geophysical Research: Atmospheres* 117 (D20), 2012JD017979. ISSN: 0148-0227. DOI: 10.1029/2012JD017979. URL: https://agupubs.onlinelibrary.wiley.com/doi/10.1029/2012JD017979.

Berg, Wesley, Tristan L'Ecuyer, and Christian Kummerow (2006). "Rainfall Climate Regimes: The Relationship of Regional TRMM Rainfall Biases to the Environment". In: *Journal of Applied Meteorology and Climatology* 45.3, pp. 434–454. ISSN: 1558-8432, 1558-8424. DOI: 10.1175/JAM2331.1. URL: https://journals.ametsoc.org/doi/10.1175/JAM2331.1.

Berner, Jim, Carolyn Symon, Lelani Arris, O. W. Heal, Arctic Climate Impact Assessment, National Science Foundation (U.S.), and United States, eds. (2005). *Arctic climate impact assessment*. OCLC: ocm62762748. Cambridge ; New York, N.Y: Cambridge University Press. 1042 pp. ISBN: 978-0-521-86509-8.

Berry, Gareth, Michael J. Reeder, and Christian Jakob (2011). "A global climatology of atmospheric fronts: GLOBAL CLIMATOLOGY OF ATMOSPHERIC FRONTS". In: *Geophysical Research Letters* 38.4, n/a–n/a. ISSN: 00948276. DOI: 10.1029/2010GL046451. URL: http://doi.wiley.com/10.1029/2010GL046451 (visited on 01/29/2024).

Bintanja, R. (2018). "The impact of Arctic warming on increased rainfall". In: *Scientific Reports* 8.1, p. 16001. ISSN: 2045-2322. DOI: 10.1038/s41598-018-34450-3. URL: https://www.nature.com/articles/s41598-018-34450-3.

Bintanja, R. and O. Andry (2017). "Towards a rain-dominated Arctic". In: *Nature Climate Change* 7.4, pp. 263–267. ISSN: 1758-678X, 1758-6798. DOI: 10.1038/nclimate3240. URL: https://www.nature.com/articles/nclimate3240.

Bintanja, R. and F. M. Selten (2014). "Future increases in Arctic precipitation linked to local evaporation and sea-ice retreat". In: *Nature* 509.7501, pp. 479–482. ISSN: 0028-0836, 1476-4687. DOI: 10.1038/nature13259. URL: https://www.nature.com/articles/nature13259.

Bintanja, R. and E. C. Van Der Linden (2013). "The changing seasonal climate in the Arctic". In: *Scientific Reports* 3.1, p. 1556. ISSN: 2045-2322. DOI: 10.1038/srep01556. URL: https://www.nature.com/articles/srep01556.

Bintanja, R., K. Van Der Wiel, E. C. Van Der Linden, J. Reusen, L. Bogerd, F. Krikken, and F. M. Selten (2020). "Strong future increases in Arctic precipitation variability linked to poleward moisture transport". In: *Science Advances* 6.7, eaax6869. ISSN: 2375-2548. DOI: 10.1126/sciadv.aax6869. URL: https://www.science.org/doi/10.1126/sciadv.aax6869.

Bjerknes, J. (1919). "ON THE STRUCTURE OF MOVING CYCLONES". In: *Monthly Weather Review* 47.2, pp. 95–99. ISSN: 0027-0644, 1520-0493. DOI: 10.1175/1520-0493(1919)47<95:OTSOMC>2.0.CO;2. URL: http://journals.ametsoc.org/doi/10.1175/1520-0493(1919)47<95:OTSOMC>2.0.CO;2 (visited on 01/29/2024).

Boisvert, L. N. and J. C. Stroeve (2015). "The Arctic is becoming warmer and wetter as revealed by the Atmospheric Infrared Sounder". In: *Geophysical Research Letters* 42.11, pp. 4439–4446. ISSN: 0094-8276, 1944-8007. DOI: 10.1002/2015GL063775. URL: https://agupubs.onlinelibrary.wiley.com/doi/10.1002/2015GL063775.

Boisvert, Linette, Mircea Grecu, and Chung-Lin Shie (2021). "Investigating Wintertime GPM-IMERG Precipitation in the North Atlantic". In: *Geophysical Research Letters* 48.20, e2021GL095391. ISSN: 0094-8276, 1944-8007. DOI: 10.1029/

2021GL095391. URL: https://agupubs.onlinelibrary.wiley.com/doi/10.1029/2021GL095391.

Boisvert, Linette N., Alek A. Petty, and Julienne C. Stroeve (2016). "The Impact of the Extreme Winter 2015/16 Arctic Cyclone on the Barents–Kara Seas". In: *Monthly Weather Review* 144.11, pp. 4279–4287. ISSN: 0027-0644, 1520-0493. DOI: 10.1175/MWR-D-16-0234.1. URL: https://journals.ametsoc.org/view/journals/mwre/144/11/mwr-d-16-0234.1.xml.

Boisvert, Linette N., Melinda A. Webster, Alek A. Petty, Thorsten Markus, David H. Bromwich, and Richard I. Cullather (2018). "Intercomparison of Precipitation Estimates over the Arctic Ocean and Its Peripheral Seas from Reanalyses". In: *Journal of Climate* 31.20, pp. 8441–8462. ISSN: 0894-8755, 1520-0442. DOI: 10.1175/JCLI-D-18-0125.1. URL: https://journals.ametsoc.org/doi/10.1175/JCLI-D-18-0125.1.

Bolton, David (1980). "The computation of equivalent potential temperature". In: *Monthly weather review* 108.7, pp. 1046–1053.

Box, Jason E, William T Colgan, Torben Røjle Christensen, Niels Martin Schmidt, Magnus Lund, Frans-Jan W Parmentier, Ross Brown, Uma S Bhatt, Eugénie S Euskirchen, Vladimir E Romanovsky, John E Walsh, James E Overland, Muyin Wang, Robert W Corell, Walter N Meier, Bert Wouters, Sebastian Mernild, Johanna Mård, Janet Pawlak, and Morten Skovgård Olsen (2019). "Key indicators of Arctic climate change: 1971–2017". In: *Environmental Research Letters* 14.4, p. 045010. ISSN: 1748-9326. DOI: 10.1088/1748-9326/aafc1b. URL: https://iopscience.iop.org/article/10.1088/1748-9326/aafc1b.

Box, Jason E., Kristian P. Nielsen, Xiaohua Yang, Masashi Niwano, Adrien Wehrlé, Dirk Van As, Xavier Fettweis, Morten A. Ø. Køltzow, Bolli Palmason, Robert S. Fausto, Michiel R. Van Den Broeke, Baojuan Huai, Andreas P. Ahlstrøm, Kirsty Langley, Armin Dachauer, and Brice Noël (2023). "Greenland ice sheet rainfall climatology, extremes and atmospheric river rapids". In: *Meteorological Applications* 30.4, e2134. ISSN: 1350-4827, 1469-8080. DOI: 10.1002/met.2134. URL: https://rmets.onlinelibrary.wiley.com/doi/10.1002/met.2134.

Bresson, Hélène, Annette Rinke, Mario Mech, Daniel Reinert, Vera Schemann, Kerstin Ebell, Marion Maturilli, Carolina Viceto, Irina Gorodetskaya, and Susanne Crewell (2022). "Case study of a moisture intrusion over the Arctic with the ICOsahedral Non-hydrostatic (ICON) model: resolution dependence of its representation". In: *Atmospheric Chemistry and Physics* 22.1, pp. 173–196. ISSN: 1680-7324. DOI: 10.5194/acp-22-173-2022. URL: https://acp.copernicus.org/articles/22/173/2022/.

C3S (2024). *Copernicus Climate Change Service*. https://www.climate.gov/news-features/understanding-climate/understanding-arctic-polar-vortex.

Carlson, Toby N. (1980). "Airflow Through Midlatitude Cyclones and the Comma Cloud Pattern". In: *Monthly Weather Review* 108.10, pp. 1498–1509. ISSN: 0027-0644, 1520-0493. DOI: 10.1175/1520-0493(1980)108<1498:ATMCAT>2.0.CO;2. URL: http://journals.ametsoc.org/doi/10.1175/1520-0493(1980)108<1498:ATMCAT>2.0.CO;2 (visited on 01/29/2024).

Catto, J. L., C. Jakob, G. Berry, and N. Nicholls (2012). "Relating global precipitation to atmospheric fronts". In: *Geophysical Research Letters* 39.10, 2012GL051736. ISSN: 0094-8276, 1944-8007. DOI: 10.1029/2012GL051736. URL: https://agupubs.onlinelibrary.wiley.com/doi/10.1029/2012GL051736 (visited on 01/29/2024).

Catto, J. L. and S. Pfahl (2013). "The importance of fronts for extreme precipitation". In: *Journal of Geophysical Research: Atmospheres* 118.19. ISSN: 2169-897X, 2169-8996.

DOI: 10.1002/jgrd.50852. URL: https://agupubs.onlinelibrary.wiley.com/doi/10.1002/jgrd.50852 (visited on 01/29/2024).

Catto, Jennifer L., Erica Madonna, Hanna Joos, Irina Rudeva, and Ian Simmonds (2015). "Global Relationship between Fronts and Warm Conveyor Belts and the Impact on Extreme Precipitation*". In: *Journal of Climate* 28.21, pp. 8411–8429. ISSN: 0894-8755, 1520-0442. DOI: 10.1175/JCLI-D-15-0171.1. URL: http://journals.ametsoc.org/doi/10.1175/JCLI-D-15-0171.1.

Chahine, Moustafa T. (1992). "The hydrological cycle and its influence on climate". In: *Nature* 359.6394, pp. 373–380. ISSN: 0028-0836, 1476-4687. DOI: 10.1038/359373a0. URL: https://www.nature.com/articles/359373a0.

Chang, Edmund K. M., Yanjuan Guo, and Xiaoming Xia (2012). "CMIP5 multimodel ensemble projection of storm track change under global warming". In: *Journal of Geophysical Research: Atmospheres* 117 (D23), 2012JD018578. ISSN: 0148-0227. DOI: 10.1029/2012JD018578. URL: https://agupubs.onlinelibrary.wiley.com/doi/10.1029/2012JD018578.

Cheng, Bin, Zhanhai Zhang, Timo Vihma, Milla Johansson, Lingen Bian, Zhijun Li, and Huiding Wu (2008). "Model experiments on snow and ice thermodynamics in the Arctic Ocean with CHINARE 2003 data". In: *Journal of Geophysical Research: Oceans* 113 (C9), 2007JC004654. ISSN: 0148-0227. DOI: 10.1029/2007JC004654. URL: https://agupubs.onlinelibrary.wiley.com/doi/10.1029/2007JC004654.

Cohen, Judah, James A. Screen, Jason C. Furtado, Mathew Barlow, David Whittleston, Dim Coumou, Jennifer Francis, Klaus Dethloff, Dara Entekhabi, James Overland, and Justin Jones (2014). "Recent Arctic amplification and extreme mid-latitude weather". In: *Nature Geoscience* 7.9, pp. 627–637. ISSN: 1752-0894, 1752-0908. DOI: 10.1038/ngeo2234. URL: https://www.nature.com/articles/ngeo2234.

Crawford, Alex D. and Mark C. Serreze (2017). "Projected Changes in the Arctic Frontal Zone and Summer Arctic Cyclone Activity in the CESM Large Ensemble". In: *Journal of Climate* 30.24, pp. 9847–9869. ISSN: 0894-8755, 1520-0442. DOI: 10.1175/JCLI-D-17-0296.1. URL: https://journals.ametsoc.org/doi/10.1175/JCLI-D-17-0296.1.

Cullather, Richard I. and Michael G. Bosilovich (2011). "The Moisture Budget of the Polar Atmosphere in MERRA". In: *Journal of Climate* 24.11, pp. 2861–2879. ISSN: 0894-8755, 1520-0442. DOI: 10.1175/2010JCLI4090.1. URL: http://journals.ametsoc.org/doi/10.1175/2010JCLI4090.1.

Curry, Judith A., Julie L. Schramm, William B. Rossow, and David Randall (1996). "Overview of Arctic Cloud and Radiation Characteristics". In: *Journal of Climate* 9.8, pp. 1731–1764. ISSN: 0894-8755, 1520-0442. DOI: 10.1175/1520-0442(1996)009<1731:OOACAR>2.0.CO;2. URL: http://journals.ametsoc.org/doi/10.1175/1520-0442(1996)009<1731:OOACAR>2.0.CO;2.

Dacre, H. F., P. A. Clark, O. Martinez-Alvarado, M. A. Stringer, and D. A. Lavers (2015). "How Do Atmospheric Rivers Form?" In: *Bulletin of the American Meteorological Society* 96.8, pp. 1243–1255. ISSN: 0003-0007, 1520-0477. DOI: 10.1175/BAMS-D-14-00031.1. URL: https://journals.ametsoc.org/doi/10.1175/BAMS-D-14-00031.1.

Dacre, H. F., O. Martínez-Alvarado, and C. O. Mbengue (2019). "Linking Atmospheric Rivers and Warm Conveyor Belt Airflows". In: *Journal of Hydrometeorology* 20.6, pp. 1183–1196. ISSN: 1525-755X, 1525-7541. DOI: 10.1175/JHM-D-18-0175.1. URL: http://journals.ametsoc.org/doi/10.1175/JHM-D-18-0175.1.

Dee, Dick P, S M Uppala, Adrian J Simmons, Paul Berrisford, Paul Poli, Shinya Kobayashi, U Andrae, MA Balmaseda, G Balsamo, d P Bauer, et al. (2011). "The ERA-Interim reanalysis: Configuration and performance of the data assimilation system". In: *Quarterly Journal of the royal meteorological society* 137.656, pp. 553–597.

Dettinger, Michael D., Fred Martin Ralph, Tapash Das, Paul J. Neiman, and Daniel R. Cayan (2011). "Atmospheric Rivers, Floods and the Water Resources of California". In: *Water* 3.2, pp. 445–478. ISSN: 2073-4441. DOI: 10.3390/w3020445. URL: http://www.mdpi.com/2073-4441/3/2/445.

DWD (2023). *Niederschlagsintensität*. https://www.dwd.de/DE/service/lexikon/Functions/glossar.html?lv2=101812&lv3=101906.

Ebell, Kerstin, Tatiana Nomokonova, Marion Maturilli, and Christoph Ritter (2020). "Radiative effect of clouds at Ny-Ålesund, Svalbard, as inferred from ground-based remote sensing observations". In: *Journal of Applied Meteorology and Climatology* 59.1, pp. 3–22.

Edel, L., C. Claud, C. Genthon, C. Palerme, N. Wood, T. L'Ecuyer, and D. Bromwich (2020). "Arctic Snowfall from CloudSat Observations and Reanalyses". In: *Journal of Climate* 33.6. Place: Boston MA, USA Publisher: American Meteorological Society, pp. 2093 –2109. DOI: 10.1175/JCLI-D-19-0105.1. URL: https://journals.ametsoc.org/view/journals/clim/33/6/jcli-d-19-0105.1.xml.

Ehrlich, A., M. Wendisch, C. Lüpkes, M. Buschmann, H. Bozem, D. Chechin, H.-C. Clemen, R. Dupuy, O. Eppers, J. Hartmann, A. Herber, E. Jäkel, E. Järvinen, O. Jourdan, U. Kästner, L.-L. Kliesch, F. Köllner, M. Mech, S. Mertes, R. Neuber, E. Ruiz-Donoso, M. Schnaiter, J. Schneider, J. Stapf, and M. Zanatta (2019). "A comprehensive in situ and remote sensing data set from the Arctic CLoud Observations Using airborne measurements during polar Day (ACLOUD) campaign". In: *Earth System Science Data* 11.4, pp. 1853–1881. DOI: 10.5194/essd-11-1853-2019. URL: https://essd.copernicus.org/articles/11/1853/2019/.

Eiras-Barca, Jorge, Alexandre M. Ramos, Joaquim G. Pinto, Ricardo M. Trigo, Margarida L. R. Liberato, and Gonzalo Miguez-Macho (2018). "The concurrence of atmospheric rivers and explosive cyclogenesis in the North Atlantic and North Pacific basins". In: *Earth System Dynamics* 9.1, pp. 91–102. ISSN: 2190-4987. DOI: 10.5194/esd-9-91-2018. URL: https://esd.copernicus.org/articles/9/91/2018/.

Fearon, Matthew G., James D. Doyle, David R. Ryglicki, Peter M. Finocchio, and Michael Sprenger (2021). "The Role of Cyclones in Moisture Transport into the Arctic". In: *Geophysical Research Letters* 48.4, e2020GL090353. ISSN: 0094-8276, 1944-8007. DOI: 10.1029/2020GL090353. URL: https://agupubs.onlinelibrary.wiley.com/doi/10.1029/2020GL090353.

Ferraro, Ralph R., Christa D. Peters-Lidard, Cecilia Hernandez, F. Joseph Turk, Filipe Aires, Catherine Prigent, Xin Lin, Sid-Ahmed Boukabara, Fumie A. Furuzawa, Kaushik Gopalan, Kenneth W. Harrison, Fatima Karbou, Li Li, Chuntao Liu, Hirohiko Masunaga, Leslie Moy, Sarah Ringerud, Gail M. Skofronick-Jackson, Yudong Tian, and Nai-Yu Wang (2013). "An Evaluation of Microwave Land Surface Emissivities Over the Continental United States to Benefit GPM-Era Precipitation Algorithms". In: *IEEE Transactions on Geoscience and Remote Sensing* 51.1, pp. 378–398. ISSN: 0196-2892, 1558-0644. DOI: 10.1109/TGRS.2012.2199121. URL: http://ieeexplore.ieee.org/document/6228527/.

Francis, Diana, Kyle S. Mattingly, Marouane Temimi, Rob Massom, and Petra Heil (2020). "On the crucial role of atmospheric rivers in the two major Weddell Polynya events in 1973 and 2017 in Antarctica". In: *Science Advances* 6.46, eabc2695. ISSN:

2375-2548. DOI: 10.1126/sciadv.abc2695. URL: https://www.science.org/doi/10.1126/sciadv.abc2695.

Francis, Jennifer A. and Elias Hunter (2007). "Drivers of declining sea ice in the Arctic winter: A tale of two seas". In: *Geophysical Research Letters* 34.17, 2007GL030995. ISSN: 0094-8276, 1944-8007. DOI: 10.1029/2007GL030995. URL: https://agupubs.onlinelibrary.wiley.com/doi/10.1029/2007GL030995.

Fuchs, T., J. Rapp, F. Rubel, and B. Rudolf (2001). "Correction of synoptic precipitation observations due to systematic measuring errors with special regard to precipitation phases". In: *Physics and Chemistry of the Earth, Part B: Hydrology, Oceans and Atmosphere* 26.9, pp. 689–693. ISSN: 14641909. DOI: 10.1016/S1464-1909(01)00070-3. URL: https://linkinghub.elsevier.com/retrieve/pii/S1464190901000703.

Gierens, Rosa, Stefan Kneifel, Matthew D Shupe, Kerstin Ebell, Marion Maturilli, and Ulrich Löhnert (2020). "Low-level mixed-phase clouds in a complex Arctic environment". In: *Atmospheric Chemistry and Physics* 20.6, pp. 3459–3481.

Gimeno, L., M. Vázquez, R. Nieto, and R. M. Trigo (2015). "Atmospheric moisture transport: the bridge between ocean evaporation and Arctic ice melting". In: *Earth System Dynamics* 6.2, pp. 583–589. ISSN: 2190-4987. DOI: 10.5194/esd-6-583-2015. URL: https://esd.copernicus.org/articles/6/583/2015/.

Gimeno, Luis, Francina Dominguez, Raquel Nieto, Ricardo Trigo, Anita Drumond, Chris J.C. Reason, Andréa S. Taschetto, Alexandre M. Ramos, Ramesh Kumar, and José Marengo (2016). "Major Mechanisms of Atmospheric Moisture Transport and Their Role in Extreme Precipitation Events". In: *Annual Review of Environment and Resources* 41.1, pp. 117–141. ISSN: 1543-5938, 1545-2050. DOI: 10.1146/annurev-environ-110615-085558. URL: https://www.annualreviews.org/doi/10.1146/annurev-environ-110615-085558.

Gimeno, Luis, Marta Vázquez, Jorge Eiras-Barca, Rogert Sorí, Iago Algarra, and Raquel Nieto (2019). "Atmospheric moisture transport and the decline in Arctic Sea ice". In: *WIREs Climate Change* 10.4, e588. ISSN: 1757-7780, 1757-7799. DOI: 10.1002/wcc.588. URL: https://wires.onlinelibrary.wiley.com/doi/10.1002/wcc.588 (visited on 01/29/2024).

Gimeno-Sotelo, Luis, Raquel Nieto, Marta Vázquez, and Luis Gimeno (2018). "A new pattern of the moisture transport for precipitation related to the drastic decline in Arctic sea ice extent". In: *Earth System Dynamics* 9.2, pp. 611–625. ISSN: 2190-4987. DOI: 10.5194/esd-9-611-2018. URL: https://esd.copernicus.org/articles/9/611/2018/.

— (2019). "The role of moisture transport for precipitation in the inter-annual and inter-daily fluctuations of the Arctic sea ice extension". In: *Earth System Dynamics* 10.1, pp. 121–133. ISSN: 2190-4987. DOI: 10.5194/esd-10-121-2019. URL: https://esd.copernicus.org/articles/10/121/2019/.

Gong, Tingting, Steven Feldstein, and Sukyoung Lee (2017). "The Role of Downward Infrared Radiation in the Recent Arctic Winter Warming Trend". In: *Journal of Climate* 30.13, pp. 4937–4949. ISSN: 0894-8755, 1520-0442. DOI: 10.1175/JCLI-D-16-0180.1. URL: https://journals.ametsoc.org/doi/10.1175/JCLI-D-16-0180.1.

Gorodetskaya, Irina V., Tiago Silva, Holger Schmithüsen, and Naohiko Hirasawa (2020). "Atmospheric River Signatures in Radiosonde Profiles and Reanalyses at the Dronning Maud Land Coast, East Antarctica". In: *Advances in Atmospheric Sciences* 37.5, pp. 455–476. ISSN: 0256-1530, 1861-9533. DOI: 10.1007/s00376-020-9221-8. URL: https://link.springer.com/10.1007/s00376-020-9221-8.

Gorodetskaya, Irina V., Maria Tsukernik, Kim Claes, Martin F. Ralph, William D. Neff, and Nicole P. M. Van Lipzig (2014). "The role of atmospheric rivers in anomalous snow accumulation in East Antarctica". In: *Geophysical Research Letters* 41.17, pp. 6199–6206. ISSN: 0094-8276, 1944-8007. DOI: 10.1002/2014GL060881. URL: https://agupubs.onlinelibrary.wiley.com/doi/10.1002/2014GL060881.

Graham, Robert M., Lana Cohen, Nicole Ritzhaupt, Benjamin Segger, Rune G. Graversen, Annette Rinke, Von P. Walden, Mats A. Granskog, and Stephen R. Hudson (2019a). "Evaluation of Six Atmospheric Reanalyses over Arctic Sea Ice from Winter to Early Summer". In: *Journal of Climate* 32.14, pp. 4121–4143. ISSN: 0894-8755, 1520-0442. DOI: 10.1175/JCLI-D-18-0643.1. URL: https://journals.ametsoc.org/view/journals/clim/32/14/jcli-d-18-0643.1.xml (visited on 01/31/2024).

Graham, Robert M., Polona Itkin, Amelie Meyer, Arild Sundfjord, Gunnar Spreen, Lars H. Smedsrud, Glen E. Liston, Bin Cheng, Lana Cohen, Dmitry Divine, Ilker Fer, Agneta Fransson, Sebastian Gerland, Jari Haapala, Stephen R. Hudson, A. Malin Johansson, Jennifer King, Ioanna Merkouriadi, Algot K. Peterson, Christine Provost, Achim Randelhoff, Annette Rinke, Anja Rösel, Nathalie Sennéchael, Von P. Walden, Pedro Duarte, Philipp Assmy, Harald Steen, and Mats A. Granskog (2019b). "Winter storms accelerate the demise of sea ice in the Atlantic sector of the Arctic Ocean". In: *Scientific Reports* 9.1, p. 9222. ISSN: 2045-2322. DOI: 10.1038/s41598-019-45574-5. URL: https://www.nature.com/articles/s41598-019-45574-5.

Graversen, Rune G., Thorsten Mauritsen, Michael Tjernström, Erland Källén, and Gunilla Svensson (2008). "Vertical structure of recent Arctic warming". In: *Nature* 451.7174, pp. 53–56. ISSN: 0028-0836, 1476-4687. DOI: 10.1038/nature06502. URL: https://www.nature.com/articles/nature06502.

Guan, Bin and Duane E. Waliser (2015a). "Detection of atmospheric rivers: Evaluation and application of an algorithm for global studies". In: *Journal of Geophysical Research: Atmospheres* 120.24, pp. 12514–12535. ISSN: 2169-897X, 2169-8996. DOI: 10.1002/2015JD024257. URL: https://agupubs.onlinelibrary.wiley.com/doi/10.1002/2015JD024257.

— (2015b). "Detection of atmospheric rivers: Evaluation and application of an algorithm for global studies". In: *Journal of Geophysical Research: Atmospheres* 120.24, pp. 12514–12535. ISSN: 2169-897X, 2169-8996. DOI: 10.1002/2015JD024257. URL: https://agupubs.onlinelibrary.wiley.com/doi/10.1002/2015JD024257.

Guan, Bin, Duane E. Waliser, and F. Martin Ralph (2018). "An Intercomparison between Reanalysis and Dropsonde Observations of the Total Water Vapor Transport in Individual Atmospheric Rivers". In: *Journal of Hydrometeorology* 19.2, pp. 321–337. ISSN: 1525-755X, 1525-7541. DOI: 10.1175/JHM-D-17-0114.1. URL: http://journals.ametsoc.org/doi/10.1175/JHM-D-17-0114.1.

Guo, Yanjuan, Toshiaki Shinoda, Bin Guan, Duane E. Waliser, and Edmund K. M. Chang (2020). "Statistical Relationship between Atmospheric Rivers and Extratropical Cyclones and Anticyclones". In: *Journal of Climate* 33.18, pp. 7817–7834. ISSN: 0894-8755, 1520-0442. DOI: 10.1175/JCLI-D-19-0126.1. URL: https://journals.ametsoc.org/view/journals/clim/33/18/jcliD190126.xml.

Haynes, John M, Tristan S L'Ecuyer, Graeme L Stephens, Steven D Miller, Cristian Mitrescu, Norman B Wood, and Simone Tanelli (2009). "Rainfall retrieval over the ocean with spaceborne W-band radar". In: *Journal of Geophysical Research: Atmospheres* 114.D8.

Hegyi, Bradley M. and Patrick C. Taylor (2018). "The Unprecedented 2016–2017 Arctic Sea Ice Growth Season: The Crucial Role of Atmospheric Rivers and Longwave Fluxes". In: *Geophysical Research Letters* 45.10, pp. 5204–5212. ISSN: 0094-8276, 1944-8007. DOI: 10.1029/2017GL076717. URL: https://agupubs.onlinelibrary.wiley.com/doi/10.1029/2017GL076717.

Henry, Alfred J. (1922). "J. BJERKNES AND H. SOLBERG ON THE LIFE CYCLE OF CYCLONES AND THE POLAR FRONT THEORY OF ATMOSPHERIC CIRCULATION [1]". In: *Monthly Weather Review* 50.9, pp. 468–473. ISSN: 0027-0644, 1520-0493. DOI: 10.1175/1520-0493(1922)50<468:JBAHSO>2.0.CO;2. URL: http://journals.ametsoc.org/doi/10.1175/1520-0493(1922)50<468:JBAHSO>2.0.CO;2.

Hersbach, Hans, Bill Bell, Paul Berrisford, Gionata Biavati, András Horányi, Joaquín Muñoz Sabater, Julien Nicolas, Carole Peubey, Raluca Radu, Iryna Rozum, et al. (2018). "ERA5 hourly data on pressure levels from 1979 to present". In: *Copernicus climate change service (c3s) climate data store (cds)* 10.10.24381.

Hersbach, Hans, Bill Bell, Paul Berrisford, Shoji Hirahara, Andras Horanyi, Joaquin Munoz-Sabater, Julien Nicolas, Carole Peubey, Raluca Radu, Dinand Schepers, Adrian Simmons, Cornel Soci, Saleh Abdalla, Xavier Abellan, Gianpaolo Balsamo, Peter Bechtold, Gionata Biavati, Jean Bidlot, Massimo Bonavita, Giovanna De Chiara, Per Dahlgren, Dick Dee, Michail Diamantakis, Rossana Dragani, Johannes Flemming, Richard Forbes, Manuel Fuentes, Alan Geer, Leo Haimberger, Sean Healy, Robin J. Hogan, Elias Holm, Marta Janiskova, Sarah Keeley, Patrick Laloyaux, Philippe Lopez, Cristina Lupu, Gabor Radnoti, Patricia de Rosnay, Iryna Rozum, Freja Vamborg, Sebastien Villaume, and Jean-Noel Thepaut (2020a). "The ERA5 global reanalysis". In: *QUARTERLY JOURNAL OF THE ROYAL METEOROLOGICAL SOCIETY* 146.730, pp. 1999–2049. ISSN: 0035-9009. DOI: 10.1002/qj.3803.

Hersbach, Hans, Bill Bell, Paul Berrisford, Shoji Hirahara, András Horányi, Joaquín Muñoz-Sabater, Julien Nicolas, Carole Peubey, Raluca Radu, Dinand Schepers, Adrian Simmons, Cornel Soci, Saleh Abdalla, Xavier Abellan, Gianpaolo Balsamo, Peter Bechtold, Gionata Biavati, Jean Bidlot, Massimo Bonavita, Giovanna De Chiara, Per Dahlgren, Dick Dee, Michail Diamantakis, Rossana Dragani, Johannes Flemming, Richard Forbes, Manuel Fuentes, Alan Geer, Leo Haimberger, Sean Healy, Robin J. Hogan, Elías Hólm, Marta Janisková, Sarah Keeley, Patrick Laloyaux, Philippe Lopez, Cristina Lupu, Gabor Radnoti, Patricia De Rosnay, Iryna Rozum, Freja Vamborg, Sebastien Villaume, and Jean-Noël Thépaut (2020b). "The ERA5 global reanalysis". In: *Quarterly Journal of the Royal Meteorological Society* 146.730, pp. 1999–2049. ISSN: 0035-9009, 1477-870X. DOI: 10.1002/qj.3803. URL: https://rmets.onlinelibrary.wiley.com/doi/10.1002/qj.3803.

Hewson, T D (1998). "Objective fronts". In: *Meteorological Applications* 5.1, pp. 37–65. ISSN: 1350-4827, 1469-8080. DOI: 10.1017/S1350482798000553. URL: https://rmets.onlinelibrary.wiley.com/doi/10.1017/S1350482798000553 (visited on 01/29/2024).

Hogan, Robin J and Christopher D Westbrook (2014). "Equation for the microwave backscatter cross section of aggregate snowflakes using the self-similar Rayleigh–Gans approximation". In: *Journal of the Atmospheric Sciences* 71.9, pp. 3292–3301.

Hu, Huancui and Francina Dominguez (2019). "Understanding the Role of Tropical Moisture in Atmospheric Rivers". In: *Journal of Geophysical Research: Atmospheres* 124.24, pp. 13826–13842. ISSN: 2169-897X, 2169-8996. DOI: 10.1029/2019JD030867. URL: https://agupubs.onlinelibrary.wiley.com/doi/10.1029/2019JD030867.

Hénin, Riccardo, Alexandre M. Ramos, Sebastian Schemm, Célia M. Gouveia, and Margarida L. R. Liberato (2019). "Assigning precipitation to mid-latitudes fronts on sub-daily scales in the North Atlantic and European sector: Climatology and trends". In: *International Journal of Climatology* 39.1, pp. 317–330. ISSN: 0899-8418, 1097-0088. DOI: 10.1002/joc.5808. URL: https://rmets.onlinelibrary.wiley.com/doi/10.1002/joc.5808 (visited on 01/29/2024).

Imura, Yuki and Takuro Michibata (2022). "Too Frequent and Too Light Arctic Snowfall With Incorrect Precipitation Phase Partitioning in the MIROC6 GCM". In: *Journal of Advances in Modeling Earth Systems* 14.12, e2022MS003046. ISSN: 1942-2466, 1942-2466. DOI: 10.1029/2022MS003046. URL: https://agupubs.onlinelibrary.wiley.com/doi/10.1029/2022MS003046.

Jeffries, Martin O., James E. Overland, and Donald K. Perovich (2013). "The Arctic shifts to a new normal". In: *Physics Today* 66.10, pp. 35–40. ISSN: 0031-9228, 1945-0699. DOI: 10.1063/PT.3.2147. URL: https://pubs.aip.org/physicstoday/article/66/10/35/414218/The-Arctic-shifts-to-a-new-normalThinning-sea-ice.

Jenkner, J., M. Sprenger, I. Schwenk, C. Schwierz, S. Dierer, and D. Leuenberger (2010). "Detection and climatology of fronts in a high-resolution model reanalysis over the Alps". In: *Meteorological Applications* 17.1, pp. 1–18. ISSN: 1350-4827, 1469-8080. DOI: 10.1002/met.142. URL: https://rmets.onlinelibrary.wiley.com/doi/10.1002/met.142.

Kašpar, M (2003). "Objective frontal analysis techniques applied to extreme/non-extreme precipitation events". In: *Studia Geophysica et Geodaetica* 47, pp. 605–631.

Kim, Hye-Mi and Baek-Min Kim (2017). "Relative Contributions of Atmospheric Energy Transport and Sea Ice Loss to the Recent Warm Arctic Winter". In: *Journal of Climate* 30.18, pp. 7441–7450. ISSN: 0894-8755, 1520-0442. DOI: 10.1175/JCLI-D-17-0157.1. URL: http://journals.ametsoc.org/doi/10.1175/JCLI-D-17-0157.1.

Kim, Kwang-Yul, Benjamin D. Hamlington, Hanna Na, and Jinju Kim (2016). "Mechanism of seasonal Arctic sea ice evolution and Arctic amplification". In: *The Cryosphere* 10.5, pp. 2191–2202. ISSN: 1994-0424. DOI: 10.5194/tc-10-2191-2016. URL: https://tc.copernicus.org/articles/10/2191/2016/.

Kirbus, Benjamin, Jan Chylik, André Ehrlich, Sebastian Becker, Michael Schäfer, Roel Neggers, and Manfred Wendisch (2023). "Analysis of an Arctic cold air outbreak during autumn and related air mass transformations forced by surface changes and advection in higher altitudes". In: *Elementa: Science of the Anthropocene* 11.1.

Knippertz, Peter and Heini Wernli (2010). "A Lagrangian Climatology of Tropical Moisture Exports to the Northern Hemispheric Extratropics". In: *Journal of Climate* 23.4, pp. 987–1003. ISSN: 1520-0442, 0894-8755. DOI: 10.1175/2009JCLI3333.1. URL: http://journals.ametsoc.org/doi/10.1175/2009JCLI3333.1.

Knudsen, Erlend M, Bernd Heinold, Sandro Dahlke, Heiko Bozem, Susanne Crewell, Georg Heygster, Daniel Kunkel, Marion Maturilli, Mario Mech, Annette Rinke, et al. (2018). "Synoptic development during the ACLOUD/PASCAL field campaign near Svalbard in spring 2017". In: *Atmos. Chem. Phys. Discuss., https://doi.org/10.5194/acp-2018-494* 5.

Komatsu, Kensuke K., Vladimir A. Alexeev, Irina A. Repina, and Yoshihiro Tachibana (2018). "Poleward upgliding Siberian atmospheric rivers over sea ice heat up Arctic upper air". In: *Scientific Reports* 8.1, p. 2872. ISSN: 2045-2322. DOI: 10.1038/s41598-018-21159-6. URL: https://www.nature.com/articles/s41598-018-21159-6.

Kulie, Mark S. and Ralf Bennartz (Dec. 2009). "Utilizing Spaceborne Radars to Retrieve Dry Snowfall". EN. In: *Journal of Applied Meteorology and Climatology* 48.12. Publisher: American Meteorological Society Section: Journal of Applied Meteorology and Climatology, pp. 2564–2580. ISSN: 1558-8424, 1558-8432. DOI: 10.1175/2009JAMC2193.1. URL: https://journals.ametsoc.org/view/journals/apme/48/12/2009jamc2193.1.xml (visited on 10/10/2022).

Küchler, Nils, Stefan Kneifel, Ulrich Löhnert, Pavlos Kollias, Harald Czekala, and Thomas Rose (Nov. 2017). "A W-Band Radar–Radiometer System for Accurate and Continuous Monitoring of Clouds and Precipitation". en. In: *Journal of Atmospheric and Oceanic Technology* 34.11, pp. 2375–2392. ISSN: 0739-0572, 1520-0426. DOI: 10.1175/JTECH-D-17-0019.1. URL: https://journals.ametsoc.org/view/journals/atot/34/11/jtech-d-17-0019.1.xml (visited on 03/08/2022).

Lauer, Melanie (2023a). *Animation ARs during ACLOUD and AFLUX*. https://av.tib.eu/media/62348. DOI: 10.5446/62348and10.5446/62349.

— (2023b). "ARs ACLOUD". In: Publisher: Copernicus Publications. DOI: 10.5446/62348. URL: https://av.tib.eu/media/62348.

Lauer, Melanie, Mario Mech, and Bin Guan (2023a). *Global Atmospheric Rivers catalog for ERA5 reanalysis*. Artwork Size: 129 data points Pages: 129 data points. DOI: 10.1594/PANGAEA.957161. URL: https://doi.pangaea.de/10.1594/PANGAEA.957161.

Lauer, Melanie, Annette Rinke, Irina Gorodetskaya, Michael Sprenger, Mario Mech, and Susanne Crewell (2023b). "Influence of atmospheric rivers and associated weather systems on precipitation in the Arctic". In: *Atmospheric Chemistry and Physics* 23.15, pp. 8705–8726. ISSN: 1680-7324. DOI: 10.5194/acp-23-8705-2023. URL: https://acp.copernicus.org/articles/23/8705/2023/ (visited on 02/04/2024).

Lavers, David A, Richard P Allan, Gabriele Villarini, Benjamin Lloyd-Hughes, David J Brayshaw, and Andrew J Wade (2013). "Future changes in atmospheric rivers and their implications for winter flooding in Britain". In: *Environmental Research Letters* 8.3, p. 034010. ISSN: 1748-9326. DOI: 10.1088/1748-9326/8/3/034010. URL: https://iopscience.iop.org/article/10.1088/1748-9326/8/3/034010.

Lavers, David A, Adrian Simmons, Freja Vamborg, and Mark J Rodwell (2022). "An evaluation of ERA5 precipitation for climate monitoring". In: *Quarterly Journal of the Royal Meteorological Society* 148.748, pp. 3152–3165.

Lavers, David A. and Gabriele Villarini (2015). "The contribution of atmospheric rivers to precipitation in Europe and the United States". In: *Journal of Hydrology* 522, pp. 382–390. ISSN: 00221694. DOI: 10.1016/j.jhydrol.2014.12.010. URL: https://linkinghub.elsevier.com/retrieve/pii/S0022169414010208.

Lebsock, Matthew D. and Tristan S. L'Ecuyer (2011). "The retrieval of warm rain from CloudSat". In: *Journal of Geophysical Research* 116 (D20), p. D20209. ISSN: 0148-0227. DOI: 10.1029/2011JD016076. URL: http://doi.wiley.com/10.1029/2011JD016076.

Leppäranta, Matti (1993). "A review of analytical models of sea-ice growth". In: *Atmosphere-Ocean* 31.1, pp. 123–138. ISSN: 0705-5900, 1480-9214. DOI: 10.1080/07055900.1993.9649465. URL: http://www.tandfonline.com/doi/abs/10.1080/07055900.1993.9649465.

Lerber, Annakaisa von, Mario Mech, Annette Rinke, Damao Zhang, Melanie Lauer, Ana Radovan, Irina Gorodetskaya, and Susanne Crewell (2022). "Evaluating seasonal and regional distribution of snowfall in regional climate model simulations in the Arctic". In: *Atmospheric Chemistry and Physics Discussions* 2022, pp. 1–44.

Leung, L. Ruby and Yun Qian (2009). "Atmospheric rivers induced heavy precipitation and flooding in the western U.S. simulated by the WRF regional climate model". In: *Geophysical Research Letters* 36.3, 2008GL036445. ISSN: 0094-8276, 1944-8007. DOI: 10.1029/2008GL036445. URL: https://agupubs.onlinelibrary.wiley.com/doi/10.1029/2008GL036445.

Li, Linghan, Forest Cannon, Matthew R Mazloff, Aneesh C Subramanian, Anna M Wilson, and F Martin Ralph (2022). "Impact of atmospheric rivers on arctic sea ice variations". In: *EGUsphere* 2022, pp. 1–21.

Liu, Chengji and Elizabeth A. Barnes (2015). "Extreme moisture transport into the Arctic linked to Rossby wave breaking". In: *Journal of Geophysical Research: Atmospheres* 120.9, pp. 3774–3788. ISSN: 2169-897X, 2169-8996. DOI: 10.1002/2014JD022796. URL: https://agupubs.onlinelibrary.wiley.com/doi/10.1002/2014JD022796.

Liu, Guosheng (2008). "Deriving snow cloud characteristics from CloudSat observations". In: *Journal of Geophysical Research: Atmospheres* 113 (D8), 2007JD009766. ISSN: 0148-0227. DOI: 10.1029/2007JD009766. URL: https://agupubs.onlinelibrary.wiley.com/doi/10.1029/2007JD009766.

Luo, Dehai, Yiqing Xiao, Yao Yao, Aiguo Dai, Ian Simmonds, and Christian L. E. Franzke (2016). "Impact of Ural Blocking on Winter Warm Arctic–Cold Eurasian Anomalies. Part I: Blocking-Induced Amplification". In: *Journal of Climate* 29.11, pp. 3925–3947. ISSN: 0894-8755, 1520-0442. DOI: 10.1175/JCLI-D-15-0611.1. URL: https://journals.ametsoc.org/view/journals/clim/29/11/jcli-d-15-0611.1.xml.

Maahn, Maximilian, Clara Burgard, Susanne Crewell, Irina V Gorodetskaya, Stefan Kneifel, Stef Lhermitte, Kristof Van Tricht, and Nicole PM van Lipzig (2014). "How does the spaceborne radar blind zone affect derived surface snowfall statistics in polar regions?" In: *Journal of Geophysical Research: Atmospheres* 119.24, pp. 13–604.

Mann, Henry B (1945). "Nonparametric tests against trend". In: *Econometrica: Journal of the econometric society*, pp. 245–259.

Marchand, Roger (2018). "Product: 2B-GEOPROF Product Version: P1_R05". en. In: p. 27.

Mateling, Marian E., Claire Pettersen, Mark S. Kulie, and Tristan S. L'Ecuyer (2023). "Marine Cold-Air Outbreak Snowfall in the North Atlantic: A CloudSat Perspective". In: *Journal of Geophysical Research: Atmospheres* 128.10, e2022JD038053. ISSN: 2169-897X, 2169-8996. DOI: 10.1029/2022JD038053. URL: https://agupubs.onlinelibrary.wiley.com/doi/10.1029/2022JD038053 (visited on 02/03/2024).

Matrosov, Sergey Y, Matthew D Shupe, and Taneil Uttal (2022). "High temporal resolution estimates of Arctic snowfall rates emphasizing gauge and radar-based retrievals from the MOSAiC expedition". In: *Elem Sci Anth* 10.1, p. 00101.

Mattingly, K. S., T. L. Mote, and X. Fettweis (2018). "Atmospheric River Impacts on Greenland Ice Sheet Surface Mass Balance". In: *Journal of Geophysical Research: Atmospheres* 123.16, pp. 8538–8560. ISSN: 2169-897X, 2169-8996. DOI: 10.1029/2018JD028714. URL: https://agupubs.onlinelibrary.wiley.com/doi/10.1029/2018JD028714.

Mattingly, Kyle S., Thomas L. Mote, Xavier Fettweis, Dirk Van As, Kristof Van Tricht, Stef Lhermitte, Claire Pettersen, and Robert S. Fausto (2020). "Strong Summer Atmospheric Rivers Trigger Greenland Ice Sheet Melt through Spatially Varying Surface Energy Balance and Cloud Regimes". In: *Journal of Climate* 33.16, pp. 6809–6832. ISSN: 0894-8755, 1520-0442. DOI: 10.1175/JCLI-D-19-0835.1. URL: https://journals.ametsoc.org/doi/10.1175/JCLI-D-19-0835.1.

Mayer, Michael, Steffen Tietsche, Leopold Haimberger, Takamasa Tsubouchi, Johannes Mayer, and Hao Zuo (2019). "An improved estimate of the coupled Arctic energy budget". In: *Journal of Climate* 32.22, pp. 7915–7934.

McCrystall, Michelle R., Julienne Stroeve, Mark Serreze, Bruce C. Forbes, and James A. Screen (2021). "New climate models reveal faster and larger increases in Arctic precipitation than previously projected". In: *Nature Communications* 12.1, p. 6765. ISSN: 2041-1723. DOI: 10.1038/s41467-021-27031-y. URL: https://www.nature.com/articles/s41467-021-27031-y.

Mech, Mario, André Ehrlich, Andreas Herber, Christof Lüpkes, Manfred Wendisch, Sebastian Becker, Yvonne Boose, Dmitry Chechin, Susanne Crewell, Régis Dupuy, Christophe Gourbeyre, Jörg Hartmann, Evelyn Jäkel, Olivier Jourdan, Leif-Leonard Kliesch, Marcus Klingebiel, Birte Solveig Kulla, Guillaume Mioche, Manuel Moser, Nils Risse, Elena Ruiz-Donoso, Michael Schäfer, Johannes Stapf, and Christiane Voigt (2022). "MOSAiC-ACA and AFLUX - Arctic airborne campaigns characterizing the exit area of MOSAiC". In: *Scientific Data* 9.1, p. 790. ISSN: 2052-4463. DOI: 10.1038/s41597-022-01900-7. URL: https://www.nature.com/articles/s41597-022-01900-7.

Mech, Mario, Maximilian Maahn, Stefan Kneifel, Davide Ori, Emiliano Orlandi, Pavlos Kollias, Vera Schemann, and Susanne Crewell (Sept. 2020). "PAMTRA 1.0: the Passive and Active Microwave radiative TRAnsfer tool for simulating radiometer and radar measurements of the cloudy atmosphere". en. In: *Geoscientific Model Development* 13.9, pp. 4229–4251. ISSN: 1991-9603. DOI: 10.5194/gmd-13-4229-2020. URL: https://gmd.copernicus.org/articles/13/4229/2020/ (visited on 03/08/2022).

Merkouriadi, Ioanna, Bin Cheng, Robert M. Graham, Anja Rösel, and Mats A. Granskog (2017). "Critical Role of Snow on Sea Ice Growth in the Atlantic Sector of the Arctic Ocean". In: *Geophysical Research Letters* 44.20. ISSN: 0094-8276, 1944-8007. DOI: 10.1002/2017GL075494. URL: https://agupubs.onlinelibrary.wiley.com/doi/10.1002/2017GL075494.

Mitrescu, Cristian, Tristan L'Ecuyer, John Haynes, Steven Miller, and Joseph Turk (2010). "CloudSat precipitation profiling algorithm—Model description". In: *Journal of Applied Meteorology and Climatology* 49.5, pp. 991–1003.

Mo, Ruping (2022). "Prequel to the Stories of Warm Conveyor Belts and Atmospheric Rivers: The Moist Tongues Identified by Rossby and His Collaborators in the 1930s". In: *Bulletin of the American Meteorological Society* 103.4, E1019–E1040. ISSN: 0003-0007, 1520-0477. DOI: 10.1175/BAMS-D-20-0276.1. URL: https://journals.ametsoc.org/view/journals/bams/103/4/BAMS-D-20-0276.1.xml.

Naakka, Tuomas, Tiina Nygård, Timo Vihma, Joseph Sedlar, and Rune Graversen (2019). "Atmospheric moisture transport between mid-latitudes and the Arctic: Regional, seasonal and vertical distributions". In: *International Journal of Climatology* 39.6, pp. 2862–2879. ISSN: 0899-8418, 1097-0088. DOI: 10.1002/joc.5988. URL: https://rmets.onlinelibrary.wiley.com/doi/10.1002/joc.5988.

Nash, Deanna, Duane Waliser, Bin Guan, Hengchun Ye, and F. Martin Ralph (2018). "The Role of Atmospheric Rivers in Extratropical and Polar Hydroclimate". In: *Journal of Geophysical Research: Atmospheres* 123.13, pp. 6804–6821. ISSN: 2169-897X, 2169-8996. DOI: 10.1029/2017JD028130. URL: https://agupubs.onlinelibrary.wiley.com/doi/10.1029/2017JD028130.

Neff, William (2018). "Atmospheric rivers melt Greenland". In: *Nature Climate Change* 8.10, pp. 857–858. ISSN: 1758-678X, 1758-6798. DOI: 10.1038/s41558-018-0297-4. URL: https://www.nature.com/articles/s41558-018-0297-4.

Neff, William, Gilbert P. Compo, F. Martin Ralph, and Matthew D. Shupe (2014). "Continental heat anomalies and the extreme melting of the Greenland ice surface in 2012 and 1889". In: *Journal of Geophysical Research: Atmospheres* 119.11, pp. 6520–6536. ISSN: 2169-897X, 2169-8996. DOI: 10.1002/2014JD021470. URL: https://agupubs.onlinelibrary.wiley.com/doi/10.1002/2014JD021470.

Newell, Reginald E., Nicholas E. Newell, Yong Zhu, and Courtney Scott (1992). "Tropospheric rivers? – A pilot study". In: *Geophysical Research Letters* 19.24, pp. 2401–2404. ISSN: 0094-8276, 1944-8007. DOI: 10.1029/92GL02916. URL: https://agupubs.onlinelibrary.wiley.com/doi/10.1029/92GL02916.

Niebler, Stefan, Annette Miltenberger, Bertil Schmidt, and Peter Spichtinger (2022). "Automated detection and classification of synoptic-scale fronts from atmospheric data grids". In: *Weather and Climate Dynamics* 3.1, pp. 113–137. ISSN: 2698-4016. DOI: 10.5194/wcd-3-113-2022. URL: https://wcd.copernicus.org/articles/3/113/2022/ (visited on 01/29/2024).

NOAA (2024). *Polar Vortex*. https://www.climate.gov/news-features/understanding-climate/understanding-arctic-polar-vortex.

Nomokonova, Tatiana, Kerstin Ebell, Ulrich Löhnert, Marion Maturilli, Christoph Ritter, and Ewan O'Connor (2019). "Statistics on clouds and their relation to thermodynamic conditions at Ny-Ålesund using ground-based sensor synergy". In: *Atmospheric Chemistry and Physics* 19.6, pp. 4105–4126.

Norin, Lars, Abhay Devasthale, TS L'Ecuyer, NB Wood, and M Smalley (2015). "Intercomparison of snowfall estimates derived from the CloudSat Cloud Profiling Radar and the ground-based weather radar network over Sweden". In: *Atmospheric Measurement Techniques* 8.12, pp. 5009–5021.

Nygård, T., T. Valkonen, and T. Vihma (2014). "Characteristics of Arctic low-tropospheric humidity inversions based on radio soundings". In: *Atmospheric Chemistry and Physics* 14.4, pp. 1959–1971. ISSN: 1680-7324. DOI: 10.5194/acp-14-1959-2014. URL: https://acp.copernicus.org/articles/14/1959/2014/ (visited on 01/29/2024).

Overland, James, Edward Dunlea, Jason E. Box, Robert Corell, Martin Forsius, Vladimir Kattsov, Morten Skovgård Olsen, Janet Pawlak, Lars-Otto Reiersen, and Muyin Wang (2019). "The urgency of Arctic change". In: *Polar Science* 21, pp. 6–13. ISSN: 18739652. DOI: 10.1016/j.polar.2018.11.008. URL: https://linkinghub.elsevier.com/retrieve/pii/S1873965218301543.

Palerme, C, C Claud, NB Wood, T L'Ecuyer, and C Genthon (2019). "How Does Ground Clutter Affect CloudSat Snowfall Retrievals Over Ice Sheets?" In: *IEEE Geosci. Remote S.* 16, pp. 342–346.

Perovich, D. K., T. C. Grenfell, B. Light, and P. V. Hobbs (2002). "Seasonal evolution of the albedo of multiyear Arctic sea ice". In: *Journal of Geophysical Research: Oceans* 107 (C10). ISSN: 0148-0227. DOI: 10.1029/2000JC000438. URL: https://agupubs.onlinelibrary.wiley.com/doi/10.1029/2000JC000438.

Petty, Grant W. (1997). "An intercomparison of oceanic precipitation frequencies from 10 special sensor microwave/imager rain rate algorithms and shipboard present weather reports". In: *Journal of Geophysical Research: Atmospheres* 102 (D2), pp. 1757–1777. ISSN: 0148-0227. DOI: 10.1029/96JD03000. URL: https://agupubs.onlinelibrary.wiley.com/doi/10.1029/96JD03000.

Pithan, Felix and Thorsten Mauritsen (2014). "Arctic amplification dominated by temperature feedbacks in contemporary climate models". In: *Nature Geoscience* 7.3, pp. 181–184. ISSN: 1752-0894, 1752-0908. DOI: 10.1038/ngeo2071. URL: https://www.nature.com/articles/ngeo2071.

Prince, Hamish D., Nicolas J. Cullen, Peter B. Gibson, Jono Conway, and Daniel G. Kingston (2021). "A Climatology of Atmospheric Rivers in New Zealand". In: *Journal of Climate* 34.11, pp. 4383–4402. ISSN: 0894-8755, 1520-0442. DOI: 10.1175/JCLI-D-20-0664.1. URL: https://journals.ametsoc.org/view/journals/clim/34/11/JCLI-D-20-0664.1.xml.

Ralph, F. M., S. F. Iacobellis, P. J. Neiman, J. M. Cordeira, J. R. Spackman, D. E. Waliser, G. A. Wick, A. B. White, and C. Fairall (2017). "Dropsonde Observations of Total Integrated Water Vapor Transport within North Pacific Atmospheric Rivers". In: *Journal of Hydrometeorology* 18.9, pp. 2577–2596. ISSN: 1525-755X, 1525-7541. DOI: 10.1175/JHM-D-17-0036.1. URL: http://journals.ametsoc.org/doi/10.1175/JHM-D-17-0036.1.

Ralph, F. Martin, Michael D. Dettinger, Mary M. Cairns, Thomas J. Galarneau, and John Eylander (2018). "Defining "Atmospheric River": How the Glossary of Meteorology Helped Resolve a Debate". In: *Bulletin of the American Meteorological Society* 99.4, pp. 837–839. ISSN: 0003-0007, 1520-0477. DOI: 10.1175/BAMS-D-17-0157.1. URL: https://journals.ametsoc.org/view/journals/bams/99/4/bams-d-17-0157.1.xml.

Ralph, F. Martin, Michael D. Dettinger, Lawrence J. Schick, and Michael L. Anderson (2020). "Introduction to Atmospheric Rivers". In: *Atmospheric Rivers*. Ed. by F. Martin Ralph, Michael D. Dettinger, Jonathan J. Rutz, and Duane E. Waliser. Cham: Springer International Publishing, pp. 1–13. ISBN: 978-3-030-28905-8 978-3-030-28906-5. DOI: 10.1007/978-3-030-28906-5_1. URL: http://link.springer.com/10.1007/978-3-030-28906-5_1.

Ralph, F. Martin, Paul J. Neiman, and Gary A. Wick (2004). "Satellite and CALJET Aircraft Observations of Atmospheric Rivers over the Eastern North Pacific Ocean during the Winter of 1997/98". In: *Monthly Weather Review* 132.7, pp. 1721–1745. ISSN: 0027-0644, 1520-0493. DOI: 10.1175/1520-0493(2004)132<1721:SACAOO>2.0.CO;2. URL: http://journals.ametsoc.org/doi/10.1175/1520-0493(2004)132<1721:SACAOO>2.0.CO;2.

Ralph, F. Martin, Paul J. Neiman, Gary A. Wick, Seth I. Gutman, Michael D. Dettinger, Daniel R. Cayan, and Allen B. White (2006). "Flooding on California's Russian River: Role of atmospheric rivers". In: *Geophysical Research Letters* 33.13, 2006GL026689. ISSN: 0094-8276, 1944-8007. DOI: 10.1029/2006GL026689. URL: https://agupubs.onlinelibrary.wiley.com/doi/10.1029/2006GL026689 (visited on 01/29/2024).

Rantanen, Mika, Alexey Yu. Karpechko, Antti Lipponen, Kalle Nordling, Otto Hyvärinen, Kimmo Ruosteenoja, Timo Vihma, and Ari Laaksonen (2022). "The Arctic has warmed nearly four times faster than the globe since 1979". In: *Communications Earth & Environment* 3.1, p. 168. ISSN: 2662-4435. DOI: 10.1038/s43247-022-00498-3. URL: https://www.nature.com/articles/s43247-022-00498-3.

Reed, Richard J. and Bruce A. Kunkel (1960). "THE ARCTIC CIRCULATION IN SUMMER". In: *Journal of Meteorology* 17.5, pp. 489–506. ISSN: 0095-9634, 0095-9634. DOI: 10.1175/1520-0469(1960)017<0489:TACIS>2.0.CO;2. URL: http://journals.ametsoc.org/doi/10.1175/1520-0469(1960)017<0489:TACIS>2.0.CO;2 (visited on 01/29/2024).

Reid, Kimberley J., Andrew D. King, Todd P. Lane, and Debra Hudson (2022). "Tropical, Subtropical, and Extratropical Atmospheric Rivers in the Australian Region". In: *Journal of Climate* 35.9, pp. 2697–2708. ISSN: 0894-8755, 1520-0442. DOI: 10.1175/JCLI-D-21-0606.1. URL: https://journals.ametsoc.org/view/journals/clim/35/9/JCLI-D-21-0606.1.xml.

Renard, Robert J. and Leo C. Clarke (1965). "EXPERIMENTS IN NUMERICAL OBJECTIVE FRONTAL ANALYSIS [1]". In: *Monthly Weather Review* 93.9, pp. 547–556. ISSN: 0027-0644, 1520-0493. DOI: 10.1175/1520-0493(1965)093<0547:EINOFA>2.3.CO;2. URL: http://journals.ametsoc.org/doi/10.1175/1520-0493(1965)093<0547:EINOFA>2.3.CO;2 (visited on 01/29/2024).

Rinke, A, M Maturilli, R M Graham, H Matthes, D Handorf, L Cohen, S R Hudson, and J C Moore (2017). "Extreme cyclone events in the Arctic: Wintertime variability and trends". In: *Environmental Research Letters* 12.9, p. 094006. ISSN: 1748-9326. DOI: 10.1088/1748-9326/aa7def. URL: https://iopscience.iop.org/article/10.1088/1748-9326/aa7def.

Rinke, A., B. Segger, S. Crewell, M. Maturilli, T. Naakka, T. Nygård, T. Vihma, F. Alshawaf, G. Dick, J. Wickert, and J. Keller (2019). "Trends of Vertically Integrated Water Vapor over the Arctic during 1979–2016: Consistent Moistening All Over?" In: *Journal of Climate* 32.18, pp. 6097–6116. ISSN: 0894-8755, 1520-0442. DOI: 10.1175/JCLI-D-19-0092.1. URL: https://journals.ametsoc.org/doi/10.1175/JCLI-D-19-0092.1.

Rose, Thomas, Susanne Crewell, Ulrich Löhnert, and Clemens Simmer (2005). "A network suitable microwave radiometer for operational monitoring of the cloudy atmosphere". In: *Atmospheric research* 75.3, pp. 183–200.

Rüdisühli, Stefan, Michael Sprenger, David Leutwyler, Christoph Schär, and Heini Wernli (2020). "Attribution of precipitation to cyclones and fronts over Europe in a kilometer-scale regional climate simulation". In: *Weather and Climate Dynamics* 1.2, pp. 675–699. ISSN: 2698-4016. DOI: 10.5194/wcd-1-675-2020. URL: https://wcd.copernicus.org/articles/1/675/2020/.

Sanò, Paolo, Daniele Casella, Andrea Camplani, Leo Pio D'Adderio, and Giulia Panegrossi (2022). "A machine learning snowfall retrieval algorithm for ATMS". In: *Remote Sensing* 14.6, p. 1467.

Schemm, Sebastian, Irina Rudeva, and Ian Simmonds (2015). "Extratropical fronts in the lower troposphere–global perspectives obtained from two automated methods". In: *Quarterly Journal of the Royal Meteorological Society* 141.690, pp. 1686–1698. ISSN: 0035-9009, 1477-870X. DOI: 10.1002/qj.2471. URL: https://rmets.onlinelibrary.wiley.com/doi/10.1002/qj.2471.

Schemm, Sebastian, Michael Sprenger, and Heini Wernli (2018). "When during Their Life Cycle Are Extratropical Cyclones Attended by Fronts?" In: *Bulletin of the American Meteorological Society* 99.1, pp. 149–165. ISSN: 0003-0007, 1520-0477. DOI: 10.1175/BAMS-D-16-0261.1. URL: https://journals.ametsoc.org/doi/10.1175/BAMS-D-16-0261.1 (visited on 01/29/2024).

Schreiber, Erika A. P. and Mark C. Serreze (2020). "Impacts of synoptic-scale cyclones on Arctic sea-ice concentration: a systematic analysis". In: *Annals of Glaciology* 61.82, pp. 139–153. ISSN: 0260-3055, 1727-5644. DOI: 10.1017/aog.2020.23. URL: https://www.cambridge.org/core/product/identifier/S0260305520000233/type/journal_article.

Sejas, Sergio A., Ming Cai, Aixue Hu, Gerald A. Meehl, Warren Washington, and Patrick C. Taylor (2014). "Individual Feedback Contributions to the Seasonality of Surface Warming". In: *Journal of Climate* 27.14, pp. 5653–5669. ISSN: 0894-8755, 1520-0442. DOI: 10.1175/JCLI-D-13-00658.1. URL: http://journals.ametsoc.org/doi/10.1175/JCLI-D-13-00658.1.

Serreze, Mark C., Andrew P. Barrett, and Fiona Lo (2005). "Northern High-Latitude Precipitation as Depicted by Atmospheric Reanalyses and Satellite Retrievals". In: *Monthly Weather Review* 133.12, pp. 3407–3430. ISSN: 1520-0493, 0027-0644.

DOI: 10.1175/MWR3047.1. URL: http://journals.ametsoc.org/doi/10.1175/MWR3047.1.

Serreze, Mark C. and Roger G. Barry (2011). "Processes and impacts of Arctic amplification: A research synthesis". In: *Global and Planetary Change* 77.1, pp. 85–96. ISSN: 09218181. DOI: 10.1016/j.gloplacha.2011.03.004. URL: https://linkinghub.elsevier.com/retrieve/pii/S0921818111000397.

Serreze, Mark C and Roger G Barry (2014). *The Arctic climate system*. Cambridge University Press.

Serreze, Mark C. and Ciaran M. Hurst (2000). "Representation of Mean Arctic Precipitation from NCEP–NCAR and ERA Reanalyses". In: *Journal of Climate* 13.1, pp. 182–201. ISSN: 0894-8755, 1520-0442. DOI: 10.1175/1520-0442(2000)013<0182:ROMAPF>2.0.CO;2. URL: http://journals.ametsoc.org/doi/10.1175/1520-0442(2000)013<0182:ROMAPF>2.0.CO;2.

Serreze, Mark C., Amanda H. Lynch, and Martyn P. Clark (2001). "The Arctic Frontal Zone as Seen in the NCEP–NCAR Reanalysis". In: *Journal of Climate* 14.7, pp. 1550–1567. ISSN: 0894-8755, 1520-0442. DOI: 10.1175/1520-0442(2001)014<1550:TAFZAS>2.0.CO;2. URL: http://journals.ametsoc.org/doi/10.1175/1520-0442(2001)014<1550:TAFZAS>2.0.CO;2 (visited on 01/29/2024).

Shapiro, M. A. and Daniel Keyser (1990). "Fronts, Jet Streams and the Tropopause". In: *Extratropical Cyclones*. Ed. by Chester W. Newton and Eero O. Holopainen. Boston, MA: American Meteorological Society, pp. 167–191. ISBN: 978-1-944970-33-8. DOI: 10.1007/978-1-944970-33-8_10. URL: http://link.springer.com/10.1007/978-1-944970-33-8_10.

Shields, Christine A., Jonathan D. Wille, Allison B. Marquardt Collow, Michelle Maclennan, and Irina V. Gorodetskaya (2022). "Evaluating Uncertainty and Modes of Variability for Antarctic Atmospheric Rivers". In: *Geophysical Research Letters* 49.16, e2022GL099577. ISSN: 0094-8276, 1944-8007. DOI: 10.1029/2022GL099577. URL: https://agupubs.onlinelibrary.wiley.com/doi/10.1029/2022GL099577.

Shupe, Matthew D, Markus Rex, Byron Blomquist, P Ola G Persson, Julia Schmale, Taneil Uttal, Dietrich Althausen, Hélène Angot, Stephen Archer, Ludovic Bariteau, et al. (2022). "Overview of the MOSAiC expedition: Atmosphere". In: *Elem Sci Anth* 10.1, p. 00060.

Simmonds, Ian, Kevin Keay, and John Arthur Tristram Bye (2012). "Identification and Climatology of Southern Hemisphere Mobile Fronts in a Modern Reanalysis". In: *Journal of Climate* 25.6, pp. 1945–1962. ISSN: 0894-8755, 1520-0442. DOI: 10.1175/JCLI-D-11-00100.1. URL: http://journals.ametsoc.org/doi/10.1175/JCLI-D-11-00100.1 (visited on 01/29/2024).

Sodemann, Harald and Andreas Stohl (2013). "Moisture Origin and Meridional Transport in Atmospheric Rivers and Their Association with Multiple Cyclones*". In: *Monthly Weather Review* 141.8, pp. 2850–2868. ISSN: 0027-0644, 1520-0493. DOI: 10.1175/MWR-D-12-00256.1. URL: http://journals.ametsoc.org/doi/10.1175/MWR-D-12-00256.1.

Sorteberg, Asgeir and John E. Walsh (2008). "Seasonal cyclone variability at 70°N and its impact on moisture transport into the Arctic". In: *Tellus A* 60.3, pp. 570–586. ISSN: 0280-6495, 1600-0870. DOI: 10.1111/j.1600-0870.2008.00314.x. URL: http://tellusa.net/index.php/tellusa/article/view/15372.

Souverijns, Niels, Alexandra Gossart, Stef Lhermitte, Irina V Gorodetskaya, Jacopo Grazioli, Alexis Berne, Claudio Duran-Alarcon, Brice Boudevillain, Christophe Genthon, Claudio Scarchilli, et al. (2018). "Evaluation of the CloudSat surface snowfall product over Antarctica using ground-based precipitation radars". In: *The Cryosphere* 12.12, pp. 3775–3789.

Sprenger, Michael, Georgios Fragkoulidis, Hanin Binder, Mischa Croci-Maspoli, Pascal Graf, Christian M. Grams, Peter Knippertz, Erica Madonna, Sebastian Schemm, Bojan Škerlak, and Heini Wernli (2017). "Global Climatologies of Eulerian and Lagrangian Flow Features based on ERA-Interim". In: *Bulletin of the American Meteorological Society* 98.8, pp. 1739–1748. ISSN: 0003-0007, 1520-0477. DOI: 10.1175/BAMS-D-15-00299.1. URL: https://journals.ametsoc.org/doi/10.1175/BAMS-D-15-00299.1.

Stephens, Graeme L and John M Haynes (2007). "Near global observations of the warm rain coalescence process". In: *Geophysical Research Letters* 34.20.

Stephens, Graeme L., Deborah G. Vane, Ronald J. Boain, Gerald G. Mace, Kenneth Sassen, Zhien Wang, Anthony J. Illingworth, Ewan J. O'connor, William B. Rossow, Stephen L. Durden, Steven D. Miller, Richard T. Austin, Angela Benedetti, and Cristian Mitrescu (Dec. 2002). "THE CLOUDSAT MISSION AND THE A-TRAIN: A New Dimension of Space-Based Observations of Clouds and Precipitation". en. In: *Bulletin of the American Meteorological Society* 83.12. Publisher: American Meteorological Society Section: Bulletin of the American Meteorological Society, pp. 1771–1790. ISSN: 0003-0007, 1520-0477. DOI: 10.1175/BAMS-83-12-1771. URL: https://journals.ametsoc.org/view/journals/bams/83/12/bams-83-12-1771.xml (visited on 07/06/2022).

Stephens, Graeme L., Deborah G. Vane, Simone Tanelli, Eastwood Im, Stephen Durden, Mark Rokey, Don Reinke, Philip Partain, Gerald G. Mace, Richard Austin, Tristan L'Ecuyer, John Haynes, Matthew Lebsock, Kentaroh Suzuki, Duane Waliser, Dong Wu, Jen Kay, Andrew Gettelman, Zhien Wang, and Rojer Marchand (2008). "CloudSat mission: Performance and early science after the first year of operation". en. In: *Journal of Geophysical Research: Atmospheres* 113.D8. _eprint: https://onlinelibrary.wiley.com ISSN: 2156-2202. DOI: 10.1029/2008JD009982. URL: https://onlinelibrary.wiley.com/doi/abs/10.1029/2008JD009982 (visited on 07/06/2022).

Tanelli, Simone, Stephen L. Durden, Eastwood Im, Kyung S. Pak, Dale G. Reinke, Philip Partain, John M. Haynes, and Roger T. Marchand (Nov. 2008). "CloudSat's Cloud Profiling Radar After Two Years in Orbit: Performance, Calibration, and Processing". In: *IEEE Transactions on Geoscience and Remote Sensing* 46.11, pp. 3560–3573. ISSN: 0196-2892. DOI: 10.1109/TGRS.2008.2002030. URL: http://ieeexplore.ieee.org/document/4685947/ (visited on 02/23/2022).

Thomas, Carl M. and David M. Schultz (2019). "What are the Best Thermodynamic Quantity and Function to Define a Front in Gridded Model Output?" In: *Bulletin of the American Meteorological Society* 100.5, pp. 873–895. ISSN: 0003-0007, 1520-0477. DOI: 10.1175/BAMS-D-18-0137.1. URL: https://journals.ametsoc.org/view/journals/bams/100/5/bams-d-18-0137.1.xml (visited on 01/29/2024).

Turner, J. and Gareth Marshall (2011). *Climate change in the polar regions*. OCLC: ocn664324532. Cambridge ; New York: Cambridge University Press. 434 pp. ISBN: 978-0-521-85010-0.

Vassel, Maiken, Luisa Ickes, Marion Maturilli, and Corinna Hoose (2019). "Classification of Arctic multilayer clouds using radiosonde and radar data in Svalbard". In: *Atmospheric Chemistry and Physics* 19.7, pp. 5111–5126.

Vavrus, Stephen J. (2013). "Extreme Arctic cyclones in CMIP5 historical simulations". In: *Geophysical Research Letters* 40.23, pp. 6208–6212. ISSN: 0094-8276, 1944-8007. DOI: 10.1002/2013GL058161. URL: https://agupubs.onlinelibrary.wiley.com/doi/10.1002/2013GL058161.

Viale, Maximiliano, Raúl Valenzuela, René D. Garreaud, and F. Martin Ralph (2018). "Impacts of Atmospheric Rivers on Precipitation in Southern South America". In: *Journal of Hydrometeorology* 19.10, pp. 1671–1687. ISSN: 1525-755X, 1525-7541.

DOI: 10.1175/JHM-D-18-0006.1. URL: http://journals.ametsoc.org/doi/10.1175/JHM-D-18-0006.1.

Viceto, Carolina, Irina V. Gorodetskaya, Annette Rinke, Marion Maturilli, Alfredo Rocha, and Susanne Crewell (2022). "Atmospheric rivers and associated precipitation patterns during the ACLOUD and PASCAL campaigns near Svalbard (May–June 2017): case studies using observations, reanalyses, and a regional climate model". In: *Atmospheric Chemistry and Physics* 22.1, pp. 441–463. ISSN: 1680-7324. DOI: 10.5194/acp-22-441-2022. URL: https://acp.copernicus.org/articles/22/441/2022/.

Vihma, Timo, James Screen, Michael Tjernström, Brandi Newton, Xiangdong Zhang, Valeria Popova, Clara Deser, Marika Holland, and Terry Prowse (2016). "The atmospheric role in the Arctic water cycle: A review on processes, past and future changes, and their impacts". In: *Journal of Geophysical Research: Biogeosciences* 121.3, pp. 586–620. ISSN: 2169-8953, 2169-8961. DOI: 10.1002/2015JG003132. URL: https://agupubs.onlinelibrary.wiley.com/doi/10.1002/2015JG003132.

Von Lerber, Annakaisa, Mario Mech, Annette Rinke, Damao Zhang, Melanie Lauer, Ana Radovan, Irina Gorodetskaya, and Susanne Crewell (2022). "Evaluating seasonal and regional distribution of snowfall in regional climate model simulations in the Arctic". In: *Atmospheric Chemistry and Physics* 22.11, pp. 7287–7317. ISSN: 1680-7324. DOI: 10.5194/acp-22-7287-2022. URL: https://acp.copernicus.org/articles/22/7287/2022/.

Vázquez, Marta, Iago Algarra, Jorge Eiras-Barca, Alexandre M. Ramos, Raquel Nieto, and Luis Gimeno (2018). "Atmospheric Rivers over the Arctic: Lagrangian Characterisation of Their Moisture Sources". In: *Water* 11.1, p. 41. ISSN: 2073-4441. DOI: 10.3390/w11010041. URL: http://www.mdpi.com/2073-4441/11/1/41.

Wahl, Sabrina, Christoph Bollmeyer, Susanne Crewell, Clarissa Figura, Petra Friederichs, Andreas Hense, Jan D. Keller, and Christian Ohlwein (2017). "A novel convective-scale regional reanalysis COSMO-REA2: Improving the representation of precipitation". In: *Meteorologische Zeitschrift* 26.4, pp. 345–361. ISSN: 0941-2948. DOI: 10.1127/metz/2017/0824. URL: http://www.schweizerbart.de/papers/metz/detail/26/87333/A_novel_convective_scale_regional_reanalysis_COSMO?af=crossref (visited on 02/03/2024).

Waliser, Duane and Bin Guan (2017). "Extreme winds and precipitation during landfall of atmospheric rivers". In: *Nature Geoscience* 10.3, pp. 179–183. ISSN: 1752-0894, 1752-0908. DOI: 10.1038/ngeo2894. URL: https://www.nature.com/articles/ngeo2894.

Walsh, J. E. (2022). "Precipitation". In: Publisher: Global Ocean Monitoring and Observing (U.S.) DOI: 10.25923/N07S-3S69. URL: https://repository.library.noaa.gov/view/noaa/48538.

Wendisch, M. et al. (2023). "Atmospheric and Surface Processes, and Feedback Mechanisms Determining Arctic Amplification: A Review of First Results and Prospects of the (AC)3 Project". In: *Bulletin of the American Meteorological Society* 104.1, E208–E242. ISSN: 0003-0007, 1520-0477. DOI: 10.1175/BAMS-D-21-0218.1. URL: https://journals.ametsoc.org/view/journals/bams/104/1/BAMS-D-21-0218.1.xml (visited on 02/04/2024).

Wendisch, Manfred, Marlen Brückner, John Burrows, Susanne Crewell, Klaus Dethloff, Kerstin Ebell, Christof Lüpkes, Andreas Macke, Justus Notholt, Johannes Quaas, Annette Rinke, and Ina Tegen (2017). "Understanding Causes and Effects of Rapid Warming in the Arctic". In: *Eos*. ISSN: 2324-9250. DOI: 10.1029/2017EO064803. URL: https://eos.org/project-updates/understanding-causes-and-effects-of-rapid-warming-in-the-arctic (visited on 02/04/2024).

Wendisch, Manfred, Andreas Macke, André Ehrlich, Christof Lüpkes, Mario Mech, Dmitry Chechin, Klaus Dethloff, Carola Barrientos Velasco, Heiko Bozem, Marlen Brückner, Hans-Christian Clemen, Susanne Crewell, Tobias Donth, Regis Dupuy, Kerstin Ebell, Ulrike Egerer, Ronny Engelmann, Christa Engler, Oliver Eppers, Martin Gehrmann, Xianda Gong, Matthias Gottschalk, Christophe Gourbeyre, Hannes Griesche, Jörg Hartmann, Markus Hartmann, Bernd Heinold, Andreas Herber, Hartmut Herrmann, Georg Heygster, Peter Hoor, Soheila Jafariserajehlou, Evelyn Jäkel, Emma Järvinen, Olivier Jourdan, Udo Kästner, Simonas Kecorius, Erlend M. Knudsen, Franziska Köllner, Jan Kretzschmar, Luca Lelli, Delphine Leroy, Marion Maturilli, Linlu Mei, Stephan Mertes, Guillaume Mioche, Roland Neuber, Marcel Nicolaus, Tatiana Nomokonova, Justus Notholt, Mathias Palm, Manuela Van Pinxteren, Johannes Quaas, Philipp Richter, Elena Ruiz-Donoso, Michael Schäfer, Katja Schmieder, Martin Schnaiter, Johannes Schneider, Alfons Schwarzenböck, Patric Seifert, Matthew D. Shupe, Holger Siebert, Gunnar Spreen, Johannes Stapf, Frank Stratmann, Teresa Vogl, André Welti, Heike Wex, Alfred Wiedensohler, Marco Zanatta, and Sebastian Zeppenfeld (2019). "The Arctic Cloud Puzzle: Using ACLOUD/PASCAL Multiplatform Observations to Unravel the Role of Clouds and Aerosol Particles in Arctic Amplification". In: *Bulletin of the American Meteorological Society* 100.5, pp. 841–871. ISSN: 0003-0007, 1520-0477. DOI: 10.1175/BAMS-D-18-0072.1. URL: https://journals.ametsoc.org/view/journals/bams/100/5/bams-d-18-0072.1.xml.

Wernli, Heini and Cornelia Schwierz (2006). "Surface Cyclones in the ERA-40 Dataset (1958–2001). Part I: Novel Identification Method and Global Climatology". In: *Journal of the Atmospheric Sciences* 63.10, pp. 2486–2507. ISSN: 1520-0469, 0022-4928. DOI: 10.1175/JAS3766.1. URL: https://journals.ametsoc.org/doi/10.1175/JAS3766.1.

Wick, Gary A., Paul J. Neiman, F. Martin Ralph, and Thomas M. Hamill (2013). "Evaluation of Forecasts of the Water Vapor Signature of Atmospheric Rivers in Operational Numerical Weather Prediction Models". In: *Weather and Forecasting* 28.6, pp. 1337–1352. ISSN: 0882-8156, 1520-0434. DOI: 10.1175/WAF-D-13-00025.1. URL: https://journals.ametsoc.org/doi/10.1175/WAF-D-13-00025.1.

Wilheit, Thomas T. (1986). "Some Comments on Passive Microwave Measurement of Rain". In: *Bulletin of the American Meteorological Society* 67.10, pp. 1226–1232. ISSN: 0003-0007, 1520-0477. DOI: 10.1175/1520-0477(1986)067<1226:SCOPMM>2.0.CO;2. URL: http://journals.ametsoc.org/doi/10.1175/1520-0477(1986)067<1226:SCOPMM>2.0.CO;2.

Wille, Jonathan D., Vincent Favier, Ambroise Dufour, Irina V. Gorodetskaya, John Turner, Cécile Agosta, and Francis Codron (2019). "West Antarctic surface melt triggered by atmospheric rivers". In: *Nature Geoscience* 12.11, pp. 911–916. ISSN: 1752-0894, 1752-0908. DOI: 10.1038/s41561-019-0460-1. URL: https://www.nature.com/articles/s41561-019-0460-1.

Wood, NB and TS L'Ecuyer (2018a). "Level 2c snow profile process description and interface control document, product version p1 r05. NASA JPL CloudSat project document revision 0, 26 pp". In: *National Aeronautics and Space Administration, Jet Propulsion Laboratory. Retrieved from https://www. cloudsat. cira. colostate. edu/data-products/2c-snow-profile#: : text C* 2.

Wood, Norman Bryce and T. S. L'Ecuyer (2018b). "Level 2C Snow Profile Process Description and Interface Control Document, Product Version P1 R05". en. In: *NASA JPL CloudSat project document revision 0., 26 pp*. URL: https://www.cloudsat.

cira.colostate.edu/cloudsat-static/info/dl/2c-snow-profile/2C-SNOW-PROFILE_PDICD.P1_R05.rev0_.pdf.

Woods, Cian and Rodrigo Caballero (2016). "The Role of Moist Intrusions in Winter Arctic Warming and Sea Ice Decline". In: *Journal of Climate* 29.12, pp. 4473–4485. ISSN: 0894-8755, 1520-0442. DOI: 10.1175/JCLI-D-15-0773.1. URL: http://journals.ametsoc.org/doi/10.1175/JCLI-D-15-0773.1.

Woods, Cian, Rodrigo Caballero, and Gunilla Svensson (2013). "Large-scale circulation associated with moisture intrusions into the Arctic during winter". In: *Geophysical Research Letters* 40.17, pp. 4717–4721. ISSN: 0094-8276, 1944-8007. DOI: 10.1002/grl.50912. URL: https://agupubs.onlinelibrary.wiley.com/doi/10.1002/grl.50912.

Yang, Daqing, Douglas Kane, Zhongping Zhang, David Legates, and Barry Goodison (2005). "Bias corrections of long-term (1973–2004) daily precipitation data over the northern regions". In: *Geophysical Research Letters* 32.19, 2005GL024057. ISSN: 0094-8276, 1944-8007. DOI: 10.1029/2005GL024057. URL: https://agupubs.onlinelibrary.wiley.com/doi/10.1029/2005GL024057.

Yang, Daqing and Douglas L. Kane, eds. (2021). *Arctic Hydrology, Permafrost and Ecosystems*. Cham: Springer International Publishing. ISBN: 978-3-030-50928-6 978-3-030-50930-9. DOI: 10.1007/978-3-030-50930-9. URL: https://link.springer.com/10.1007/978-3-030-50930-9.

You, Cheng, Michael Tjernström, Abhay Devasthale, and Daniel Steinfeld (2022). "The Role of Atmospheric Blocking in Regulating Arctic Warming". In: *Geophysical Research Letters* 49.12, e2022GL097899. ISSN: 0094-8276, 1944-8007. DOI: 10.1029/2022GL097899. URL: https://agupubs.onlinelibrary.wiley.com/doi/10.1029/2022GL097899.

Zahn, Matthias, Mirseid Akperov, Annette Rinke, Frauke Feser, and Igor I. Mokhov (2018). "Trends of Cyclone Characteristics in the Arctic and Their Patterns From Different Reanalysis Data". In: *Journal of Geophysical Research: Atmospheres* 123.5, pp. 2737–2751. ISSN: 2169-897X, 2169-8996. DOI: 10.1002/2017JD027439. URL: https://agupubs.onlinelibrary.wiley.com/doi/10.1002/2017JD027439.

Zhang, Pengfei, Gang Chen, Mingfang Ting, L. Ruby Leung, Bin Guan, and Laifang Li (2023). "More frequent atmospheric rivers slow the seasonal recovery of Arctic sea ice". In: *Nature Climate Change* 13.3, pp. 266–273. ISSN: 1758-678X, 1758-6798. DOI: 10.1038/s41558-023-01599-3. URL: https://www.nature.com/articles/s41558-023-01599-3.

Zhang, Xiangdong, Juanxiong He, Jing Zhang, Igor Polyakov, Rüdiger Gerdes, Jun Inoue, and Peili Wu (2013). "Enhanced poleward moisture transport and amplified northern high-latitude wetting trend". In: *Nature Climate Change* 3.1, pp. 47–51. ISSN: 1758-678X, 1758-6798. DOI: 10.1038/nclimate1631. URL: https://www.nature.com/articles/nclimate1631.

Zhang, Xiangdong, John E. Walsh, Jing Zhang, Uma S. Bhatt, and Moto Ikeda (2004). "Climatology and Interannual Variability of Arctic Cyclone Activity: 1948–2002". In: *Journal of Climate* 17.12, pp. 2300–2317. ISSN: 0894-8755, 1520-0442. DOI: 10.1175/1520-0442(2004)017<2300:CAIVOA>2.0.CO;2. URL: http://journals.ametsoc.org/doi/10.1175/1520-0442(2004)017<2300:CAIVOA>2.0.CO;2 (visited on 01/29/2024).

Zhang, Zhenhai and F. Martin Ralph (2021). "The Influence of Antecedent Atmospheric River Conditions on Extratropical Cyclogenesis". In: *Monthly Weather Review* 149.5, pp. 1337–1357. ISSN: 0027-0644, 1520-0493. DOI: 10.1175/MWR-D-20-0212.1. URL: https://journals.ametsoc.org/view/journals/mwre/149/5/MWR-D-20-0212.1.xml.

Zhang, Zhenhai, F. Martin Ralph, and Minghua Zheng (2019). "The Relationship Between Extratropical Cyclone Strength and Atmospheric River Intensity and Position". In: *Geophysical Research Letters* 46.3, pp. 1814–1823. ISSN: 0094-8276, 1944-8007. DOI: 10.1029/2018GL079071. URL: https://agupubs.onlinelibrary.wiley.com/doi/10.1029/2018GL079071.

Zhu, Yong and Reginald E. Newell (1998). "A Proposed Algorithm for Moisture Fluxes from Atmospheric Rivers". In: *Monthly Weather Review* 126.3, pp. 725–735. ISSN: 0027-0644, 1520-0493. DOI: 10.1175/1520-0493(1998)126<0725:APAFMF>2.0.CO;2. URL: http://journals.ametsoc.org/doi/10.1175/1520-0493(1998)126<0725:APAFMF>2.0.CO;2 (visited on 01/29/2024).

— (1999). "Atmospheric rivers and bombs". In: *Geophysical Research Letters* 21.18, pp. 1999–2002. ISSN: 0094-8276, 1944-8007. DOI: 10.1029/94GL01710. URL: https://agupubs.onlinelibrary.wiley.com/doi/10.1029/94GL01710.

Łupikasza, E. B. and K. Cielecka-Nowak (2020). "Changing Probabilities of Days with Snow and Rain in the Atlantic Sector of the Arctic under the Current Warming Trend". In: *Journal of Climate* 33.7, pp. 2509–2532. ISSN: 0894-8755, 1520-0442. DOI: 10.1175/JCLI-D-19-0384.1. URL: http://journals.ametsoc.org/doi/10.1175/JCLI-D-19-0384.1.

Acknowledgements

This PhD dissertation was carried out within and funded by the Transregional Collaborative Research Center TRR 172 "ArctiC Amplification: Climate Relevant Atmospheric and SurfaCe Processes, and Feedback Mechanisms (AC)3 ", funded by the Deutsche Forschungsgemeinschaft (DFG, German Research Foundation). The Integrated Research Training Group (IRTG) of the (AC)3 consortium, and the Graduate School of Geosciences (GSGS) of the University of Cologne provided training, support, and travel funds.

Great thanks go to Prof. Dr. Susanne Crewell for giving me the opportunity to start my PhD in the $(AC)^3$ project while working for her at the University of Cologne. I would like to thank for her support and helpful input in our regular meetings during the last four years. I was also glad that you gave me the chance to participate in a variety of research and teaching activities that broadened my horizons in addition to writing my thesis. Thank you very much!

I would also like to thank Prof. Dr. Nikki Vercauteren for evaluating this thesis as a second reviewer, as well as Prof. Dr. Tony Reimann and Dr. Christoph Böhm for their participation in the defense.

Then, I would like to thank Prof. Dr. Johannes Quaas from the University of Leipzig. He gave me the possibility to write my master's thesis in his research group. This Master's thesis opened the door to the $(AC)^3$ project. He was always on hand with help and advice during both my Master's thesis and my doctoral thesis.

Further, I would like to thank Dr. Annette Rinke from the Alfred-Wegener Institute in Potsdam. Thank you very much for your support, I am very happy that you were my co-supervisor during this time. The discussions with you were always fruitful. It was also nice to have me in Potsdam for almost 5 weeks to work on my thesis. I really enjoyed my time in Potsdam. It was a very nice work environment which allowed me to focus on my thesis.

I am also happy to thank Dr. Irina Gorodetskaya for her expertise in Atmospheric Rivers. I learned a lot from her about the synoptic feature which was one of the biggest focuses of my thesis. Thank you for your support and having me in Portugal for almost a week.

Next, I would like to thank Dr. Mario Mech, especially for the technical support in the beginning and also during my PhD. It was nice to learn PAMTRA and to use it. Unfortunately, there was no further group retreat that allowed us to run around a lake in the early morning.

This PhD thesis would also not be possible without Dr. Bin Guan and Dr. Michael Sprenger. Bin provided me with the second version of the ARs detection algorithm. Thank you very much and also for the discussion about your algorithm and how to use it. Michael provided me the detected cyclones and fronts for the ERA5 reanalysis. Thank you for the discussion and support during my PhD.

Further, I would like to thank Dr. Vera Schemann who gave me the opportunity to use her resources on Mistral at the German Computing Centre (DKRZ) in Hamburg. In this way, I would also the DKRZ. Without the resources, a climatological analysis on this scale would not have been possible.

Before I started with my PhD, I had the possibility to meet Carolina Viceto from the University of Aveiro during the Atmospheric Rivers Summer School in San Diego. It was a very nice and also intense time. Thank you for your support during this journey, for listening to my problems, and for having me in Portugal to work on the AR algorithm. I'm really glad that a friendship has developed and I'm looking forward to visiting you at the Azores!!!

I would also like to thank Sofie. I am very glad that you were Jerome's successor. Thank you so much for your support! It was nice a pleasure to be on a project with you! Of course, I have to thank for 'Watschel' who supported me during the last few months. It was nice to be in Potsdam and to discuss my results with you and the other people from the AWI (AC)3 group.

In this way, I would like to thank all the (AC)3 people for the last four years. It was nice to meet you and spend time with you! A special thanks goes to Christa who motivated me in bad times. It was so nice to have you as the IRTG coordinator in the second phase. Thank you for all your support!

Further, I would like to thank the whole AWARES group. A big thanks to Christoph who supported me a lot in the beginning. Thank you for your wise advice. Further, it was nice to have international PhD students in our group: DC and José! It was nice to learn something about your culture. It was very nice to have you in our working group. Kerstin, thank you for proofreading some parts of this thesis.

In the end, I would like to thank Tracy, Fiona, and Imke for their support during the last few years. In between it was a very hard time. Thank you for giving me the strength to finish this thesis. Imke, you and Leonie were the best office mates!!! I was glad to share the office with you.

A special thanks goes to my family, especially to my mother! Thank you so much for your support. I am so happy to have you as my mum. I can always rely on you! I would also like to thank Hanny and Luna who had to leave us during this journey.

The very greatest thank, however, goes to Nils. Thank you so much for always supporting me. For catching me when things aren't going well. I'm so happy to have you by my side. Thank you sooo much for your support during the last days and nights.